Strojniški vestnik – Journal of Mechanical Engineering (SV-JME)

Cover: Deserving of contribution to the Faculty development (from up-left to right-down):

Acad. Prof. Emer. Feliks Lobe (Eng.)
Prof. Emer. Albert Struna, PhD. (Hon. Causa) (Eng.)
Acad. Prof. Emer. Anton Kuhelj, PhD. (Eng.)
Prof. Emer. Zoran Rant, PhD. (Eng.)
Prof. Emer. Franček Kovačec (Eng.)
Prof. Emer. Ervin Prelog. PhD. (Eng.)
Prof. Emer. Bojan Kraut, PhD. (Hon. Causa) (Eng.)
Acad. Prof. Emer. Janez Peklenik, PhD., (Eng.)

Image courtesy:
Photo: Aleš Fevžer

ISSN 0039-2480, ISSN 2536-2948 (online)

Contents

Strojniški vestnik - Journal of Mechanical Engineering
volume 65, (2019), number 11-12
Ljubljana, November-December 2019
ISSN 0039-2480

Published monthly

University *of Ljubljana*
Faculty *of Mechanical Engineering*

Editorial

The beginning of a great age for the small Slovenian nation: the hearth and home of science and (technical) culture is born

Centenary of the University of Ljubljana and the study of mechanical engineering

On 23 July 1919, Prince Regent Alexander Karađorđević came to Ljubljana to sign an act with only three articles, founding the University of the Kingdom of Serbs, Croats and Slovenes, today known as the University of Ljubljana (UL). It was that simple in the newly established Kingdom of Serbs, Croats and Slovenes. The founding members were the Faculty of Arts, Faculty of Medicine, Faculty of Law, Technical Faculty and Faculty of Theology. Brushing aside some objections that the Slovenian university was founded more than a hundred years ago – there are even opinions that it happened three centuries ago – we are celebrating one of the first milestones in the arrival of higher education on our soil.

Special credit for the foundation of a Slovenian University in Ljubljana goes to its mayor Ivan Hribar (holding office between 1896 and 1910). In 1912, he initiated the establishment of the University sector with the Ljubljana City Council, which sought young and talented Slovenian specialists and provided them financial support to prepare for an academic career. Special mention also goes to Dr. Mihajlo Rostohar, assistant professor at the Prague university, who founded the University Commission under the National government in November 1918, and Dr. Danilo Majaron who was elected to become its president on 5 December 1919. Dr. Danilo Majaron became the first honorary doctor at the University of Ljubljana on 22 June 1929.

First lectures were held on 3 December 1919 and this is also the official birth date of the UL. However, if the official birth of the UL was moved back to the time when the first chairs for the study of philosophy were opened in Ljubljana (for logic and canon law and for physics and mathematics), UL would now be more than three hundred years old. UL is now celebrating the hundredth anniversary of university in Slovenian language. On Wednesday, the 3rd of December 2019 from 9 to 10am, Dr. Fran Ramovš held the first lecture in Slovenian language in the hall of the Provincial Mansion, today's University assembly hall. His lecture about the historical grammar of Slovenian language began with the following address: "On this day, as we are expecting a new era, a new life, as we are establishing a Slovenian university, allow me to greet you as the first students of our Alma mater. In this holy moment, our nation is entering history that can never be erased."

This was the beginning of a great age for the small Slovenian nation and our hearth of science and culture was born.

The first rector was Dr. Josip Plemelj, one of the most important mathematicians at the beginning of the 20th century, the first dean of the Technical faculty was Dr. Karol Hinterlechner, a geologist and external member of the Czechoslovak Academy of Sciences, and the first doctoral student was Ana Mayer, who

successfully defended her thesis "The effects of formalin on starch" on 15 July 1920.

In the first academic year, the five founding faculties accepted 942 students, and only 3 percent of them were women. On 31 August 1919, the first 18 professors of UL were appointed by royal decree, one person not accepting the professorship. In the first decade of the University, more than ten top Russian scholars joined the ranks after fleeing their homeland during the revolution. The Russian lecturers introduced several new scientific fields, thereby bringing the UL to the level of other comparable European universities despite its young age. The quality of lectures on the university was significantly influenced both by Slovenian scientists who were previously active in the international academic circles, like mathematician Dr. Josip Plemelj, chemist Dr. Maks Samec and Dr. Milan Vidmar, and the foreign scientists.

Money was important then as it is today, and there were attempts to abolish the Technical faculty and ideas to establish departments of technical faculties in Beograd, Zagreb and Ljubljana. This would curtail the activities of the Technical faculty in Ljubljana, which was almost entirely equipped by the private capital of Slovenian industrialists. At the end of the 1930s, construction of the institutes of mechanical and chemical engineering under the Technical faculty began.

For the sake of comparison: there are 37,874 students enrolled at 26 member faculties of the UL in 2019, 60 percent of them women, placing the institution among the top 3% universities worldwide. In the ARWU ranking (Academic Ranking of World Universities, one of the most important academic rankings), the UL has had a spot among the 500 best universities for a number of years, in the CWUR ranking (The Center for World University Rankings) it holds the 370. spot, and in the THE ranking (Times Higher Education) it ranks in the 601–800 group.

Organisational development of the Technical faculty and the Faculty of mechanical engineering:
- 1919–1945: UL, Technical faculty, Department for electrical and mechanical engineering (two-year study of mechanical engineering)
- 1945–1950: UL, Technical faculty, Department of mechanical engineering (full study of mechanical engineering)
- 1950-1954: Technical college, Faculty of mechanical engineering
- 1954–1957: UL, Technical faculty, Department of mechanical engineering
- 1957–1960: UL, Faculty of electrical and mechanical engineering
- From 1960: UL, Faculty of mechanical engineering.

Even before the UL was formally founded, higher-education lectures of mechanical, electrical and construction engineering began on 19 May 1919. By autumn, the students were delivered the whole subject matter for year one. In 1919, Dobromil Uran, Albert Struna and Franc Smolik were among the enrollees in the "Temporary technical college course". After World War II, they were appointed higher-education teachers at the Technical faculty. Previous to that, all of them had successful careers in the industry. The Technical faculty's curriculum was divided as follows: mathematical courses, natural sciences, construction and architecture, mechanical and electrical engineering, mining and blast-furnace practice, political science and law courses, as well as two courses in the "various" category.

One of the first 18 professors was Dr. Milan Vidmar, an expert in electrical and mechanical engineering who earned his PhD in classical mechanical engineering in 1922 with his thesis "Theory of centrifugal pumps" (Theorie der Kreiselpumpe). Dr. Vidmar – also a chess grandmaster – loved electrical engineering, but he was aware of the significance of mechanical engineering and therefore lectured the Theoretical mechanical engineering course. The enrolment at the UL's Technical faculty was relatively good, with two ladies attending the first study year. The enrolment figures dropped in the 1930s, probably due to the Great Depression.

Dr. Milan Vidmar personally invited Feliks Lobe to come to the Technical faculty. Due to his vast experience in the industry, Lobe was immediately appointed associate professor. The arrival of Feliks Lobe significantly invigorated the field of mechanical engineering at the Technical faculty, but it has not gained full momentum for several reasons. Dr. Milan Vidmar is regarded as the initiator of the study of mechanical engineering at the UL. He understood the importance of our profession and supported Feliks Lobe throughout. Lobe invested several years of personal efforts to realise the study of mechanical engineering in full extent and started to lecture the Thermodynamics and Prime movers courses, adding the Mechanical technology course after 1937. His assistant was Leopold Andrée and his associate Boris Černigoj. Both became higher-education teachers after World War II. The great spirit of Feliks Lobe, who later became an academician and was awarded an honorary PhD degree by the UL, envisaged two major branches of mechanical engineering: – solid body

mechanics and fluid mechanics, meaning a parallel development of technological and energy engineering.

The lecturers in the 1940/41 study year were: assoc. prof. Romeo Strojnik (Mechanical drafting, Machine elements II, Elevators), full prof. Feliks Lobe (Prime movers I, Prime movers II, General mechanical technology II), assist. prof. Dr. Dušan Avsec (Themodynamics), part-time lecturer Albert Struna, later full professor and rector at the UL (Construction and theory of motor vehicles) and part-time lecturer Ciril Rekar (General mechanical technology II). After World War II, the Technical faculty was divided into six departments, one of them being the mechanical engineering department. The study of mechanical engineering in full extent brought an expanded syllabus and several new lecturers, most of them picked by Feliks Lobe. In 1946, the following lecturers were appointed to higher-education titles and became fully employed: assist. prof Leopold Andrée, full prof. Leon Kavčnik, assoc. prof. Franček Kovačec, assoc. prof. Bojan Kraut, full prof. Zoran Rant and full prof. Anton Vakselj. Nine institutes were founded under the department of mechanical engineering at the Technical faculty, about a half of them devoted to energy engineering and the other half to technology.

On 31 July 1948, Jožef Herman and Josip Kuralt graduated as the first mechanical engineers, and Zoran Rant was one of the first to obtain a doctoral degree (in 1950).

In addition to everyone mentioned above, the following lecturers have left a great mark on the development of the study of mechanical engineering in the period until 1960 (in alphabet order): Josip Boncelj, Jože Hlebanja, Leon Kavčnik, Branko Kozina, Anton Kuhelj, Boleslav Likar, Ervin Prelog, Stane Premelč, Ciril Rekar, Viktor Savnik, Franc Smolik, Albert Struna, Vladimir Staněk, Dobromil Uran, Anton Vakselj and Ivo Vušković.

The Technical faculty was abolished in 1957 and the departments for electrical and mechanical engineering merged to form the Faculty of electrical and mechanical engineering. However, this association only lasted three years. The Faculty of mechanical engineering (FS) came to existence on 1 October 1960 as an independent unit under the UL. FS began to grow in staff and facilities. The first dean of the independent Faculty of mechanical engineering was Zoran Rant.

When founded, FS had four chairs: Chair for mathematics and other basic courses, Chair for work machines and transport, Chair for technology and Chair for prime movers and heat engines. In academic year 1960/61, 264 students were enrolled in year one, 167 students in year two, 143 students in year three, and 113 students in year four. There were also 214 graduate year students. The number of chairs rose to six in academic year 1971/72, and then to seven a year later. This number remained unchanged for 25 years. One third of the chairs dealt with energy engineering and two thirds covered technology and manufacturing.

What was then the Faculty council founded in 1962 the Institute of mechanical engineering as a financially independent institution that was inextricably linked to the FS. The purpose of the Institute was to do research work and collaborate with the industry. A three-cycle study programme was introduced in 1960 (bachelor's, master's and doctoral degree). The undergraduate studies were shortened from ten to nine semesters, including the diploma thesis, while completing the master's studies became a requirement for the doctoral studies. It was a change in the tradition of several decades, which extended the path to the doctoral thesis. After approximately 40 years, the study programme was again reverted to the old model: ten semesters including the diploma thesis and then direct transition to writing the doctoral thesis.

In academic year 1996/97, the Faculty started educating students at the university level with a more theoretical approach (10 semesters) and introduced a practically oriented professional higher education study programme (8 semesters, including 6 months of practical training and the diploma thesis). The Faculty Senate consisted solely of full professors and the decision that every full professor can have a chair led to the number of chairs rising from 7 to 13 in the academic year 1997/98. In the academic year 2008/9, the FS has started executing the renewed academic and professional study programmes according to the Bologna principles.

Today, the FS is the leading multidisciplinary research-oriented faculty in the field of mechanical engineering in Slovenia. It recognises young talents and raises them to become excellent scientists and progressive experts. Many famous Slovenians who studied or graduated at the FS are now in leadership positions or work in scientific institutions worldwide, the enterprise sector, politics etc. Internationalization has also enabled international student and young researcher exchange programs.

In academic year 2018/19, there were 1,652 students enrolled in the 1st cycle academic programme, the Bologna 2nd cycle master study programme and the 1st cycle professional study programme, as well as 95 doctoral students in the 3rd cycle doctoral study programme. 415 students have graduated and 11

students have earned their doctoral degrees in 2018. Among the staff of 373 there were 44 teachers, 79 assistants and 158 researchers who participated in 45 international research projects and 179 collaborative projects with the industry. They have published 161 original research articles and submitted 6 patent applications. The FS comprised 18 chairs with 39 research laboratories and centres.

The University of Ljubljana rectors recruited from the Technical faculty and the Faculty of mechanical engineering were: Milan Vidmar (1928–1929), Anton Kuhelj (1954–1956), Albert Struna (1964–1967), Ervin Prelog (1976–1978), Polde Leskovar (1987) and Janez Peklenik (1987–1989).

The foundation of the UL 100 years ago made it possible to start educating scientists in Slovenia. Slovenian scientists were very successful even previous to that, but they were usually active in the Germanic-speaking area and used to write and lecture in German. The birth of the UL also made Slovenian a language of science. Science promotion is indispensable for an educated society, for the usage of Slovenian language in higher education, and for preserving the language of our small Slovenian nation.

This special issue of SV-JME celebrates the 100th anniversary of the UL and the studies of mechanical engineering and presents the research achievements of Slovenian UL scientists in the field of mechanical engineering. We have become a part of Slovenian intelligence objectively setting the boundaries for the development and advance of Slovenian nation. A particular nation's culture is based in its entirety on the nuance of the ebb and flow of life.

VIVAT, CRESCAT, FLOREAT!

Vincenc Butala
Editor-in-Chief

References:

University of Ljubljana, Faculty of Mechanical Engineering: Zgodovina strojništva in tehniške kulture na Slovenskem, Ljubljana, May 2010.
75 years of the University of Ljubljana, Ljubljana, 1994
Celebration of the 90th anniversary of study of mechanical engineering – proceedings, University of Ljubljana, Faculty of Mechanical Engineering, 2010
University of Ljubljana, https://www.uni-lj.si/o_univerzi_v_ljubljani/100_let_ul/, retrieved on 29 October 2019
University of Ljubljana, Faculty of Mechanical Engineering: Annual Report 2018

Elastocaloric Cooling: State-of-the-art and Future Challenges in Designing Regenerative Elastocaloric Devices

Parham Kabirifar – Andrej Žerovnik – Žiga Ahčin – Luka Porenta – Miha Brojan – Jaka Tušek*
University of Ljubljana, Faculty of Mechanical Engineering, Slovenia

The elastocaloric cooling, utilizing latent heat associated with martensitic transformation in shape-memory alloys, is being considered in the recent years as one of the most promising alternatives to vapour compression cooling technology. It can be more efficient and completely harmless to the environment and people. In the first part of this work, the basics of the elastocaloric effect (eCE) and the state-of-the-art in the field of elastocaloric materials and devices are presented. In the second part, we are addressing crucial challenges in designing active elastocaloric regenerators, which are currently showing the largest potential for utilization of eCE in practical devices. Another key component of elastocaloric technology is a driver mechanism that needs to provide loading for active elastocaloric regenerators in an efficient way and recover the released energy during their unloading. Different driver mechanisms are reviewed and the work recovery potential is discussed in the third part of this work.
Keywords: elastocaloric effect, cooling, active elastocaloric regenerator, fatigue life, driver mechanism

Highlights
- Elastocaloric cooling technology shows high potential as an alternative to vapour compression cooling.
- Active elastocaloric regenerator was demonstrated as the most promising concept of utilizing the elastocaloric effect in practical devices.
- Compressive loading can significantly increase fatigue life of elastocaloric materials compared to tensile loading.
- Driver mechanisms utilizing mechanical work recovery can decrease the input work that is needed to run the elastocaloric cooling cycle.

0 INTRODUCTION

Modern society is totally dependent on cooling, refrigeration and air-conditioning. In Europe, 70 % of food is chilled or frozen; 90 % of all vaccines must be chilled; and air-conditioning is essentially everywhere, in our homes, cars, offices, etc. In the USA, 87 % of households use air-conditioning, the energy consumption of which is more than Africa's total electricity output. Moreover, the energy consumption required for cooling and air-conditioning is growing exponentially. Nowadays, in the developed countries it accounts for around 20 % of the total energy consumption; by 2060, the energy used for cooling will overtake that of heating and by the end of the century, cooling will outstrip heating by 60 % [1]. Nevertheless, that is only half of the problem. Nearly all cooling and air-conditioning devices out there, as well as heat-pumps, are based on vapour compression technology, which is over a century old. In fact, this is one of the oldest electricity-based technologies still in use, without a viable alternative [2]. Over the decades of development, vapour compression technology has increased its efficiency and specific power (and therefore its compactness) along with reducing its environmental impact. However, from the thermodynamic perspective, the

efficiency of the vapour compression cooling cycle has reached its limit and no significant improvements should be expected in the future. Despite decades of development, vapour compression technology has still three important disadvantages. The first problem is its efficiency. The exergy efficiency, which is the ratio between the actual and Carnot's coefficient of performance (COP), of the vast majority of the cooling systems in use is well below 30 %. The second problem is the refrigerants that could leak into the atmosphere and harm the environment/ people when the refrigerator is discarded or damaged. Nowadays, these refrigerants are no longer ozone depleting (such as chlorofluorocarbons), as they have been banned since 1989 by the Montreal Protocol on Substances that Deplete the Ozone Layer [3]. We have replaced them mostly with hydrofluorocarbons, which have another problem; they cause a significant greenhouse effect (up to a few thousand times more than carbon dioxide). As a consequence, these types of refrigerants are already subject to a ban (according to the Kigali Agreement to the Montreal Protocol [3] signed in 2016) and in the near future need to be replaced preferably with natural refrigerants such as hydrocarbons (e.g. isobutene), carbon dioxide and ammonia. Nonetheless, such alternatives can be explosive in large quantities (hydrocarbons), require

---

very high pressures (carbon dioxide) and be toxic (ammonia) [4] and [5]. Therefore, the problem of refrigerants is not yet sufficiently solved and further research and development is required to fulfil all the environmental and safety requirements. The third weakness of vapour compression technology, which can be very important for some applications, is the presence of vibrations and noises that are inevitable during the operation of a compressor.

In recent decades, several alternatives to vapour compression were discovered and developed but owing to various reasons such as either low efficiency or low specific power or impractical applications, none of them has proven to be a serious alternative for the everyday cooling needs. However, more recently the so-called caloric cooling technologies have shown significant potentials as serious alternatives to vapour compression technology [6] and [7]. By caloric cooling technologies, we mean magnetocaloric (magnetic), electrocaloric, elastocaloric and barocaloric cooling. The basis of caloric cooling is to exploit the latent heat of a solid-state phase transformation of a ferroic material by applying an external magnetic, electric or mechanical field. These technologies can be significantly more efficient (with theoretical exergy efficiency above 50 %), completely harmless to the environment (by applying solid-state refrigerants) and potentially vibration and noise free [8]. Among the caloric cooling technologies, the most matured and developed is the magnetic (magnetocaloric) refrigeration with up to 100 prototypes developed in universities and laboratories around the world [8] and [9]. However, more than 20 years of research on magnetocaloric materials and magnetic refrigeration systems has still failed to provide the necessary breakthrough that could lead to a commercial realisation of this technology and satisfy the urgent global need for a more efficient and environmentally harmless refrigeration. The possibility of inducing a solid-state phase transformation via martensitic phase transformation and generating a caloric effect by means of mechanical stress i.e. the elastocaloric effect (eCE) in superelastic shape-memory alloys (SMAs), opens up new avenues for solid-state refrigeration. According to the great potential of eCE, the US Department of Energy in 2014 [2] and more recently also the European Commission in 2016 [10] selected the elastocaloric cooling technology as the most promising alternative to the vapour compression refrigeration in the future.

In this work, the basics of eCE and the state-of-the-art in the field of elastocaloric materials and devices are presented. Since the most promising results (in terms of cooling and heat-pumping characteristics) were achieved using a regenerative elastocaloric cooling cycle, the second part of this work focuses on the challenges of designing an elastocaloric porous structure to be utilized in an active elastocaloric regenerator, which is the first key component of a regenerative elastocaloric cooling device. The second key component of an elastocaloric cooling device is a driver mechanism that exerts mechanical stress on the elastocaloric material. Different elastocaloric driver mechanisms are reviewed and discussed in the third part of the paper.

1 STATE-OF-THE-ART IN ELASTOCALORIC TECHNOLOGY

1.1 Shape-memory Materials and the Basics of the eCE

The eCE is strongly related to the superelasticity of SMAs and the latent heat that is released/absorbed during the forward/reverse martensitic phase transformation. Martensitic transformation is a reversible solid-state displacive (non-diffusional) crystalline phase transformation dominated by a shear between a high-symmetry high-temperature parent phase and a low-symmetry low-temperature product phase (ordered B2 austenite parent phase and B19′ monoclinic phase in the case of the near-equiatomic Ni-Ti alloy) [11]. The martensitic phase transformation is responsible for two unique properties of SMAs i.e. shape-memory effect and superelasticity. In shape-memory effect, a mechanically deformed SMA can "remember" its initial shape (before being deformed) and regain it upon being heated. In superelasticity, the SMA can be loaded to very large strains (up to 8.5 %) and release the transformation heat. Upon being unloaded, it can regain its initial shape (without any permanent deformation) and absorb the heat. Occurrence of shape-memory effect or superelasticity in a particular SMA sample depends on its temperature. Above austenite stability temperature (A_f), a SMA sample is superplastic and below martensite stability temperature (M_f), the sample exhibits shape-memory behaviour. These two properties make SMAs very attractive to various applications in different areas such as the automotive and aircraft industries (actuators, dampers, variable geometry chevrons, etc.), robotics, civil engineering (concrete beam reinforced with SMA) and in particular in medical and biomedical applications (implants, orthodontic wires, self-expandable stents, minimally invasive surgical instruments, etc.) [12]. The most well-known SMA is the binary near-equiatomic Ni-Ti alloy, which was first reported in 1963 and remains by far the most widely

applied SMA in various applications owing to its superior fatigue behaviour (among other SMAs) and biocompatibility. Other shape-memory (superelastic) alloys which are developed and characterized are Ni-Ti based (alloyed with Cu, Co, Pd, Fe, etc.), Cu-based (alloyed with Al, Ni, Zn, etc.), Fe-based (alloyed with Pd, Mn, Si, Ni, etc.) and magnetic SMAs (e.g. Ni-Fe-Ga and Ni-Mn-Co). The shape-memory effect and superelasticity are also exhibited by polymers (e.g. natural rubber) although such behaviours in polymers are not caused by the martensitic phase transformation [12].

Even though the latent heat release and absorption during the martensitic phase transformation in superelastic alloys and the temperature changes associated with them have been known for almost 40 years [13], it was not until recently that the eCE was recognized as a potential cooling or heat-pumping mechanism [14]. In Ni-Ti alloys, the released transformation (latent) heat can be as high as 35 J/g [15]. The basics of an elastocaloric cycle are the following. When an SMA in the austenite phase (at temperatures above A_f) is strained/stressed, the exothermic forward martensitic transformation (austenite to martensite) occurs. The generated heat could be slowly dissipated (under isothermal conditions) or under adiabatic conditions, heat the sample up and enable it to subsequently transfer the generated heat to the surroundings (or the heat sink). When the stress is removed, the endothermic reverse transformation (martensite to austenite) occurs, which under adiabatic conditions, cools down the sample and enables it to absorb the heat from the surrounding (or the heat source). An elastocaloric cooling cycle is shown in Fig. 1.

The eCE can be quantitatively described by isothermal entropy change (Eq. (1)) and/or adiabatic temperature change (Eq. (2)), which can be calculated using the following equations (derived from Maxwell relation):

$$\Delta s_{iso} = \frac{1}{\rho} \int_{\sigma_1}^{\sigma_2} \left(\frac{\partial \varepsilon}{\partial T} \right)_\sigma d\sigma, \qquad (1)$$

$$\Delta T_{ad} \approx -\frac{1}{\rho} \frac{T_0}{c} \Delta s_{iso}. \qquad (2)$$

In the above equations, ρ, ε, σ, c and T_0 are material's density, applied strain, applied stress, specific heat of the material and material's temperature, respectively. It should be noted that in the presented form, Eq. (2) can be used only for estimating the adiabatic temperature changes since the specific heat (c) is taken as a constant value and the temperature at
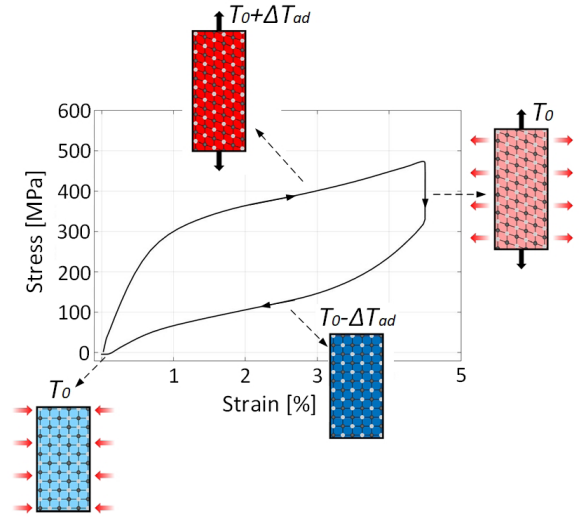
Fig. 1. *Schematic representation of the eCE in the superelastic cycle*

which adiabatic temperature change is calculated does not include the sample's self-heating and self-cooling under the adiabatic conditions. Details on a more accurate way of calculating the adiabatic temperature changes could be found elsewhere [16].

1.2 Elastocaloric Materials

Generally speaking, all SMAs (and also shape-memory polymers) can be considered as potential elastocaloric materials if their transformation temperatures (A_f) are below the working temperature of the device, which is a precondition for reversible superelasticity. Table S1 of the **Supplementary Data** shows the basic elastocaloric properties for the most interesting elastocaloric materials published to date. The elastocaloric materials can be divided into three main groups: shape-memory alloy-based (Ni-Ti-based, Cu-based and Fe-based), shape-memory polymer-based (SMP) and magnetic shape-memory alloy-based (MSMA). In addition to the adiabatic temperature changes (and their corresponding applied stress/strain), which are the most important elastocaloric parameters, Table S1 of the **Supplementary Data** also shows other parameters such as sample preparation, sample's microstructure and geometry, sample's history (stabilization and training), loading mode (tension or compression) and measuring technique (thermocouples or IR camera) that can all significantly affect the eCE. For example, it has been demonstrated [17] that eCE is decreasing during the initial cycling before the sample is stabilized. Moreover, it is well known that

SMAs exhibit tension-compression asymmetry [18] and that their behaviour strongly depends on their microstructure (e.g. grain size, texture, presence and type of precipitates, etc.) [19] and [20]. It is therefore important to specify such parameters when comparing different elastocaloric materials.

The most studied eCE is that of the binary Ni-Ti alloy under tensile loading, where adiabatic temperature changes of up to around 25 K were measured at room temperature [21] and [22]. Much less explored is the eCE in Ni-Ti alloys under compressive loading, nevertheless, the initial results show that adiabatic temperature changes similar to those of tension can be obtained under compression as well. It has been demonstrated that alloying binary Ni-Ti with Cu, V and/or Co improves its fatigue life and/or decreases its hysteresis but at the expense of decreasing its adiabatic temperature changes [17] and [23] to [26]. In Cu-based SMAs, such as Cu-Zn-Al and Cu-Al-Ni, adiabatic temperature changes of up to 15 K were measured. The main advantage of these alloys is that such adiabatic temperature changes are generated under smaller transformation stresses compared to Ni-Ti [13], [14] and [27]. In Fe-based SMAs, such as Fe-Rh and Fe-Pd, adiabatic temperature changes of up to 5 K were measured along with a minor hysteresis, which is the main advantage of these alloys [28] and [29]. Nonetheless, high prices of Rh and Pd prevents practical applications of these alloys.

The adiabatic temperature changes in MSMA are up to around 10 K at moderate stresses but since most of these alloys are brittle, their application in practical cooling devices would be impractical [30] and [31]. Very recently, a new elastocaloric alloy (Ni-Mn-Ti-B) was discovered in which a reversible adiabatic temperature change of 31.5 K was measured, which is the largest directly measured reproducible caloric effect so far [32]. With that, the authors showed that there is still plenty of room for improvements in the eCE by designing new elastocaloric materials. In the near future, we can, therefore, expect elastocaloric materials with even higher eCE.

Among shape-memory polymers, the most studied for elastocaloric proposes is natural rubber [33], where adiabatic temperature changes of up to 12 K were measured at very small stresses (up to 2 MPa), however, its main disadvantages for practical elastocaloric applications are poor thermal (heat transfer) properties and in particular, very high required strains (up to 600 %), which makes application of elastocaloric polymers very unpractical.

A recent comprehensive review on elastocaloric alloys can be found in [34].

1.3 Elastocaloric Devices

In recent years, concurrent with the research and development in elastocaloric materials, a significant progress was made in the design and development of the elastocaloric cooling/heat-pumping devices [35] to [45] and the corresponding numerical models [46] to [49] for simulation and optimization of their performance. In general, the proposed concepts of elastocaloric devices can be divided into two main groups:
- concepts based on single elastocaloric element(s) with solid-to-solid contact heat transfer;
- concepts based on porous elastocaloric structures with convective heat transfer.

The most widely applied thermodynamic cycle for exploitation of eCE (for both of the above-mentioned concepts) is Brayton thermodynamic cycle, which is based on four basic operational steps (Fig. 2):
- adiabatic loading (where austenite (A) to martensite (M) transformation occurs), which owing to the eCE, heats up the elastocaloric material;
- heat transfer from the elastocaloric material to the heat sink (by contact or convective heat transfer);
- adiabatic unloading (where martensite (M) to austenite (A) transformation occurs), which owing to the eCE, cools down the elastocaloric material;
- heat transfer from the heat source to the elastocaloric material (by contact or convective heat transfer).

In general, elastocaloric materials in cooling/heat-pumping devices can also operate based on other thermodynamic cycles such as Ericsson, Carnot or some combination of them [50]. Moreover, cooling/heat-pumping devices can operate in compliance with single-stage or multi-stage thermodynamic cycles. The latter can be further divided into heat-recovery, active regenerative and cascade cycles.

The main difference between a single-stage and a multi-stage thermodynamic cycle is in the generated temperature span. In single-stage devices, the maximum temperature span is limited by the adiabatic temperature changes (ΔT_{ad}) of the material. Therefore, such devices can only operate around a surrounding temperature (T_{surr}) as shown in Fig. 2c. On the other hand, multi-stage thermodynamic cycles enable an increase in the temperature span (T_{span}) between the heat sink and the heat source. Among them, currently, the largest potential for practical applications is demonstrated by an active regenerative thermodynamic cycle (owing to its compactness
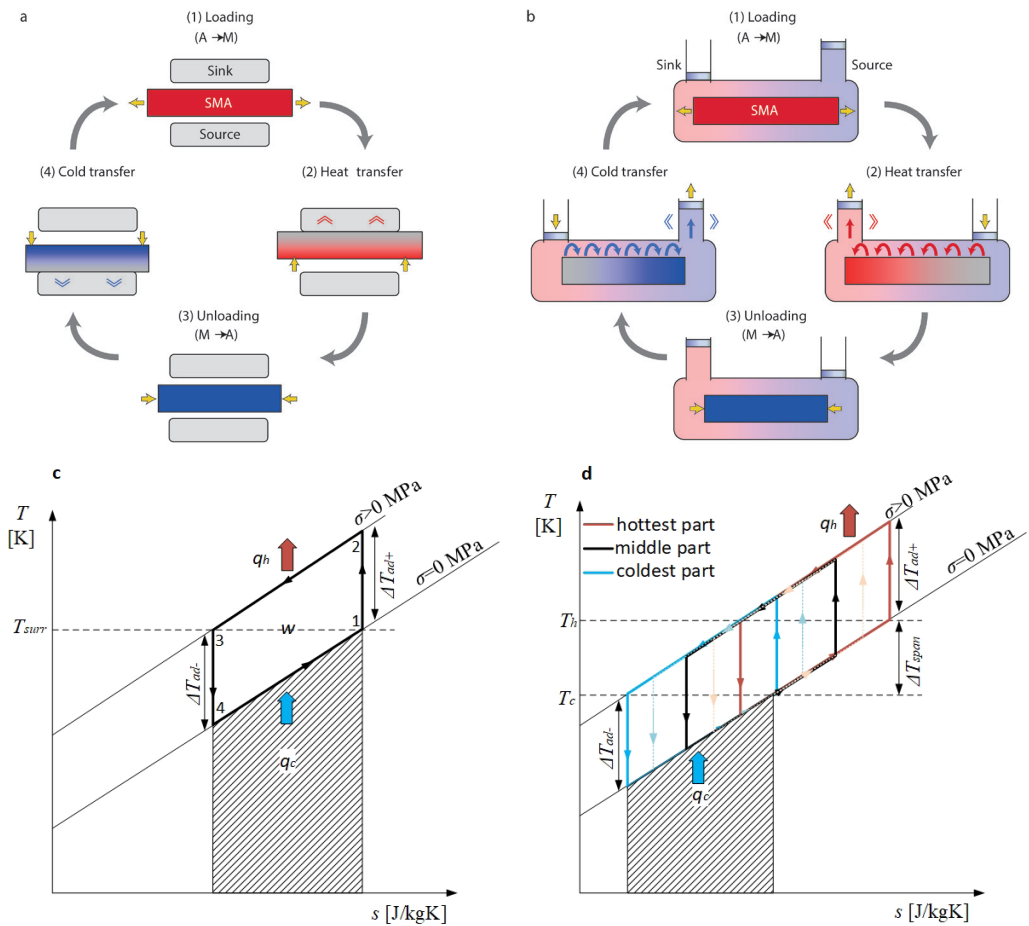
Fig. 2. *A schematic representation of four basic operational steps of: a) a single-stage elastocaloric device with a solid-to-solid contact heat transfer mechanism, and b) a regenerative elastocaloric device with a convective (through porous material) heat transfer mechanism [51] and temperature (T)-entropy (s) diagrams: of c) a single-stage, and d) a regenerative elastocaloric Brayton thermodynamic cycle*

and good cooling characteristics). This concept was first presented for utilizing the magnetocaloric effect in magnetic refrigeration [8] and enables generating temperature spans along the length of the regenerator that can be several times larger than the adiabatic temperature changes of the magnetocaloric or elastocaloric material itself. This is crucial for application in practical cooling or heat-pumping devices where temperature spans of 30 K or more are usually required. An active elastocaloric regenerator is a porous structure made of an elastocaloric material through which a heat-transfer fluid is pumped in the counter-flow direction. If the operating conditions (frequency, mass flow rate, etc.) are appropriate, a temperature span between the heat source temperature (T_h) and the heat sink temperature (T_c) is established under the steady-state conditions. Accordingly, each element of the elastocaloric material along its

length performs its own thermodynamic cycle at a slightly different temperature (between T_h and T_c) as shown in Fig. 2d. As also shown in Fig. 2d, the entire elastocaloric material in the regenerator does not generate useful cooling (q_c) or heating energy (q_h) since a portion of the energy generated by the eCE is spent for establishing the temperature span. In general, the active regenerative cycle is similar to the cascade system, where several thermodynamic cycles (connected in series) are used to increase the temperature span. As explained in [8], the major difference between a cascade cycle and an active regenerative one is in the fact that in the latter, the heat is not pumped directly between the neighbouring particles and instead, all the particles, which are indirectly coupled through the heat-transfer fluid, simultaneously accept or reject the heat to the heat-transfer fluid.

In the recent years, researchers from Saarland University [36] and Karlsruhe Institute of Technology [39] and [40] have presented several different single-stage cooling/heat-pumping systems that operate based on a single (or double) elastocaloric foil that is loaded in tension and moves between the heat sink and the heat source and transfers the heat by contacting them directly. The maximum temperature span measured on this type of device was up to 14 K [39]. Such a concept was suggested to be applied in novel microelectromechanical systems (MEMS) such as temperature control of lab-on-chip systems or micro cooling in biomedical applications. Very recently, a 3-stage cascade elastocaloric device with a solid-to-solid contact heat transfer mechanism was developed and tested [45]. The authors demonstrated that, compared with a single-stage system, a 3-stage cascade system can increase the temperature span by a factor of two and reach a maximum temperature span of 15 K. On the other hand, the specific cooling power and the COP was reduced by almost a factor of 3 compared to a single-stage operation. In 2015, Qian et al. [35] presented an elastocaloric cooling system with Ni-Ti tubes loaded in compression, through which a heat-transfer fluid was pumped. The system utilizes the so-called heat recovery principle by using a bypass between the elastocaloric structure (tubes) and the external heat exchangers that stores a part of the energy produced by the eCE and then preheats or precools the heat transfer fluid with an aim of increasing the generated temperature span. The maximum measured temperature span of this device was 4.7 K and the maximum specific cooling power was 600 W per kg of the elastocaloric material. Even better results were obtained using active regenerative principle as shown by Tušek et al. [37] and Engelbrecht et al. [38]. This device, which was based on a set of thin Ni-Ti plates under tension, operated as a heat-pump and generated a maximum measured temperature span of 20 K, a corresponding specific heating power of up to 800 W per kg of the elastocaloric material, a maximum COP value of up to 7 and an exergy efficiency of 19 % (at a temperature span of 13 K). In 2018, Kirsch et al. [41] and [42] presented a new rotary elastocaloric device based on a set of Ni-Ti wires loaded in tension and air as the heat transfer medium. This device can be considered as the first pre-industrial prototype of an elastocaloric device, but full experimental results are not yet available. Recently, also a cascade elastocaloric cooling system with Ni-Ti tubes loaded in compression was proposed [43]. As a heat transfer medium, a two-phase medium (gas/liquid) controlled with check valves was used in

order to increase the convective heat transfer (similar to a heat-pipe concept). Unfortunately, no cooling characteristics other than the temperature span of the device are published to date. In 2019, another three-stage cascade elastocaloric device with a single Ni-Ti wire loaded in tension was designed, built and tested [44]. A maximum temperature span of 28.3 K was measured, which is currently the largest temperature span measured for elastocaloric devices. Table 1 shows the overview and comparison of the developed proof-of-the-concept elastocaloric devices to date. Maximum temperature span, maximum specific cooling/heating power per mass of the elastocaloric material and the maximum COP and exergy efficiency are presented in Table 1 (if available). The COP is defined as the ratio between the cooling/heating power and the input work, while exergy efficiency is defined as the ratio between the actual COP and the maximum theoretical COP (also called the Carnot COP) that would be possible over a certain temperature span. It should be noted that all the COP values published for elastocaloric devices are based on the assumptions that a perfect recovery of the released mechanical energy is achieved during the unloading and that the input work is only related to the area enclosed in the stress-strain diagram (hysteresis) – see Section 3.2. for more details on mechanical work recovery.

2 DEVELOPMENT OF SUPERELASTIC POROUS STRUCTURES (ACTIVE ELASTOCALORIC REGENERATORS)

The focus of this section is on the development of elastocaloric (superelastic) porous structures that will serve as active elastocaloric regenerators. The crucial challenges in designing efficient and fatigue-resistant active elastocaloric regenerators are addressed and discussed.

2.1 Potential Geometries of an Active elastocaloric regenerator

Active elastocaloric regenerators can be made from different basic shapes of SMAs such as wires, rods, plates, tubes and blocks. Using these shapes, it is possible to make parallel-plate (Fig. 3a) [37] and [38] or wire-based (Fig. 3b) [41] and [42] regenerator for tensile loading. Wires are particularly challenging as they are not in a dog-bone shape and the stress concentration at the grip section usually results in their premature failure. On the other hand, potential geometries for compressive loading can be made from tubes with supporting elements placed along their length (Fig. 3c) or as a set of tubes in a holder (Fig. 3d)

Table 1. *Overview of experimentally obtained cooling/heating characteristics of elastocaloric devices tested to date*

Institution	Concept/ principle	eCM	Max. temp. span	Max. specific cooling/heating power	Max. COP / Max. exergy eff.	Ref.
Univ. of Maryland (2015)	Heat recovery	Ni-Ti tubes in compression	4.7 K	600 W/kg (at $\Delta T_{span}=0$ K)	n/a	[35]
Saarland Univ. (2015)	Single-stage	Ni-Ti sheet in tension	7 K	n/a	n/a	[36]
Technical Univ. of Denmark and Univ. of Ljubljana (2016, 2017)	Active elastocaloric regeneration	Ni-Ti sheets in tension	20 K	800 W/kg (at $\Delta T_{span}=15$ K)	7 (at $\Delta T_{span}=5$ K) / 19 % (at $\Delta T_{span}=13$ K)	[37] and [38]
Karlsruhe Inst. of Technology (2017)	Single-stage	Ni-Ti-Fe and Ti-Ni-Cu-Co sheets in tension	14 K	n/a	6.7 (at $\Delta T_{span}=6.3$ K) / 15 % (at $\Delta T_{span}=10.5$ K)	[39] and [40]
Saarland Univ. (2018)	Active elastocaloric regeneration	Ni-Ti wires in tension	9 K	n/a	n/a	[41] and [42]
Fraunhofer IPM (2018)	Cascade (heat pipe – like)	Ni-Ti tubes in compression	10 K	n/a	n/a	[43]
Cornell Univ. (2019)	3-stage cascade	Ni-Ti wires in tension	28.3 K	n/a	7.7 (at $\Delta T_{span}=5.2$ K) / n/a	[44]
Karlsruhe Inst. of Technology (2019)	3-stage cascade	Ti-Ni-Cu-Co sheets in tension	15 K	n/a	1.9 (at $\Delta T_{span}=5$ K) / n/a	[45]
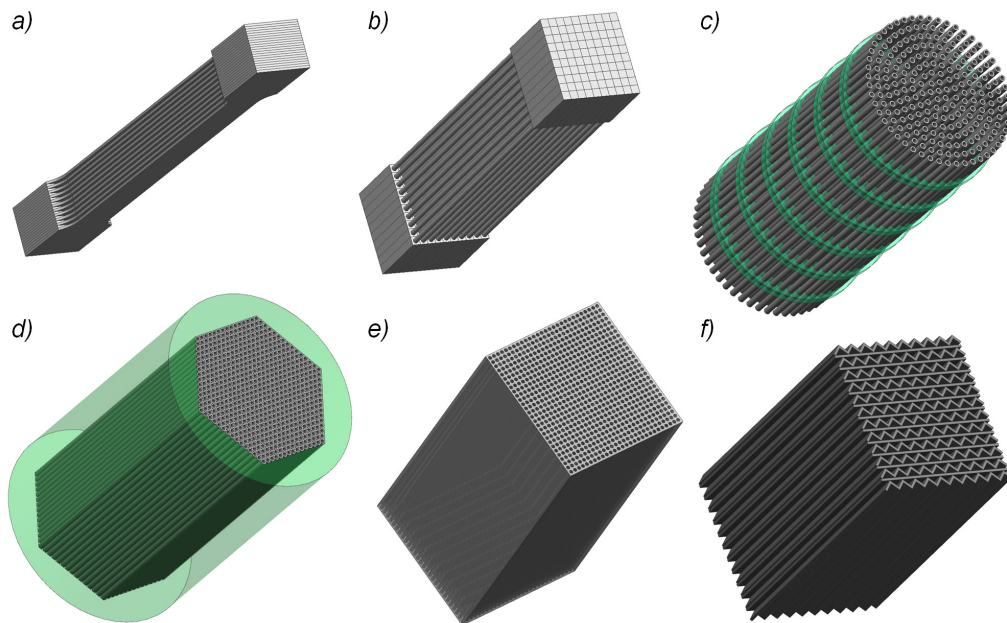
Fig. 3. *Potential geometries of an active elastocaloric regenerator*

[35] that prevents the tubes from buckling. The major difference between these two geometries is the flow of the heat-transfer fluid. In the case of the geometry shown in Fig. 3c, the heat-transfer fluid flows in the cross-flow regime, thus, it does not flow inside the tubes as is the case of the geometry shown in Fig. 3d. This is an important feature for practical applications. As explained below in this section, it is desirable that the fluid flow is in the loading direction of the active elastocaloric regenerator. Therefore, in contrast to the case of the regenerator shown in Fig. 3d, in which the heat-transfer fluid enters from the top and through the bulky loading grips, the heat-transfer fluid can enter from the side in the case of the regenerator shown in Fig. 3c. In this way, the dead volume (the volume between the regenerator and the heat sink/source) and the heat losses to the grips as well as the complexity of the grips can be reduced. Another potential porous geometry for compressive loading can be made of blocks with holes (Fig. 3e), but since Ni-Ti-based materials (as the most promising elastocaloric materials) are hard-to-machine materials, this can be

a very time consuming and expensive solution. Fig. 3f shows a honeycomb geometry made from corrugated plates with an enhanced buckling stability and good heat transfer properties [52]. However, the geometry made of block with holes and the honeycomb geometry also require fluid flow inlet/outlet through the grips, which is their disadvantage (as already mentioned above).

Using conventional methods to fabricate complex geometries and porous (or hollow) structures, such as the ones shown in Fig. 3, could be challenging since multiple fine elements should be assembled and joined together. Such elements (structures) might have been manufactured by different methods and consequently have different properties. Furthermore, it is difficult to machine and weld Ni-Ti [53] and [54] and the large number of required joints (and interfaces) along with the probable variations in their quality and properties can weaken the structure and reduce its performance and fatigue life. Therefore, methods such as additive manufacturing could be adopted to fabricate a uniform jointless active elastocaloric regenerator. Recently, additive manufacturing, in particular selective laser sintering (SLS) and selective laser melting (SLM), have become potential alternative methods for making porous superelastic implants for biomedical applications [55]. Fabrication of Ni-Ti using different additive manufacturing techniques, especially SLM [56], has been the subject of multiple studies [57]. Achieving superelasticity in Ni-Ti samples that are fabricated using SLM, usually requires a post-process heat treatment, nevertheless, a recent study has demonstrated the possibility of achieving superelasticity in as-fabricated SLM samples by adjusting the parameters of the process [58]. Thermomechanical response of additively manufactured Ni-Ti parts, including their fatigue life as well as their elastocaloric response, has been investigated and some promising results have been achieved. Nonetheless, there is still room for further improvements by investigating new techniques, chemical compositions, process parameters, heat treatments etc. [57] and [59] to [62].

Another important factor in designing active elastocaloric regenerators is the aspect ratio (cross section to length). Since relatively high stresses (up to 1000 MPa) are required to induce the martensitic transformation, the cross sectional area needs to be as small as possible to reduce the required force. This further means that in order to keep a constant mass of the elastocaloric material (which is directly related to the generated cooling/heating power), the regenerator's length needs to be increased. In addition,

as shown previously for active magnetic regenerators made of ordered structures with straight fluid flow channels [63] (e.g. parallel-plate, set of tubes, etc.), it is desirable that the active elastocaloric regenerator is relatively long (above 50 mm) in order to increase the length of the path along which a temperature span can be established. Therefore, the heat-transfer fluid should flow along the length and the loading direction of the active elastocaloric regenerator.

Furthermore, under the steady-state conditions a temperature profile is established along the regenerator in the fluid flow direction. As each part of the elastocaloric material along the regenerator works at a different temperature (see Fig. 2b) and in accordance with the dependence of transformation strain on the temperature of the SMA [21], that further means that the coldest part of the regenerator would be strained much more than its hottest part and the eCE in the coldest part of the regenerator would be larger compared to its hottest part. In order to overcome this issue and ensure an equal eCE along the regenerator under the steady-state conditions, a layered active elastocaloric regenerator [64] should be applied (analogous to a layered active magnetic regenerator [65] and [66]). That means that different elastocaloric materials with different transformation temperatures should be stacked along the length of the regenerator (in the fluid flow direction).

2.2 Tension vs. Compression

In general, the active elastocaloric regenerator can be loaded in tension or compression, each of which has some pros and cons concerning the elastocaloric cooling. Although very interesting, other loading modes such as bending [67] or torsion [68] will not be considered here since they cannot provide a homogenous strain distribution over the porous structure. Homogenous strain distribution that results in homogenous distribution of the eCE is the first precondition of an efficient active elastocaloric regenerator. The main advantage of tensile loading is the possibility of utilizing thin elements with high specific heat transfer area per unit volume and small hydraulic diameters that result in good heat transfer properties, while its main disadvantage is a reduced fatigue life compared to compressive loading. It is known [69] that any cracks on the surface or impurities in the material, which are practically inevitable, will grow and expand during tensile loading and eventually lead to the failure of the material (see Fig. 4). Nevertheless, under compressive loading, those cracks and impurities do not have

much space to grow. This can significantly prolong the fatigue life of the material, which is an important advantage of compressive loading. On the other hand, thin elements, which would enhance the heat transfer characteristics of an active elastocaloric regenerator, cannot be compressed without solving the buckling stability problem associated with them. It is, therefore, challenging to design a porous geometry that can be compressed in a stable manner and at the same time assure an efficient and rapid heat transfer.
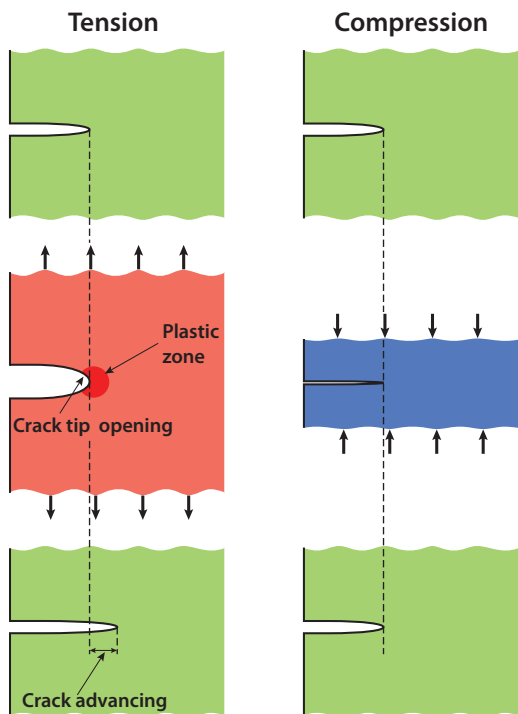
Fig. 4. *Schematic representation of crack growth during tension and compression* [69]

Fig. 5a shows the stress-strain behaviour of a superelastic Ni-Ti alloy under isothermal (strain rate of 0.0002 s⁻¹) and adiabatic (strain rate of 0.06 s⁻¹) conditions where tension-compression asymmetry [18] is clearly observable. Dog-bone shaped thin sheets (with a thickness of 250 μm) were tested under tension [70], while thin-walled tubes (with an outer diameter of 3 mm and a wall thickness of 250 μm) were tested under compression. In order to stabilize the stress-strain behaviour of the samples before the experiments, both samples were subjected to a mechanical stabilization (training), which consisted of 100 superelastic cycles at a strain-rate of 0.002 s⁻¹ up to the stresses/strains that corresponded to the end of the transformation plateau. From Fig. 5a, it is evident that in compressive loading, the slope of

the transformation plateau is significantly steeper compared to the tensile loading, which means that a higher stress is required to complete the transformation, while the resulting transformation strain is smaller. Fig. 5b shows positive and negative adiabatic temperature changes for tensile and compressive loadings as functions of the applied strain and stress.
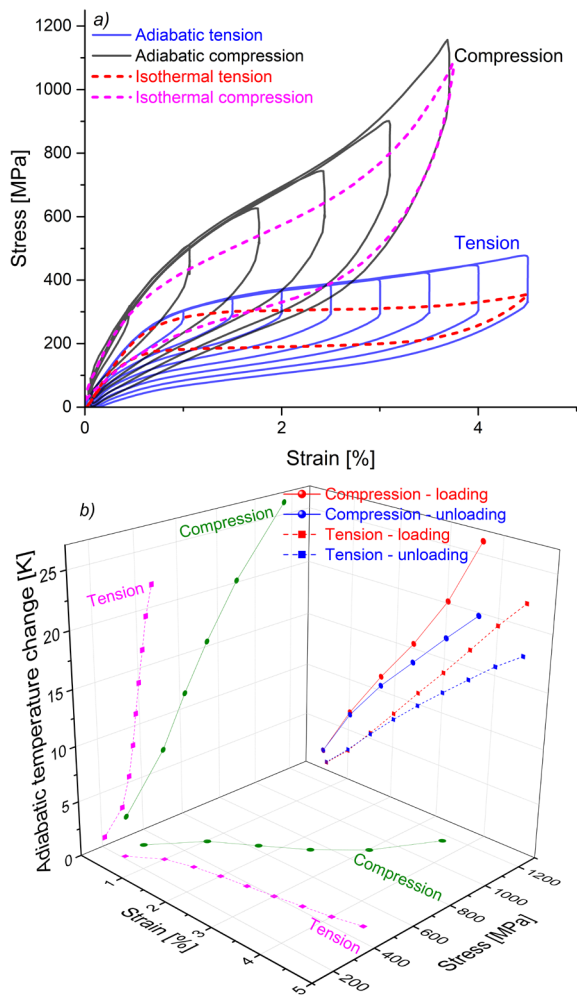
Fig. 5. *a) Stress-strain response of Ni-Ti tubes and dog-bone shaped sheets under compression and tension, and b) the corresponding adiabatic temperature changes as functions of the applied stress and strain*

From the adiabatic temperature change-strain projection of Fig. 5b, one can see that larger adiabatic temperature changes can be obtained in compression, where (positive) adiabatic temperature changes of up to 28 K were measured. The reason for this could be related to the smaller transformation strain in compression compared to tension, which means that a more complete transformation (with a larger

transformation latent heat) is obtained at smaller strains under compression. This could be clearly observed in the stress-strain projection of Fig. 5b. It is also seen that the typical (almost flat) transformation plateau region that is observable in tension, turns into a strain-hardening region in compression. As a consequence, the transformation start stress and the stress that is needed to complete the transformation under tension are much smaller than under compression. Therefore, as seen from the adiabatic temperature change-stress projections of Fig. 5b, in tension, larger adiabatic temperature changes can be obtained at small and moderate stresses compared to compression. This is where tension is superior to compression. It is further evident form Fig. 5b that positive adiabatic temperature changes (during loading) are in all cases larger than negative ones (during unloading), which is due to the intrinsic mechanical dissipative heat of the internal friction that manifests itself as the hysteresis.

Fig. 6 shows the distribution of the temperature changes over the sample during loading and unloading Ni-Ti thin-walled tubes under compression and Ni-Ti dog-bone shaped thin sheets under tension. One can see that in compression, the temperature change in the sample is fully homogenous (neglecting heat losses through the grips), while in tension, temperature bands related to the Lüders-type transformation [71] are clearly visible, which is in agreement with the presence of strain-hardening region and flat plateau under compressive and tensile loading respectively. With regard to the eCE, the homogenous temperature change is an advantage of compressive loading.
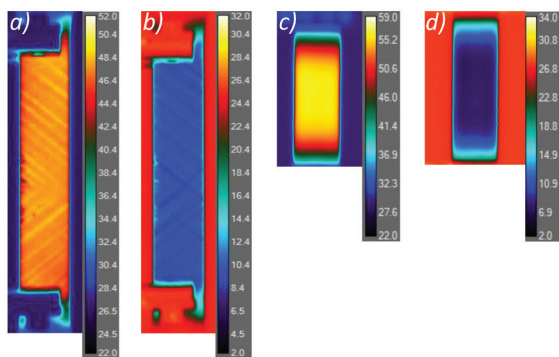
fatigue life. It is estimated that a cooling or heat-pumping device should withstand more than 10 million loading/unloading cycles with no functional and structural fatigue in its lifetime (10 years). Fig. 7 shows the adiabatic temperature changes of Ni-Ti that correspond to different strains/stresses as functions of fatigue life (number of cycles until failure or runout) obtained from dog-bone shaped thin sheets under tension [70] and thin-walled tubes under compression. As shown in Fig. 7, in tensile loading, high-cycle fatigue regime ($>10^5$ cycles) can be reached only by using small strains (stresses) that do not correspond to a completed phase transformation and thus can only result in limited adiabatic temperature changes of below 8 K. It should be noted that, in most cases (for tensile loading), Ni-Ti samples withstanding 10^5 fatigue cycles have also reached 10^6 or even 10^7 cycles as shown in [72]. Furthermore, Chluba et al. [25] and [73] developed an ultra-low fatigue Ni-Ti-Cu-Co thin film by sputtering deposition that could withstand 10 million loading cycles under tension with strains of up to 2.50 % and adiabatic temperature changes of up to 10 K. The results are highly encouraging, but the disadvantage is that the applied sputtering deposition technique is still too time-consuming for large-scale production of this material that would be required in practical cooling or heating applications. On the other hand, our preliminary results on thin-walled tubes as well as other authors' results on bulk blocks or cylinders [74] and [75] show that it is possible to reach well above 1 million loading and unloading cycles under compression with strain (stress) amplitudes

Fig. 6. *Distribution of temperature changes [°C] over the elastocaloric sample during tensile; a) loading, and b) unloading under a strain of 4.6 %, and during compressive c) loading, and d) unloading under a strain of 3.8 %*

2.3 Fatigue Life of Elastocaloric Materials

As already mentioned above, the major difference between tensile and compressive loading is the
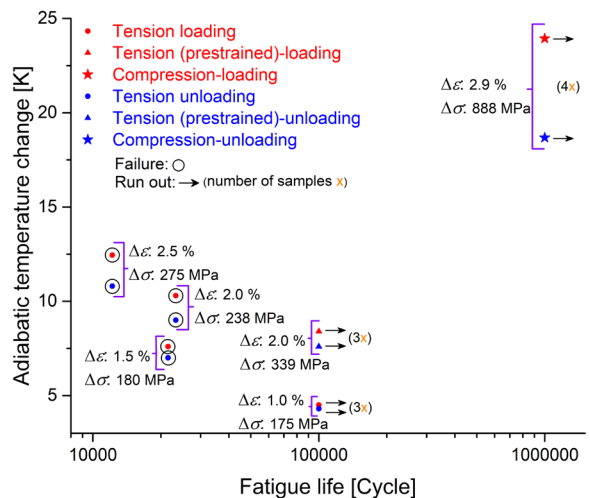
Fig. 7. *Adiabatic temperature changes of Ni-Ti alloy as functions of fatigue-life under tension and compression at different applied strains/stresses*

high enough to cover the entire transformation plateau (note that in compression, transformation strain of a fully transformed sample is smaller than that of the tension). This can result in stable adiabatic temperature changes of up to around 25 K even after 1 million cycles as shown in Fig. 7. Accordingly, compressive loading shows a very high potential for designing fatigue-resistant elastocaloric cooling systems capable of reaching up to 10 million operation cycles. However, a precondition for reaching a long fatigue life in compression is the buckling stability of the specimen.

3 DEVELOPMENT OF THE DRIVER MECHANISM

In addition to the active elastocaloric regenerator, another key component of the elastocaloric technology is the driver mechanism that provides the elastocaloric material with the mechanical loading. There are two crucial requirements that present a challenge in developing a driver mechanism. The first requirement is providing the elastocaloric material with a sufficiently high mechanical load since phase transformation occurs at relatively high stresses. The second requirement is to ensure that the work that is released during unloading the material is effectively exploited (work recovery). The efficient use of the recoverable work helps to increase the efficiency of the driver mechanism and the entire elastocaloric device.

3.1 Review of Different Driver Concepts Applied in Elastocaloric Technology

The prototypes and proof-of-the-concept elastocaloric devices developed to date are based on a hydraulic actuator [35], linear actuators with a spindle motor [36], [37] and [44] and a rotary driver using a cam-disk [41]. Different potential driver mechanisms for elastocaloric technology are presented and reviewed also in [76]. In general, one can distinguish between linear driver mechanisms (such as pneumatic or hydraulic actuators, linear motors, piezo actuators, SMA actuators and magnetostriction actuators) and rotary driver mechanisms (where using an electromotor seems to be the most reasonable option). The linear drivers are mostly suitable for loading an individual regenerator or a pair of regenerators operating simultaneously. On the other hand, by utilizing rotary drivers, several regenerators distributed in a ring can be loaded and the whole system can be more compact.

Pneumatic actuators usually operate with relatively small working pressures of up to 10 bar and therefore the high forces, which are required to induce and complete the phase transformation in the elastocaloric material, can only be generated using small contact surfaces. The hydraulic actuators on the other hand, can provide higher pressures (up to 300 bar), but are only useful for laboratory testing owing to their poor overall efficiency. Linear motors allow of a direct tensile or compressive loading with relatively high efficiencies owing to the absence of transmissions, but have difficulty in providing the required high forces [76]. Solid-state actuators, utilizing ferroic properties of functional materials, could be interesting alternatives. Among them, the most widely applied are piezo actuators [77], but their small obtainable displacements (below 0.1 mm) are not enough to generate large eCE in an active elastocaloric regenerator. In 2018, Huo et al. [78] applied a magnetostriction actuator (Terfenol-D), which could generate strains of up to 0.2 % to load/unload a Cu–Al–Mn elastocaloric alloy. In 2019, Qian et al. [79] proposed a linear heat-driven SMA actuator to load and unload the elastocaloric materials. It can generate the required stresses and strains, but its drawback is its relatively low operating frequency.

Most actuators that operate continuously and with a relatively high efficiency are based on a rotary motion (e.g. car engine, electric motor, existing vapour compression cooling systems, etc.). Rotary drivers in combination with a camshaft, a cam-disc or a cam-ring, are therefore promising solutions for designing compact elastocaloric systems. The active elastocaloric regenerators can be positioned radially or axially with respect to the direction of rotation. The ability to adjust the shape of the cam-disk or cam-ring and the fluid flow regime of the heat transfer medium can ensure adiabatic, isothermal or combined loading of the elastocaloric material [41].

Another interesting and promising solution is a hybrid system [80], which is based on exploiting the pressure difference between the evaporation and condensation phases in a classic vapour compression refrigeration system. Such a pressure difference could be used to run an actuator that would further load and unload the elastocaloric material. Since elastocaloric systems require high loads, combining them with a CO_2 vapour compression system (owing to the high pressure difference between their evaporator and condenser) could result in the most appropriate hybrid system. A hybrid system could be utilized to design a vapour compression system with a higher efficiency.

3.2 Recovery of the Released Mechanical Work

The first step in assessing the viability of work recovery is a theoretical analysis of the amount of recoverable work available in an active elastocaloric regenerator (material). Such an analysis was performed on the two extremes of loading rate i.e. adiabatic and isothermal loading conditions (data from Fig. 5). Fig. 8 shows an example of force variations during phase-shifted tensile loading and unloading of two regenerators under adiabatic and isothermal conditions, where the normalized force (F_{norm}) is taken into account. It is assumed that during the first half of the cycle, one regenerator is loaded (blue curves) and another one is simultaneously unloaded (red curves), while in the second half of the cycle, the opposite happens. Such an operation in an elastocaloric device was demonstrated in [35] and [40]. In Fig. 8, the area between the loading curve and the x-axis represents the invested or required work (F_{norm} above 0), while the area between the unloading curve and the x-axis represents the available or recoverable work (F_{norm} below 0). The difference between the loading and unloading forces (the net force) is shown with the green curves in Fig. 8. One can see that at the very beginning of the cycle, the force released during the unloading is higher than the required force for loading (net force is negative). If both active elastocaloric regenerators are directly connected to each other (without utilizing the natural frequency, a flywheel or a similar system to store the kinetic energy) the negative net force cannot be recovered since the regenerator that is being loaded at that time, requires a much smaller force than can be provided by the regenerator being unloaded. Under such circumstances, only 78 % and 77 % of the available work can be recovered under isothermal and adiabatic loading conditions respectively. That means that, in order to overcome the hysteresis losses and the lost negative net force, the driver needs to provide 73 % and 47 % of the required invested work in the case of each adiabatic and isothermal loading cycle respectively. However, by introducing a flywheel, which is a mechanical device specifically designed to efficiently store rotational energy (kinetic energy), the negative net force can also be recovered. By using a flywheel, the input work, which is provided by the driver in each loading cycle, is only related to the hysteresis losses that are 65 % and 32 % of the required invested work in the cases of adiabatic and isothermal loadings respectively and the rest of the required invested work can be recovered. This is the main reason that isothermal loading can result in a

more efficient operation of an elastocaloric device as already shown in the literature [50].
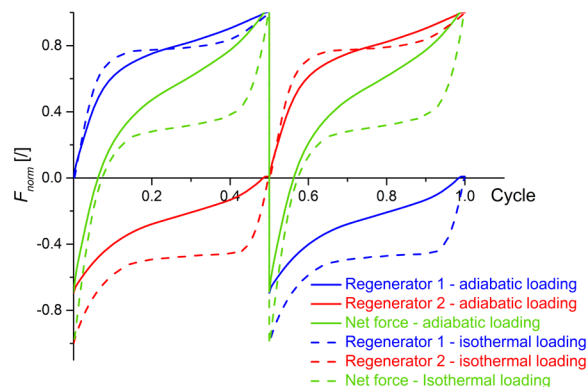
Fig. 8. *Force variations during loading and unloading (1 cycle) two phase-shifted active elastocaloric regenerators under adiabatic and isothermal conditions*

Another way to recover the negative net force is utilization of natural frequency work recovery systems. Such systems make it possible to recover the mechanical unloading work by storing it in an oscillating mass that oscillates within the natural frequency range of the system. Nevertheless, the natural frequency of a typical active elastocaloric regenerator [37] is in the kHz range, which is significantly higher than the operating frequency required for an efficient elastocaloric cooling (up to 10 Hz). In general, the natural frequency could be reduced by methods such as using an additional spring system in order to decrease the stiffness of the system.

5 CONCLUSIONS

In conclusion, the state-of-the-art and future challenges of elastocaloric cooling technology, as one of the most promising alternatives to vapour compression cooling technology, are reviewed. Active elastocaloric regenerators show a promising performance regarding the generated temperature span, specific cooling/heating power and COP. Adding a work recovery mechanism to such systems can decrease the required input work and improve the overall efficiency of the system.

Fatigue life of the elastocaloric materials is a challenging issue concerning the commercialization of elastocaloric cooling devices. This issue can be tackled by designing new material systems, utilizing new fabrication methods and developing new devices that operate under compressive loading. In order to define the optimal geometry of an active elastocaloric regenerator under compressive loading, buckling

stability and heat transfer properties should be considered. To assure a fast and efficient heat transfer between an elastocaloric material and a heat-transfer fluid, thin-walled structures with small hydraulic diameters and therefore high specific heat transfer areas are required. Nevertheless, such geometries are, in general, not favourable from the buckling stability point of view. Consequently, a compromise between these two opposing requirements needs to be reached.

6 ACKNOWLEDGEMENTS

7 REFERENCES

[1] Isaac, M., van Vuuren, D.P. (2009). Modeling global residential sector energy demand for heating and air conditioning in the context of climate change. *Energy Policy*, vol. 37, no. 2, p. 507-521, **DOI:10.1016/j.enpol.2008.09.051**.

[2] Navigant Consulting Inc. (2014). *Energy Savings Potential and RD&D Opportunities for Non-Vapor-Compression HVAC Technologies*, **DOI:10.2172/1220817**.

[3] *Handbook for the Montreal Protocol on Substances That Deplete the Ozone Layer.* (2019). UNEP Ozone Secretariat (13th ed.)

[4] McLinden, M.O., Brown, J.S., Brignoli, R., Kazakov, A.F., Domanski, P.A. (2017). Limited options for low-global-warming-potential refrigerants. *Nature Communications*, vol. 8, no. 1, p. 14476, **DOI:10.1038/ncomms14476**.

[5] Ciconkov, R. (2018). Refrigerants: There is still no vision for sustainable solutions. *International Journal of Refrigeration*, vol. 86, p. 441-448, **DOI:10.1016/j.ijrefrig.2017.12.006**.

[6] Fähler, S. (2018). Caloric Effects in Ferroic Materials: New Concepts for Cooling. *Energy Technology*, vol. 6, no. 8, p. 1394-1396, **DOI:10.1002/ente.201800201**.

[7] Moya, X., Kar-Narayan, S., Mathur, N.D. (2014). Caloric materials near ferroic phase transitions. *Nature Materials*, vol. 13, no. 5, p. 439-450, **DOI:10.1038/nmat3951**.

[8] Kitanovski, A., Tušek, J., Tomc, U., Plaznik, U., Ožbolt, M., Poredoš, A. (2015). Magnetocaloric Energy Conversion. *Green Energy and Technology*, Springer, Cham, **DOI:10.1007/978-3-319-08741-2**.

[9] Greco, A., Aprea, C., Maiorino, A., Masselli, C. (2019). A review of the state of the art of solid-state caloric cooling processes at room-temperature before 2019. *International Journal of Refrigeration*, vol. 106, p. 66-88, **DOI:10.1016/j.ijrefrig.2019.06.034**.

[10] VHK and ARMINES. (2016). *Technology Roadmap in Preparatory/Review Study on Commission Regulation (EC) No. 643/2009 with Regard to Ecodesign Requirements for Household Refrigeration Appliances and Commission Delegated Regulation (EU) No. 1060/2010 with Regard to Energy Labelling of Household Refrigeration Appliances*, European Union, Brussels.

[11] Elahinia, M.H., Hashemi, M., Tabesh, M., Bhaduri, S.B. (2012). Manufacturing and processing of NiTi implants: A review. *Progress in Materials Science*, vol. 57, no. 5, p. 911-946, **DOI:10.1016/j.pmatsci.2011.11.001**.

[12] Mohd Jani, J., Leary, M., Subic, A., Gibson, M. A. (2014). A review of shape memory alloy research, applications and opportunities. *Materials & Design (1980-2015)*, vol. 56, p. 1078-1113, **DOI:10.1016/j.matdes.2013.11.084**.

[13] Rodriguez, C., Brown, L.C. (1980). The thermal effect due to stress-induced martensite formation in β-CuAlNi single crystals. *Metallurgical and Materials Transactions A*, vol. 11, no. 1, p. 147-150, **DOI:10.1007/BF02700450**.

[14] Bonnot, E., Romero, R., Mañosa, L., Vives, E., Planes, A. (2008). Elastocaloric effect associated with the martensitic transition in shape-memory alloys. *Physical Review Letters*, vol. 100, no. 12, p. 1-4, **DOI:10.1103/PhysRevLett.100.125901**.

[15] Wu, Y., Ertekin, E., Sehitoglu, H. (2017). Elastocaloric cooling capacity of shape memory alloys - Role of deformation temperatures, mechanical cycling, stress hysteresis and inhomogeneity of transformation. *Acta Materialia*, vol. 135, p. 158-176, **DOI:10.1016/j.actamat.2017.06.012**.

[16] Tušek, J., Engelbrecht, K., Mañosa, L., Vives, E., Pryds, N. (2016). Understanding the thermodynamic properties of the elastocaloric effect through experimentation and modelling. *Shape Memory and Superelasticity*, vol. 2, no. 4, p. 317-329, **DOI:10.1007/s40830-016-0094-8**.

[17] Schmidt, M., Ullrich, J., Wieczorek, A., Frenzel, J., Schütze, A., Eggeler, G., Seelecke, S. (2015). Thermal Stabilization of NiTiCuV Shape Memory Alloys: Observations During Elastocaloric Training. *Shape Memory and Superelasticity*, vol. 1, no. 2, p. 132-141, **DOI:10.1007/s40830-015-0021-4**.

[18] Gall, K., Sehitoglu, H., Chumlyakov, Y. I., Kireeva, I. V. (1999). Tension–compression asymmetry of the stress–strain response in aged single crystal and polycrystalline NiTi. *Acta Materialia*, vol. 47, no. 4, p. 1203-1217, **DOI:10.1016/S1359-6454(98)00432-7**.

[19] Sutou, Y., Omori, T., Koeda, N., Kainuma, R., Ishida, K. (2006). Effects of grain size and texture on damping properties of Cu-Al-Mn-based shape memory alloys. *Materials Science and Engineering: A*, vol. 438-440, p. 743-746, **DOI:10.1016/j.msea.2006.02.085**.

[20] Srivastava, A.K., Schryvers, D., Van Humbeeck, J. (2007). Grain growth and precipitation in an annealed cold-rolled $Ni_{50.2}Ti_{49.8}$ alloy. *Intermetallics*, vol. 15, no. 12, p. 1538-1547, **DOI:10.1016/j.intermet.2007.06.003**.

[21] Tušek, J., Engelbrecht, K., Mikkelsen, L.P., Pryds, N. (2015). Elastocaloric effect of Ni-Ti wire for application in a cooling device. *Journal of Applied Physics*, vol. 117, no. 12, **DOI:10.1063/1.4913878**.

[22] Ossmer, H., Lambrecht, F., Gültig, M., Chluba, C., Quandt, E., Kohl, M. (2014). Evolution of temperature profiles in TiNi films for elastocaloric cooling. *Acta Materialia*, vol. 81, p. 9-20, **DOI:10.1016/j.actamat.2014.08.006**.

[23] Kim, Y., Jo, M.G., Park, J.W., Park, H.K., Han, H.N. (2018). Elastocaloric effect in polycrystalline Ni50Ti45.3V4.7 shape memory alloy. *Scripta Materialia*, vol. 144, p. 48-51, **DOI:10.1016/j.scriptamat.2017.09.048**.

[24] Bechtold, C., Chluba, C., Lima de Miranda, R., Quandt, E. (2012). High cyclic stability of the elastocaloric effect in sputtered TiNiCu shape memory films. *Applied Physics Letters*, vol. 101, no. 9, p. 1-5, **DOI:10.1063/1.4748307**.

[25] Chluba, C., Ossmer, H., Zamponi, C., Kohl, M., Quandt, E. (2016). Ultra-low fatigue quaternary tini-based films for elastocaloric cooling. *Shape Memory and Superelasticity*, vol. 2, no. 1, p. 95-103, **DOI:10.1007/s40830-016-0054-3**.

[26] Ossmer, H., Chluba, C., Gueltig, M., Quandt, E., Kohl, M. (2015). Local evolution of the elastocaloric effect in TiNi-based films. *Shape Memory and Superelasticity*, vol. 1, no. 2, p. 142-152, **DOI:10.1007/s40830-015-0014-3**.

[27] Mañosa, L., Jarque-Farnos, S., Vives, E., Planes, A. (2013). Large temperature span and giant refrigerant capacity in elastocaloric Cu-Zn-Al shape memory alloys. *Applied Physics Letters*, vol. 103, no. 21, **DOI:10.1063/1.4832339**.

[28] Nikitin, S.A., Myalikgulyev, G., Annaorazov, M.P., Tyurin, A.L., Myndyev, R.W., Akopyan, S.A. (1992). Giant elastocaloric effect in FeRh alloy. *Physics Letters A*, vol. 171, no. 3-4, p. 234-236, **DOI:10.1016/0375-9601(92)90432-L**.

[29] Xiao, F., Fukuda, T., Kakeshita, T. (2013). Significant elastocaloric effect in a Fe-31.2Pd (at. %) single crystal. *Applied Physics Letters*, vol. 102, no. 16, p. 161914, **DOI:10.1063/1.4803168**.

[30] Li, D., Li, Z., Yang, J., Li, Z., Yang, B., Yan, H., Wang, D., Hou, L., Li, X., Zhang, Y., Esling, C., Zhao, X., Zuo, L. (2019). Large elastocaloric effect driven by stress-induced two-step structural transformation in a directionally solidified $Ni_{55}Mn_{18}Ga_{27}$ alloy. *Scripta Materialia*, vol. 163, p. 116-120, **DOI:10.1016/j.scriptamat.2019.01.014**.

[31] Liu, J., Zhao, D., Li, Y. (2017). Exploring magnetic elastocaloric materials for solid-state cooling. *Shape Memory and Superelasticity*, vol. 3, no. 3, p. 192-198, **DOI:10.1007/s40830-017-0118-z**.

[32] Cong, D., Xiong, W., Planes, A., Ren, Y., Mañosa, L., Cao, P., Nie, Z., Sun, X., Yang, Z., Hong, X., Wang, Y. (2019). Colossal elastocaloric effect in ferroelastic Ni-Mn-Ti alloys. *Physical Review Letters*, vol. 122, no. 25, p. 255703, **DOI:10.1103/PhysRevLett.122.255703**.

[33] Xie, Z., Sebald, G., Guyomar, D. (2017). Temperature dependence of the elastocaloric effect in natural rubber. *Physics Letters A*, vol. 381, no. 25-26, p. 2112-2116, **DOI:10.1016/j.physleta.2017.02.014**.

[34] Mañosa, L., Planes, A. (2017). Materials with giant mechanocaloric effects: cooling by strength. *Advanced Materials*, vol. 29, no. 11, **DOI:10.1002/adma.201603607**.

[35] Qian, S., Wang, Y., Geng, Y., Ling, J., Muehlbauer, J., Hwang, Y., Radermacher, R., Takeuchi, I. (2016). Experimental evaluation of a compressive elastocaloric cooling system. *16th International Refrigeration and Air Conditioning Conference at Purdue (vol. 16)*, 2385.

[36] Schmidt, M., Schütze, A., Seelecke, S. (2015). Scientific test setup for investigation of shape memory alloy based elastocaloric cooling processes. *International Journal of Refrigeration*, vol. 54, p. 88-97, **DOI:10.1016/j.ijrefrig.2015.03.001**.

[37] Tušek, J., Engelbrecht, K., Eriksen, D., Dall'Olio, S., Tušek, J., Pryds, N. (2016). A regenerative elastocaloric heat pump. *Nature Energy*, vol. 1, no. 10, p. 16134, **DOI:10.1038/nenergy.2016.134**.

[38] Engelbrecht, K., Tušek, J., Eriksen, D., Lei, T., Lee, C.Y., Tušek, J., Pryds, N. (2017). A regenerative elastocaloric device: experimental results. *Journal of Physics D: Applied Physics*, vol. 50, no. 42, p. 424006, **DOI:10.1088/1361-6463/aa8656**.

[39] Bruederlin, F., Ossmer, H., Wendler, F., Miyazaki, S., Kohl, M. (2017). SMA foil-based elastocaloric cooling: From material behavior to device engineering. *Journal of Physics D: Applied Physics*, vol. 50, no. 42, p. 424003, **DOI:10.1088/1361-6463/aa87a2**.

[40] Bruederlin, F., Bumke, L., Chluba, C., Ossmer, H., Quandt, E., Kohl, M. (2018). Elastocaloric cooling on the miniature scale: a review on materials and device engineering. *Energy Technology*, p. 1588-1604, **DOI:10.1002/ente.201800137**.

[41] Kirsch, S.M., Welsch, F., Michaelis, N., Schmidt, M., Wieczorek, A., Frenzel, J., Eggeler, G., Schütze, A., Seelecke, S. (2018). NiTi-based elastocaloric cooling on the macroscale: From basic concepts to realization. *Energy Technology*, vol. 6, no. 8, p. 1567-1587, **DOI:10.1002/ente.201800152**.

[42] Kirsch, S.-M., Welsch, F., Michaelis, N., Motzki, P., Schütze, A., Seelecke, S. (2019). Continuous Operating Elastocaloric Cooling Device: First Experimental Results. *Shape Memory and Superelastic Technology Conference*, Konstanz.

[43] Bartholome, K. (n.d.). Efficient elastocaloric heat pumps. Fraunhofer IPM, from *https://www.google.com/url?sa=t&rct =j&q=&esrc=s&source=web&cd=1&cad=rja&uact=8&ved=2 ahUKEwjQ_LiPp8HlAhXSMewKHRxSA68QFjAAegQIAxAC&url =https%3A%2F%2Fwww.ipm.fraunhofer.de%2Fcontent% 2Fdam%2Fipm%2Fen%2FPDFs%2Freports%2Far-2016-17 articles%2FAR-52-53-elastocaloric-heat-pumps.pdf&usg =AOvVaw3XQXtf-wRYzA8E4bBP5YF0*, accessed 10-9-2019.

[44] Snodgrass, R., Erickson, D. (2019). A two-stage elastocaloric cooler for increased temperature span. *Shape Memory and Superelastic Technology Conference*, Konstanz.

[45] Bruederlin, F., Bumke, L., Quandt, E., Kohl, M. (2019). Cascaded SMA-film based elastocaloric cooling. *20th International Conference on Solid-State Sensors, Actuators and Microsystems & Eurosensors XXXIII (TRANSDUCERS & EUROSENSORS XXXIII)*, p. 1467-1470, **DOI:10.1109/TRANSDUCERS.2019.8808605**.

[46] Tušek, J., Engelbrecht, K., Millán-Solsona, R., Mañosa, L., Vives, E., Mikkelsen, L.P., Pryds, N. (2015). The elastocaloric effect: a way to cool efficiently. *Advanced Energy Materials*, vol. 5, no. 13, p. 1500361, **DOI:10.1002/aenm.201500361**.

[47] Qian, S., Ling, J., Hwang, Y., Radermacher, R., Takeuchi, I. (2015). Thermodynamics cycle analysis and numerical modeling of thermoelastic cooling systems. *International Journal of Refrigeration*, vol. 56, p. 65-80, **DOI:10.1016/j.ijrefrig.2015.04.001**.

[48] Qian, S., Yuan, L., Yu, J., Yan, G. (2017). Numerical modeling of an active elastocaloric regenerator refrigerator with phase transformation kinetics and the matching principle for materials selection. *Energy*, vol. 141, p. 744-756, **DOI:10.1016/j.energy.2017.09.116**.

[49] Luo, D., Feng, Y., Verma, P. (2017). Modeling and analysis of an integrated solid state elastocaloric heat pumping

system. *Energy*, vol. 130, p. 500-514, **DOI:10.1016/j. energy.2017.05.008**.

[50] Schmidt, M., Kirsch, S.M., Seelecke, S., Schütze, A. (2016). Elastocaloric cooling: From fundamental thermodynamics to solid state air conditioning. *Science and Technology for the Built Environment*, vol. 22, no. 5, p. 475-488, **DOI:10.1080/23 744731.2016.1186423**.

[51] Ossmer, H., Kohl, M. (2016). Elastocaloric cooling: Stretch to actively cool. *Nature Energy*, vol. 1, no. 10, p. 1-2, **DOI:10.1038/nenergy.2016.159**.

[52] Šarlah, A., Tušek, J., Poredoš, A. (2012). Comparison of thermo-hydraulic properties of heat regenerators applicable to active magnetic refrigerators. *Strojniški vestnik - Journal of Mechanical Engineering*, vol. 58, no. 1, p. 16-22, **DOI:10.5545/sv-jme.2010.250**.

[53] Oliveira, J.P., Miranda, R.M., Braz Fernandes, F.M. (2017). Welding and joining of NiTi shape memory alloys: A review. *Progress in Materials Science*, vol. 88, p. 412-466, **DOI:10.1016/j.pmatsci.2017.04.008**.

[54] Weinert, K., Petzoldt, V. (2004). Machining of NiTi based shape memory alloys. *Materials Science and Engineering A*, vol. 378, no. 1-2 spec. iss., p. 180-184, **DOI:10.1016/j. msea.2003.10.344**.

[55] Elahinia, M H., Hashemi, M., Tabesh, M., Bhaduri, S.B. (2012). Manufacturing and processing of NiTi implants: A review. *Progress in Materials Science*, vol. 57, no. 5, p. 911-946, **DOI:10.1016/j.pmatsci.2011.11.001**.

[56] Saedi, S., Saghaian, S.E., Jahadakbar, A., Shayesteh Moghaddam, N., Taheri Andani, M., Saghaian, S.M., Lu, Y.C., Elahinia, M., Karaca, H.E. (2018). Shape memory response of porous NiTi shape memory alloys fabricated by selective laser melting. *Journal of Materials Science: Materials in Medicine*, vol. 29, no. 4, p. 40, **DOI:10.1007/s10856-018-6044-6**.

[57] Elahinia, M., Shayesteh Moghaddam, N., Taheri Andani, M., Amerinatanzi, A., Bimber, B. A., Hamilton, R. F. (2016). Fabrication of NiTi through additive manufacturing: A review. *Progress in Materials Science*, vol. 83, p. 630-663, **DOI:10.1016/j.pmatsci.2016.08.001**.

[58] Shayesteh Moghaddam, N., Saedi, S., Amerinatanzi, A., Hinojos, A., Ramazani, A., Kundin, J., Mills, M.J., Karaca, H., Elahinia, M. (2019). Achieving superelasticity in additively manufactured NiTi in compression without post-process heat treatment. *Scientific Reports*, vol. 9, no. 1, p. 1-11, **DOI:10.1038/s41598-018-36641-4**.

[59] Bagheri, A., Mahtabi, M.J., Shamsaei, N. (2018). Fatigue behavior and cyclic deformation of additive manufactured NiTi. *Journal of Materials Processing Technology*, vol. 252, p. 440-453, **DOI:10.1016/j.jmatprotec.2017.10.006**.

[60] Bernard, S., Krishna Balla, V., Bose, S., Bandyopadhyay, A. (2012). Compression fatigue behavior of laser processed porous NiTi alloy. *Journal of the Mechanical Behavior of Biomedical Materials*, vol. 13, p. 62-68, **DOI:10.1016/j. jmbbm.2012.04.010**.

[61] Speirs, M., Van Hooreweder, B., Van Humbeeck, J., Kruth, J.P. (2017). Fatigue behaviour of NiTi shape memory alloy scaffolds produced by SLM, a unit cell design comparison. *Journal of the Mechanical Behavior of Biomedical Materials*, vol. 70, p. 53-59, **DOI:10.1016/j.jmbbm.2017.01.016**.

[62] Hou, H., Simsek, E., Stasak, D., Hasan, N.Al, Qian, S., Ott, R., Cui, J., Takeuchi, I. (2017). Elastocaloric cooling of additive manufactured shape memory alloys with large latent heat. *Journal of Physics D: Applied Physics*, vol. 50, no. 40, ID 404001, **DOI:10.1088/1361-6463/aa85bf**.

[63] Tušek, J., Kitanovski, A., Poredoš, A. (2013). Geometrical optimization of packed-bed and parallel-plate active magnetic regenerators. *International Journal of Refrigeration*, vol. 36, no. 5, p. 1456-1464, **DOI:10.1016/j.ijrefrig.2013.04.001**.

[64] Engelbrecht, K. (2019). Future prospects for elastocaloric devices. *Journal of Physics: Energy*, vol. 1, no. 2, ID 021001, **DOI:10.1088/2515-7655/ab1573**.

[65] Tušek, J., Kitanovski, A., Tomc, U., Favero, C., Poredoš, A. (2014). Experimental comparison of multi-layered La–Fe–Co–Si and single-layered Gd active magnetic regenerators for use in a room-temperature magnetic refrigerator. *International Journal of Refrigeration*, vol. 37, no. 1, p. 117-126, **DOI:10.1016/j.ijrefrig.2013.09.003**.

[66] Zhang, M., Abdelaziz, O., Momen, A.M., Abu-Heiba, A. (2017). A numerical analysis of a magnetocaloric refrigerator with a 16-layer regenerator. *Scientific Reports*, vol. 7, no. 1, ID 13962, **DOI:10.1038/s41598-017-14406-9**.

[67] Sharar, D.J., Radice, J., Warzoha, R., Hanrahan, B., Chang, B. (2018). First Demonstration of a Bending-Mode Elastocaloric Cooling 'Loop'. *17th IEEE Intersociety Conference on Thermal and Thermomechanical Phenomena in Electronic Systems (ITherm)*, p. 218-226, **DOI:10.1109/itherm.2018.8419513**.

[68] Wang, R., Fang, S., Xiao, Y., Gao, E., Jiang, N., Li, Y., Mou, L., Shen, Y., Zhao, W., Li, S., Fonseca, A.F., Galvão, D.S., Chen, M., He, W., Yu, K., Lu, H., Wang, X., Qian, D., Aliev, A.E., Li, N., Haines, C.S., Liu, Z., Mu, J., Wang, Z., Yin, S., Lima, M.D., An, B., Zhou, X., Liu, Z., Baughman, R.H. (2019). Torsional refrigeration by twisted, coiled, and supercoiled fibers. *Science*, vol. 366, no. 6462, p. 216-221, **DOI:10.1126/ science.aax6182**.

[69] Hou, H., Cui, J., Qian, S., Catalini, D., Hwang, Y., Radermacher, R., Takeuchi, I. (2018). Overcoming fatigue through compression for advanced elastocaloric cooling. *MRS Bulletin*, vol. 43, no. 4, p. 285-290, **DOI:10.1557/mrs.2018.70**.

[70] Tušek, J., Žerovnik, A., Čebron, M., Brojan, M., Žužek, B., Engelbrecht, K., Cadelli, A. (2018). Elastocaloric effect vs fatigue life: Exploring the durability limits of Ni-Ti plates under pre-strain conditions for elastocaloric cooling. *Acta Materialia*, vol. 150, p. 295-307, **DOI:10.1016/j.actamat.2018.03.032**.

[71] Sittner, P., Liu, Y., Novak, V. (2005). On the origin of Lüders-like deformation of NiTi shape memory alloys. *Journal of the Mechanics and Physics of Solids*, vol. 53, no. 8, p. 1719-1746, **DOI:10.1016/j.jmps.2005.03.005**.

[72] Alarcon, E., Heller, L., Chirani, S.A., Šittner, P., Kopeček, J., Saint-Sulpice, L., Calloch, S. (2017). Fatigue performance of superelastic NiTi near stress-induced martensitic transformation. *International Journal of Fatigue*, vol. 95, p. 76-89, **DOI:10.1016/j.ijfatigue.2016.10.005**.

[73] Chluba, C., Ge, W., Lima de Miranda, R., Strobel, J., Kienle, L., Quandt, E., Wuttig, M. (2015). Ultralow-fatigue shape memory alloy films. *Science*, vol. 348, no. 6238, p. 1004-1007, **DOI:10.1126/science.1261164**.

[74] Zhang, K., Kang, G., Sun, Q. (2019). High fatigue life and cooling efficiency of NiTi shape memory alloy under cyclic compression. *Scripta Materialia*, vol. 159, p. 62-67, **DOI:10.1016/j.scriptamat.2018.09.012**.

[75] Chen, J., Zhang, K., Kan, Q., Yin, H., Sun, Q. (2019). Ultra-high fatigue life of NiTi cylinders for compression-based elastocaloric cooling. *Applied Physics Letters*, vol. 115, no. 9, ID 093902, **DOI:10.1063/1.5115793**.

[76] Qian, S., Geng, Y., Wang, Y., Ling, J., Hwang, Y., Radermacher, R., Takeuchi, I., Cui, J. (2016). A review of elastocaloric cooling: Materials, cycles and system integrations. *International Journal of Refrigeration*, vol. 64, p. 1-19, **DOI:10.1016/j.ijrefrig.2015.12.001**.

[77] Dong, S. (2012). Review on piezoelectric, ultrasonic and magnetoelectric actuators. *Journal of Advanced Dielectrics*, vol. 02, no. 01, ID 1230001, **DOI:10.1142/S2010135X12300010**.

[78] Hou, H., Finkel, P., Staruch, M., Cui, J., Takeuchi, I. (2018). Ultra-low-field magneto-elastocaloric cooling in a multiferroic composite device. *Nature Communications*, vol. 9, no. 1, ID 4075, **DOI:10.1038/s41467-018-06626-y**.

[79] Qian, S., Wang, Y., Yuan, L., Yu, J. (2019). A heat driven elastocaloric cooling system. *Energy*, vol. 182, p. 881-899, **DOI:10.1016/j.energy.2019.06.094**.

[80] Žerovnik, A., Tušek, J. (2019). *Hybrid Thermal Apparatus, Patent, no. US 2019 264 958 A1*, US Patent Office, Washington.

Harmonic Equivalence of the Impulse Loads in Vibration Fatigue

Primož Ogrinec - Janko Slavič* - Miha Boltežar

University of Ljubljana, Faculty of Mechanical Engineering, Slovenia

In vibration fatigue, three unique types of loads are typical: random, harmonic and impulse. In an application any of these loads are possible. A fatigue-life analysis is possible in the time and frequency domains using the frequency-response function of a structure. Recent studies demonstrated that the impulse loads influence the accuracy of a fatigue-life prediction in the frequency domain. The focus of this research is a theoretical study of an equivalent harmonic load to the impulse load on a single-degree-of-freedom system in order to investigate the feasibility of impulse loads in vibration testing. This research shows that there is a relationship between the impulse and harmonic loads that is related to the underlying dynamic properties (e.g., damping, natural frequency). Based on a theoretical analysis an experimental procedure was developed for both cases of excitation, which was able to confirm the theoretical analysis. Using the modal decomposition the single-degree-of-freedom approach can be generalized to multiple-degrees-of-freedom systems.

Keywords: vibration fatigue, random loads, spectral methods, fatigue life, stationary and non-stationary loading, non-Gaussian loading, vibration testing

Highlights
- *Non-stationary and non-Gaussian loads lead to significantly shorter fatigue lives of a structure.*
- *Impulses, that can occur in the loading signal, render the loading signal non-Stationary and non-Gaussian.*
- *The equivalence between impulse and harmonic loads, with regard to fatigue testing is presented with an analytical derivation.*
- *Control strategies for impulse and harmonic fatigue tests are presented.*
- *The theoretical procedure was experimentally verified on 18 samples, with impulse and harmonic loading.*
- *Material's fatigue parameters were identified for G-AlSi8Cu3(226).*

0 INTRODUCTION

As structures are becoming lighter and loads optimised, the effects of structural dynamics [1] and random loads on the fatigue life of flexible structures are becoming more important. This is known as vibration fatigue and has been the subject of various studies in recent years [2] to [7].

Vibration fatigue is focused in loads well below the yield stress (i.e., high-cycle fatigue), which is typically researched in the time domain (e.g., rainflow-counting algorithm [8]) or in the frequency domain (e.g., the narrow band [9], Dirlik [2] or Tovo-Bennasciutti methods [5] and [3]). When studying fatigue life in the frequency domain it is common to assume that the excitation signals and consequently the stress response of a structure are Gaussian and stationary [10] and [11].

In recent years great efforts have been made to develop the frequency-counting methods in the analysis of the fatigue life of structures excited with non-Gaussian and non-stationary excitation signals [12] to [16]. Tovo and Bennasciutti studied non-stationary switching random loads [4]. Song and Wang [17] presented a spectral-moment-equivalence lumped block method that improves the accuracy of the fatigue-life analysis for non-stationary, non-Gaussian loads and incorporates the material parameters into the equivalent spectral moments formula. Bracessi et al. [18] and Niu et al. [19] researched the influence of load Kurtosis and skewness on the damage rate in the case of non-Gaussian signals; Wolfsteiner and Sedlmair [20] and Cianetti et al. [21] presented correction factors based on those two characteristics of the loading signal.

In real cases it is common to experience some forms of non-Gaussian loading [22], which can also be the result of the impulses superimposed on the random loading of a structure [23]. These impulses can be the consequence of geometric non-linearities, contact conditions, clearances, wear, etc.

While the fatigue life under a combination of harmonic and random loads can be studied in the frequency domain [24], [25] and [6], the effects of these impulse loads are not well researched. The presence of impulses renders the signal non-stationary. Capponi et al. [15] and Palmieri et al. [16] noted that in the case of such signals the fatigue-life assessments with spectral methods in the frequency domain return a significantly longer life prediction than were observed in the experimental testing. Hence, the development of new methods that can account for the presence of impulses in the stress response is of great importance.

*Corr. Author's Address: University of Ljubljana, Faculty of Mechanical Engineering,
Laboratory for Dynamics of Machines and Structures, Aškerčeva 6, 1000 Ljubljana, Slovenia, janko.slavic@fs.uni-lj.si

As was recently shown by Ogrinec et al. [23] the most influential parameters on the accuracy of the frequency-domain methods on the fatigue-life prediction at impulse excitation are: the significant natural frequency, the length of the impulse [26], the coefficient of damping, the modal mass, and the material parameters of the Wöhler curve. For that reason, accurate identification of the material's fatigue parameters is crucial. The material parameters, however, can sometimes vary based on the method used to obtain them. It is known, for instance, that the strain rate can significantly influence measurements of the yield stress and the ultimate tensile strength [27]. Similarly, the identification of the material's fatigue parameters can be influenced [28].

For reasons of simplicity, it is common to use a harmonic loading signal for fatigue testing [29], although some other loading signals are possible [30] and [31]. However, since the influence of the material's fatigue parameters on the fatigue-life estimation's accuracy was proven [23], the question of the validity of the parameters of the Wöhler curve obtained with a harmonic test remains open. Therefore, an experimental exploration of the effects of impulse loading on the identification of material's fatigue properties is necessary.

The main goal of this study is to analyse the possibility to determine the parameters of the Wöhler curve, based on a fatigue test, where the sample is excited with impulses. An experimental setup is presented, where only one significant mode shape was excited. The system is free to respond to the half-sine impulse; therefore, the sample experiences a variety of cycles with varying amplitudes. To produce an equivalent load, the hypothesis of a linear accumulation of damage [32] is assumed. The parameters of the Wöhler curve are compared to an equivalent test, where the sample is excited harmonically.

This manuscript is organised as follows. Sec. 1 presents the theoretical background. The theoretical comparison between the damage accumulation due to harmonic and impulse excitionx is presented in Sec. 2. In Sec. 3 the experimental setup with control algorithms for both load cases is presented. The results are presented in Sec. 4. Sec. 5 draws the conclusions.

1 THEORETICAL BACKGROUND

When a dynamic system is excited in the frequency range of its natural frequencies the response of the system is amplified. If the system is excited with a half-sine impulse, the frequency range of the excitation is determined with the length of the impulse. To take advantage of the response amplification, which is particularly useful in fatigue testing, the impulse has to be specified with this range of excitation in mind.

However, when the system is excited harmonically, the frequency of excitation has to be close enough to a significant natural frequency to obtain the dynamic amplification.

1.1 Structural Dynamics

Any real structure can be regarded as a continuum and can therefore be modelled as a multi-degrees-of-freedom (MDOF) system. The equation of motion for a general MDOF structure is [33], [34]:

$$\mathbf{M}\,\ddot{\mathbf{x}} + \mathbf{C}\,\dot{\mathbf{x}} + \mathbf{K}\,\mathbf{x} = \mathbf{f}, \tag{1}$$

where $\mathbf{M}$, $\mathbf{C}$ and $\mathbf{K}$ are the mass, viscous damping and stiffness matrices of the structure, respectively. $\mathbf{f}$ represents the vector of the excitation forces and $\mathbf{x}$ is the displacement vector of the stucture's degrees of freedom. After introducing the proportional viscous damping ξ and modal coordinates $\mathbf{q}$, the equations of motion become uncoupled [35].

$$\mathbf{I}\,\ddot{\mathbf{q}} + \left[\diagdown 2\boldsymbol{\xi}\,\boldsymbol{\omega_0}\diagdown\right]\dot{\mathbf{q}} + \left[\diagdown\boldsymbol{\omega_0^2}\diagdown\right]\mathbf{q} = \boldsymbol{\Phi}^T\mathbf{f}, \tag{2}$$

where:

$$\mathbf{x} = \boldsymbol{\Phi}\,\mathbf{q}. \tag{3}$$

$\boldsymbol{\Phi}$ is the mass-normalized modal matrix [35]. $\mathbf{I}$ represents the identity matrix, $\left[\diagdown 2\boldsymbol{\xi}\,\boldsymbol{\omega_0}\diagdown\right]$ is the diagonal damping matrix and $\left[\diagdown\boldsymbol{\omega_0^2}\diagdown\right]$ is the diagonal matrix of the natural frequencies. For the i-th modal coordinate q_i the uncoupled equation of motion is [35]:

$$\ddot{q}_i + 2\xi_i\omega_{0,i}\,\dot{q}_i + \omega_{0,i}^2\,q_i = \Phi_i^T\mathbf{f}, \tag{4}$$

where Φ_i is i-th mass-normalized eigenvector. It is worth noting that the transformation to the modal coordinates transforms a MDOF system with N degrees of freedom, to N decoupled single-degree-of-freedom (SDOF) systems.

1.2 Impulse Response

When a SDOF system [35] is excited with an ideal unit impulse, which can be defined with the Dirac delta function:

$$\delta(t) = \begin{cases} \infty, & t = 0 \\ 0, & t \neq 0 \end{cases}, \tag{5}$$

the system responds with the impulse response function $g(t)$ [33] and [35]:

$$g(t) = \frac{e^{-\delta\omega_0 t}\sin\left(\sqrt{1-\delta^2}\omega_0 t\right)}{\sqrt{1-\delta^2}\omega_0}. \qquad (6)$$

When the damping coefficient is small ($\delta \ll 1$, $\sqrt{1-\delta^2} \approx 1$) then Eq. (6) simplifies to:

$$g(t) = \frac{e^{-\delta\omega_0 t}\sin(\omega_0 t)}{\omega_0}. \qquad (7)$$

In order to obtain the response for a general force excitation $f(t)$, the convolution integral of the impulse $f(t)$ and the impulse-response function $g(t)$ are required [36].

$$x(t) = f(t) * g(t) = \int_{-\infty}^{t} f(\tau)g(t-\tau)d\tau, \qquad (8)$$

where t is the time variable and $x(t)$ is the time response of the SDOF system.

The half sine impulse excitation and the impulse load of a SDOF structure are presented in Fig. 1.

1.3 Fatigue-life Estimation

In order to obtain the fatigue damage in the case of an impulse excitation a counting method has to be employed. In this paper the rainflow counting method [8] will be used in combination with the hypothesis of linear damage accumulation [32] and [37]. Here, the basics (used later in this paper) of the time-domain high-cycle approach to the fatigue-life estimation are presented (for details see, e.g. [38]).

The rainflow algorithm [8] transforms the stress-time history into a series of stress reversals. After the stress-time history is determined, the Miners rule of damage accumulation is applied and the damage is calculated as:

$$D^{RF} = \sum_{i=1}^{P} \frac{n_i}{N_i}, \qquad (9)$$

where P is the number of ranges in the stress-reversal series that are identified by the rainflow algorithm and n_i is the number of stress reversals at each individual stress level. Together with the fatigue parameters, which determine the expected number of cycles N_i at a stress level σ_i, Eq. (9) leads to the accumulated damage in the structure. The number of expected cycles N_i that a structure survives at the stress level σ_i is theoretically described with the Wöhler curve [39]:

$$\sigma_i^k N_i = C, \qquad (10)$$

where k and C are the material's fatigue parameters. It is important to be aware that this simple S-N relationship does not account for the material's endurance limit and can only be used when dealing with high-cycle fatigue [40] or with materials that do not exhibit a fatigue limit.

2 HARMONIC EQUIVALENCE OF THE IMPULSE LOADS

2.1 Damage at impulse excitation

In order to compare the harmonic and impulse excitations, the accumulated fatigue damage, which is the consequence of the individual loads, has to be determined analytically. The modal decomposition, as presented in Sec. 1, makes it possible to apply the methods developed for the single-degree-of-freedom (SDOF) system, to multiple-degree-of-freedom (MDOF) systems [35]. As was shown in [23] the dynamic stress response to an impulse excitation can be simplified to a scaled impulse-response function Eq. (7) for the analysis of the fatigue damage in the time domain, assuming the impulses are well separated, meaning that the response of the impulse is completely damped before the next impulse occurs. Therefore, the relatively complex solution of the convolution integral Eq. (8) is not necessary. The stress response of the structure σ_I can be written as a scaled impulse-response function:

$$\sigma_I(t) = \sigma_P \frac{e^{-\delta\omega_0 t}\sin(\omega_0 t)}{\omega_0}, \qquad (11)$$

for small coefficients of damping $\delta \ll 1$. In Eq. (11) the ω_0 stands for the natural frequency of a SDOF system and σ_P the peak stress of the response (envelope). As the rainflow algorithm [8] considers only the peaks and valleys of the stress response, Eq. (11) can be further simplified for the peaks:

$$\sigma_I(i) = e^{-\frac{1}{2}\pi\delta(2i+1)}(-1)^i\sigma_p, \qquad (12)$$

where i is an integer. In this manner the stress response can be discretized to a series of local maximum and minimum values of the stress response, also known as a turning-point sequence. Since the rainflow algorithm requires only the amplitudes of the extreme stress values, the individual stress cycles χ_i can be defined as the summation of the absolute values of the successive extreme points:

$$\chi_i = \frac{1}{2}\left(\sigma_I(i) + \sigma_I(i+1)\right). \qquad (13)$$

After introducing Eq. (12), Eq. (13) becomes:

$$\chi_i = \frac{1}{2}\left(e^{\pi\delta} + 1\right)e^{-\frac{1}{2}\pi\delta(2i+3)}\sigma_p. \qquad (14)$$
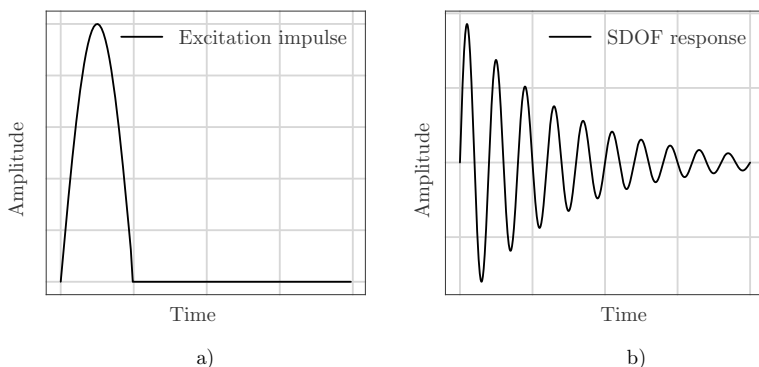
Fig. 1. *a) Normalised half-sine impulse excitation, and b) the impulse response of a SDOF structure*

The Palmgren-Miner rule of linear damage accumulation Eq. (9) can now be employed to determine the damage D as:

$$D = N_I \sum_{i=0}^{\infty} \frac{1}{N_i}, \qquad (15)$$

where N_i is the number of cycles until failure at the level χ_i and N_I is the number of impulse excitations (resulting in the impulse-response cycle load χ_i). By using the definition of the cycles Eq. (14) and the Wöhler curve Eq. (10), the respective number of cycles N_i that the structure would endure for any given stress-cycle amplitude can be determined as:

$$D_I = N_I \sum_{i=0}^{\infty} \left(\frac{\chi_i^k}{C} \right). \qquad (16)$$

The Cauchys criterion for convergence [41] states that for each $\varepsilon > 0$ a pair $k > n$ exists for which:

$$\left| \sum_{j=n+1}^{r} \chi_j \right| = |\chi_{n+1} + \chi_{n+2} + \cdots + \chi_r| < \varepsilon. \qquad (17)$$

Since the stress cycles of a damped SDOF structure limit towards 0, $\lim_{n \to \infty} \chi_n = 0$, the Cauchys criterion is satisfied and the sum in Eq. (16) is final:

$$D_I = -\frac{N_I \, 2^{-k} \left(e^{-\frac{1}{2}(3\pi\delta)} \left(e^{\pi\delta} + 1 \right) \sigma_p \right)^k}{C \left(\left(e^{-\pi\delta} \right)^k - 1 \right)}. \qquad (18)$$

2.2 Damage at Harmonic Excitation

If the load on the structure is harmonic with a constant stress amplitude σ_{eq}, using the Palmgren-Miner rule for linear damage accumulation [32], the cumulative damage is:

$$D_H = N_H \frac{\sigma_{eq}^k}{C}, \qquad (19)$$

where N_H is the number of stress cycles at σ_{eq}.

2.3 The Equivalent Impulse Load to Harmonic Excitation

Here, the damage D_I Eq. (18) of the N_I repetitions of impulse excitation, where the response load is a damped impulse response as shown in Fig. 1, will be related to the damage D_H Eq. (19) due to the harmonic excitation with N_H harmonic cycles at amplitude σ_{eq}:

$$D_I = D_H. \qquad (20)$$

Using Eqs. (18) and (19) and the assumption that the fatigue parameters are the same for impulse and harmonic excitations:

$$-\frac{N_I \, 2^{-k} \left(e^{-\frac{1}{2}(3\pi\delta)} \left(e^{\pi\delta} + 1 \right) \sigma_p \right)^k}{C \left(\left(e^{-\pi\delta} \right)^k - 1 \right)} = N_H \frac{\sigma_{eq}^k}{C}, \qquad (21)$$

which can be simplified to:

$$\sigma_{eq} = \cosh\left(\frac{\pi\delta}{2} \right) \sigma_p \left(\frac{N_I}{N_H \left(e^{\pi\delta k} - 1 \right)} \right)^{1/k}. \qquad (22)$$

For small coefficients of damping $\delta \ll 1$, which is often the case in real structures, this can be further simplified to:

$$\sigma_{eq} = \sigma_p \left(\frac{N_I}{N_H \left(e^{\pi\delta k} - 1 \right)} \right)^{1/k}. \qquad (23)$$

As can be seen from this derivation, the influencing factors on the relation between the impulse and harmonic loads are the coefficient of damping δ, the amplitudes σ_{eq} for harmonic and σ_P impulse loads, the number of harmonic cycles N_H and impulses N_I and the slope of the Wöhler curve k. This analytical derivation proves that for any impulse-response load there exists an equivalent harmonic load that yields the

same damage. Eq. (22) can be rearranged into a form that resembles the notation for the Wöhler curve:

$$\frac{\sigma_{eq}}{\sigma_P} = \left(\frac{1}{e^{\pi\delta k}-1}\right)^{1/k} \left(\frac{N_I}{N_H}\right)^{1/k}. \qquad (24)$$

3 EXPERIMENTAL SETUP

For the experimental validation an electrodynamic shaker capable of impulse and harmonic excitations with closed-loop control was used. In order to obtain the parameters of the Wöhler curve at impulse excitation, the sample's mode shape of interest must be excited with a translational movement in the axis of the shaker. Additionally, the sample's natural frequency of interest must be distinct, well separated from the other natural frequencies and be within the shaker's frequency range [42]. The area where the maximum stresses in the sample occur, must be on a surface where strain-gauge measurements are possible. It is also preferable to correlate strain with the relative displacements, since they can be measured throughout the test more reliably [40],[42].

The Y-shaped sample was chosen as it meets all of these criteria. Its natural frequencies are well separated; therefore, only one mode can be excited. Subsequently, the sample can be regarded as a SDOF system. The specimen consists of three rectangular cross-sections, 10 mm × 10 mm in size, that are arranged at 120° around the main axis. A circular hole in the centre ensures the fatigue zone is concentrated in the centre between the arms of the specimen. The samples are cast from the aluminium alloy G-AlSi8Cu3(226). The thickness is determined by milling and the overall shape by wire EDM (electrical discharge machining). The fatigue zones, which can be clearly seen in Fig. 2, are additionally ground and polished in order to remove any initial surface defects, which could start the crack growth prematurely. On the arms of the specimen two steel dead-weights can be positioned; using different dead-weights the natural frequency and the damping of the system can be changed. The design idea of the specimen is explained in detail in [40]. A total of 18 samples were experimentally tested: 9 of them at impulse excitation and the other 9 samples at harmonic excitation, similar to the description in [23] and [40].

During preparation of the Y-sample, extreme care was taken while machining, as well as during the preparation of the fixture of the sample in order to excite only one significant mode. The material G-AlSi8Cu3(226) was chosen because of its good casting properties that reduce the porosity of the cast

sample. The material is, however, notorious for relatively large silicon inclusions, which affect the variance in the fatigue lives between samples.

The natural frequency of the system was varied with the selection of different weights; three different system setups were researched (each setup was researched with 3 samples with impulse and 3 with harmonic excitation), see Tables 1 and 2 for the natural frequency of the samples, while other parameters given in the table will be discussed later.

3.1 Impulse Test

During the fatigue testing the sample was excited with well-separated half-sine impulses. In the first step an experimental modal analysis was performed to obtain the natural frequencies of the samples. The duration of the impulse was determined with:

$$t_i = \frac{2\pi}{a\omega_0}, \qquad (25)$$

where ω_0 is the focused natural frequency that was excited and a is a constant $a = 2$, as proposed in [23]. Due to the fatigue damage the natural frequency will decrease. In vibration fatigue a change in the natural frequency of 2 % is considered as fatigue failure [43]; with the small change it is reasonable to assume that the mechanical system is still linear. The control loop for impulse testing is presented in Fig. 3. If x_S is the amplitude of displacement of the shaker base and x_A is the amplitude of displacement of one of the Y-sample arms, then the relative displacement amplitude Δx can be related to the stress σ in the fatigue zone via the coefficient k_σ [23]:

$$k_\sigma = \frac{\sigma}{\Delta x} = \frac{E\,\varepsilon\,\omega^2}{\ddot{x}_S - \ddot{x}_A}, \qquad (26)$$

where ε is the strain, measured in the fatigue zone, ω is the frequency of excitation, $\ddot{x}_A$ is the acceleration of the arm of the sample, $\ddot{x}_S$ is the acceleration of the armature of the shaker, and E is the elastic modulus. The relation between the accelerations and deflections is simple since the response of the structure is harmonic in both excitation cases. This calibration was performed on a separate sample, so as not to induce any initial damage to the samples that were used for the identification of the material's fatigue properties.

As the natural frequency was well excited in the impulse testing, it was possible to identify and track the natural frequency for every impulse-excitation response. Thus it was possible to identify the critical
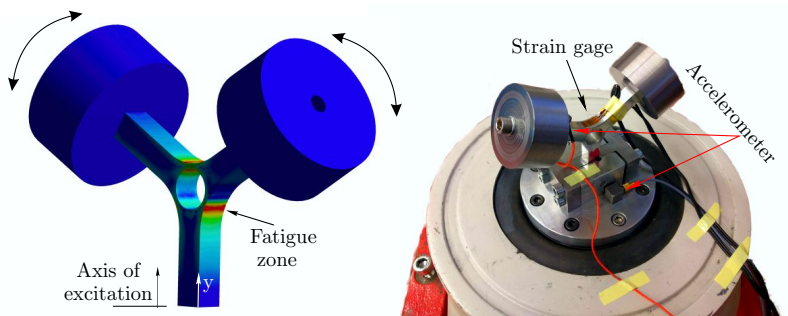
Fig. 2. *Experimental setup*

Table 1. *Samples for the impulse test*

Sample nr.	Natural frequency [Hz]	σ_P [MPa]	N_I [/]	δ^{init} [/]	D_I^{init} [/]	δ^{fin} [/]	D_I^{fin} [/]
1.1	300.0	126.1	7 300	0.0241	1.64	0.0301	1.19
1.2	300.0	88.34	155 000	0.0218	1.29	0.0236	1.16
1.3	300.0	125.9	6 460	0.0246	1.38	0.0253	1.33
2.1	330.0	88.4	105 560	0.0178	1.16	0.0188	1.08
2.2	334.0	84.0	226 180	0.0189	1.40	0.0363	0.55
2.3	328.0	83.2	233 080	0.0165	1.57	0.0186	1.34
3.1	402.0	74.2	309 660	0.0145	0.82	0.0153	0.76
3.2	398.5	78.3	120 420	0.0100	0.83	0.0169	0.44
3.3	402.0	82.7	206 140	0.0170	1.27	0.0183	1.15

Table 2. *Samples for the harmonic test*

Sample nr.	Natural frequency [Hz]	δ [/]	σ_H [MPa]	N_H [/]	D_H [/]
4.1	298.0	0.0276	55.3	13 122 486	1.11
4.2	300.0	0.0284	65.0	2 629 897	1.06
4.3	300.0	0.0232	50.0	37 004 975	1.19
5.1	331.0	0.0169	60.3	4 463 862	0.83
5.2	333.0	0.0171	40.1	508 457 676	1.94
5.3	330.0	0.0181	49.9	26 809 448	0.85
6.1	400.5	0.0138	44.2	68 807 660	0.68
6.2	399.0	0.0145	80.0	284 920	0.85
6.3	402.0	0.0121	46.1	67 629 488	1.00

damage of the sample when the natural frequency fell by 2 %.

During the fatigue test, as the damage increases, the damping can change [**29**]. For an accurate damage estimation it is therefore important to identify the damping coefficient throughout the test. Table 1 shows the initial δ^{init} and the final δ^{fin} values of the coefficient of damping. Due to the open-loop strategy, also the stress load, estimated from the two accelerometers, can slightly change. During the fatigue test, a peak amplitude deviated less than to 2 % for all samples, but the sample 1.1, a 6 % decrease was observed.

3.2 Harmonic Test

Under the harmonic test, the samples were excited harmonically with a frequency close to the significant

natural frequency. A control strategy was used, where the phase shift Φ between the accelerometer mounted on the shaker's armature and the arm of the sample (see Fig. 2) was monitored to adjust the excitation frequency and to control the stress amplitude [**40**], see Fig. 4. During the harmonic test, the amplitude and natural frequency were updated every 500 ms.

The damping coefficient does not influence the fatigue-life prediction in the case of harmonic excitation. The excitation amplitudes can, however, still vary. Although a closed-loop control algorithm was used, the excitation amplitudes could vary by up to 0.5 %.

3.3 Damage Criteria

As the structural dynamics of the sample changes long before its complete failure, it is practical to identify
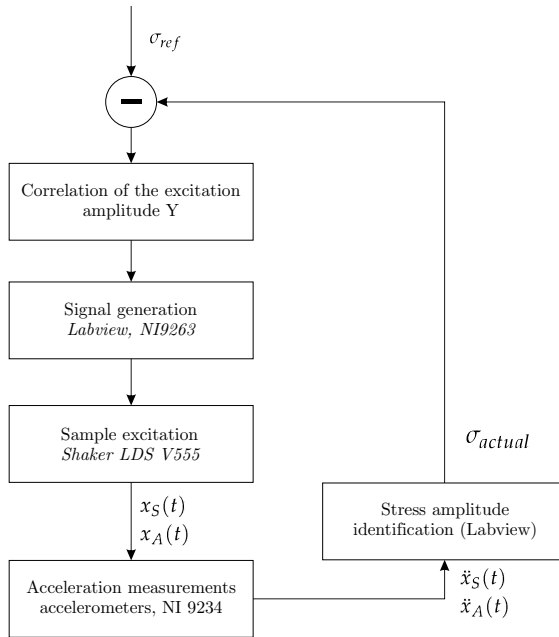
Fig. 3. *Control loop for impulse excitation*
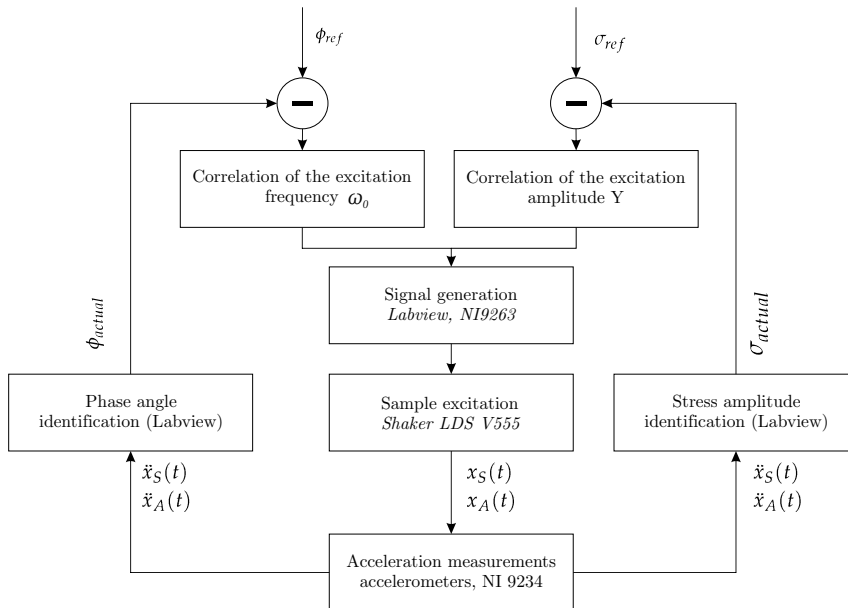
Fig. 4. *Control loop for harmonic excitation*

a failure when the natural frequency starts to change rapidly [40] and [42]. Therefore, in this research a drop of 2 % in the natural frequency was considered as a failure. For details about the failure on damage identification from the natural frequency, the interested reader is referred to [44].

During the impulse test the identification of the natural frequency is fairly straight forward, as it can be identified as the frequency at the peak value in the Fourier transform of the stress signal, see Fig. 5. During the harmonic test, the natural frequency had to be identified indirectly, from the

phase difference between the signals of the top and bottom accelerometers. As the frequency falls, the excitation frequency required to keep the same dynamic gain and the phase shift between the signals falls likewise. Therefore, the fall of the significant natural frequency can be determined by recording the excitation frequency. The tracked excitation frequency is shown in Fig. 6.
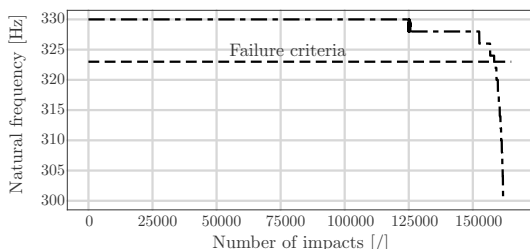
Fig. 5. *Decreasing of natural frequency during the impulse fatigue test*
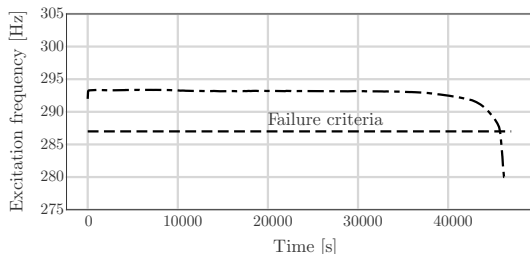
Fig. 6. *Fall of excitation frequency during harmonic excitation.*

4 RESULTS

4.1 Identification of the Wöhler Curve

Since the goal of this paper is to prove the equivalence of the impulse and harmonic loads, the Wöhler curve was identified on the harmonic test results, only. The fatigue parameters for the equiprobability curve identified on the harmonic test results were:

$$C_{\mathrm{H}} = 7.2450 \times 10^{23}, \tag{27}$$

$$k_{\mathrm{H}} = 9.6347. \tag{28}$$

The parameters were identified with the cost function:

$$\varepsilon(\tilde{k},\tilde{C}) = \min\left[\sum_{i=1}^{S} D_i(\tilde{k},\tilde{C}) - 1\right], \tag{29}$$

where S is the number of samples, $\tilde{k}$ and $\tilde{C}$ are the material parameters used in each individual iteration of the optimisation, and $\varepsilon(\tilde{C},\tilde{k})$ is the error between the optimal value of the damage and the damage in current iteration.

4.2 Comparing the Two Loading Strategies

With the fatigue parameters obtained from the harmonic test Eq. (27), Eq. (19) is used to theoretically estimate the damage for the harmonic test. As the fatigue parameters were fitted to the experimental results of the harmonic test it is expected that D_H would be close to 1. From Table 2 we can see that this is the case for most of the samples; the deviation from 1 is reasonable and expected in the fatigue test.

It is reasonable to assume that the fatigue parameters between the harmonic and the impulse test are the same. Therefore, the fatigue parameters obtained from the harmonic test Eq. (27) can be used with the damage estimation at impulse excitation Eq. (18). The resulting damage D_i^{init} and D_i^{fin} based on the damping identified at the beginning and the end of the test are given in Table 1. We can see that the damage is reasonably close to 1.

This experimental result validates the theoretical relation between the impulse and the harmonic load introduced in Eq. 24.

5 CONCLUSIONS

The harmonic loads for high-cycle fatigue are well understood and can be theoretically and experimentally researched relatively easily. The contrary is true for the impulse loads; the impulse excitation is frequently exciting mechanical systems, leading to a damped free response related to the structural dynamic's of the system. Based on the structural dynamics theoretical background and classic fatigue theory in the time domain, a theoretical relation between the vibration-fatigue damage in the case of the impulse load and the harmonic load is introduced.

The theoretical model was experimentally evaluated using the Y-sample. A total of 18 samples were experimentally tested; 9 for harmonic loads and 9 for impulse excitation. The samples were grouped in sets of 3. Using different mass loadings to the Y-sample, three different dynamic systems were researched (different natural frequencies and damping). Based on the time-domain experimental data from the harmonic test, the fatigue parameters were identified. The identified material parameters were then used to recalculate the damage at failure for every individual sample, for both excitation strategies. The identified damage was reasonably close to 1 confirming the introduced theoretical relation between the impulse and harmonic excitations.

The introduced relation between the impulse and harmonic excitations can be used for the

further development of frequency-counting methods, specifically with impulse loads as a source of non-stationarity.

6 ACKNOWLEDGEMENTS

7 REFERENCES

[1] Luznar, J., Slavič, J., Boltežar, M. (2019). Structure-borne noise at PWM Excitation using an extended field reconstruction method and modal decomposition. *Strojniški vestnik - Journal of Mechanical Engineering*, vol. 65, no. 9, p. 471-481, **DOI:10.5545/sv-jme.2019.6115**.

[2] Dirlik, T. (1985). Application of Computers in Fatigue Analysis. PhD thesis, University of Warwick, Warwick.

[3] Benasciutti, D (2004). Fatigue Analysis of Random Loadings. PhD thesis, University of Ferrara, Ferrara.

[4] Benasciutti, D., Tovo, R. (2007). Frequency-based fatigue analysis of non-stationary switching random loads. *Fatigue & Fracture of Engineering Materials & Structures*, vol. 30, no. 11, p. 1016-1029, **DOI:10.1111/j.1460-2695.2007.01171.x**.

[5] Benasciutti, D., Tovo, R. (2018). Frequency-based analysis of random fatigue loads: Models, hypotheses, reality. *Material Science and Engineering Technology*, vol. 49, no. 3, p. 345-367, **DOI:10.1002/mawe.201700190**.

[6] Mršnik, M., Slavič, J., Boltežar, M. (2013). Frequency-domain methods for a vibration-fatigue-life estimation–application to real data. *International Journal of Fatigue*, vol. 47, p. 8-17, **DOI:10.1016/j.ijfatigue.2012.07.005**.

[7] Mršnik, M., Slavič, J., Boltežar, M. (2018). Vibration fatigue using modal decomposition. *Mechanical Systems and Signal Processing*, vol. 98, p. 548-556, **DOI:10.1016/j.ymssp.2017.03.052**.

[8] Matsuishi, M., Endo, T. (1968). Fatigue of metals subjected to varying stress. *Japan Society of Mechanical Engineers*, vol. 68, no. 2, p. 37-40.

[9] Miles, J.W. (1954). On structural fatigue under random loading. *Journal of the Aeronautical Sciences*, vol. 21, no. 11, p. 753-762, DOI:10.2514/8.3199.

[10] Newland, D.E. (2012). *An Introduction to Random Vibrations, Spectral & Wavelet Analysis*. Dover Publication, Mineola.

[11] Bendat, J., Piersol, A. (2011). *Random Data: Analysis and Measurement Procedures*, vol. 729, John Wiley & Sons, Hoboken.

[12] Braccesi, C., Cianetti, F., Tomassini, L. (2017). Fast evaluation of stress state spectral moments. *International Journal of Mechanical Sciences*, vol. 127, p. 4-9, **DOI:10.1016/j.ijmecsci.2016.11.007**.

[13] Böhm, M., Łagoda, T. (2018). Fatigue life assessment with the use of the spectral method for non-Gaussian loading histories with the use of the energy parameter. *Journal of Machine Construction and Maintenance*, vol. 1, p. 27-31.

[14] Fan, Z., Jiang, Y., Zhang, S., Tao, J., Chen, X. (2017). Research on vibration fatigue of carbon fibre-reinforced composites under non-Gaussian random load. *Prognostics and System Health Management Conference*, p. 1-8, **DOI:10.1109/PHM.2017.8079154**.

[15] Capponi, L, Česnik, M., Slavič, J., Cianetti, F., Boltežar, M. (2017). Non-stationarity index in vibration fatigue: Theoretical and experimental research. *International Journal of Fatigue*, vol. 104, p. 221-230, **DOI:10.1016/j.ijfatigue.2017.07.020**.

[16] Palmieri, M., Česnik, M., Slavič, J., Cianetti, F., Boltežar, M. (2017). Non-Gaussianity and non-stationarity in vibration fatigue. *International Journal of Fatigue*, vol. 97, p. 9-19, **DOI:10.1016/j.ijfatigue.2016.12.017**.

[17] Song, X., Wang, S. (2019). A novel spectral moments equivalence based lumping block method for efficient estimation of offshore structural fatigue damage. *International Journal of Fatigue*, vol. 118, p. 162-175, **DOI:10.1016/j.ijfatigue.2018.09.016**.

[18] Braccesi, C., Cianetti, F., Lori, G., Pioli, D. (2009). The frequency domain approach in virtual fatigue estimation of non-linear systems: The problem of non-Gaussian states of stress. *International Journal of Fatigue*, vol. 31, no. 4, p.766-775, **DOI:10.1016/j.ijfatigue.2008.03.007**.

[19] Niu, Q., Yang, S., Li, X. (2018). An empirical mode decomposition-based frequency-domain approach for the fatigue analysis of nonstationary processes. *Fatigue & Fracture of Engineering Materials & Structures*, vol. 41, no. 9, p. 1980-1996, **DOI:10.1111/ffe.12836**.

[20] Wolfsteiner, P., Sedlmair, S. (2015). Deriving Gaussian fatigue test spectra from measured non Gaussian service spectra. *Procedia Engineering*, vol. 101, p. 543-551, **DOI:10.1016/j.proeng.2015.02.065**.

[21] Cianetti, F., Palmieri, M., Braccesi, C., Morettini, G. (2018). Correction formula approach to evaluate fatigue damage induced by non-Gaussian stress state. *Procedia Structural Integrity*, vol. 8, p. 390-398, **DOI:10.1016/j.prostr.2017.12.039**.

[22] Rychlik, I. (1996). Fatigue and stochastic loads. *Scandinavian Journal of Statistics*, p. 387-404.

[23] Ogrinec, P., Slavič, J., Česnik, M., Boltežar, M. (2019). Vibration fatigue at half-sine impulse excitation in the time and frequency domains. *International Journal of Fatigue*, vol. 123, p. 308-317, **DOI:10.1016/j.ijfatigue.2019.02.031**.

[24] Angeli, A., Cornelis, B., Troncossi, M. (2018). Synthesis of sine-on-random vibration profiles for accelerated life tests based on fatigue damage spectrum equivalence. *Mechanical Systems and Signal Processing*, vol. 103, p. 340-351, **DOI:10.1016/j.ymssp.2017.10.022**.

[25] Carpinteri, A., Spagnoli, A., Vantadori, S. (2017). A review of multiaxial fatigue criteria for random variable amplitude loads. *Fatigue & Fracture of Engineering Materials & Structures*, vol. 40, no. 7, p. 1007-1036, **DOI:10.1111/ffe.12619**.

[26] Rizzi, S., Przekop, A., Turner, T.L. (2011). On the response of a nonlinear structure to high kurtosis non-Gaussian random loadings. *8th International Conference on Structural Dynamics*, p. 1-8.

[27] Eibl, J., Curbach, M. (1989). An attempt to explain strength increase due to high loading rates. *Nuclear Engineering*

and Design, vol. 112, p. 45-50, **DOI:10.1016/0029-5493(89)90144-1**.

[28] Song, W.Q., Beggs, P., Easton, M. (2009). Compressive strain-rate sensitivity of magnesium–aluminum die casting alloys. *Materials & Design*, vol. 30, no. 3, p. 642-648, **DOI:10.1016/j.matdes.2008.05.050**.

[29] Česnik, M., Slavič, J. (2014). Vibrational fatigue and structural dynamics for harmonic and random loads. *Strojniški vestnik - Journal of Mechanical Engineering*, vol. 60, no. 5, p. 339-348, **DOI:10.5545/sv-jme.2013.1831**.

[30] Pahor Kos, V., Slavič, J., Boltežar, M. (2014). Fatigue damage for sweep-sine and random accelerated vibration testing. *Advances in Mechanical Engineering*, vol. 7, no. 2, p. 1-8, **DOI:10.1155/2014/340545**.

[31] Česnik, M., Slavič, J., Boltežar, M. (2016). Assessment of the fatigue parameters from random vibration testing: Application to a rivet joint. *Strojniški vestnik - Journal of Mechanical Engineering*, vol. 62, no. 7-8, p. 471-482, **DOI:10.5545/sv-jme.2016.3774**.

[32] Miner, M.A. (1959). Estimation of fatigue life with particular emphasis on cumulative damage. *Metal Fatigue*, p. 278-289.

[33] Géradin, M., Rixen, D.J. (2014). *Mechanical Vibrations: Theory and Application to Structural Dynamics*. John Wiley & Sons, Hoboken.

[34] Rao, S., Yap, F.F. (2011). *Mechanical Vibrations*, vol. 4. Prentice Hall, Upper Saddle River.

[35] Maia, N.M.M., e Silva J.M.M. (1997). *Theoretical and Experimental Modal Analysis*. Research Studies Press, Taunton.

[36] Smith, S.W. (1997). *The Scientist and Engineer's Guide to Digital Signal Processing*. California Technical Pub., San Diego.

[37] Palmgren, A. (1924). Die lebensdauer von kugellagern. *Zeitschrift des Vereines Deutscher Ingenieure (ZVDI)*, vol. 14, p. 339-341. (in German)

[38] Socie, D.F., Marquis, G.B. (2000). *Multiaxial Fatigue*. Society of Automotive Engineers, Warrendale.

[39] Wöhler, A. (1870). *Über die Festigkeits-versuche mit Eisen und Stahl*. Ernst and Korn, Berlin. (in German)

[40] Česnik, M., Slavič, J., Boltežar, M. (2012). Uninterrupted and accelerated vibrational fatigue testing with simultaneous monitoring of the natural frequency and damping. *Journal of Sound and Vibration*, vol. 331, no. 24, p. 5370-5382, **DOI:10.1016/j.jsv.2012.06.022**.

[41] Rudin, W. (1976). Principles of Mathematical Analysis, volume 3. McGraw-Hill, New York.

[42] George, T.J., Seidt, J., Shen, M-H H., Nicholas, T., Cross, C.J. (2004). Development of a novel vibration-based fatigue testing methodology. *International Journal of Fatigue*, vol. 26, no. 5, p. 477-486, **DOI:10.1016/j.ijfatigue.2003.10.012**.

[43] Mršnik, M., Slavič, J., Boltežar, M. (2016). Multiaxial vibration fatigue; a theoretical and experimental comparison. *Mechanical Systems and Signal Processing*, vol. 76-77, p. 409-423, **DOI:10.1016/j.ymssp.2016.02.012**.

[44] Kim, J.T., Ryu, Y.S., Cho, H.M., Stubbs, N. (2003). Damage identification in beam-type structures: frequency-based method vs mode-shape-based method. *Engineering Structures*, vol. 25, no. 1, p. 57-67, **DOI:10.1016/S0141-0296(02)00118-9**.

Cavitation as a Potential Technology for Wastewater Management – An Example of Enhanced Nutrient Release from Secondary Pulp and Paper Mill Sludge

Mija Sežun[1] – Janez Kosel[2] – Mojca Zupanc[3] – Marko Hočevar[3] –
Janez Vrtovšek[3] – Martin Petkovšek[3] – Matevž Dular[3,*]

[1]Pulp and Paper Institute, Slovenia
[2]Institute for the Protection of Cultural Heritage of Slovenia, Slovenia
[3]University of Ljubljana, Faculty of Mechanical Engineering, Slovenia

Wastewater recycling and sludge removal in the paper industry account for about 60 % of all process costs. New and environmentally friendly wastewater treatment techniques are, therefore, continually being developed. Cavitation exploitation is currently a well-investigated topic that is also interesting for the paper production industry. This study investigates efficiency of hydrodynamic cavitation alone and in combination with the addition of NaOH for the treatment of secondary pulp and paper mill sludge in order to enhance nutrient release. First, two laboratory-scale devices were tested: the blow-through and the rotating hydrodynamic cavitation generator. The latter set-up proved to be more efficient: therefore, further experiments were performed on its pilot-scale version. The results showed an increase of soluble chemical oxygen demand (COD_s) by 514 mg/L, total nitrogen (N_t) by 17.4 mg/L, and total phosphorous (P_t) by 2.3 mg/L. To further increase nutrient release combination of cavitation and sludge sample alkalinization was tested. The addition of NaOH and 30 min cavitation of secondary sludge (500 L) significantly improved COD_s and N_t release by 2400 mg/L and 120 mg/L, respectively. Microbiological photos revealed a definite disintegration of sludge flocks. According to our estimates, 1.9 kg of released COD_s from alkaline pre-treated and cavitated sludge would cost only one euro.
Keywords: hydrodynamic cavitation, nutrients, paper mill plant, secondary sludge, sludge disintegration, wastewater treatment

Highlights
- *Hydrodynamic cavitation improves paper mill secondary sludge disintegration and nutrient release.*
- *Experiments were performed on a pilot scale (volume of 500 L).*
- *Cavitation alone increased COD_s (2× compared to initial value).*
- *The addition of NaOH in cavitation treatment increased COD_s further (9× compared to the initial value).*
- *1.9 kg of released COD_s costs only one euro.*

0 INTRODUCTION

Cavitation can be described as the appearance of vapour bubbles (cavities) inside a liquid medium. The phenomenon is similar to boiling, but in contrast, is initiated by the sudden decrease in pressure while the temperature remains approximately constant. As the pressure recovers, the bubble goes through a violent collapse. If the bubble collapses spherically, pressure shocks up to several 100 MPa [1] can be emitted. In contrast, with an asymmetrical collapse, so-called microjets with high velocities above 100 m/s can form [2]. In addition, so-called hot spots with extreme temperatures in the order of several 1000 K [3] can form at the centre of the bubble at its collapse, which can cause the formation of highly reactive radicals such as OH [4].

In general, two types of cavitation are recognized: hydrodynamic (HC) and acoustic cavitation (AC). The difference is in the mechanism, which causes the local pressure to drop, while the principles that govern the hydrodynamically and acoustically generated bubbles are basically the same. In the case of HC, acceleration of the liquid flow causes local pressure drop, which can, if the pressure drops below saturated pressure, trigger the cavitation formation. Depending on the flow conditions, the size of the formed cavitation bubbles varies, usually between a few nm to a few mm. Flow conditions and the geometry of the submerged body define cavitation behaviour and its characteristics. HC can be in general divided into i) attached cavitation, ii) developed cloud shedding cavitation, and iii) supercavitation. In the case of attached cavitation, a large number of vapor bubbles are attached to the surface of the constriction, forming an attached cloud-like shape. If we further increase the flow velocity or decrease the static pressure in the system, the previously attached cavitation cloud becomes unstable and starts (partly or completely) to shed from the main cavitation structure; this stage is called developed or cloud shedding cavitation. This condition is also known as the most aggressive one. With further increases of the flow velocity (or decrease of system pressure), the so-called supercavitation

forms. It starts when the individual bubbles coalesce and eventually form a single, large, and stable vapor pocket.

Cavitation is usually associated with engineering problems, such as material loss, noise, vibration, and the decreased of efficiency of hydraulic machines. However, cavitation is a potentially useful phenomenon: the extreme conditions are increasingly used for a wide variety of applications, such as surface cleaning, enhanced chemistry, and wastewater treatment (bacteria eradication and virus inactivation).

Nowadays, the availability of clean water is becoming an increasing concern in the globalized world, in both developed and developing countries. Therefore, an efficient and clean wastewater cleaning and disinfection technology, such as cavitation, would be readily welcome to substitute or be combined with the existing ones.

The regulations regarding waste management have become stricter and, in order to satisfy set environmental limits, many industries must implement their own wastewater treatment facilities. One such industry is the paper production industry. For paper production, 54 % of materials are raw, and the rest are sourced from recovered paper and board. Therefore, paper is the most recycled product in Europe, and Europe is the global leader in paper recycling, with a recycling rate of 72 % [5]. Globally, the pulp and paper industry is currently on the rise, and, subsequently, an enormous amount of waste is generated every day. The most common waste material generated in pulp and paper mills is ash, dregs, grits, pulp mill sludge, and a significant amount of wastewater depending on the type of processes used in the plant. In the past, these wastes were simply deposited on the landfills; however, with changes in regulation and with increased environmental awareness, new alternatives have been investigated, especially reappraising these materials as valuable [6]. Due to the numerous impurities, health hazards, and environmental risks present in wastewater, an effective cleaning measure has to be implemented [7]. Accordingly, in the pulp and paper industry, several wastewater treatment systems exist for the removal of organic and inorganic substances in order to meet the effluent discharge standards. These include anaerobic treatments, activated sludge lagoons, and clarifier systems. Established wastewater recycling and sludge removal are, therefore, very expensive, amounting to as much as 60 % of all process costs [8]; consequently, new and alternative solutions are being developed.

Numerous studies have been made to reduce energy consumption, to produce new materials and products and to reuse or circulate the sludge [9], for example, anaerobic digestion [10] and [11] for the formation of biogas and for the production of biohydrogen [12] and [13], addition into building materials [14] and [15], and for the production of activated carbon [16].

One ever more commonly applied mechanical pre-treatment alternative is cavitation. It can be used alone or in combination with various treatments. During the cavitation process, extreme conditions can occur, forming highly intensive shockwaves, microjets, and extreme temperatures, which can drive mechanical and chemical effects. Shear forces released and production of ·OH by decomposition of water molecules [4] can both influence sludge disintegration [17] and [18]. AC alone and coupled with chemical treatment has been thoroughly investigated for the disintegration of different waste sludges before aerobic processes for nutrient reuse [17], [19], and [20] and anaerobic processes for biogas production [21] to [23].

0.1 Contributions of Our Research Group on the Topic of HC Use in Wastewater Treatment

Since 2012, our research group has been engaged in the development of efficient cavitation-based technologies for wastewater treatment and sludge remediation, mainly for the removal of chemical and microbiological pollutants.

Our initial focus was on the removal of persistent pharmaceuticals, such as ibuprofen, ketoprofen, diclofenac, naproxen, carbamazepine, and clofibric acid [24] and [25]; we applied HC for waste-activated sludge disintegration [23]. Concurrently, we developed several cavitation reactors [26] and filed several national [27] and international [28] patents. The shift from applied towards basic research came with studies of cavitation influence on bacteria *Legionella pneumophila* [29]. In our next study, it was demonstrated that the least aggressive cavitation type (supercavitation) hydrodynamically is the most destructive against the bacteria [30]. We questioned several well-established postulates [31] and [32]. By gaining new knowledge, we again progressed in applied science and for the first time showed that cavitation can be exploited for virus inactivation [33], and even for "exotic" applications, such as intensification of aqueous laundry detergent solution preparation [34].

In 2018, we were awarded a European Research Council (ERC) project CABUM, with which we aim, during the course of five years, to

gain a deeper understanding of the mechanisms [35] that will eventually enable reliable cavitation exploitation in various disciplines. Recently, we have also investigated the application of cavitation in the paper production industry. We have shown that cavitation can be used to replace processes such as homogenization, fibrillation, and refining of paper pulp [36].

We have continued with the investigations of applicability of cavitation in paper producing plants. The main objective and innovation of this study were thus to determine the effectiveness of a hydrodynamic cavitation set-up for the treatment of paper mill secondary sludge. By implementing cavitation, our objective was to achieve a greater nutrient release and greater disintegration of biological compounds. Different cavitation set-ups, the addition of NaOH to sludge samples, as well as different treatment times were tested. The first experiments were conducted in the laboratory, and pilot scale experiments followed.

1 MATERIALS AND METHODS

1.1 Sample Characterization

Total chemical oxygen demand (COD_t) and soluble COD (COD_s) were measured using COD cuvette tests (Hach Lange LCK 314 for samples with a COD value between 15 mg O_2 /L and 150 mg O_2 /L and LCK 714 for samples with a COD value between 100 mg O_2 /L and 600 mg O_2 /L). Total nitrogen (N_t) was determined by using N_t cuvette tests (Hach Lange LCK 138 for samples with values of N_t between 1 mg/L/L and 16 mg/L/L and LCK 338 for samples with N_t values between 20 mg/L/L and 100 mg/L). Total phosphorous (P_t) was measured using the PhosVer 3 (Ascorbic Acid) method (#8048, Hach Lange). For these measurements, a DR3900 spectrophotometer (Hach-Lange, Germany) was used. pH value and redox potential were determined during sampling on site, with a Multi 340i analyser (WTW, Germany). Settleable solids were analysed according to the Deutsches Institut fur Normung (DIN 38409-2, 1980) [37], in which settleable substances were shaken, and timed sedimentation was determined in a measuring container. The calorific value was determined using ASTM methods [38].

1.2 Hydrodynamic Cavitation Set-ups

The effects of HC on pulp and paper mill secondary sludge were investigated on lab-scale and pilot-scale cavitation devices. For lab-scale experiments, the effects of two different HC set-ups were investigated. Firstly, the blow-through hydrodynamic cavitation (BTHC) set-up using a symmetrical Venturi constriction was tested. Second, the rotating generator of hydrodynamic cavitation (RGHC) was tested. The lab-scale experiments were performed on 1 L samples for 30 minutes, below 30 ºC. While the BTHC device was designed only for lab-scale experiments, the RGHC was additionally scaled up to perform pilot experiments. The pilot-scale experiments were performed on 500 L samples for 30 min, below 30 ºC. All cavitation devices used in this paper were developed and designed by Laboratory for Hydraulic Machines, Department of Power Engineering, Faculty of the Mechanical Engineering, University of Ljubljana, Slovenia.

1.2.1 Blow-Through Hydrodynamic Cavitation Set-up (BTHC)

The lab-scale reactor for cavitation generation, BTHC (Fig. 1), consists of two reservoirs connected by a symmetrical Venturi constriction. 1 L of sample is introduced into the right reservoir (state 1, Fig. 1) and pushed through the Venturi constriction, where cavitation occurs, into the left reservoir using compressed air (state 2, Fig. 1). After the whole sample is pushed into the left reservoir (state 3, Fig. 1), the procedure is repeated, and the sample is pushed back to the right reservoir (state 4, Fig. 1). The time needed to push 1 L of the sample from one reservoir to another is 6 seconds at 7 bar pressure difference. The BTHC set-up is in more detail described in [24].

1.2.2 Rotating Hydrodynamic Cavitation Generator (RGHC) Set-up

The lab-scale device (Fig. 1) consists of a reservoir, RGHC, and a heat exchanger. The sample introduced into the reservoir flows through the RGHC, where it is exposed to cavitation and through the heat exchanger, which provides the constant temperature of the sample, back into the reservoir. The heat exchanger (water to air) is force-cooled by an external fan. RGHC is based on a rotor-stator design, in which the rotor and stator have specially designed geometry, which causes periodically repeating pressure oscillations. With the pressure oscillations, the cavitation periodically forms in the gap between rotor-stator, on the rotor's teeth and in the rotor's and stator's grooves. The rotor with 50 mm in diameter is driven by a 400 W electrical motor at approx. 10.000 rpm. The RGHC is in presented more detail in [39].
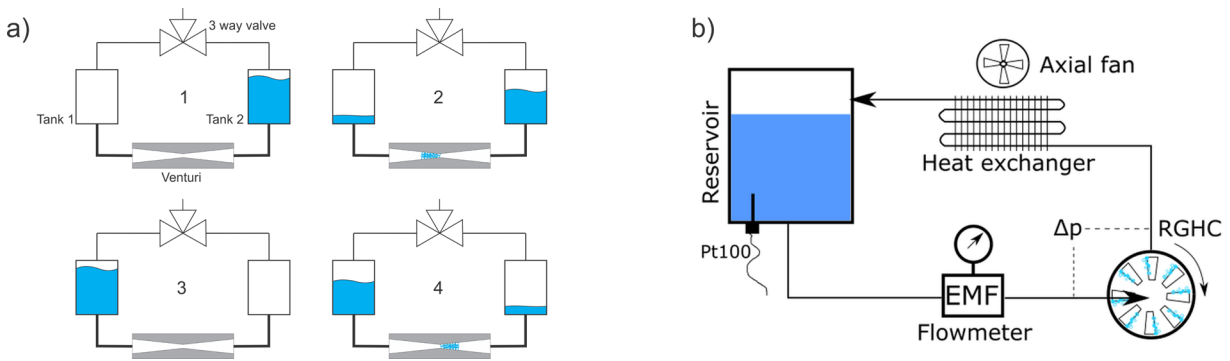
Fig. 1. *a) Schematic presentation of BTHC [24], and b) schematic presentation of lab-scale RGHC experimental set-up*

The pilot-scale RGHC design is similar to the lab-scale and is described in more detail in [23]. The main differences are that the pilot-scale RGHC does not have a heat exchanger, has a rotor with 190 mm in diameter and is driven by a 5.5 kW electric motor at 2800 rpm. In the pilot-scale device, larger samples can be treated, in our case 500 L.

2 RESULTS AND DISCUSSION

2.1 Lab-scale Experiments

The effect of the hydrodynamic cavitation generated inside the laboratory scaled RGHC and BTHC devices on the composition of pulp and paper mill secondary sludge is presented in Fig. 2. In these experiments, the samples were exposed to cavitation for 30 min; after treatment N_t, COD_t and COD_s were measured.

Based on the results, we can see that both cavitation devices significantly decreased the COD_t the value of the secondary pulp and paper mill sludge. We suspect that this was due to the mineralization of compounds, i.e., the degradation/oxidation of compounds in organic matter and the release of simple nutrients [40]. We can also see that COD_s and N_t

increased in both cavitation devices. That is probably because extreme conditions during cavitation ruptured the membranes of microorganisms and released their intercellular contents into the bulk solution [23]. These released compounds, which are, together with wastewater, returned to the biological wastewater treatment process can replace a part of the outside nutrient source, which are necessary for a stable operation of the pulp and paper mill wastewater plant. Additionally, with the destruction of microorganisms, the amount of sediment decreases, which has beneficial effects on the final treatment of pulp and paper mill sludge.

In the case of the RGHC, the increase of N_t and COD_s is higher than for the BTHC device, which indicates its higher efficiency at approximately the same energy input per litre of the sample (Fig. 2). The reason for its greater COD_s and N_t release may be in the fact that the sample was subjected to more intensive shear flow conditions during this type of cavitation [30]. In the RGHC device, the rotor's and stator's teeth are periodically interacting with each other, resulting in intense pressure fluctuations. Each rotor-stator teeth pair (with a 1 mm gap between opposite teeth) forms a quasi-Venturi constriction,
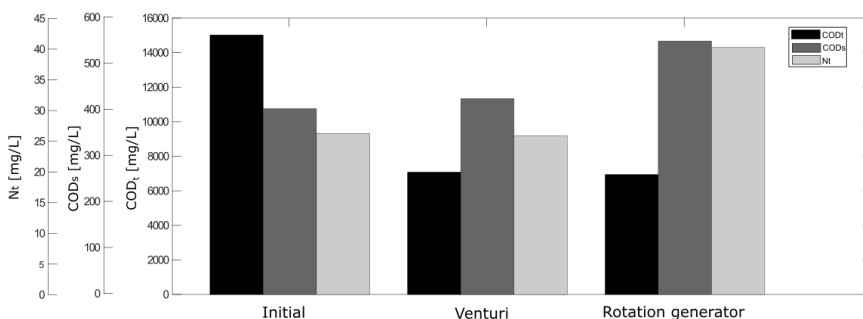
Fig. 2. *N_t, COD_t and COD_s measurements before and after treatment with two types of cavitation devices (BTHC and RGHC) on lab-scale*

which might explain the higher efficiency of RGHC with a high number of constrictions, compared to only one in BTHC [30].

In addition to the laboratory-scale experiments with the RGHC device, which resulted in the highly positive effect of HC towards mineralization, additional experiments of the sole effect of alkalinization (addition of NaOH until the pH value was 10) on the chemical composition of secondary pulp and paper mill sludge were also performed. These tests were conducted in 1 L jars which were stirred for 30 min by a magnetic stirrer.

The results showed that alkalinization alone increased the COD_s value from 315 mg/L to 990 mg/L. Therefore, we decided to evaluate the possible synergistic effect of cavitating alkaline pre-treated secondary pulp and paper mill sludge (pH value of 10) in the pilot-scale RGHC device.

2.2 Pilot-scale Experiments

In Table 1, the effect of HC generated inside the pilot-scale RGHC device on the chemical characteristics of the secondary pulp and paper mill sludge is presented. After 30 min of cavitation, the COD_s value increased by 514 mg/L. Apart from the N_t (17.4 mg/L), the cavitation treatment generated inside the pilot-

scale RGHC also increased the total phosphorous released (P_t) from 0.6 mg/L to 2.9 mg/L. Therefore, as stated previously, cavitation increases the release of valuable nutrients making them available for future applications. Moreover, cavitation in the scaled-up cavitator decreased the calorific value of dry mass as well as the amount of settleable solids. Decreasing the weight of dry matter can have positive effects on lower transportation, deposition and incineration costs.

Fig. 3 shows the COD_s and N_t values before and after cavitation treatment (15 min and 30 min) of secondary pulp and paper mill sludge and alkaline treated secondary pulp and paper mill sludge (pH 10) using the pilot-scale RGHC device. The obtained results clearly show a parallel increase of the COD_s and N_t values with the cavitation treatment time and additionally confirm that the addition of NaOH intensively boosts the disintegration process. In an alkaline environment, autoxidation [41] and a minimum degradation of proteins, which are released from ruptured microorganisms, takes place producing various oxidized radicals [42] and cysteine, methionine, tryptophan, histidine, and tyrosine residues are especially susceptive to oxidative destruction whereas asparagine and aspartic acid undergo deamination [43]. In zones of HC development, high pressures and

Table 1. *Effect of HC generated inside the pilot-scale RGHC device (30 min) on the chemical characteristics of the secondary pulp and paper mill sludge*

	P_t [mg/L]	N_t [mg/L]	COD_s [mg/L]	Calorific value of dry mass [kJ/kg dry mass]	Settleable solids [%]
Secondary pulp and paper mill sludge	0.6	8.1	509	18097	18.5
Cavitated secondary pulp and paper mill sludge	2.9	25.5	1023	17793	16.5
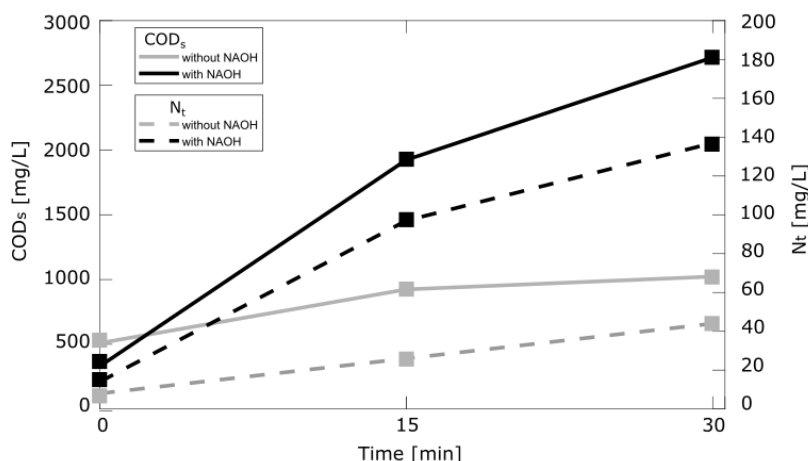
Fig. 3. *The effect of secondary pulp and paper mill sludge alkalinization (pH of 10) on the N_t and COD_s measurements before and after cavitation in the pilot-scale RGHC device*

temperatures cause water molecules to dissociate into hydroxyl radicals (•OH) and •H [44]. When cavitation takes place in an alkaline environment, a further recombination reaction between these radicals can lead to the formation of peroxide (H_2O_2), hydroperoxy radicals (HOO•) and superoxide anions (•O^{-2}). Oxidized radicals derived from proteins then undergo reactions with the •OH, •OOH and •O^{-2} radicals to form simple organic acids, carbon dioxide and other low molecular weight organic products [45] and [41]. Therefore, in theory, alkaline pre-treatment initializes the protein degradation process, and HC provides additional oxidative potential, which is required for the intensification and acceleration of reactions and consequently for the increased release of nutrients from biomass (such as nitrogen and phosphorous).

The assumption of microbial rupture during cavitation with secondary pulp and paper mill sludge was confirmed by microbiological photos and microbial counts under the microscope (40 and 100 times magnified). These were taken before and after the pilot-scale RGHC experiments with secondary pulp and paper mill sludge, which are described above (Fig. 3).

From the microscope photos (Fig. 4 frame A40), it can be clearly seen that non-cavitated secondary pulp and paper mill sludge is made of many solid irregularly shaped flocs of microorganisms which range from 100 mm to 400 mm in diameter. At higher magnitude (Fig. 4, frame A100), one can see that the flocs are mainly composed of a mixture of bacteria, primarily Zoogloea and the filamentous bacteria. Zoogloea plays an important role in wastewater treatment because it is capable of lowering BOD5. It also creates habitats for secondary sludge flocs [46]. In contrast, excessive growth of filamentous bacteria in secondary sludge causes poor settlement of secondary sludge flocs, creating a severe operational problem in wastewater treatment systems that is referred to as bulking [47]. After a 30 min cavitation treatment (Fig. 4

frames B40 and B100), the big flocs have been almost completely broken, and the surviving microorganisms are equally dispersed across the whole volume, which indicates a better microbial disintegration.
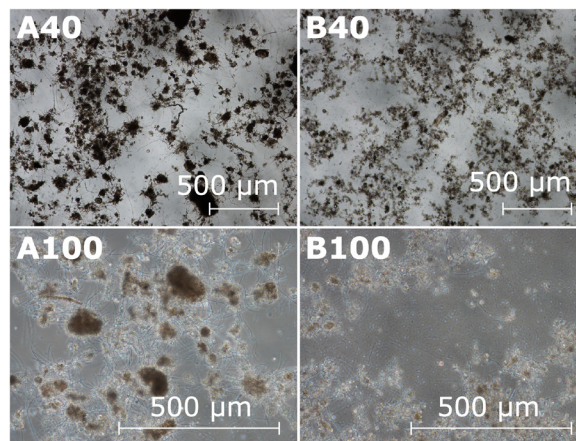
Fig. 4. *Microbiological photographs (A40 and A100: non-treated secondary pulp and paper mill sludge; B40 and B100: secondary pulp and paper mill sludge after 30 min of treatment using the pilot-scale RGHC device)*

Flocculated aggregates are usually colonized by numerous protozoans, which graze on bacteria and the extracellular polymeric substances of the bacteria, and affect the floc size, shape and its functional characteristics [48] to [50].

2.2.1 Estimation of Energy Efficiency in Waste Water Samples

Energy (EnE (mg/(Wh))) and economic efficiency (EcE (mg/€)) were estimated for pilot-scale experiments, where HC alone, HC with the addition of NaOH and only NaOH treatment of secondary paper mill sludge were investigated. Calculations are based on the energy consumption (EC) needed to drive the pilot RGHC, on the increase in soluble COD ($DCOD_s$) and on the addition of NaOH and were evaluated in

Table 2. *Energy and economic efficiency of different treatments*

	t [min]	ΔCOD_s [mg/L]	EC [Wh]	cost/V [€/m³]	EnE [mg/(Wh)]	EcE [kg/€]
Hydrodynamic cavitation	15	415	1955	0.339	106	1.224
	30	514	3913	0.678	66	0.758
Hydrodynamic cavitation + NaOH (pH of 10)	15	1594	2000	0.346+0.5	399	1.884
	30	2386	3925	0.80+0.5	304	1.835
NaOH*	8.9	40	/	0.5	/	0.080
	11	675	/	0.5	/	1.350

*stirred for 30 min on magnetic stirrer

euro (€) per volume. For each experiment, the EC of the pilot-scale RGHC device was precisely measured with Fluke Norma 4000 power analyser. Higher EnE values correspond to higher treatment efficiencies.

According to the Eurostat [51] statistics, one kWh is on average worth €0.0866 and 1 L of Slovenian purchased NaOH is worth approximately €1.00. These values were considered for the calculations in Table 2.

From Table 2, it can clearly be seen that in terms of EC and cost efficiency the most promising procedure is comprised of a 15 min HC treatment of alkaline treated secondary pulp and paper mill sludge, for which the cost of 1.9 kg of released COD_s was only €1.00.

3 CONCLUSIONS

In this study, we investigated the effects of different HC treatments on secondary pulp and paper mill sludge, which originated from the local paper mill plant. The experiments were performed on lab- and pilot-scale. The results were evaluated in terms of chemical and microbiological characterization. In addition, energy and economic feasibility calculations were performed.

It can be seen from the presented results that HC has many beneficial effects on pulp and paper mill secondary sludge disintegration, which leads to improved nutrient release. Moreover, the alkalinization of sludge (pH 10) prior to cavitation, additionally improved the economic efficiency of the pilot scale RGHC device. An additional beneficial effect of sludge disintegration is in a decreased weight of dry matter, which is directly reflected in lower transportation, deposition and incineration costs. All these effects can improve wastewater management and reduce operational costs for the paper mill plant. The most effective pilot-scale treatment resulted in 1.9 kg of released COD_s for which the cost was only 1.00 €. Based on the presented results, cavitation seems a promising technique that could be used for various paper mill plant sections.

4 ACKNOWLEDGEMENTS

5 REFERENCES

[1] Wang, Y., Brennen, C.E. (1994). Shock wave development in the collapse of a cloud of bubbles. *American Society of Mechanical Engineers, Fluids Engineering Division (Publication) FED*, vol. 194, p. 15-19.

[2] Franc, J.P., Michel, J.M. (2004). *Fundamentals of Cavitation*, Kluwer Academic Publishers, Dordrecht.

[3] Fujikawa, S., Akamatsu, T. (1980). Effects of the non-equilibrium condensation of vapour on the pressure wave produced by the collapse of a bubble in a liquid. *Journal of Fluid Mechanics*, vol. 97, no. 3, p. 481-512, **DOI:10.1017/S0022112080002662**.

[4] Braeutigam, P., Franke, M., Schneider, R.J., Lehmann, A., Stolle, A., Ondruschka, B. (2012). Degradation of carbamazepine in environmentally relevant concentrations in water by Hydrodynamic-Acoustic-Cavitation (HAC). *Water Research*, vol. 46, no. 7, p. 2469-2477, **DOI:10.1016/j.watres.2012.02.013**.

[5] Confederation of EU Paper Industries (2018). EU's new circular bioeconomy strategy - European forest fibre and paper industry ready to lead, from *http://www.cepi.org/EU_bioeconomy_strategy*, accessed on 2019-09-10.

[6] Simão, L., Hotza, D., Raupp-Pereira, F., Labrincha, J.A., Montedo, O.R.K. (2018). Wastes from pulp and paper mills - a review of generation and recycling alternatives. *Ceramica*, vol. 64, no. 371, p. 443-453, **DOI:10.1590/0366-69132018643712414**.

[7] Ashrafi, O., Yerushalmi, L., Haghighat, F. (2015). Wastewater treatment in the pulp-and-paper industry: A review of treatment processes and the associated greenhouse gas emission. *Journal of Environmental Management*, vol. 158, p. 146-157, **DOI:10.1016/j.jenvman.2015.05.010**.

[8] Mahmood, T., Elliott, A. (2006). A review of secondary sludge reduction technologies for the pulp and paper industry. *Water Research*, vol. 40, no. 11, p. 2093-2112, **DOI:10.1016/j.watres.2006.04.001**.

[9] Bousios, S., Worrell, E. (2017). Towards a Multiple Input-Multiple Output paper mill: Opportunities for alternative raw materials and sidestream valorisation in the paper and board industry. *Resources, Conservation and Recycling*, vol. 125, p. 218-232, **DOI:10.1016/j.resconrec.2017.06.020**.

[10] Saha, M., Eskicioglu, C., Marin, J. (2011). Microwave, ultrasonic and chemo-mechanical pretreatments for enhancing methane potential of pulp mill wastewater treatment sludge. *Bioresource Technology*, vol. 102, no. 17, p. 7815-7826, **DOI:10.1016/j.biortech.2011.06.053**.

[11] Bayr, S., Kaparaju, P., Rintala, J. (2013). Screening pretreatment methods to enhance thermophilic anaerobic digestion of pulp and paper mill wastewater treatment secondary sludge. *Chemical Engineering Journal*, vol. 223, p. 479-486, **DOI:10.1016/j.cej.2013.02.119**.

[12] Zhang, L., Xu, C.C., Champagne, P. (2010). Energy recovery from secondary pulp/paper-mill sludge and sewage

sludge with supercritical water treatment. *Bioresource Technology*, vol. 101, no. 8, p. 2713-2721, **DOI:10.1016/j.biortech.2009.11.106**.

[13] Hay, J.X.W., Wu, T.Y., Juan, J.C., Jahim, J.M. (2015). Improved biohydrogen production and treatment of pulp and paper mill effluent through ultrasonication pretreatment of wastewater. *Energy Conversion and Management*, vol. 106, p. 576-583, **DOI:10.1016/j.enconman.2015.08.040**.

[14] de Azevedo, A.R., Alexandre, J., de C. Xavier, G., Pedroti, L.G. (2018). Recycling paper industry effluent sludge for use in mortars: A sustainability perspective. *Journal of Cleaner Production*, vol. 192, p. 335-346, **DOI:10.1016/j.jclepro.2018.05.011**.

[15] Singh, S., Kulkarni, S., Kumar, V., Vashistha, P. (2018). Sustainable utilization of deinking paper mill sludge for the manufacture of building bricks. *Journal of Cleaner Production*, vol. 204, p. 321-333, **DOI:10.1016/j.jclepro.2018.09.028**.

[16] Jaria, G., Calisto, V., Silva, C.P., Gil, M.V., Otero, M., Esteves, V.I. (2019). Obtaining granular activated carbon from paper mill sludge – A challenge for application in the removal of pharmaceuticals from wastewater. *Science of The Total Environment*, vol. 653, p. 393-400, **DOI:10.1016/j.scitotenv.2018.10.346**.

[17] Jin, Y., Li, H., Mahar, R.B., Wang, Z., Nie, Y. (2009). Combined alkaline and ultrasonic pretreatment of sludge before aerobic digestion. *Journal of Environmental Sciences*, vol. 21, no. 3, p. 279-284, **DOI:10.1016/S1001-0742(08)62264-0**.

[18] Patil, P.N., Gogate, P.R., Csoka, L., Dregelyi-Kiss, A., Horvath, M. (2016). Intensification of biogas production using pretreatment based on hydrodynamic cavitation. *Ultrasonics Sonochemistry*, vol. 30, p. 79-86, **DOI:10.1016/j.ultsonch.2015.11.009**.

[19] Carrère, H., Dumas, C., Battimelli, A., Batstone, D.J., Delgenès, J.P., Steyer, J.P., Ferrer, I. (2010). Pretreatment methods to improve sludge anaerobic degradability: A review. *Journal of Hazardous Materials*, vol. 183, no. 1, p. 1-15, **DOI:10.1016/j.jhazmat.2010.06.129**.

[20] Wang, X., Qiu, Z., Lu, S., Ying, W. (2010). Characteristics of organic, nitrogen and phosphorus species released from ultrasonic treatment of waste activated sludge. *Journal of Hazardous Materials*, vol. 176, no. 1, p. 35-40, **DOI:10.1016/j.jhazmat.2009.10.115**.

[21] Tyagi, V.K., Lo, S.-L., Rajpal, A. (2014). Chemically coupled microwave and ultrasonic pre-hydrolysis of pulp and paper mill waste-activated sludge: effect on sludge solubilisation and anaerobic digestion. *Environmental Science and Pollution Research*, vol. 21, no. 9, p. 6205-6217, **DOI:10.1007/s11356-013-2426-y**.

[22] Oz, N.A., Uzun, A.C. (2015). Ultrasound pretreatment for enhanced biogas production from olive mill wastewater. *Ultrasonics Sonochemistry*, vol. 22, p. 565-672, **DOI:10.1016/j.ultsonch.2014.04.018**.

[23] Petkovšek, M., Mlakar, M., Levstek, M., Stražar, M., Širok, B., Dular, M. (2015). A novel rotation generator of hydrodynamic cavitation for waste-activated sludge disintegration. *Ultrasonics Sonochemistry*, vol. 26. p. 408-414, **DOI:10.1016/j.ultsonch.2015.01.006**.

[24] Zupanc, M., Kosjek, T., Petkovšek, M., Dular, M., Kompare, B., Širok, B., Blažeka, Ž., Heath, E. (2013). Removal of pharmaceuticals from wastewater by biological processes, hydrodynamic cavitation and UV treatment. *Ultrasonics Sonochemistry*, vol. 20, no. 4, p. 1104-1112, **DOI:10.1016/j.ultsonch.2012.12.003**.

[25] Zupanc, M., Kosjek, T., Petkovšek., M., Dular, M., Kompare, B., Širok, B., Stražar, M., Heath, E. (2014). Shear-induced hydrodynamic cavitation as a tool for pharmaceutical micropollutants removal from urban wastewater, *Ultrasonics Sonochemistry*, vol. 21, no. 3, p. 1213-1221, **DOI:10.1016/j.ultsonch.2013.10.025**.

[26] Petkovšek, M., Zupanc, M., Dular, M., Kosjek, T., Heath, E., Kompare, B., Širok, B. (2013). Rotation generator of hydrodynamic cavitation for water treatment. *Separation and Purification Technology*, vol. 118, p. 415-423, **DOI:10.1016/j.seppur.2013.07.029**.

[27] Širok, B., Dular, M., Petkovšek, M., Zupanc, M. Heath, E. (2014). *Rotation Generator of Hydrodynamic Cavitation for Water Treatement*, SI24180 A, Slovenian Intellectual Property Office, Ljubljana. (in Slovene)

[28] Širok, B., Dular, M., Petkovšek, M. (2019). *Cavitation Device for Treatment of Water by Cavitation*. United States patent US10202288 B2, United States Patent and Trademark Office, Washington.

[29] Šarc, A., Oder, M., Dular, M. (2016). Can rapid pressure decrease induced by supercavitation efficiently eradicate Legionella pneumophila bacteria? *Desalination and Water Treatment*, vol. 57, no. 5, p. 2184-2194, **DOI:10.1080/19443994.2014.979240**.

[30] Šarc, A., Kosel, J., Stopar, D., Oder, M., Dular, M. (2018). Removal of bacteria Legionella pneumophila, Escherichia coli, and Bacillus subtilis by (super)cavitation. *Ultrasonics Sonochemistry*, vol. 42, p. 228-236, **DOI:10.1016/j.ultsonch.2017.11.004**.

[31] Dular, M., Griessler-Bulc, T., Gutierrez-Aguirre, I., Heath, E., Kosjek, T., Krivograd Klemenčič A., Oder, M., Petkovšek, M., Rački, N., Ravnikar, M., Šarc, A., Širok, B., Zupanc, M., Žitnik, M., Kompare, B. (2016). Use of hydrodynamic cavitation in (waste)water treatment. *Ultrasonics Sonochemistry*, vol. 29, p. 577-588, **DOI:10.1016/j.ultsonch.2015.10.010**.

[32] Šarc, A., Stepišnik-Perdih, T., Petkovšek, M., Dular, M. (2017). The issue of cavitation number value in studies of water treatment by hydrodynamic cavitation. *Ultrasonics Sonochemistry*, vol. 34, p. 51-59, **DOI:10.1016/j.ultsonch.2016.05.020**.

[33] Kosel, J., Gutiérrez-Aguirre, I., Rački, N., Dreo, T., Ravnikar, M., Dular, M. (2017). Efficient inactivation of MS-2 virus in water by hydrodynamic cavitation. *Water Research*, vol. 124, p. 465-471, **DOI:10.1016/j.watres.2017.07.077**.

[34] Stepišnik Perdih, T., Širok, B., Dular, M. (2017). Influence of hydrodynamic cavitation on intensification of laundry aqueous detergent solution preparation. *Strojniški vestnik - Journal of Mechanical Engineering*, vol. 63, no. 2, p. 83-91, **DOI:10.5545/sv-jme.2016.3970**.

[35] Zupanc, M., Pandur, Ž., Stepišnik Perdih, T., Stopar, D., Petkovšek, M., Dular, M. (2019). Effects of cavitation on different microorganisms: The current understanding of the

mechanisms taking place behind the phenomenon. A review and proposals for further research. *Ultrasonics Sonochemistry*, vol. 57, p. 147-165, **DOI:10.1016/j.ultsonch.2019.05.009**.

[36] Kosel, J., Šinkovec, A., Dular, M. (2019). A novel rotation generator of hydrodynamic cavitation for the fibrillation of long conifer fibers in paper production. *Ultrasonics Sonochemistry*, vol. 59, ID 104721, **DOI:10.1016/j.ultsonch.2019.104721**.

[37] DIN 38409-2 (1980). *German Standard Methods for the Examination of Water, Waste Water and Sludge; General Measures of Effects and Substances (Group H), Determination of the Total Nonfilterable Residue and Residue on Ignition (H2)*, German Institute for Standardisation, Berlin.

[38] ASTM E711-87 (2004). *Standard Test Method for Gross Calorific Value of Refuse-Derived Fuel by the Bomb Calorimeter*, ASTM International, **DOI:10.1520/E0711-87r04.**

[39] Stepišnik Perdih, T., Širok, B., Dular, M. (2017). On the bubble-surfactant interaction. *Chemical Engineering and Processing: Process Intensification*, vol. 121, p. 198-204, **DOI:10.1016/j.cep.2017.08.016**.

[40] Beare, M.H., Cabrera, M.L., Hendrix, P.F., Coleman, D.C. (1994). Aggregate-protected and unprotected organic matter pools in conventional- and no-tillage soils. *Soil Science Society of America Journal*, vol. 58, no. 3, p. 787-795, **DOI:10.2136/sssaj1994.03615995005800030021x.**

[41] Hart, P.W., Rudie, A.W. (2012). *The Bleaching of Pulp*, TAPPI press, Norcross.

[42] Irwin, W.J. (1995). Stability and characterization of protein and peptide drugs. case histories. Pharmaceutical Biotechnology vol. 5, Wang, Y.J., Pearlman, R. (eds.), *Journal of Pharmacy and Pharmacology*, vol. 47, p. 176, **DOI:10.1111/j.2042-7158.1995.tb05773.x.**

[43] Manning, M.C., Chou, D.K., Murphy, B.M., Payne, R.W., Katayama, D.S. (2010). Stability of protein pharmaceuticals: An update. *Pharmaceutical Research*, vol. 27, no. 4, p. 544-575, **DOI:10.1007/s11095-009-0045-6**.

[44] Badve, M.P., Gogate, P.R., Pandit, A. B., Csoka, L. (2014). Hydrodynamic cavitation as a novel approach for delignification of wheat straw for paper manufacturing. *Ultrasonics Sonochemistry*, vol. 21, no. 1, p. 162-168, **DOI:10.1016/j.ultsonch.2013.07.006**.

[45] Das, A.B., Nagy, P., Abbott, H.F., Winterbourn, C.C., Kettle, A.J. (2010). Reactions of superoxide with the myoglobin tyrosyl radical. *Free Radical Biology and Medicine*, vol. 48, no. 11, p. 1540-1547, **DOI:10.1016/j.freeradbiomed.2010.02.039**.

[46] Golyshin, P.N., Martins Dos Santos, V.A.P., Kaiser, O., Ferrer, M., Sabirova, Y.S., Lünsdorf, H., Chernikova, T.N., Golyshina, O.V., Yakimov, M.M., Pühler, A., Timmis, K.N. (2003). Genome sequence completed of Alcanivorax borkumensis, a hydrocarbon-degrading bacterium that plays a global role in oil removal from marine system. *Journal of Biotechnology*, vol. 106, no. 2, p. 215-220, **DOI:10.1016/j.jbiotec.2003.07.013**.

[47] Aruga, S. Kamagata, Y., Kohno, T., Hanada, S., Nakamura, K., Kanagawa, T. (2002). Characterization of filamentous Eikelboom type 021N bacteria and description of Thiothrix disciformis sp. nov. and Thiothrix flexilis sp. nov. *International Journal of Systematic and Evolutionary Microbiology*, vol. 52, no. 4, p. 1309-1316, **DOI:10.1099/00207713-52-4-1309**.

[48] Böhme, A., Risse-Buhl, U., Küsel, K. (2009). Protists with different feeding modes change biofilm morphology. *FEMS Microbiology Ecology*, vol. 69, no. 2, p. 158-169, **DOI:10.1111/j.1574-6941.2009.00710.x.**

[49] Hahn, M.W., Höfle, M.G. (2001). Grazing of protozoa and its effect on populations of aquatic bacteria. *FEMS Microbiology Ecology*, vol. 35, no. 2, p. 113-121, **DOI:10.1016/S0168-6496(00)00098-2**.

[50] Weerman, E.J., Van Der Geest, H.G., Van Der Meulen, M.D., Manders, E.M.M., Van De Koppel, J., Herman, P.M.J. Admiraal, W. (2011). Ciliates as engineers of phototrophic biofilms. *Freshwater Biology*, vol. 56, no. 7, p. 1358-1369, **DOI:10.1111/j.1365-2427.2011.02574.x.**

[51] Eurostat (2109). Electricity Price Statistics, from *https://ec.europa.eu/eurostat/statistics-explained/index.php/Electricity_price_statistics*, accessed on 2019-09-10.

Distributed Manufacturing Systems with Digital Agents

Niko Herakovič* – Hugo Zupan – Miha Pipan – Jernej Protner – Marko Šimic

University of Ljubljana, Faculty of Mechanical Engineering, Slovenia

This paper presents a novel approach to implement manufacturing nodes using the combined strength of digital twins, holons, and digital agents. Manufacturing nodes are based on holon theory and present a universal manufacturing platform that consists of cyber-physical systems (CPS) with an integrated digital twin, digital agent, databases and various communication protocols. The manufacturing node network is controlled globally using the global digital twin of logistics process and locally using the local nodes and local digital agents, digital twins and information shared by the node network. The main objective of this research was to develop and test a new concept of distributed system modelling and distributed system control for easy implementation of distributed manufacturing nodes in a smart factory concept.

Keywords: smart factory, distributed control, nodes, communication, digital twin

Highlights
- *Distributed control model based on holons, digital agents and digital twins.*
- *Developed global digital agents connected to a digital twin for order and logistics optimization.*
- *Local digital agents for communication and control of local manufacturing process.*
- *Proof of concept on physical system.*

0 INTRODUCTION

Manufacturing is constantly changing due to new disruptive technologies that enable implementation of new innovative concepts. Current enablers for innovative changes are new Information Technologies (IT) that consist of Internet of Things (IoT), big data, Artificial Intelligence (AI) and are all backed up by the Industry 4.0 concept [1]. This technology connects and improves Cyber-Physical Systems (CPS - is a mechanism that is controlled or monitored by computer-based algorithms) to communicate, control processes and have decision-making/problems solving capabilities. Together they enable the development of smart manufacturing.

The backbone for implementation of these technologies is information connectivity that has evolved over the years from using machine operators for controlling machines and gather data (first and second phase / industrial revolution) to manufacturing equipment connected via networked computers (third and fourth industrial revolution/phase - Fig. 1). The communication between different CPS systems and other manufacturing execution systems can be sufficiently implemented using current communication technologies and protocols, however, its main problem is cybersecurity.

The biggest current obstacle in smart manufacturing is efficient control of all CPS elements in production processes to enable optimal production order execution, fast error detection and solving as well as predictive maintenance. The main reason for the existence of this problem is an increasing number of CPS systems that need to be controlled decreases usefulness of the centralized (MES – Manufacturing execution system and ERP - Enterprise resource planning) control approach. In recent research papers, different hierarchical organizational structures (decentralized and distributed systems, hierarchical systems and holarchies) and components/structures of CPS (IIoT – Industrial IoT, holons, agents, AI, etc.) are proposed to solve these challenges [2]. The other author's presents the Digital factory and the advanced digital technologies as one of the possible solutions that have major influence on improving the production process. Performing the near real-time efficient production control results in higher profit of the company [3].
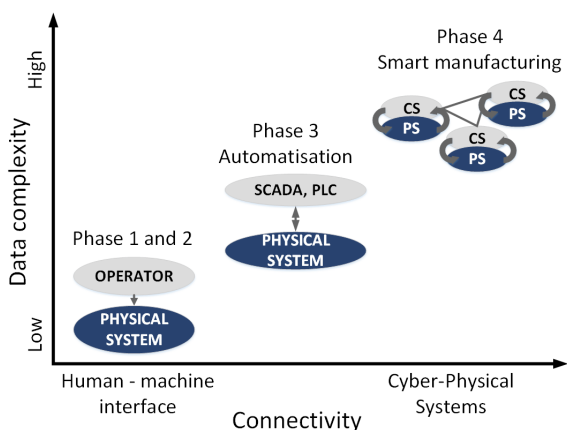
Fig. 1. *Evolution of connectivity in manufacturing*

*Corr. Author's Address: University of Ljubljana, Faculty of Mechanical Engineering, Laboratory for Handling, Assembly and Pneumatics, Aškerčeva 6, 1000 Ljubljana, Slovenia, niko.herakovic@fs.uni-lj.si

1 DISTRIBUTED MANUFACTURING NODES

1.1 Distributed Systems

The baseline for modern industrial infrastructures is automation pyramid model defined in standard IEC 62264 [4]. The IEC proposed structure consists of five hierarchical layers:

- ERP,
- MES,
- supervisory control and data acquisition (SCADA),
- programmable logic controller (PLC),
- sensors and actuators (SA).

This structure presents centralized control and it is not the optimal solution to control larger system with hundreds of CPS units due to boundary rationality. In other words, classical command and control hierarchies become ineffective and counterproductive at some point of growth. For this reason the system needs to be managed with non-centralized coordination and control [5].

The research community developed several models based on RAMI 4.0 - Industry 4.0 reference model. The foundation for distributed control and manufacturing processes is defining CPS unit structure that will be able to connect, communicate, decide and control. The basis for the definition of such "smart" CPS units rests on holons (first proposed in 1971) [6], that became a synonym for distributed control and manufacturing. Basic holon structure is presented in Fig. 2. Holon usage in manufacturing reached its peak now because new technology has been developed sufficiently to support this concept in manufacturing.
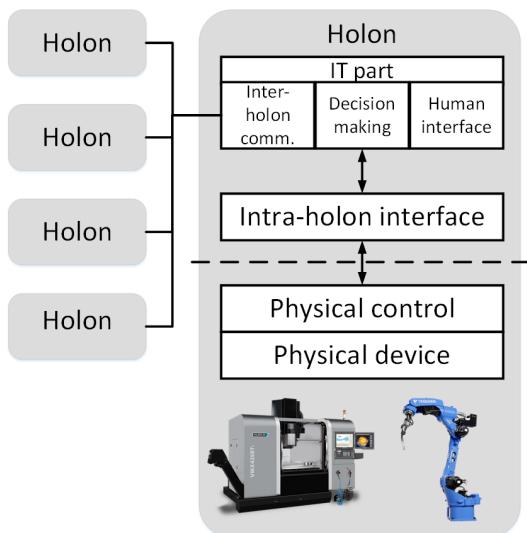
The holon concept enables the introduction of distributed control called holarchy (an entity with a capability to cooperate to achieve a goal or objective). Holon consists of physical and informational process part and is an autonomous manufacturing building block for transforming, transporting, sorting and/or validating information and physical objects (Fig. 3).

The final step is the introduction of digital agents to the concept of holons. The digital agent's main characteristics are presented in Fig. 3 [7]:

- sensing their environment and reacting to it,
- designed to achieve their designated goal,
- having enough knowledge to act on their own,
- ability to interact with each other,
- ability to learn from their previous behaviour,
- and ability to move through the network.

The proposed distributed architecture is based on combining the holon and digital agents to form a manufacturing node that is interconnected with other nodes, which form a smart factory platform. Similar approaches have been used with combining holons and agents using function blocks [8]. The drawback of the proposed model was the weak connection between the production holon definition and connected agents.
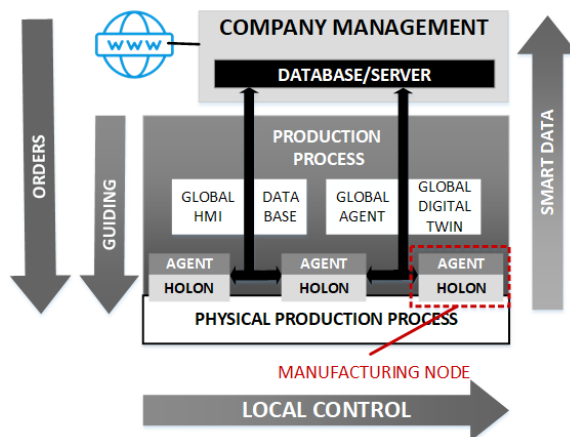
Fig. 3. *Structure of proposed distributed control*

In our concept, this is done with the introduction of a digital twin of the entire production processes upgraded with multiple digital agents. Digital twins present fundamental concept for smart manufacturing as they are used to create high-fidelity virtual models for physical objects digitally to simulate their behaviour [9]. With the digital twin complex, manufacturing processes can be integrated to achieve closed-loop control and optimization of manufacturing process [10] and [11]. The base structure for combining benefits of distributed control based on holons, digital

Fig. 2. *General architecture of a holon*

agents and digital twins to form distributed control of manufacturing system is shown in Fig. 3.

The proposed model uses directed communication between enterprise management systems and to manufacturing/assembly processes. All orders are arranged based on current manufacturing status and optimal manufacturing order obtained from the global digital twin. The process is controlled and problems are solved locally by digital agents on manufacturing nodes. During the manufacturing process, smart data is sent via local network to the company management system to enable tracking of orders and status of all the nodes.

1.2 Distributed System Modelling

The most efficient way to model the distributed system is to use graph or network theory. The network theory by using the 3D networks was successfully implemented in several engineering applications in order to solve complex problems. The authors in [12] show intelligent hybrid system of machine learning and statistical pattern recognition for a 3D visibility network. A graph is a mathematical structure used to model pairwise relations between objects from a certain collection and is used to describe manufacturing nodes connections. In this context, a graph consists of vertices or nodes connected by edges or arcs. It may have different configurations: directed and undirected. Directed graphs consist of edges allowing the flow only in one direction, while the undirected graphs have no restriction on flow direction. Such an example of directed and undirected graph is shown in Fig. 4 [13].
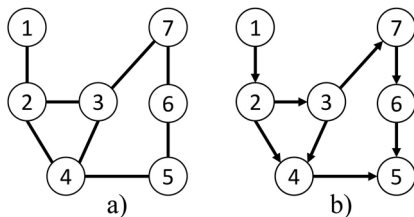
Fig. 4. *a) Undirected graph and b) directed graph*

As seen from Fig. 4a the graph consists of 7 nodes and 8 arcs. It is undirected which means that the information can flow from Node 1 to Node 5, or Node 5 to Node 1. In the case of a directed graph (also called digraph) shown in Fig. 4b, an arrow shows the direction of the edge. As an example, the flow from Node 1 to Node 5 can be allowed while Node 5 to Node 1 may not be allowed [13].

In our case the graphs G are directed graphs:

$$G = (V(G); E(G)), \qquad (1)$$

where $V(G)$ is an n-set of vertices or nodes, and $E(G)$ is an m-set of directed edges or arcs.

For every edge e there are two vertices: ini(e) and ter(e), (start and end vertex). If e is a loop, then ini(e) = ter(e). If e and f are parallel, then ini(e) = ini(f) and ter(e) = ter(f). If e and f are opposite, then ini(e) = ter(f) and ter(e) = ini(f) [14].

We often study complex objects by looking at simpler objects of the same type contained in them, and smaller objects are often named "sub-".

A subgraph G' of a graph G is another graph composed of a subset of vertices $V(G')$ from a set of vertices $V(G)$ and subset edges $E(G')$ from a set of vertices $E(G)$. The vertices subset must include all endpoints of the vertices subset, but may also include additional edges.

A spanning subgraph G' is a graph that includes all vertices of the graph $V(G') = V(G)$; an induced subgraph G' is a graph that includes all the edges whose endpoints belong to the vertex subset. Formally, let $G = (V(G), E(G))$ be any graph, and let $G' \subset V(G)$ be any subset of vertices of G. Then the induced subgraph G' is the graph whose vertex set is G' and whose edge set $E(G')$ consists of all of the edges in $E(G)$ that have both endpoints in $E(G')$ [14].

On Fig. 5 G_1 is a subgraph of graph G, induced on edges $\{a, b, c, d, f, g\}$, graph G_2 is a subgraph induced on vertices $\{ef, eh, fg, fh, fi, hi, hj, ij, jk\}$. G_3 is a spanning subgraph of the graph G.
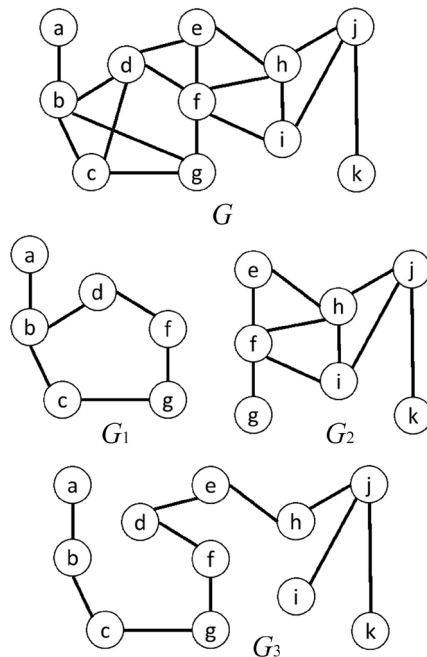
Fig. 5. *Graph G with subgraph G_1, G_2 and G_3*

Herakovič, N. – Zupan, H. – Pipan, M. – Protner, J. – Šimic, M.

A bipartite graph (or bigraph) is a graph whose vertices can be divided into two disjoint and independent sets A and B such that every edge connects a vertex in A to a vertex in B. The two sets A and B are designated as a coloring of the graph with two colors: if one colors all nodes in A black, and all nodes in B white, each edge has endpoints of differing colors, as required by the graph coloring problem [12].

A complete bipartite graph or biclique is a special kind of bipartite graph where every black vertex of the first set is connected to every white vertex of the second set. Vertices in a complete bipartite graph can be partitioned into two subsets V_1 and V_2 such that no edge has both endpoints in the same subset, and every possible edge that could connect vertices in different subsets is a part of the graph. That is, it is a bipartite graph (V_1, V_2 and E) such that for every two vertices $v_1 \in V_1$ and $v_2 \in V_2$, v_1, v_2 is an edge in E. A complete bipartite graph with partitions of size $|V_1| = m$ and $|V_2| = n$, is denoted $K_{m,n}$; A complete bipartite graph for any k, $K_{1,k}$ is called a star [14] and [15].
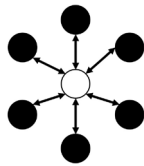
Fig. 6. *Graph $K_{1,6}$*

We can also study the topology of distribution systems using graph theory. In the distribution system context, the vertices represent the nodes while the arcs represent the connection between the nodes. A feature of a distributed system is that a graph I representing a distributed system, has a spanning complete bipartite subgraph $G_{1,k}'$ (See Fig. 7).
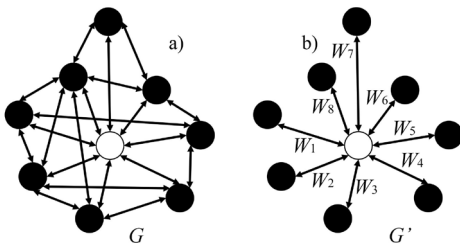
Fig. 7. *a) Distributed system and b) spanning complete bipartite subgraph $G'_{1,k}$ of a distributed system*

A weighted graph is a graph in which a number (the weight) is assigned to each edge. Such weights might represent, for example costs, lengths or capacities, depending on the problem at hand. Such graphs arise in many contexts, for example in shortest path problems such as the traveling salesman problem. A weighted directed graph associates a value (weight) with every edge in the directed graph. If $w = (e_1, e_2, \ldots, e_{n-1})$ is a finite directed walk with vertex sequence $(v_1, v_2, \ldots, v_n)$ then w is said to be a walk from v_1 to v_n. The weight of a directed walk (or trail or path) in a weighted directed graph G is the sum of the weights of the traversed edges [15].

In our case we can weigh the graph with the data necessary for it to be transferred from one node to another. Because of the properties of the distributed networks there is no need to transfer all the data from one node to another. The information is distributed amongst the nodes. Nodes also have local digital agents with local process control and decision making capabilities. This is opposite to a centralized network, where the master node needs to receive all the data from other nodes and has global process control and decision-making capabilities. In Fig. 8 we can see weighted directed graphs for a central network 8a, and a distributed network 8b.
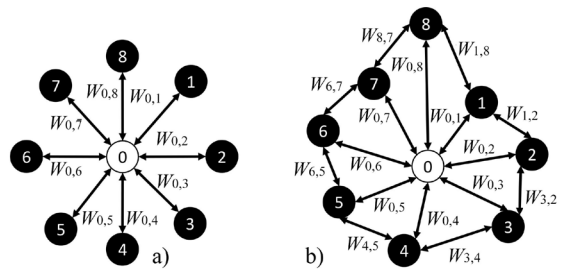
Fig. 8. *Weighted directed graphs for a) centralized network, and b) distributed network*

If there is a single connection between nodes in a distributed and a centralized network, then the weight is:

$$w_{i,j}^{distributed} \leq w_{i,j}^{centralized}. \tag{2}$$

That means that the path in the walk for the graph $G^{distributed} = G^{centralized}$ is:

$$D(G)^{distributed} \leq D(G)^{centralized}. \tag{3}$$

That means the distributed manufacturing network acts faster and exchanges less data than centralized network.

2 EXPERIMENTAL

2.1 Experimental Setup

An experimental case study has been used to validate the proposed architecture concept, aiming to verify its

correctness and applicability. The case study covers a manufacturing line schematically shown in Fig. 9. It consists of a transport system, two industrial robots, warehouse, and seven workstations (one of them being manual) and produces different types of products. The parts are acquired from the warehouse and transported from the first workstation to the last with a belt conveyor. Operations are performed with robots on six of the workstations and, if necessary, on the seventh manual workstation. For a representation of the proposed architecture, nine nodes are used:

- seven workstation nodes (Nodes 1 through 6 and Node 8) and
- warehouse node (Node 7).

These eight nodes consist of digital agents, a local digital twin and a holon. The last part of the proposed architecture is the so-called Node 0, which is similar to the other eight nodes since it encapsulates digital agents and a holon, but instead of a local digital twin it includes a global digital twin, which coordinates the entire manufacturing process. Node 0 serves as a direct communication link from the user to the rest of the system. Different sets of connections among these nodes (black straight arrows in Fig. 8) represent the possible inter-node communications for dynamic planning, scheduling and execution that can be implemented by digital agents and local

digital twins in coordination with a global digital twin of the process. As seen in Fig. 8, the regular nodes are interconnected only where necessary but all are individually connected to Node 0, therefore even though the physical connection between certain regular nodes does not exist, the information flow is still established through Node 0.

The process starts with a user confirming orders through a user interface to Node 0 which commences the information flow between the nodes by requesting information about the availability of the product parts from Node 7 (warehouse). Its global digital twin generates the process plan based on the information from Node 7. Node 0 now waits for local process information request from Node 1, which therefore states it is free and ready for a new order. Node 0 responds by sending information about local operations to be performed on the workstation of Node 1. Node 1 communicates with Node 7 and Robot 1 to acquire the necessary parts. Depending on whether a product is to be manufactured on workstation two or three (Nodes 2 or 3) or both, the information flow is propagated there, meaning that nodes which are not part of the process plan for an order do not participate in the communication flow for this order. When the parts are transported to the appropriate workstation, its node initiates the communication with Node 0 and
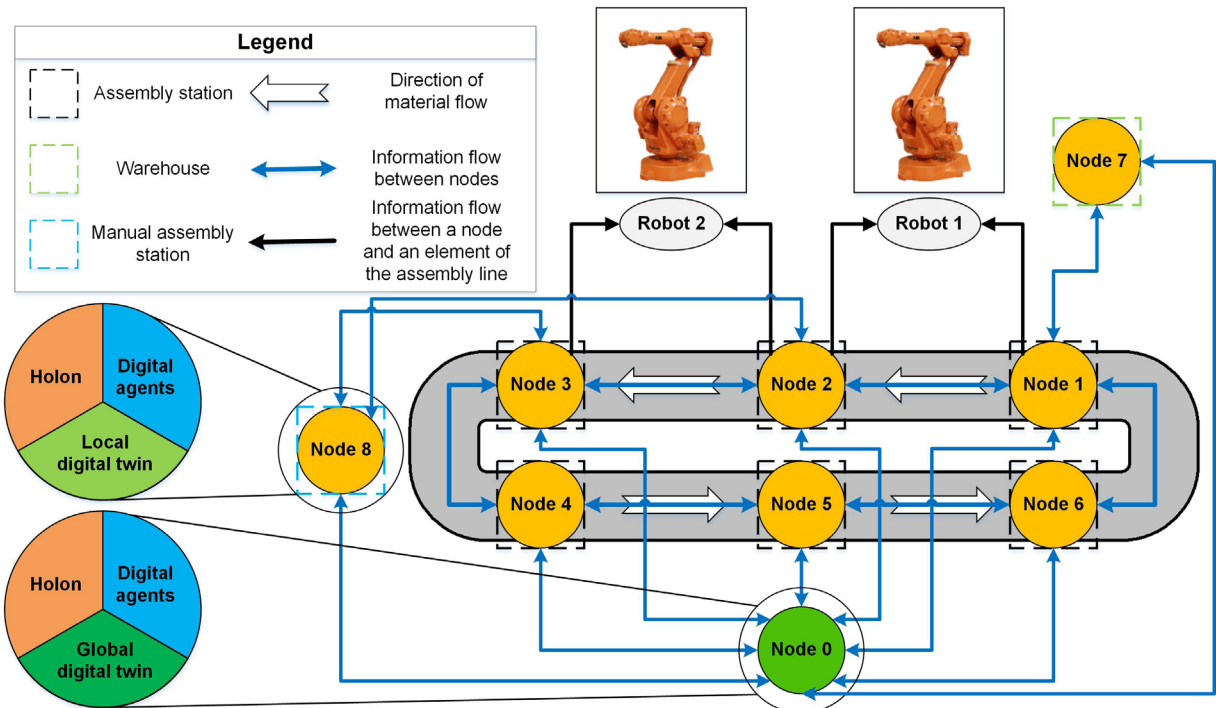
Fig. 9. *Experimental setup of distributed manufacturing nodes*

requests its local manufacturing process information. Both Nodes 2 and 3 communicate with Robot 2 to perform the necessary operations. Depending on the type of the product, either Node 2 or Node 3 initiates the communication link with Node 8 (manual workstation) which, after the semi-finished product is transported there, requests the appropriate information about the process from Node 0. When the product is transported to Node 4, and machine vision analysis is performed, the result is locally compared to the real data (previously acquired from Node 0). The result, whether the product is finished or the repair of the product is needed, is propagated through Node 0 to Node 1, which locally acts on this information. Node 5 and 6 exchange a similar information flow to Node 0 as Nodes 1, 2, and 3. It is important to note that the communication link between regular nodes and Node 0 is bi-directional. This means that the requested information about the manufacturing process is processed locally on each of the nodes which then send back the locally acquired new information i.e. start and finish times of the operations, information about errors etc.

For example, let's assume an error occurs while Node 1 is in the middle of the manufacturing process. To prevent more damage, the local digital twin immediately stops the process and moves processed parts away to another available node to remove them from the manufacturing line. Considering the current state of the system, global digital twin of Node 0 adjusts the production plan. The holon of Node 1 starts communication with Robot 1 and notifies it about the current situation so that it can delay or slow down its processing. In order for the global digital twin of Node 0 to generate different production plan, it also needs to acquire information from the local digital twin of Node 1 (updates on its current state, status of assembly, etc.). Let's suppose that, for example, Node 2 (second workstation) is currently free. Furthermore, assume that Node 0 in accordance

with Nodes 1 and 7 generates the best new production plan, however, the total process time would be now much longer than before. Communicating with Node 0, Node 1 finds out that, considering that the error has happened, current production rate does not satisfy the demand. Node 1 communicates with Node 2, to check whether it can help, in order to finish the product in time. Node 1 then communicates with the Node 7, to acquire the needed parts for Node 2 and itself. It then enables transportation of new parts to Node 2 and the manufacturing process continues.

2.2 Manufacturing Execution

This experimental case study considers the production of two different products named P1 and P2. Products have a different manufacturing process and a different information flow between the nodes. The information flow between the nodes for both products is presented in a matrix in Table 1. Information flow for product P1 is described in the left section of the columns in the table and information flow for product P2 is described in the right section of the columns. The sequence of communication is presented with consecutive numbers starting with 1. Considering that some nodes communicate with each other multiple times, some sections hold two numbers, which are separated by a comma.

Manufacturing of both products starts when the user confirms orders through a user interface connected to Node 0. It then requests information about parts availability from Node 7 and generates a production plan accordingly. Node 0 holds information about the process until Node 1 confirms it's free and ready for a new order. Node 1 therefore requests information about operations to be done at the first workstation and Node 0 responds with appropriate data. The information flow between the nodes from this point on differentiates for products P1 and P2.

Table 1. *Matrix of information flow between the nodes for P1 and P2*

	N0		N1		N2		N3		N4		N5		N6		N7		N8	
N0			4, 16	4, 14	8			8	13	11					1	1		
N1	3, 15	3, 13			6			6							5, 17	5, 15		
N2	7																9	
N3		7								9								
N4	12	10	14	12														
N5																		
N6																		
N7	2	2																
N8	10								11									

As stated in section 1.2 (Distributed systems modelling), distributed system and connections between its nodes could also be represented in the form of a bipartite directed graph G. The representation of information flow for products P1 and P2 is therefore presented as a subgraph G_1 for product P1 and subgraph G_2 for product P2 (as shown in Fig. 10) where Nodes 0 through 8 are represented with "N" 0 to 8.
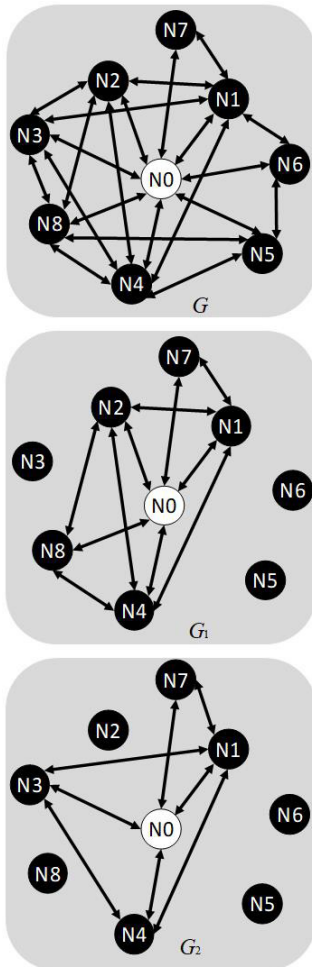
Fig. 10. *Graph G of distributed system in the case study, subgraphs G_1 for information flow of product P1 and G_2 for information flow of product P2*

For the evaluation of the proposed distributed architecture, a production plan was generated and the manufacturing process of both orders was simulated. Results of the material flow simulation are forecasted in terms of start and finish times of operations on separate workstations (Nodes 1 through 6 and Node 8) and a sequence order. Simulation results were compared to the experimental results of the case study.

3 RESULTS

To test the system, the comparison of digital twin forecasted manufacturing times of different nodes with transport times (Node 1-S is the time when the manufacturing started and Node 1-F is the time when manufacturing on the node was finished) was calculated. Fig. 11 shows results for orders P1 and P2.
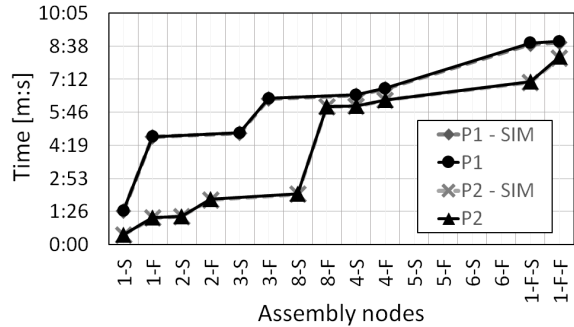
Fig. 11. *Comparison of simulated (P1-SIM and P2-SIM) time with experimental (P1 and P2) manufacturing time of nodes*

The analysis shows that the simulated node manufacturing order and times have high correlation between the simulated process and the experiment and that experimental distributed manufacturing node control functioned as simulated. The analysis of time differences (simulation error) for incoming and outgoing times for both orders was calculated and is shown in Fig. 12.
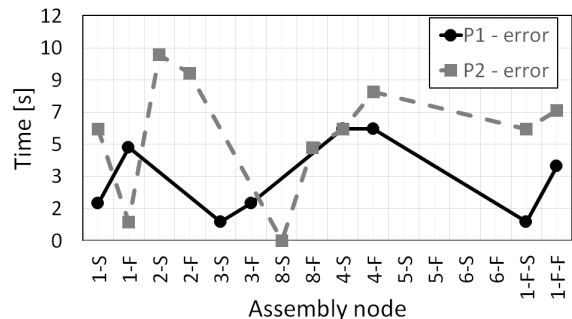
Fig. 12. *Simulated manufacturing time (node input and output time) error*

The time differences between simulated and experimental manufacturing time is between 0 seconds and 10 seconds, while mean error is shown in Table 2.

The mean error and correlation factor R^2 for both products P1 and P2 show good correlation between the simulation results and results obtained by real experimental distributed manufacturing nodes,

which means that the simulation and the real process behave as designed. The minor error appears is mainly due to simulation's poor definition of physical system description of acceleration of products on the conveyor belt and lag of pneumatic components used for positioning of pallets on robot grippers.

Table 2. *Calculated simulation mean error and R^2 for products P1 and P2*

Error	Mean error [s]	R^2
P1	3.90	0.9979
P2	6.71	0.8748

4 CONCLUSION

This research presents a new approach to modelling and controlling the distributed manufacturing nodes with a unique hierarchical structure and a global digital twin for logistic control. Each node consists of CPS with internal cyber components to foster its connectivity (support for multiple communication protocols), data collection (database), decision-making capabilities (digital agent), manufacturing process tracking, and monitoring (digital twin).

The new concept is illustrated using graph theory. We show that in order to have a distributed system, there needs to be a spanning complete bipartite subgraph. Graphs were also used to highlight the main difference between centralised and distributed systems and to explain why the distributed systems react and perform actions faster.

The new approach was tested using simulation and prototype production line performing the manufacturing process (manufacturing process with multiple manufacturing nodes). The results show that distributed manufacturing node control using the digital twin for global control (logistic process optimisation) and local problem solving control capabilities of single manufacturing nodes presents the most optimal solution when controlling multiple semi-independent CPS in modern manufacturing, where tasks become too demanding for a centralised system.

5 ACKNOWLEDGEMENTS

6 REFERENCES

[1] Plaga, S., Wiedermann, N., Duque, S., Tatschner, S., Schotten, H., Newe, T. (2019). Securing future decentralised industrial IoT infrastructures: Challenges and free open source solutions. *Future Generation Computer Systems*, vol. 93, p. 596-608, **DOI:10.1016/j.future.2018.11.008**.

[2] Kusiak, A. (2019). Fundamentals of smart manufacturing: A multi-thread perspective. *Annual Reviews in Control*, vol. 47, p. 214-220, **DOI:10.1016/j.arcontrol.2019.02.001**.

[3] Prester, J., Buchmeister, B., Palčič, I. (2018). Effects of Advanced Manufacturing Technologies on Manufacturing Company Performance. *Strojniški vestnik – Journal of Mechanical Engineering*, vol. 12, p 763-771, **DOI:10.5545/sv-jme.2018.5476**.

[4] IEC 62264-1 (2003). *Enterprise-control System Integration - Part 1: Models and Terminology*. IEC Copyright Office, Genève.

[5] Valckenaers, P., van Brussel, H. (2015). *Design for the Unexpected: From Holonic Manufacturing Systems towards a Humane Mechatronics Society*. Elsevier, Amsterdam, **DOI:10.1016/C2014-0-04226-8**.

[6] Koestler A. (1971). The Ghost in the Machine. Henry Regnery Company, New York.

[7] Tharumarajah, A. (1996). Comparison of the bionic, fractal and holonic manufacturing system concepts. *International Journal of Computer Integrated Manufacturing*, vol. 9, no. 3, p. 217-226, **DOI:10.1080/095119296131670**.

[8] Wang, L., Haghighi, A. (2016). Combined strength of holons, agents and function blocks in cyber-physical systems. *Journal of Manufacturing Systems*, vol. 40, p. 25-34, **DOI:10.1016/j.jmsy.2016.05.002**.

[9] Qi, Q., Tao, F., Zuo, Y., Zhao, D. (2018). Digital twin service towards smart manufacturing. *Procedia CIRP*, vol. 72, p. 237-242, **DOI:10.1016/j.procir.2018.03.103**.

[10] Resman, M., Pipan, M., Šimic, M., Herakovič, N. (2019). A new architecture model for smart manufacturing: A performance analysis and comparison with the RAMI 4.0 reference model. *Advances in Production Engineering and Management*, vol. 14, no. 2, p. 153-165, **DOI:10.14743/apem2019.2.318**.

[11] Tao, F., Cheng, J., Qi, Q., Zhang, M., Zhang, H., Sui, F. (2018). Digital twin-driven product design, manufacturing and service with big data. *International Journal of Advanced Manufacturing Technology*, vol. 94, no. 9-12, p. 3563-3576, **DOI:10.1007/s00170-017-0233-1**.

[12] Babič, M., Skala, K., Kumar, D., Šturm, R. (2018). New Hybrid System of Machine Learning and Statistical Pattern Recognition for a 3D Visibility Network. *Strojniški vestnik – Journal of Mechanical Engineering*, vol. 6, p 393-400, **DOI:10.5545/sv-jme.2017.5189**.

[13] Labrini, H. (2015). *Graph-Based Model for Distribution Systems: Application to Planning Problem*, PhD thesis. University of Waterloo, Waterloo.

[14] Žerovnik, J. (2012). *Selected Topics in Operations Research*. Faculty of Mechanical Engineering, Ljubljana. (in Slovene)

[15] Hillier, F.S., Liebermann, G.J. (1990). *Introduction to Operations Research*. McGraw-Hill, New York.

Multi-Physics and Multi-Scale Meshless Simulation System for Direct-Chill Casting of Aluminium Alloys

Božidar Šarler[1,2*] - Tadej Dobravec[2] - Gašper Glavan[1] - Vanja Hatić[1,2] - Boštjan Mavrič[1,2] - Robert Vertnik[2] -
Peter Cvahte[3] - Filip Gregor[3] - Marina Jelen[3] - Marko Petrovič[3]

[1]University of Ljubljana, Faculty of Mechanical Engineering, Slovenia
[2]Institute of Metals and Technology, Slovenia
[3]IMPOL 2000, d.d., Slovenia

This paper represents an overview of the elements of the user-friendly simulation system, developed for computational analysis and optimization of the quality and productivity of the electromagnetically direct-chill cast semi-products from aluminium alloys. The system also allows the computational estimation of the design changes of the casting equipment. To achieve this goal, the electromagnetic and the thermofluid process parameters are coupled to the evolution of Lorentz force, temperature, velocity, concentration, strain and stress fields as well as microstructure evolution. This forms a multi-physics and multi-scale problem of great complexity, which has not been demonstrated before. The macroscopic fluid mechanics, solid mechanics, and electromagnetic solution framework is based on local strong-form meshless formulation, involving the radial basis functions and monomials as trial functions, and local collocation or weighted least squares approximation. It is coupled to the micro-scale by incorporating the point automata solution concept. The entire macro-micro solution concept does not require meshing and space integration. The solution procedure can be easily and efficiently automatically adapted in node redistribution and/or refinement sense, which is of utmost importance when coping with fields exhibiting sharp gradients, which occur in the phase-change problems. The simulation system is coded from scratch in modern Fortran. The elements of the experimental validation of the system and the demonstration of its use for round billet casting in IMPOL Aluminium Industry are shown.

Keywords: direct-chill casting, aluminium alloys, computational solid and fluid mechanics, multi-physics modelling, multi-scale modelling, meshless methods, point automata method

Highlights
- *Multiphysics and multi-scale simulation system for DCC with topmost capabilities.*
- *Solution procedure based on originally developed meshless methods.*
- *Possibility of virtual computational changes in caster design and product properties.*

0 INTRODUCTION

Direct-chill casting (DCC) (see Fig. 1) represents the most important process for production of aluminium alloys [1]. The process involves molten metal being fed vertically through a bottomless, water-cooled mould where it is sufficiently solidified around the outer surface to take the shape of the mould and acquire sufficient mechanical strength to contain the molten core at the centre. As the strand emerges from the mould, water impinges directly from the mould onto the surface, flows over the cast surface and completes the solidification [2]. The technology, despite being almost hundred years old, is still prone to different defects of the products such as porosity, macrosegregation, hot tearing, surface non-homogeneity, shape defects, and cracking. The additional action of the external fields such as electromagnetic, ultrasound, and mechanical stirring is used in the contemporary DCC devices. The casthouse

of IMPOL company produces alloys with around 200 different compositions in form of round billets and rods as well as rectangular ingots with a total annual capacity of 130,000 tons. Such quantities are not sufficient to achieve cost efficiency in mass production, yet they are ideal for covering the market niches where there is a strong demand for high-quality semi-finished products. The company started to use the first, simple computational model of DCC to address these points almost thirty years ago. The multi-scale computational modelling of solidification, by starting with alloy composition and process conditions and finishing with microstructure formation, has gained significant and essential importance in the last decade, accompanied by multi-physics approaches, which couple solid- and fluid mechanics aspects with the external field effects. This novel viewpoints have been increasingly taken into account in modelling of the DCC in IMPOL company. The paper represents our own contemporary state-of-the-art multi-physics and multi-scale model of the DCC process, developed from scratch.
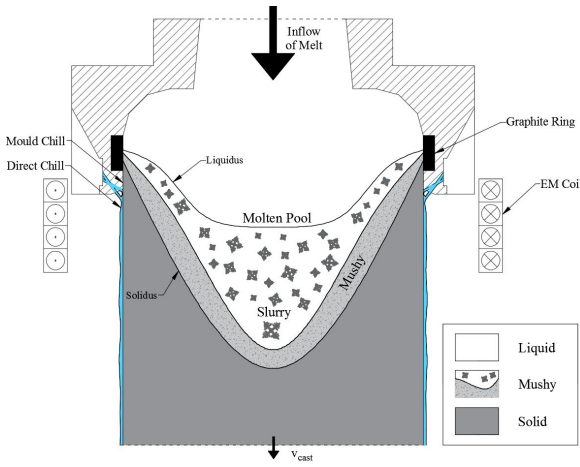
Fig. 1. *Scheme of the DCC process*

1 SIMULATION SYSTEM OVERVIEW

The overview of the simulation system is shown in Fig. 2. From the user perspective, three steps are required. The graphical user interfaces are provided for each step. The first step is the configuration of the input parameters and the material properties [3], the second step is the simulation run and the final step is inspection of the results. Internally, the simulation system consists of four coupled modules. The calculation starts with fully coupled electromagnetic and thermofluid models, described in Section 2. Obtained results are then used as inputs for thermomechanical model, described in Section 3 and microstructure model, described in Section 4.

The nature of the coupling between the simulation system modules is illustrated in Fig. 3. The thermofluid model considers a limited part of the casting device, focused around the casting head, where the solidification takes place. The temperature field, solid fraction and pressure field are forwarded to Eulerian thermomechanical model, where the computational domain is restricted to the coherent part of the solid material, delimited by dashed lines in Fig. 3.

The microstructure model requires the thermal and chemical history of a piece of material to be extracted from the thermofluid model along a material pathline. Several possible pathline selections are indicated in Fig. 3 with white lines.

The outputs of each module are listed in Fig. 2. They are provided to the casting engineer in a report-like format. In this paper, the results are shown in the form of representation-friendly plots.

2 THERMOFLUID MODEL

The macroscopic equations for the conservation of mass, momentum, heat, and species are solved in the thermofluid model. The volume-averaging method is used to formulate the equations for the two-phase problem [4] to [6]. The electromagnetic induction equation is used to calculate the magnetic vector potential and the Lorenz force.

2.1 Conservation Equations

The saturated conditions are presumed for each representative elementary volume. Furthermore, the densities of the liquid and the solid phase are equal and constant ($\rho_l = \rho_s = \rho$). The mass conservation equation thus takes the following form:

$$\nabla \cdot (g_l \langle \mathbf{v}_l \rangle^l + g_s \langle \mathbf{v}_s \rangle^s) = 0. \tag{1}$$

The liquid phase is an incompressible Newtonian fluid in the laminar flow regime. The buoyancy effects due to thermal and compositional variations are modelled with the Boussinesq approximation. The solid grains are assumed to instantaneously form a coherent network when the liquid fraction is less than one. The interfacial drag is therefore modelled for the porous medium with the Darcy equation. The permeability in the mushy zone is defined by the Kozeny-Karman model [7], which means that it is calculated from the secondary dendrite arm spacing and the liquid fraction. The effect of electro-magnetic field (EMF) is included with the Lorentz force. The following equation is solved for the conservation of the liquid phase momentum:

$$\frac{\partial \left(\rho g_l \langle \mathbf{v}_l \rangle^l \right)}{\partial t} + \nabla \cdot \left(\rho g_l \langle \mathbf{v}_l \rangle^l \langle \mathbf{v}_l \rangle^l \right) = -g_l \nabla \langle p_l \rangle^l$$
$$- \frac{g_l^2 \mu_l}{K_0 \frac{g_l^3}{(1-g_l)^2}} \left(\langle \mathbf{v}_l \rangle^l - \langle \mathbf{v}_s \rangle^s \right) + g_l \widehat{\mathbf{b}}^{\mathrm{EM}}$$
$$+ \mu_l \nabla \cdot \left[\nabla \left(g_l \langle \mathbf{v}_l \rangle^l \right) + \left(\nabla \left(g_l \langle \mathbf{v}_l \rangle^l \right) \right)^T \right]$$
$$+ \rho g_l \mathbf{g} \left[1 + \beta_T \left(T_{\mathrm{ref}} - T \right) + \sum_i \beta_C^i \left(C_{\mathrm{ref}}^i - \langle C_l^i \rangle^l \right) \right]. \tag{2}$$

The equation for the conservation of the solid phase is not solved, since the velocity of the solid phase is constant and equal to the billet withdrawal rate $\mathbf{v}_s = \mathbf{v}_{\mathrm{cast}}$.
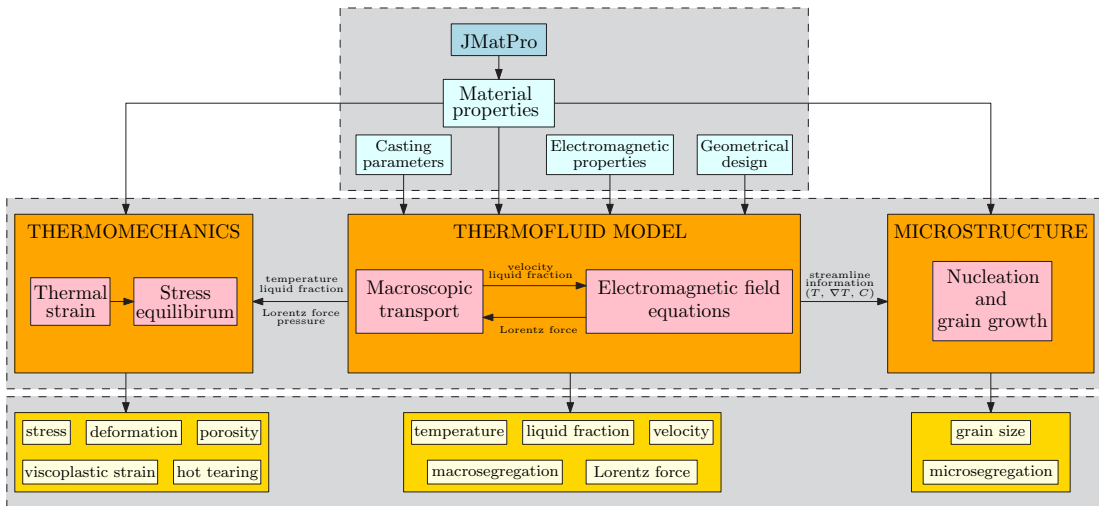
Fig. 2. *Overview of the input parameters, coupling between the models, and the output parameters*
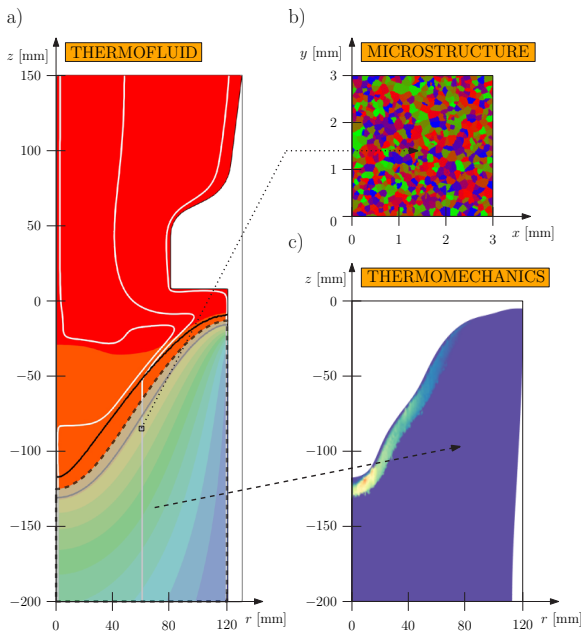
Fig. 3. *Coupling of the simulation system; a) the results of the coupled electromagnetic and thermofluid model - temperature contours, solidus and liquidus isolines, and the streamline paths at the centre, $r/2$, and at the surface; b) the results of the microstructure - the grain structure, which is calculated along each of the three streamlines; c) the thermomechanical results - the hot-tearing susceptibility and the deformations, which are scaled by a factor 10 to achieve better visualisation*

The velocity-pressure coupling is treated with the non-incremental correction scheme [8] and [9]. The intermediate velocity $\mathbf{v}^*$ is first calculated without the pressure term $-g_l\nabla\langle p_l\rangle^l$. The Poisson equation $\nabla\cdot\mathbf{v}^* = \nabla^2\phi$ is solved next and the correction term ϕ is obtained. The divergence-free velocity is finally obtained by adding the correction term to the intermediate velocity. This procedure is elaborated in [10].

In the energy conservation, the effect of Joule heating is neglected due to its insignificant contribution. The equations for the conservation of the solid and the liquid phase enthalpy are summed up and the equation for the volume-averaged enthalpy is solved:

$$\frac{\partial h_m}{\partial t} + \nabla\cdot\left(g_s\langle h_s\rangle^s\langle\mathbf{v}_s\rangle^s + g_l\langle h_l\rangle^l\langle\mathbf{v}_l\rangle^l\right) = \nabla\cdot\left(\frac{k}{\rho}\nabla T\right). \tag{3}$$

The species diffusivity is negligibly small in comparison with the thermal diffusivity in aluminium alloys, resulting in the species conservation equation which exhibits pure convection on the macroscopic level. The volume-averaged concentration is propagated with time:

$$\frac{\partial C_m^i}{\partial t} + \nabla\cdot\left(g_s\langle C_s^i\rangle^s\langle\mathbf{v}_s\rangle^s + g_l\langle C_l^i\rangle^l\langle\mathbf{v}_l\rangle^l\right) = 0. \tag{4}$$

2.2 Phase Diagram and Lever Rule

The solidus and the liquidus temperatures are calculated from the linearised phase diagram:

$$
\begin{aligned}
T_s &= \max\left[T_f + m_s^i C_m^i, T_e\right], \\
T_l &= \max\left[T_f + m_l^i C_m^i, T_e\right].
\end{aligned}
\tag{5}
$$

The concentration of the liquid phase is calculated with the lever rule:

$$
C_l^i = \frac{C_m^i}{1 - \left(1 - k_0^i\right)g_s}.
\tag{6}
$$

The temperature and the enthalpies are correlated with the constitutive relations:

$$
\begin{aligned}
\langle h_s \rangle^s &= h_{\text{ref}} + \int_{T_{\text{ref}}}^{T} c_{ps}(T)\,dT, \\
\langle h_l \rangle^l &= h_{\text{ref}} + \int_{T_{\text{ref}}}^{T_s} c_{ps}(T)\,dT + \int_{T_s}^{T} c_{pl}(T)\,dT + L_f, \\
h_m &= g_l \langle h_l \rangle^l + g_s \langle h_s \rangle^s.
\end{aligned}
\tag{7}
$$

2.3 Electromagnetic Field

The electromagnetic field is calculated from the induction equation:

$$
\nabla^2 \mathbf{A}_0 = i\delta^{-2}\mathbf{A}_0 - \mu_0 \sigma \mathbf{v} \times (\nabla \times \mathbf{A}_0) - \mu_0 \mathbf{J}_{0,\text{ext}}.
\tag{8}
$$

The current density is the source term, which is calculated from the coil specifications. Harmonic time dependence of the magnetic vector potential and the current density is imposed. The time-averaged Lorentz force is then calculated as the cross product of the complex amplitudes of the current density and the magnetic field:

$$
\widehat{\mathbf{b}}^{\text{EM}} = -\frac{1}{2}\,\text{Re}\left(\mathbf{J}_0^* \times \mathbf{B}_0\right).
\tag{9}
$$

2.4 Boundary Conditions

The molten metal is fed at the top of geometry. The casting temperature and species concentration are prescribed by the casting parameters. The Poiseuille flow distribution is used to prescribe the inflow velocity. The symmetry boundary conditions are employed on the centreline. The outflow boundary conditions are used at the bottom of geometry. The outer surface is isolated for the species transport and is assumed as a wall for the liquid velocity. The boundary conditions for heat transfer involve film boiling, subcooled nucleate boiling, and forced convection, as defined by the Weckman-Niessen correlation [11]. This generic correlation is tuned by experiments to the plant-specific conditions.

3 THERMOMECHANICAL MODEL

The thermomechanical model is stated in small-strain approximation and considers three contributions to the total strain: the elastic strain $\overline{\overline{\varepsilon}}^e$, the viscoplastic strain $\overline{\overline{\varepsilon}}^p$ and the thermal strain $\overline{\overline{\varepsilon}}^t$. The thermal strain is the driving term of the model and is given by:

$$
\overline{\overline{\varepsilon}}^t(T) = \overline{\overline{I}}\int_{T_s}^{T}\alpha(T)\,dT = \overline{\overline{I}}\varepsilon^t,
\tag{10}
$$

where $\alpha(T)$ is the temperature dependent coefficient of thermal expansion. The viscoplastic strain rate:

$$
\dot{\overline{\overline{\varepsilon}}}^p = -\mathbf{v}_{\text{cast}}\nabla\overline{\overline{\varepsilon}}^p + \frac{3\overline{\overline{\tau}}}{2\sigma_e}\dot{\varepsilon}_0(T, \overline{\overline{\sigma}}),
\tag{11}
$$

is determined by two terms. The first term is the advection term, which is the result of the Eulerian description of the material moving through the computational domain. The second term describes the contribution of the viscoplastic deformation, caused by the stresses in the billet. The effective strain rate $\dot{\varepsilon}_0(T, \overline{\overline{\sigma}})$ is given by:

$$
\dot{\varepsilon}_0(T, \overline{\overline{\sigma}}) =
\begin{cases}
A\exp\left(-\dfrac{Q}{RT}\right)\left(\dfrac{\sigma_e}{\sigma_0}\right)^p, & \text{if } T < T_s \\[2ex]
A'\left(\dfrac{\sigma_e}{\sigma_0'}\right)^{p'}, & \text{otherwise.}
\end{cases}
\tag{12}
$$

Two variations of the Norton-Hoff's law are used to describe the behavior of the material in the mushy zone ($T_s < T < T_{coh}$) and in the solid material ($T < T_s$) as proposed in [12]. By expressing the total strain with displacement vector $\mathbf{u}$, the following equilibrium equation is obtained:

$$
\begin{aligned}
0 = {} & G\nabla^2\mathbf{u} + (G + \lambda)\nabla(\nabla\cdot\mathbf{u}) \\
& + \nabla\lambda(\nabla\cdot\mathbf{u}) + \nabla G\left(\nabla\mathbf{u} + (\nabla\mathbf{u})^T\right) \\
& - \nabla\cdot(2G\overline{\overline{\varepsilon}}^p) - \nabla\left((3\lambda + 2G)\varepsilon^t\right) \\
& + \mathbf{f}_g.
\end{aligned}
\tag{13}
$$

The equation accounts for inhomogeneous material properties and the coupling of the deformation field with the thermal and the plastic strain.

3.1 Boundary Conditions

The computational domain is determined by the extent of the computational domain of the heat and mass transfer model. At the top, the computational domain is limited by the position of the isoline at coherency temperature T_{coh}, above which the material cannot transfer stress and is governed by the equations of fluid dynamics.

At the coherency isoline, the material has to support the metalostatic pressure of the liquid $\mathbf{t} = -p\mathbf{n}^*$, where p is the pressure of the liquid, calculated by the heat and momentum transfer model. The outer surface is traction free ($\mathbf{t} = 0$) except at the top, where the contact with the mold is possible. In that area, an iterative method is used to satisfy the boundary conditions $u_r \leq 0$ and $t_r \leq 0$.

There are no specific boundary conditions for the viscoplastic strain for the most of the boundary and the rate equation is used to calculate the values on the boundary also. The only exception to this is the top boundary, where the material is solidifying. We assume that the freshly solidified material does not accumulate any plastic strain by setting $\bar{\bar{\varepsilon}}^p = 0$ at the top boundary.

3.2 Prediction of Hot-Tearing

Once the stresses and strains in the material are known, the parameters related to the occurrence of casting defects can be calculated. The model used to calculate the micro-porosity in the material and the susceptibility of the material to hot tearing relies on the Suyitno-Kool-Katgerman model, which was developed specifically for use with numerical models of the casting process [13]. The model starts by stating the conservation equation for three phases, each associated with a volume fraction:

$$g_s + g_l + g_v = 1, \qquad (14)$$

where g_s is solid fraction, g_l is liquid fraction and g_v is volume fraction of voids. Mass conservation for a control volume gives a rate equation for void fraction:

$$\dot{g}_v = \dot{g}_r + \dot{g}_e, \qquad (15)$$

where $\dot{g}_r$ is the shrinkage rate and $\dot{g}_e$ is the feeding rate. The model states that the voids start to nucleate

when $\dot{g}_r - |\dot{g}_e| > \dot{g}_c$. The parameter $\dot{g}_c$ is the critical rate for void nucleation. It is material dependent but very small, so $\dot{g}_c = 0$ can be used instead of its actual value.

The shrinkage rate takes into account solidification shrinkage and material deformation:

$$\dot{g}_r = -\left(\frac{\rho_s}{\rho_l} - 1\right)\dot{g}_l + \frac{\rho_s}{\rho_l}g_s\mathrm{tr}\left(\dot{\bar{\bar{\varepsilon}}}\right). \qquad (16)$$

The feeding term accounts for the liquid feeding of the melt. In the coherent part of the mushy zone, the liquid has to flow through a solidified network of dendrites. Such a flow can be described by Darcy law. By combining it with Carman-Kozeny relation, which is the standard model to calculate the permeability of the mushy zone [1], the following expression for the feeding term is obtained:

$$\dot{g}_e = \nabla \cdot \left(\frac{d_{as}^2}{180\mu_l}\frac{g_l^3}{1 - g_l}\nabla p\right). \qquad (17)$$

In the locations, where the condition for cavity growth is fulfilled, the void formation rate can be integrated to obtain the fraction of voids. By assuming spherical voids, their diameter is given by:

$$a = \left(\frac{3}{2\pi}r_p d_g^3 g_v\right)^{1/3}. \qquad (18)$$

The value of packing parameter for grains packed in body-centered configuration is $r_p = 8/(3\sqrt{3})$. The size of the voids in the material determines the critical stress σ_{SKK} needed for crack growth. For this we can use the result from Griffith theory of brittle fracture which connects the diameter of a void with the critical tensile stress needed for a crack to nucleate on the void:

$$\sigma_{SKK} = \sqrt{\frac{4\gamma_s E}{\pi a}}. \qquad (19)$$

The only additional parameter in this equation is the surface energy γ_s. From this the criterion:

$$HCS = \frac{\sigma_{max}}{\sigma_{SKK}}, \qquad (20)$$

can be devised to describe the hot tearing susceptibility of the material.

4 MICROSTRUCTURE

In the microstructure evolution model, solidification of a multicomponent alloy (nucleation and grain growth)

in two dimensions is considered. In the model, athermal nucleation [14] of the solid phase from an undercooled melt is assumed. The heterogeneous nucleation is initialized by grain refiner particles present in the melt. The nucleation density change, induced by the change of the undercooling, is described by the normal distribution:

$$\frac{dn}{d\Delta T} = \frac{n_{max}}{\sqrt{2\pi}\Delta T_\sigma} \exp\left[-\frac{1}{2}\left(\frac{\Delta T - \Delta T_\mu}{\Delta T_\sigma}\right)^2\right], \quad (21)$$

where $\Delta T = T_l(\mathbf{C}_l) - T$ and $\mathbf{C}_l = (C_l^1, C_l^2, ...)$. By neglecting any interaction between the alloying elements and performing the linearization of the liquidus line in the phase diagram near the initial concentration for each alloying element, T_l can be calculated as:

$$T_l(\mathbf{C}_l) = T_l(\mathbf{C}_0) + \sum_{i=1}^{N_{alloy}} m_l^i(C_l^i - C_0^i), \quad (22)$$

where $\mathbf{C}_0 = (C_0^1, C_0^2, ...)$.

In general, grain growth is determined by the diffusion of heat and solute, while the boundary condition at the solid-liquid interface accounts for the release of the heat and the solute during the phase change. The diffusion of heat is approximately three orders of magnitude faster than the diffusion of solute, hence, the temperature field can be considered as an input parameter obtained from the macroscopic thermofluid model. Uniform concentration of solute in the liquid phase is assumed. It is obtained from the macroscopic thermofluid model. The solute diffusion in the solid phase is typically few orders of magnitude slower than the solute diffusion in the liquid phase, hence, a case without diffusion in the solid phase is considered in this study.

The solute balance of the i-th alloying element at the solid-liquid interface is given as [14]:

$$D_s^i \nabla C_s^i\Big|^* \cdot \mathbf{n}^* - D_l^i \nabla C_l^i\Big|^* \cdot \mathbf{n}^* = \mathbf{v}^* \cdot \mathbf{n}^*(C_l^{i*} - C_s^{i*}), \quad (23)$$

where $C_s^{i*} = k_0^i C_l^{i*}$. The temperature at the curved solid-liquid interface is given as [14]:

$$T^* = T_l(\mathbf{C}_l^*) - 2\Gamma f_a(\mathbf{n}^*)\kappa. \quad (24)$$

In case of the crystalline solid phase with a cubic crystal structure, the following anisotropy function is in use [14]:

$$f_a(\mathbf{n}^*) = 1 - 3\varepsilon_4 + 4\varepsilon_4(n_x^{*4} + n_y^{*4}), \quad (25)$$

where $\mathbf{n}^* = (n_x^*, n_y^*)$.

5 SOLUTION PROCEDURE

5.1 Meshless Numerical Method

The whole simulation system is solved with the meshless numerical methods [15], which in comparison to the classical numerical approaches (finite volume, finite element, and finite difference method) do not require a predefined mesh for domain discretisation. Two different types of meshless approaches are used in this multi-scale system. The meshless diffuse approximate method (DAM) [16] to [19] is used for solving the thermofluid and the EMF model while the local radial basis function collocation method (LRBFCM) [20] to [23] is used for solving the thermomechanical model. Both methods are local, which means that local neighbourhoods are used to evaluate either approximation (DAM) or collocation (LRBFCM). The details of the numerical implementation with meshless methods are given in the related publications [19] to [23].

5.2 Thermofluid Model

The problem is solved in two stages. In the first stage the conservation equations and the Poisson equation are solved in the cylindrical coordinate system for axial symmetry in case of round billets. Here the spatial discretization is performed with the local meshless diffuse approximate method [10] and [19] and the time stepping is performed with the explicit-Euler scheme. The liquid velocity, the volume-averaged enthalpy, and the volume-averaged species at the new time step are obtained in this stage. The EMF equations are also solved at this stage, with the time step, which is 1000 times larger than the one used to solve the conservation equations.

The quantities from the first stage are used to calculate the temperature and the liquid fraction in the second stage. The temperature is locally calculated by combining Eqs. 6 and 7:

$$T = \frac{-b - \sqrt{b^2 - 4ac}}{2a},$$
$$a = (1 - k_0^i)c_{pl} + (c_{ps} - c_{pl}),$$
$$b = (h_0 - c_{pl}T_f - h_m)(1 - k_0^i) + (c_{pl} - c_{ps})T_l - h_0,$$
$$c = (h_m T_f - h_0 T_f)(1 - k_0^i) + T_l h_0,$$
$$h_0 = (c_{ps} - c_{pl})T_s + L_f.$$

$$(26)$$

The liquid fraction is subsequently locally calculated by using Eqs. 5 and 6:

$$g_l = \frac{\frac{T_f - T_l}{T_f - T} - k_0^i}{1 - k_0^i}. \qquad (27)$$

The computational node arrangement (CNA) is unstructured and has variable density of the nodes. A smaller computational domain is used to solve the conservation equations, while a larger one is used to solve the EMF model (see Fig. 4). The number of the nodes is increased in the mushy zone and in the coil area and decreased in the solid phase and at the outer boundary of the EMF domain. The mushy zone is not constant with time, which means that the CNA is adapted on demand. This does not need any additional interference of the user, since an automatic node generation is used in the model.
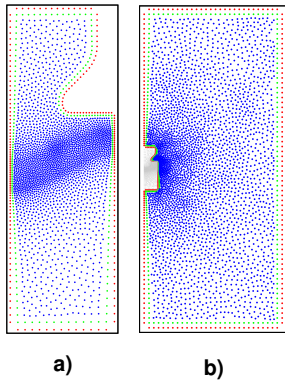
Fig. 4. *The computational node arrangement used to solve; a) the conservation and b) EMF equations; The node density is decreased for better visibility*

5.3 Point Automata Method

Point automata (PA) method [24] is used for the simulation of nucleation and grain growth. In the PA method, the randomly distributed points are used instead of square cells like in the classical cellular automata (CA) method [25]. Each point has a defined neighbourhood containing N_{neigh} nearest points. Similar as in the CA method, the possible states of the point and the rules for transition between states have to be determined. Each point has three possible states: solid (S), liquid (L), and interface (I). To each point, the concentration in the solid and in the liquid phase for each alloying element and the solid fraction are assigned. The time-dependent temperature and the concentrations in the liquid phase, obtained
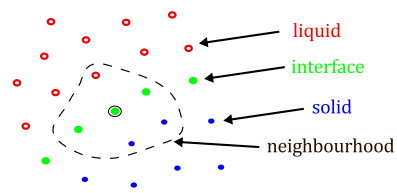
Fig. 5. *Representation of the solid-liquid interface by PA method; five points inside the dashed line represent the neighbourhood of a point marked with black circle*

from the thermofluid model, are assumed to be uniform in the computational domain. At the beginning of the simulation, state L and concentrations $\mathbf{C} = \mathbf{C}_0$ are assigned to each point in the computational domain. At each time step, all the points in the computational domain are checked.

Nucleation is described by the state L being changed to I if:

$$\mathscr{R} < V_p \int_{\Delta T}^{\Delta T + \delta \Delta T} \frac{dn}{d\Delta T'} d\Delta T', \qquad (28)$$

where $\mathscr{R} \in [0,1)$.

To describe solidification, state I is changed to S if $g_s = 1$. When the state I is changed to the state S in a point, the neighbourhood of that point is checked and the state L is changed to the state I in all liquid neighbours.

Melting is described by state I being changed to L if $g_s = 0$. When the state I is changed to the state L in a point, the neighbourhood of that point is checked and the state S is changed to the state I in all solid neighbours.

5.3.1 Calculation of Solid Fraction and Concentration

By assuming the uniform concentration on the scale of a point in the state I, the lever rule can be written for each alloying element [26]:

$$C^i + \delta C^i = \left(1 + g_s(k_0^i - 1)\right)\left(C_l^{i*} + \delta C_l^{i*}\right), \qquad (29)$$

where δ represents a change of a variable during one explicit time step. Eq. (29) for each alloying element together with Eq. (24) yield a system of $N_{alloy} + 1$ equations, which are solved by the use of LU decomposition in order to obtain $\delta \mathbf{C}_l^*$ and g_s in each point in the state I. Temperature T^* in Eq. (24) and δC^i are obtained from the thermofluid model. $\mathbf{n}^*$ and κ in Eq. (24) are calculated according to the modified weighted-counting-cell procedure [27].

6 EXPERIMENTAL VALIDATION

The verification of the simulation system has been done by a spectrum of solidification related benchmark tests of which several have been originally proposed by our group [**10**] and [**19**]. The validation of the simulation system follows a complicated interconnected plant and laboratory measurements strategy. The plant measurements include: the electromagnetic field measurements by insertion of the measuring coil in the empty mould; the temperature measurements by insertion of the thermocouples in the melt (see Figs. 6 and 7); measurements of the sump depth by insertion of a steel rod during operation (Fig. 8); the flooding of the sump by pure zinc and then cutting the strand (Fig. 9); measurement of the direct-chill water temperature increase; macrosegregation evaluation by point chemical analysis along the cross section; measurement of the strand deformation. The microstructure model is validated by comparison of the calculated and laboratory measured grain sizes and microsegregation.

Fig. 6. *Billet instrumented with thermocouples for temperature measurement*

6.1 Temperature Measurements

The temperature measurements have been performed with the K type thermocouples, which were inserted into the melt at four different locations. First location was at the billet surface, second one at the centre and the other two at the distance of 50 mm from the centreline. All of the locations are just approximate and are determined in detail by slicing of the finished product. Validation is performed in the sense of modifying the boundary conditions for heat transfer in the mould and direct-chill area. The results with the modified boundary conditions are in a very good agreement with the temperature measurements (see Fig. 7).
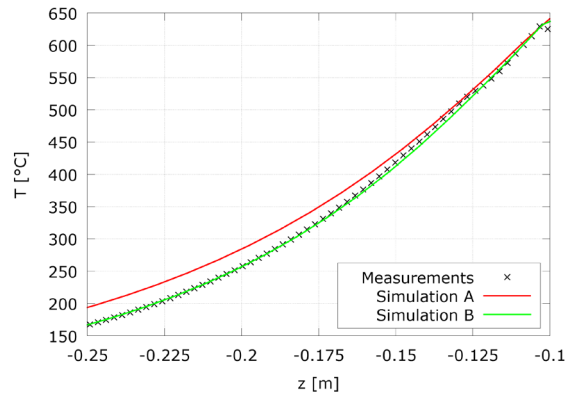
Fig. 7. *Comparison of temperature measurement and simulation along the z-axis at $r = 52$ mm; simulation A is performed with generic heat transfer boundary conditions [*11*]; simulation B is performed with the plant-specific boundary conditions*

6.2 Sump Depth Measurements

Sump depth measurements have been performed by insertion of a steel rod into the melt at three different positions - at the centre, at the $r/2$ and at the surface of the billet. The measurement procedure is the following: the rod is inserted from the top in the vertical direction until the coherency isotherm is met. Next the rod is held in that position and the distance from the bottom of the rod to the melt level is measured. Fig. 8 shows the comparison between the sump depth measurements and the simulation results. The solidus and the liquidus isolines are shown with the solid and dashed line, respectively. The results show that the simulated sump depth is a good representation of the actual sump depth, especially considering the measurement error and the fact that it is difficult to define the alloy coherency isotherm.
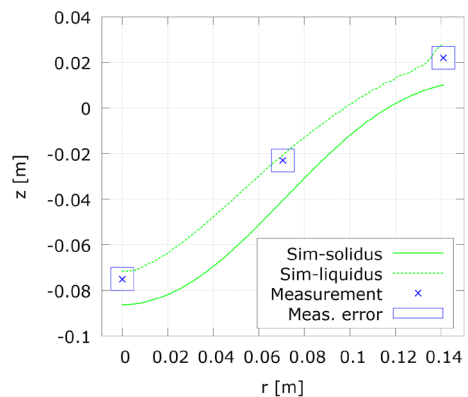
Fig. 8. *Comparison of the simulated and measured mushy area*
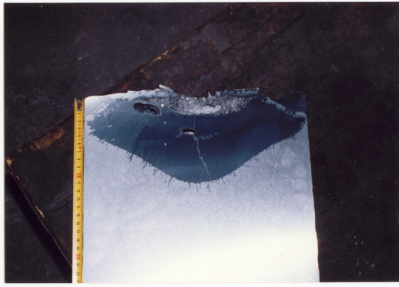
Fig. 9. *Flooding of AlCuBiPb (AA2011) sump with zinc, which has approximately 3 times higher density than aluminium; zinc displaced the aluminium alloy and the position of liquid-solid interphase region is clearly visible after cutting of the billet*

7 RESULTS

The results presented in this section demonstrate the capabilities of the simulation system and are not meant to be exhaustive. The parameters of the casting process are given in Table 2. The material properties and other required physical parameters are listed in Table 1. The parameters correspond to a typical production configuration of Al-5.25wt%Cu alloy.

Table 1. *The material properties of Al-5.25wt%Cu alloy and the steel support structure used in the DCC and LFEC simulations*

Property	Symbol	Unit	Value
Liquid phase specific heat capacity	c_{pl}	$J\,kg^{-1}\,K^{-1}$	1.13×10^3
Solid phase specific heat capacity	c_{ps}	$J\,kg^{-1}\,K^{-1}$	1.03×10^3
Liquid phase thermal conductivity	k_l	$W\,m^{-1}\,K^{-1}$	80.0
Solid phase thermal conductivity	k_s	$W\,m^{-1}\,K^{-1}$	180
Liquid species diffusivity	D_l^i	$m^2\,s^{-1}$	0
Solid species diffusivity	D_s^i	$m^2\,s^{-1}$	0
Density	ρ	$kg\,m^{-3}$	2.6×10^3
Dynamic viscosity	μ	$kg\,m^{-1}\,s^{-1}$	1.40×10^{-3}
Gravity acceleration	g_{acc}	$m\,s^{-2}$	9.81
Secondary dendrite arm spacing	d_{as}	μm	25.0
Latent heat	L_f	$J\,kg^{-1}$	3.77×10^5
Fusion temperature	T_f	$°C$	660
Eutectic temperature	T_e	$°C$	548
Eutectic concentration	C_e	wt%	32.60
Liquidus slope	m_l	$°C\,wt\%^{-1}$	-3.43
Partition coefficient	k_0	$-$	0.173
Thermal expansion coefficient	β_T	K^{-1}	1.17×10^{-4}
Solutal expansion coefficient	β_C	$wt\%^{-1}$	-7.3×10^{-3}
Reference temperature	T_{ref}	$°C$	700
Reference concentration	C_{ref}	wt%	5.25
Steel electrical conductivity	σ_{Steel}	$S\,m^{-1}$	1.7×10^6
Liquid phase electrical conductivity	$\sigma_{Al,l}$	$S\,m^{-1}$	4.00×10^6
Solid phase electrical conductivity	$\sigma_{Al,s}$	$S\,m^{-1}$	8.00×10^6
Stand. dev. of normal dist.	ΔT_σ	K	6.5
Mean value of normal dist.	ΔT_μ	K	0.75
Maximal nucleation density	n_{max}	m^{-2}	5.5×10^{11}

7.1 Thermofluid

Results of the thermofluid model are summed up in Figs. 10 and 11. The results include the temperature contours for DCC (Fig. 10a), the concentration contours for DCC (Fig. 10b), the velocity magnitude contours with streamlines for DCC (Fig. 11a), and the velocity magnitude contours with streamlines for the case with EMF (Fig. 11b). The solid lines are used to denote the liquidus and solidus isoline. The results without the EMF are used as input parameters for the microstructure and thermomechanical model.
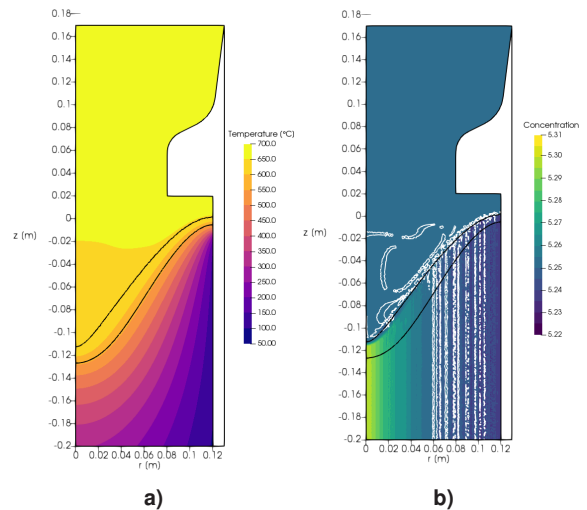
Fig. 10. *Results of the thermofluid model; a) temperature field for DCC; b) concentration field for DCC*
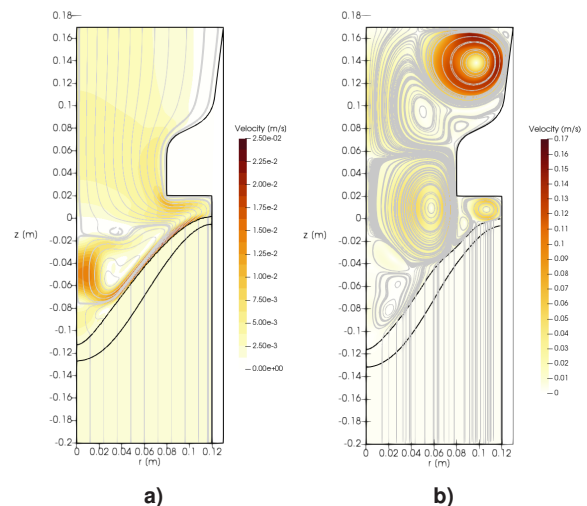
Fig. 11. *Results of the thermofluid model; a) velocity field for DCC; b) Velocity field for LFEC*

Table 2. *Casting parameters for the simulated DCC case; parameters below the double line are the additional parameters used to define the electromagnetic field*

Property	Symbol	Unit	Value
Casting temperature	T_{cast}	°C	680
Casting velocity	v_{cast}	$mm\,min^{-1}$	120
Cooling water temperature	T_w	°C	25
Cooling water discharge	Q_w	$m^3\,h^{-1}$	6
Current amplitude	I	A	150
Current frequency	f	Hz	10
Coil turns	n_{coil}	—	40
Coil height	h_{coil}	mm	60
Coil width	w_{coil}	mm	15

7.2 Microstructure Evolution

The results of the microstructure model are represented in Figs. 12 and 13. The microsegregation and ASTM index can be predicted. The final microstructure in a sample with dimensions $3\,mm \times 3\,mm$ at the center of the billet is given in the Fig. 12. Corresponding concentration field of Cu is shown in Fig. 13. The microsegregation with increasing concentration of the copper as a function of the radius of a grain is observed.
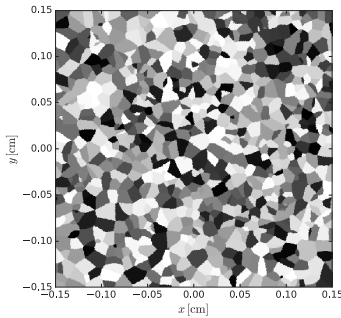
Fig. 12. *Results of the microstructure evolution model: grain structure*
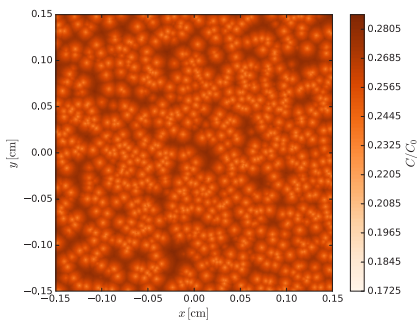
Fig. 13. *Results of the microstructure evolution model: rescaled concentration field of Cu*

7.3 Thermomechanics

The results of thermomechanical model adjacent to the thermofluid model are represented in Figs. 14 and 15. The primary outputs of the mechanical model are the deformation field and the plastic strain field. The magnitude of the latter is shown in Fig. 14a, while Fig. 14b shows the hoop stress obtained from the deformation field. The primary results are combined by models described in Section 3 to predict formation of casting defects. The thermomechanical model can predict the size of the porosity, shown in Fig. 15a, and the susceptibility to hot-tearing, shown in Fig. 15b.
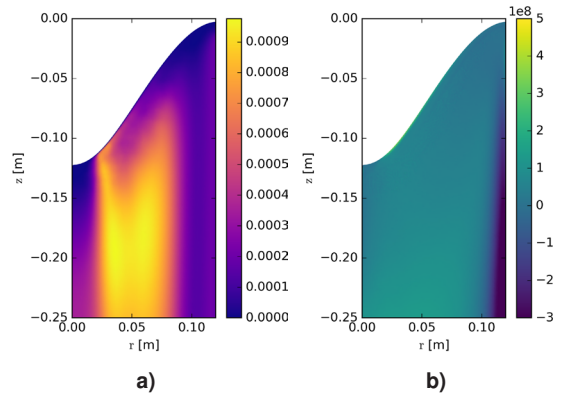
Fig. 14. *Illustration of results of thermomechanical model; a) plastic strain magnitude; b) hoop stress in Pa*
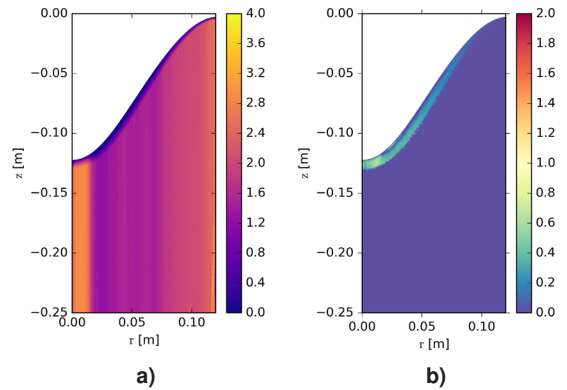
Fig. 15. *Illustration of prediction of casting defects; a) predicted size of voids in* μm*; b) hot-tearing susceptibility according to SKK criterion*

8 CONCLUSIONS AND OUTLOOK

The presented numerical model of DCC provides additional insight in the DCC process and gives plant

operators options to virtually experiment with the casting parameters to investigate the relations between the casting parameters and presence of chemical and mechanical defects in the produced ingots.

The presented simulation system is unique in the sense that it couples the electromagnetic phenomena with the thermofluid and solid mechanics phenomena on the macroscopic levels ($\sim$1 m) with the phenomena on the micro-scale ($\sim$0.1 mm), which has not been demonstrated before.

The described models are in the process of further improvement. The thermofluid model will be improved by Eulerian-Eulerian description of the grain movement of the solid phase, the microstructure model will obtain another scale ($\sim$ 0.001 mm) for solving the detailed shape and structure of the dendrites and its primary and secondary spacing. This scale will be resolved by the phase-field formulation. The solid mechanics level will be improved by replacing the current solution procedure with the state-of-the art return-mapping algorithms, which will allow more complicated constitutive equations to be added to better describe the behaviour of the mushy zone.

The simulation output of all the models will be validated on typical aluminium alloy compositions from the 1000 to 8000 series. The validation will proceed with additional plant and laboratory measurements, to improve the nucleation model in particular.

Additionally, the model will be extended to describe three dimensional geometry of slab casting. Such simulations result in computational times on the order of few days on shared-memory computers, requiring supercomputer implementation to achieve reasonable computational times. The computational time will be further reduced by extensive use of automatic adaptive node refinement and coarsening.

To help with validation of the models, we plan to establish a water model of the DCC as already performed for continuous casting of steel [28].

The system will be further improved in the sense of user-friendliness by establishment of alloy specific quality, productivity, and safety object functions as well as automatic searching for the best casting parameters, based on evolutionary computing.

9 NOMENCLATURE

$*$	Value at the solid-liquid interface, [-]
$\alpha(T)$	Temperature dependent coefficient of thermal expansion, [1/K]
$\alpha_{\Delta t}$	Ratio between time steps at different scales, [-]
β_C	Solutal expansion coefficient, [-]
β_T	Thermal expansion coefficient, [1/K]
$\mathbf{f}_g$	Gravitational force, [N/m^3]
$\mathbf{t}$	Traction, [Pa]
ΔT	Undercooling, [K]
ΔT_μ	Mean of the normal distribution, [K]
ΔT_σ	Standard deviation of the normal distribution, [K]
δ	Skin depth, [-]
ε_4	Strength of anisotropy, [-]
Γ	Gibbs-Thomson coefficient, [Km]
γ_s	Surface tension, [N/m]
κ	Curvature of the solid-liquid interface, [1/m]
λ	Lamé parameter, [Pa]
$\langle C_k^i \rangle^k$	Intrinsic average concentration of phase k, [-]
$\langle h_k \rangle^k$	Intrinsic average enthalpy of phase k, [J/kg]
$\langle p_k \rangle^k$	Intrinsic average pressure of phase k, [N/m^2]
$\langle \mathbf{v}_k \rangle^k$	Intrinsic average velocity of phase k, [m/s]
$\widehat{\mathbf{b}}^{EM}$	Lorentz force, [N/m^3]
$\mathbf{g}$	Gravitational acceleration, [m^2/s]
$\mathcal{R}$	Random number, [-]
$\overline{\overline{\tau}}$	Octahedral stress $\overline{\overline{\tau}} = \overline{\overline{\sigma}} - \overline{\overline{I}}\mathrm{tr}\overline{\overline{\sigma}}/3$, [Pa]
$\overline{\overline{\varepsilon}}^e$	Elastic strain, [-]
$\overline{\overline{\varepsilon}}^p$	Plastic strain, [-]
$\overline{\overline{\varepsilon}}^t$	Thermal strain, [-]
$\overline{\overline{I}}$	Identity tensor, [-]
μ_0	Magnetic permeability of vacuum, [H/m]
μ_l	Dynamic viscosity, [kg/(m$\cdot$s)]
ρ	Density, [kg/m^3]
σ	Electrical conductivity, [S/m]
σ_e	Effective stress $\sigma_e = \sqrt{2\overline{\overline{\tau}} : \overline{\overline{\tau}}/3}$, [Pa]
σ_o, σ_0'	Reference stress, [Pa]
σ_{max}	Maximal principal stress, [Pa]
σ_{SKK}	Critical stress according to SKK criterion, [Pa]
$\mathbf{A}_0$	Magnetic vector potential, amplitude, [Vs/m]
$\mathbf{B}_0$	Magnetic field, amplitude, [T]
$\mathbf{C}$	Array of concentrations, [-]
$\mathbf{C}_0$	Array of initial concentrations, [-]
$\mathbf{C}_l$	Array of concentrations in the liquid phase, [-]
$\mathbf{J}_{0,\mathrm{ext}}$	External electric current density, amplitude, [A/m^2]
$\mathbf{n}^*$	Normal to the solid-liquid interface, [-]
$\mathbf{v}^*$	Solid-liquid interface velocity, [m/s]
a	Typical diameter of spherical voids, [m]

A, A'	Reference strain rate, $[1/\text{s}]$
C_0^i	Initial concentration of the i-th alloying element, [-]
C_k^i	Concentration of the i-th alloying element in the k-th phase, [-]
C_{ref}^i	Reference concentration of the i-th alloying element, [-]
C_m^i	Volume-averaged concentration, [-]
c_{pk}	Specific heat capacity of phase k, $[\text{J}/(\text{kg}\cdot\text{K})]$
d_{as}	Secondary dendrite arm spacing, [m]
d_g	Grain size, [m]
D_k^i	Diffusion coefficient of the i-th alloying element in the k-th phase, $[\text{m}^2/\text{s}]$
E	Young's modulus, [Pa]
f_a	Anisotropy function, [-]
G	Shear modulus, [Pa]
g_k	Volume fraction of phase k, [-]
h_{ref}	Reference enthalpy, [J/kg]
h_m	Volume-averaged enthalpy, [J/kg]
h_{PA}	Average spacing between neighbouring points in PA, [m]
k	Thermal conductivity, $[\text{W}/(\text{m}\cdot\text{K})]$
K_0	Permeability constant, $[\text{m}^2]$
k_0^i	Partition coefficients of the i-th alloying element, [-]
l	Liquid phase, [-]
L_f	Latent heat, [J/kg]
L_x, L_y	Side lengths of rectangular computational domain for PA, [m]
m_l^i	Liquidus slope of the i-th alloying element, [K]
n	Nucleation density, $[1/\text{m}^3]$
N_{alloy}	Number of alloying elements, [-]
n_{max}	Maximal nucleation density, $[1/\text{m}^3]$
N_{neigh}	Number of neighbours, [-]
p, p'	Garafalo law exponent, [-]
Q	Activation energy of viscoplastic deformation, [kJ/kg]
R	General gas constant, [-]
r_p	Packing ratio, [-]
s	Solid phase, [-]
T	Temperature, [K]
t	Time, [s]
T_{ref}	Reference temperature, [K]
T_e	Eutectic temperature, [K]
T_f	Fusion temperature, [K]
T_l	Liquidus temperature, [K]
T_s	Solidus temperature, [K]
V_p	Volume, represented by one point, [-]
I	Interface PA state, [-]
L	Liquid PA state, [-]
S	Solid PA state, [-]

ACKNOWLEDGEMENTS

REFERENCES

[1] Eskin, D. G. (2008). *Physical Metallurgy of Direct Chill Casting of Aluminum Alloys*. CRC Press, Boca Raton, 1 edition edn.

[2] Vertnik, R., Založnik, M., Šarler, B. (2006). Solution of transient direct-chill aluminium billet casting problem with simultaneous material and interphase moving boundaries by a meshless method. *Engineering Analysis with Boundary Elements*, vol. 30, no. 10, p. 847–855, DOI:10.1016/j.enganabound.2006.05.004.

[3] Saunders, N., Guo, U. K. Z., Li, X., Miodownik, A. P., Schillé, J.-P. (2003). Using JMatPro to model materials properties and behavior. *JOM*, vol. 55, no. 12, p. 60–65.

[4] Ganesan, S., Poirier, D. R. (1990). Conservation of mass and momentum for the flow of interdendritic liquid during solidification. *Metallurgical Transactions B*, vol. 21, no. 1, p. 173–181, DOI:10.1007/BF02658128.

[5] Poirier, D. R., Nandapurkar, P. J., Ganesan, S. (1991). The energy and solute conservation equations for dendritic solidification. *Metallurgical Transactions B*, vol. 22, no. 6, p. 889–900, DOI:10.1007/BF02651165.

[6] Ni, J., Beckermann, C. (1991). A volume-averaged two-phase model for transport phenomena during solidification. *Metallurgical Transactions B*, vol. 22, no. 3, p. 349–361, DOI:10.1007/BF02651234.

[7] Kozeny, J. (1927). Über kapillare Leitung des Wassers im Boden. *Sitzungsber Akad. Wiss., Wien*, vol. 136, no. 2a, p. 271–306.

[8] Chorin, A. (1967). A Numerical Method for Solving Incompressible Viscous Flow Problems. *Journal of Computational Physics*, vol. 2, no. 1, p. 12–26, DOI:10.1006/jcph.1997.5716.

[9] Chorin, A. J. (1968). The numerical solution of the Navier-Stokes equations. *Mathematics of Computation*, vol. 22, no. 104, p. 745–762, DOI:10.1090/S0002-9904-1967-11853-6.

[10] Hatić, V., Mavrič, B., Šarler, B. (2018). Simulation of a macrosegregation benchmark with a meshless diffuse approximate method. *International Journal of Numerical Methods for Heat & Fluid Flow*, vol. 28, no. 2, p. 361–380, DOI:10.1108/HFF-04-2017-0143.

[11] Weckman, D. C., Niessen, P. (1982). A numerical simulation of the D.C. continuous casting process including nucleate boiling heat transfer. *Metallurgical*

Transactions B, vol. 13, no. 4, p. 593–602, DOI:10. 1007/BF02650017.

[12] Kumar, A., Tyagi, M., Specht, E., Bertram, A. (2011). Thermomechanical simulation of direct chill casting. *Transactions of The Indian Institute of Metals*, vol. 64, no. 1, p. 13–19.

[13] Suyitno, Kool, W., Katgerman, L. (2009). Integrated Approach for Prediction of Hot Tearing. *Metallurgical and Materials Transactions A*, vol. 40, no. 10, p. 2388–2400, DOI:10.1007/s11661-009-9941-y.

[14] Dantzig, J., Rappaz, M. (2009). *Solidification*. Engineering Sciences. EPFL Press.

[15] Liu, G. (2009). *Mesh Free Methods: Moving Beyond the Finite Element Method*. CRC Press, Boca Raton, FL.

[16] Sadat, H., Prax, C. (1996). Application of the diffuse approximation for solving fluid flow and heat transfer problems. *International Journal of Heat and Mass Transfer*, vol. 39, no. 1, p. 214–218, DOI:10.1016/ S0017-9310(96)85018-6.

[17] Bertrand, O., Binet, B., Combeau, H., Couturier, S., Delannoy, Y., Gobin, D., Lacroix, M., Le Quéré, P., Médale, M., Mencinger, J., Sadat, H., Vieira, G. (1999). Melting driven by natural convection A comparison exercise: first results. *International Journal of Thermal Sciences*, vol. 38, no. 1, p. 5–26, DOI:10. 1016/S0035-3159(99)80013-0.

[18] Talat, N., Mavrič, B., Belšak, G., Hatić, V., Bajt, S., Šarler, B. (2018). Development of meshless phase field method for two-phase flow. *International Journal of Multiphase Flow*, vol. 108, p. 169–180, DOI:10.1016/ j.ijmultiphaseflow.2018.06.003.

[19] Hatić, V., Cisternas Fernandez, M., Mavrič, B., Založnik, M., Combeau, H., Šarler, B. (2019). Simulation of a macrosegregation benchmark in a cylindrical coordinate system with a meshless method. *International Journal of Thermal Sciences*, vol. 142, p. 121–133, DOI:10.1016/j.ijthermalsci.2019.04.009.

[20] Šarler, B., Vertnik, R. (2006). Meshfree explicit local radial basis function collocation method for diffusion problems. *Computers & Mathematics with Applications*, vol. 51, no. 8, p. 1269–1282, DOI:10.1016/j.camwa. 2006.04.013.

[21] Mramor, K., Vertnik, R., Šarler, B. (2013). Low and intermediate Re solution of lid driven cavity problem by local radial basis function collocation method. *Computers, Materials & Continua*, vol. 36, no. 1, p. 1–21.

[22] Mavrič, B., Šarler, B. (2015). Local radial basis function collocation method for linear thermoelasticity in two dimensions. *International Journal of Numerical Methods for Heat & Fluid Flow*, vol. 25, no. 6, p. 1488–1510, DOI:10.1108/HFF-11-2014-0359.

[23] Hanoglu, U., Šarler, B. (2019). Hot Rolling Simulation System for Steel Based on Advanced Meshless Solution. *Metals*, vol. 9, no. 7, p. 788, DOI:10.3390/ met9070788.

[24] Lorbiecka, A. Z., Sarler, B. (2010). Simulation of Dendritic Growth with Different Orientation by Using the Point Automata Method. *CMC: Computers, Materials & Continua*, vol. 18, no. 1, p. 69–104, DOI:10.3970/cmc. 2010.018.069.

[25] Gandin, C. A., Rappaz, M. (1994). A coupled finite element-cellular automaton model for the prediction of dendritic grain structures in solidification processes. *Acta Metallurgica et Materialia*, vol. 42, no. 7, p. 2233–2246, DOI:10.1016/0956-7151(94)90302-6.

[26] Jacot, A., Rappaz, M. (2002). A pseudo-front tracking technique for the modelling of solidification microstructures in multi-component alloys. *Acta Materialia*, vol. 50, no. 8, p. 1909–1926, DOI:10.1016/ S1359-6454(01)00442-6.

[27] Raabe, D., Roters, F., Barlat, F., Chen, L.-Q., editors (2004). *Continuum Scale Simulation of Engineering Materials: Fundamentals - Microstructures - Process Applications*. Wiley-VCH, Weinheim, 1 edition edn.

[28] Gregorc, J., Šarler, B. (2018). Experimental research of recirculation zones during continuous casting by using a water model : design of experimental system. Tech. rep., LFDT, Faculty of Mechanical Engineering, Ljubljana. (In Slovene.)

Sustainability Assessment of Advanced Machining Technologies

Luka Sterle – Damir Grguraš – Matjaž Kern – Franci Pušavec*
University of Ljubljana, Faculty of Mechanical Engineering, Slovenia

Efficient cooling and lubrication techniques are required to obtain sustainable machining of difficult-to-cut materials, which are the pillars of aerospace, automotive, medical and nuclear industries. Cryogenic machining with the assistance of lubricated Liquid Carbon Dioxide (LCO$_2$) is a novel approach for sustainable manufacturing without the use of harmful water-based metalworking fluids (MWFs). In case of unavoidable use of MWFs under high pressure, such as turning finishing processes of difficult-to-cut materials, the pulsating high pressure delivery of MWFs prolongs the tool life and enables the control over chip length to prevent surface damage of high value-added parts. In this paper, sustainability assessment of both advanced principles was carried out, considering overall costs and operational safety. Experimental tests were executed on difficult-to-cut materials in comparison to conventional flood lubrication. For both techniques, longer tool life compared to flood lubrication was observed additional cleaner production and higher part quality led to reduced long-term overall costs. These advanced machining technologies are also operation safe, proving to be a sustainable alternative to conventional machining.
Keywords: cryogenic machining, high pressure machining, sustainability, cost assessment, risk assessment

Highlights
- This paper presents sustainability assessment of both cryogenic machining with the assistance of lubricated LCO$_2$ and pulsating high pressure assisted machining.
- For both cryogenic and pulsating high pressure machining, tool life tests were carried out compared to conventional flood lubrication.
- The cost analysis was performed to show the feasibility of both technologies.
- Risk assessment for operational safety of LCO$_2$ was conducted.

0 INTRODUCTION

Machining present an important step in production to achieve the final shape of a product. Although additive manufacturing technologies aim to reduce the need for material removal by cutting, demanded dimensional and surface tolerances are mainly obtainable by machining processes. Furthermore, the global consumption of natural resources and the resulting pollution are leading factors for development of sustainable technologies, which can improve machining performance on economic, social and environmental levels.

The use of metalworking fluids (MWFs) in machining processes aims to improve machinability through prolonged tool life, improved surface integrity and chip evacuation. However, their use is correlated to environmental and health hazards and can present up to 17 % of total manufacturing costs [1]. Dry cutting and Minimum Quantity Lubrication (MQL) are alternatives to conventional flood lubrication, but their application is limited, especially when difficult-to-cut materials are considered [1] to [3]. These materials, namely titanium- and nickel-based alloys are known for their high temperature resistance, high ductility and low temperature conductivity, thus resulting in poor machining performance. To counteract these effects, while

offering a cleaner and safer approach of cooling and lubrication, cryogenic machining has been under development in the last decade [4] and [5]. The most used cryogenic medium was Liquid Nitrogen (LN$_2$), which exists in liquid state at –195.8 °C and is delivered as such into the cutting zone, offering cooling mechanisms without lubrication. Moreover, due to its low temperature, lubricant cannot be added to the LN$_2$ without freezing [6]. In addition, the cooling capability of LN$_2$ is inferior to Liquid Carbon Dioxide (LCO$_2$) [7]. Low temperature of the LN$_2$ is also its disadvantage; therefore, it's delivery through spindle/turret is challenging and risky, the LN$_2$ leakage can cause serious damage to spindle/turret mechanics. Although it presents a cleaner alternative, the drawbacks of the LN$_2$ prevent its wider use in industrial sector.

Machining with the assistance of LCO$_2$ is thus becoming the focus of cryogenic machining research. The cooling mechanism here is different to liquid nitrogen; LCO$_2$ is in liquid state at 57 bar and 20 °C. Due to the decrease of the saturation pressure upon exiting the nozzle, the LCO$_2$ vaporizes and expands, absorbing heat from the surroundings. If the amount of LCO$_2$ is sufficient, the micro-region is cooled down to the boiling point of CO$_2$, –78.5 °C [6] and [8]. This phase change (from liquid to gas) is shown in Fig. 1.
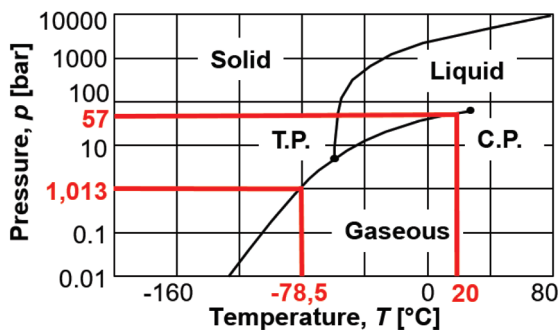
Fig. 1. *P-T phase diagram of CO_2*

As the LCO_2 is at room temperature right up to the exiting point, it can transport lubrication media with it [9]. This combination can also be denoted as LCO_2 + MQL, as the two principles are combined. State-of-the-art LCO_2 assisted machining shows promising results in terms of prolonged tool life [10] to [17], improved surface integrity [11], [13], [14], [17] and [20], lower cutting forces [13], [14], and [16] and reduced cutting temperatures compared to MQL and/ or dry machining [10], [11], [16] and [18]. However, the LCO_2 is freely released into the atmosphere, contrary to conventional MWFs, which are stored back into the reservoir. Therefore, the cost assessment is needed to economically justify the use of LCO_2 based machining processes. In addition, CO_2 concentration should be monitored, as the workplace CO_2 levels in surrounding air should not exceed 0.5 % concentration for 8-hour exposure time according to Occupational Safety and Health Administration (OSHA) [19].

Contrary, total elimination of MWFs may be hard to reach, especially when considering their benefits when delivered to the cutting zone under high pressure. In continuous cutting, such as turning or drilling, long chips can be problematic especially when machining difficult-to-cut materials. In conventional High Pressure Jet Assisted Machining (HPJAM), one or more focused and high-energetic coolant jets are delivered into the chip-forming zone, thus increasing the productivity [20] to [22], tool life [15], [20] to [23] and chip breakability [24] and [25]. Two main high pressure MWFs supply variants are shown in Fig. 2; blue arrow indicate the high pressure MWFs supply: a) between chip and rake face, b) between workpiece and flank face, or combination of a) and b) is also in use [26].

Despite the positive effects of HPJAM, the industrial application is not yet wide spread, due to: (i) High energy consumption [21], [23], and [24]; (ii) Surface anomalies by interaction between broken chips and machined surface [22], [24] and [25]; (iii)

Unpredictable behaviour of broken chips [22] and [23] and (iv) Unknown potential in wider scope [15] and [23]. Moreover, in practical applications HPJAM is still limited to roughing processes. The extension to finishing processes is desired, but currently challenging due to stated reasons. In order to address these issues, pulsating HPJAM has been proposed in collaboration with WZL, RWTH Aachen, Germany [27]. Principle of operation is presented in Fig. 3. By pulsating the high pressure jet, the high pressure is achieved only at short intervals when chip breakage and removal is required. In the meantime, the pressure is reduced to lower values only to provide the necessary cooling and lubrication with considerable savings in energy consumption. Presented pulsating HPJAM concept represents novelty in the field, wherein only few scientific studies have been found, yet all of them based on pulsating MQL [28] to [34]. Pulsating MQL does not have the same pressure nor flow rate (jet force) compared to pulsating HPJAM and therefore these two cannot be directly comparable.
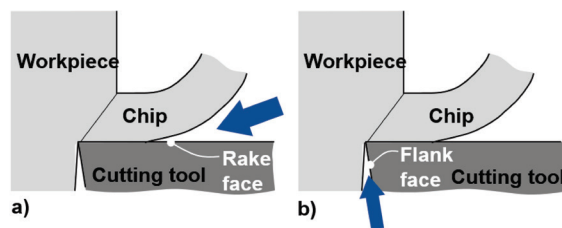
Fig. 2. *MWFs supply: a) between chip and rake face; b) between workpiece and flank face*
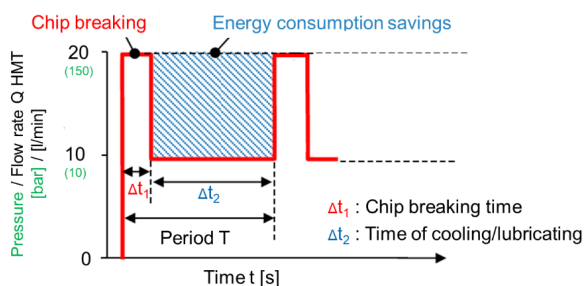
Fig. 3. *Pulsating high-pressure supply of MWFs – basic principle*

Both presented machining technologies are advanced with great research potential. In addition, both advanced principles are currently holding the status of patent pending [9] and [27]. This paper presents their performance. Therefore, the goal of this study is to: (i) Evaluate machining performance on difficult-to-cut materials; (ii) Perform cost assessment and (iii) Perform risk assessment.

1 EXPERIMENTAL PROCEDURE

1.1 LCO$_2$ + MQL Machining Experiments

Milling experiments were performed on CNC machining centre Doosan NX 6500 II with through tool delivery. Workpiece material was Ti-alloy Ti-6Al-4V (α+β). Prototype milling cutter with four 0.4 mm nozzles for LCO$_2$ + MQL mixture was used. The flow rates were 12 kg/h for LCO$_2$ and 60 ml/h for MQL oil. The principle of mixing oil into the stream of LCO$_2$ is shown in Fig. 4a. More detailed explanation of the principle can be found in [9]. Cutting parameters

are found in Fig. 5. For tool life comparison, LCO$_2$ + MQL principle was directly compared to flood lubrication, where the emulsion Blaser B-Cool 9665 with 7 % concentration was used. Same parameters and tools were used in both cases and the tool wear was monitored at specified time intervals. After the experiments, the chips were collected to study their morphology. At the same time, CO$_2$ levels in the air were monitored using Witt-Gasetechnik RLA 100 air monitor. The measurements were taken in close proximity of CNC command module, where the operator is usually located when operating the machine. Due to the nature of the expanding LCO$_2$,
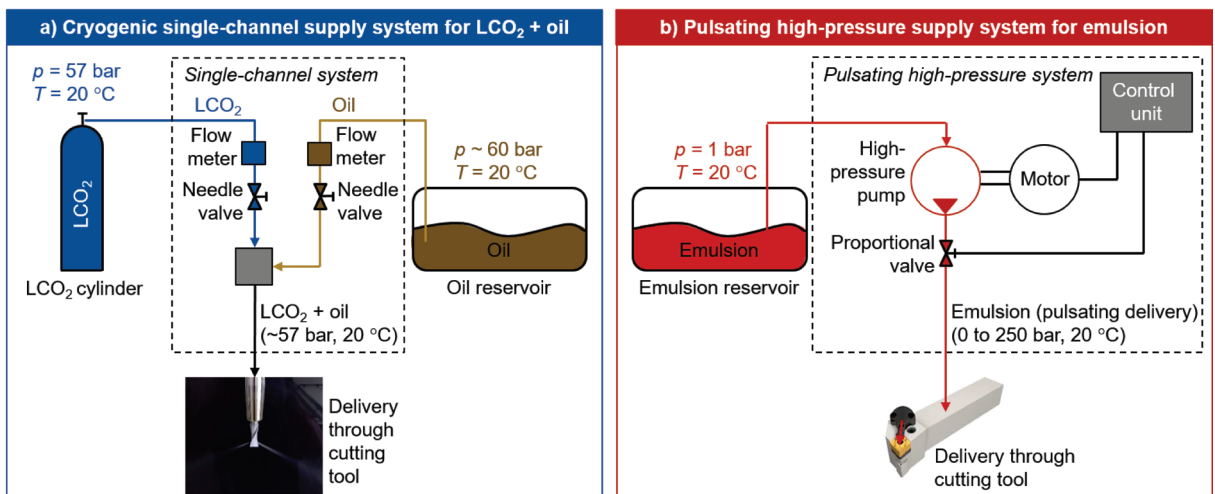
Fig. 4. *Schematic setups a) for single-channel supply of LCO$_2$+MQL; and b) pulsating HPJAM*
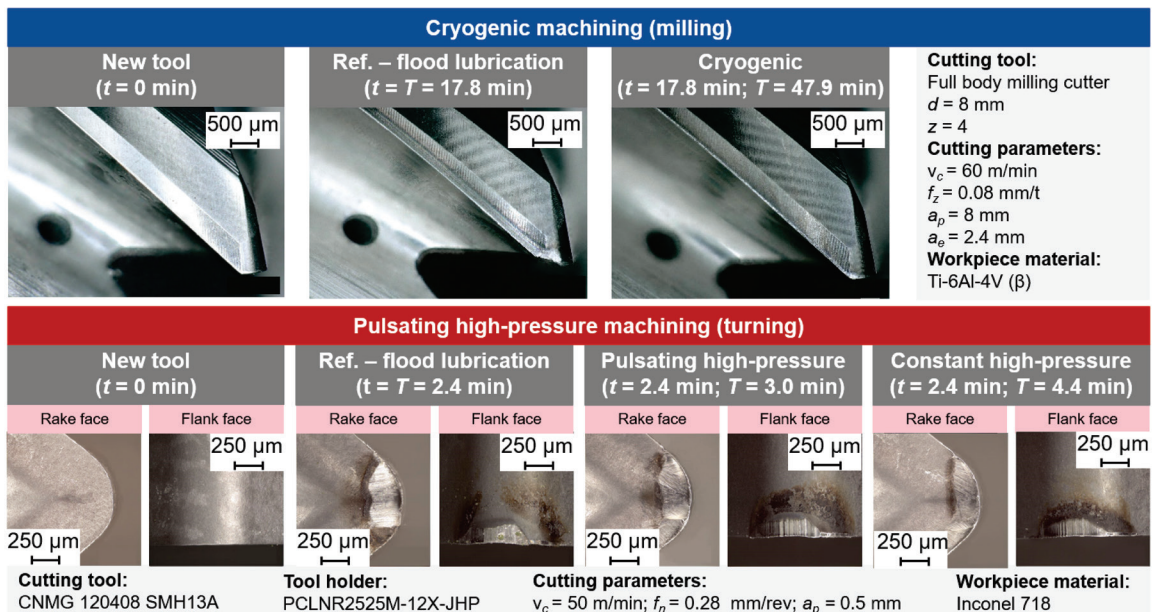
Fig. 5. *Tool wear in cryogenic machining and pulsating HPJAM (t – time; T – tool life)*

oil droplets are atomized to about 10 μm in diameter [9] and the monitoring of sufficient ventilation is necessary for risk assessment. Power consumption of single-channel supply system of LCO_2 + MQL was also monitored using multifunction instrument PowerQ MI2492.

1.2 Pulsating HPJAM Experiments

Turning experiments were performed on CNC lathe Mori Seiki SL153. Cutting parameters are found in Fig. 5. Inconel 718 was used as workpiece material and Sandvik CNMG 11408 SMH13A cutting inserts as tools. Iscar tool holder with high pressure nozzle (up to 300 bar, d = 1 mm) was used to guide the jet between the chip and the rake face (Fig. 2a). Similar as for cryogenic machining, pulsating HPJAM was compared to conventional flood lubrication (Blaser B-Cool 9665, 7 %) and conventional HPJAM. For flood lubrication, emulsion was supplied through standard 5 mm pipe under the pressure of 1 bar. Pulsating parameters were: high pressure 200 bar, low pressure 1 bar, pulsating frequency 5 Hz, (high pressure pulse time 60 ms, low pressure pulse time 140 ms). For conventional HPJAM pressure was set to same but constant value of 200 bar. Schematic presentation of the system is shown in Fig. 4b. Measured were: tool wear, chip morphology and overall power consumption using PowerQ MI2492 multifunction instrument. Emulsion atomization in machining area was also observed due to jet's high preossure. This has been evaluated based on visual observation of time needed for mist elimination.

2 RESULTS AND DISCUSSION

2.1 Tool Life Experiments

For cryogenic milling, critical flank face wear was achieved after 47.9 minutes, which is a great improvement over the time of 17.8 minutes when using flood lubrication. The criteria for worn tool was maximum flank face wear VB_{max} of 200 μm. It was also observed that the tool wear mechanism in flood lubrication was edge chipping, whereas in cryogenic machining main wear mechanism was abrasion that was evenly distributed between all four cutting edges of an end mill (Fig. 5).

Pulsating high-pressure turning experiments with same tool life criteria resulted in tool life of 3.2 minutes was reached. In comparison, tool life for flood lubrication was 2.4 minutes and for conventional high-pressure machining 4.4 minutes. Additionally to the

flank face wear, crater wear was also observed (Fig. 5). The main tool wear mechanism was abrasion, as this coincides with the machining of Inconel 718 [21].

For both techniques, every experiment was conducted two times and the average value was calculated, while the difference between the values was within 5 %.

2.2 Chip Morphology

Cryogenic machining produced similar chips to conventional flood lubrication throughout all experiments, as seen in Fig. 6. As there are no visible differences in shape and color, we can assume the cryogenic machining provides sufficient cooling and lubrication, which are critical properties for sustainability of cryogenic machining.
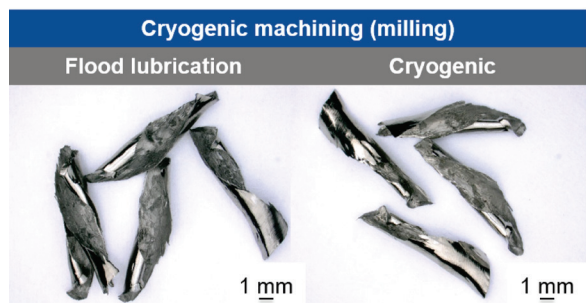
Fig. 6. *Chip morphology by using flood lubrication versus cryogenic machining*

On the other side, pulsating high-pressure had strong influence on chip morphology (Fig. 7). In conventional flood lubrication, the chips were long tubular chips. Shorter tubular chips were observed with the use of constant high-pressure machining, while the most suitable chips were produced by using pulsating HPJAM. Inconel is notorious for work-hardening and very elastic chips that are hard to break. In conventional HPJAM, sufficient pressure of coolant delivery must be achieved to break the chips [22]. From Fig. 7 we can see that the chips under constant high-pressure conditions had smaller up-curling radius compared to flood lubrication due to the high energy of the jet. However, the pressure was still not sufficient to achieve constant chip breakage. By maintaining the same pressure, but employing pulsating principle, chip breakage occurred controlably, with chips having much shorter and consistent overall length. The change in chip up-curling radius due to the impulse of the pulsating jet can be seen on the lower right side of Fig. 7. These differences imply that higher pressure is not

necessarily needed to improve chip breakability; it is also important to consider its dynamic ability of sudden impact on chip deformation and consequently, chip breakage. Additionally, the cost savings are evident as sufficient pressure of coolant supply may be lower as well as overall flow rate that is closely related to the power of the pump.
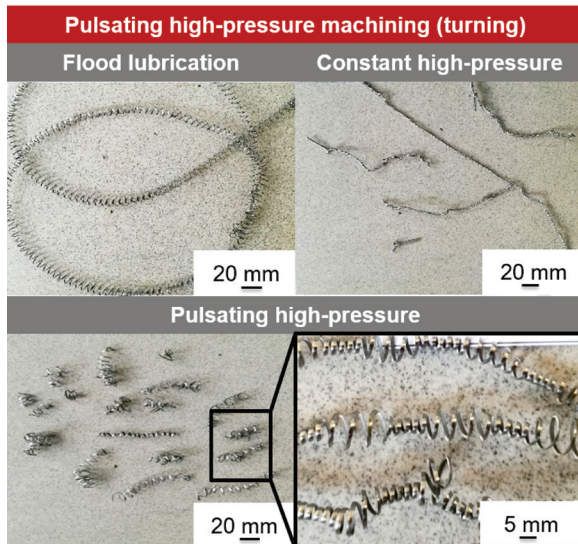
Fig. 7. *Chip morphology by using flood lubrication versus pulsating HPJAM*

Chip morphology is especially important in finishing processes. A stable process is always desired and the control over chips is a part of that. In finishing processes, the product has the greatest added value and errors in manufacturing should be avoided. In finishing turning, long chips can damage the machined surface or in worst case damage the operator or machine tool. To gain control over chip breakage, pulsating HPJAM can show great benefits while also discarding some of the disadvantages of the conventional HPJAM such as high energy consumption, surface anomalies due to chip-workpiece collisions at higher pressures and higher costs related to the equipment needed to produce higher pressure.

2.3 Cost Assessment

In machining, total manufacturing cost of a produced part is usually a sum of manufacturing overheads (salaries, property taxes, rents, machine tools, depreciation, etc.), administrative overheads (salaries, travel costs, legal fees, etc.), direct labor costs and material costs (direct and indirect). For the purpose of this paper, the cost assessment is focused on indirect material cost as we assume that the manufacturing and administrative overheads as well as direct labour and material costs are constant, regardless of the cooling and lubrication technique.

Indirect material costs in this case are related to the purchase, maintenance and disposal costs of MWFs (emulsion), C_{MWF}, to the purchase of LCO_2 and MQL oil, C_{CRYO}, to the electrical consumption, C_{EL}, and to the cutting tool costs, C_{TOOL}. The cost of the system purchase and installation is separately included (C_{SYS}). In addition, t_{TOOL} presents tool lifetime as described in section 2.1, where the time of 5 minutes has been added as a tool change time. For turning operation, this combined time has been additionally multiplied by 4, as there are four usable cutting edges on each insert. 3840 working hours per year (20 days, two working shifts) were considered for this calculation; working hours are denoted as t_{WORK}. Down time of the machine was not included in this study. Cryogenic consumptions, Q_{CRYO}, are the flow rates of both LCO_2 and MQL oil as mentioned in section 1.1, and cryogenic costs, C_{CRYO}, are based on their market price.

Measured electrical power in kW was multiplied by 0.20 €/kWh, the approximate European average price. Average power consumption when cryogenic machining was approximately 0.4 kW due to innovative and patented principle of using the pressure energy of LCO_2 to inject the oil in its flow [9]. Flood lubrication used on average 0.75 kW, conventional high-pressure 8 kW and pulsating high-pressure 3 kW of electricity. The energy consumption ratio of 0.38 between pulsating high-pressure and conventional high-pressure is close to theoretical ratio of 0.43, calculated by using high and low pressure pulse times of 60 ms and 140 ms, respectively.

The total cost, C_{TOT}, for the first year of running, based on Fig. 8, can be expressed as:

$$C_{TOT} = C_{MWF} + C_{SYS} + (C_{EL} + C_{TOOL}/t_{TOOL} + C_{CRYO} \cdot Q_{CRYO}) \cdot t_{WORK}. \quad (1)$$

Total annual costs for both advanced machining methods in comparison to conventional techniques are shown in Fig. 9. It can be observed that cost reduction of 44.7 % is possible by the implementation of cryogenic machining instead of conventional flood lubrication. The difference would be even greater in favor of cryogenic machining if costs related to part cleaning due to emulsion contamination were considered. According to Eq. (1), the most influential factor is the tool cost, especially due to short tool life as a result of machining of difficult-to-cut material.

Cryogenic machining (milling)		
	Flood lubrication	**Cryogenic machining**
Tool costs C_{TOOL}	Full body end mill – 100 €/tool	
Emulsion costs C_{MWF}	600 €/year	/
Cryogenic costs C_{CRYO}	/	LCO$_2$: 1.13 €/kg; oil 8 €/kg
Electrical power C_{EL}	0.15 €/hour	0.08 €/hour
System installation costs C_{SYS}	/	50.000 €
Tool life time (tool life + change) t_{TOOL}	0.4 hour/tool	0.9 hour/tool
Cryogenic consumption Q_{CRYO}	/	LCO$_2$: 12 kg/hour; Oil: 0.05 kg/hour
Work hours per year t_{WORK}	3840 hours	

Pulsating high-pressure machining (turning)		
	Flood lubrication	**Pulsating high-pressure**	**Constant high-pressure**
Tool costs C_{TOOL}	CNMG 120408 SMH13A cutting insert (4 cutting edges), 5 €/tool		
Emulsion costs C_{MWF}	600 €/year		
Electrical power C_{EL}	0.15 €/hour	0.6 €/hour	1.6 €/hour
System installation costs C_{SYS}	/	15.000 €	5.000 €
Tool life time (tool life + change) t_{TOOL}	0.25 hour/tool	0.29 hour/tool	0.38 hour/tool
Work hours per year t_{WORK}	3840 hours		

Fig. 8. *Operational costs for cryogenic machining and pulsating HPJAM*
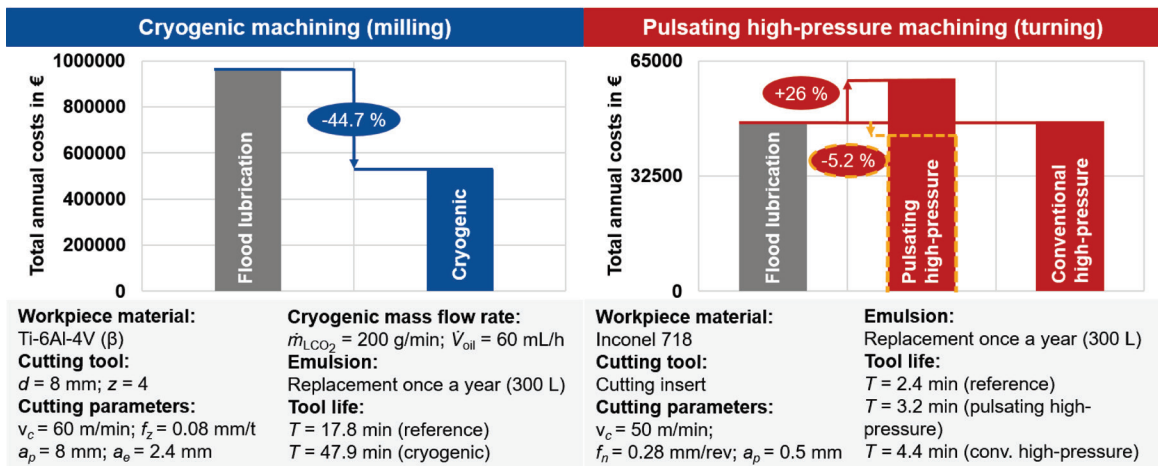
Fig. 9. *Calculation of total annual costs for cryogenic machining and pulsating HPJAM*

The second most influential factor is the cost of LCO$_2$. As it is non-renewable, its consumption should be optimised in order to achieve optimal cutting temperature at lowest possible flow rate, as also discussed in [7].

On the other side, pulsating high-pressure showed highest costs between all three principles; with the 26 % increasement in costs over the flood lubrication. The tool cost is by far the most important factor of the total annual cost. Conventional high-pressure costs were almost identical to those of flood lubrication. However, the system installation costs are also included in the calculation. Assuming little to no maintenance to high-pressure systems, the cost savings would be evident on the 2nd year of use. If the system installation costs are excluded, the use of pulsating high-pressure technique results in roughly 5.2 % reduced annual costs compared to flood lubrication, shown with yellow dashed line in Fig. 9. The use of conventional high-pressure results in 9.2 % reduction if installation costs are not considered.

Although the initial costs for installation of pulsating high-pressure system are high, apart from longer tool life, other benefits can be visible. One

such example is shown in Fig. 10 where turning of AISI 4142 alloy under flood lubrication led to long, continuous chips which wrapped around the workpiece, causing the damage to the workpiece and production delay. The main advantage of pulsating principle, over conventional high-pressure machining, is the ability to precisely control the chip length. If chips are tool short they can partially absorb the energy of the high-pressure jet and fly with high velocity in unpredictable directions. This means that there is a high probability they will collide with the workpiece, causing collision anomalies on the already machined surface. This can be avoided by pulsating, so the chips have time to reach critical length at which they present the least risk to overtake high speed from emulsion jet.

Fig. 10. *Continuous chips wrapped around workpiece when turning AISI4142 alloy*

2.4 Risk Assessment

During cryogenic machining, CO_2 levels in the air, near vicinity of the machining area, did not exceed the OSHA prescribed value of 0.5 % (Fig. 11). However, it was observed that adequate suction and air filtration is needed to remove oil mist from the machining area. As described in section 1.1, LCO_2 atomizes the oil into small particles. The current OSHA prescribed maximum level of oil mist in air is 5 mg/m^3 as an 8-hour time-weighted average [19]. Workplace exposure to MWFs can lead to various health problems such as dermatitis, respiratory problems or even several types of cancer if the exposure is long-term [35]. Workplace measurements of the oil mist in air concentration are still scarce and further work is needed. By using the

LCO_2 + MQL principle, the machining area should be an enclosed space with sufficient suction and ventilation to remove as much oil mist as possible before human intervention into the machining area occurs (workpiece clamping, tool replacement, etc.).
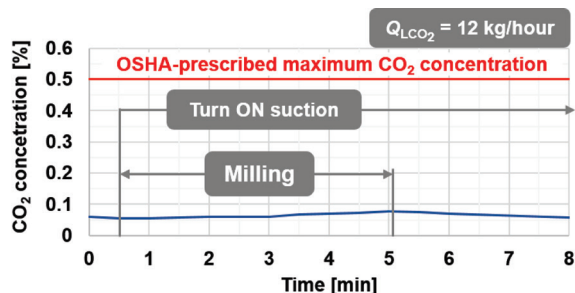
Fig. 11. *Cryogenic machining: CO_2 in air concentration at CNC command module*

Using the high-pressure cooling and lubrication principle results also in emulsion atomization. It has been observed that the total time for mist elimination after machining has been reduced by approx. 30 % when using pulsating high-pressure principle, compared to conventional high-pressure method where demisting happened after approx. 20 seconds. This time was determined solely on visual examination of the machining area through the door window. Further work with precise instruments to measure workplace air quality is needed. In conventional high-pressure machining short chips with high velocity present a threat to the operator if machining area is not an enclosed space. On the other side, continuous chips as shown in Fig. 10 are also dangerous due to sharp edges and unpredictable behaviour. Thus, pulsating high-pressure principle may reduce the risk of workplace injury due to unsuitable chips.

3 CONCLUSIONS

Two advanced machining technologies, i.e. cryogenic machining using lubricated LCO_2 and pulsating HPJAM, were presented and their sustainability was estimated over: (i) tool life; (ii) chip morphology; (iii) cost assessment and (iv) risk assessment. Main conclusions can be drawn, as follows.

- Cryogenic machining using LCO_2 + MQL and pulsating HPJAM exhibit prolonged tool life of 169 % and 33 %, respectively, in comparison to conventional flood lubrication.
- No major difference in chip morphology was observed in cryogenic machining compared to flood lubrication. On the other hand, pulsating

HPJAM offered superior control over chip shape and size compared to both conventional flood lubrication and HPJAM.

- Transition to cryogenic machining reflects in 44.7 % lower running costs compared to conventional flood lubrication due to significantly longer tool life (+169 %). Both conventional and pulsating HPJAM offer lower running costs by 9.2 % and 5.2 %, respectively, compared to conventional flood lubrication.

- Cryogenic machining represents risk-free advanced machining technology if suitable safety measurements are met, such as enclosed machining area and appropriate ventilation. In such running conditions, CO_2 concentration near the machine tool is significantly lower than OSHA-prescribed maximum concentration. For pulsating HPJAM, approx. 30 % time reduction for mist elimination was achieved; however, bigger risk reduction impact using pulsating technology presents ability to precisely control the chip length. Moreover, future work will feature mist analysis (mist size and distribution) in the workplace zone for both cryogenic and pulsating high-pressure technologies.

4 ACKNOWLEDGEMENTS

5 REFERENCES

[1] Klocke, F., Eisenblätter, G. (1997). Dry cutting. CIRP Annals, vol. 42, no. 2, p. 519-526, **DOI:10.1016/S0007-8506(07)60877-4**.

[2] Byrne, G., Dornfeld, D.A., Denhkena, B. (2003). Advancing cutting technology. *CIRP*, vol. 52, no. 2, p. 483-507, **DOI:10.1016/S0007-8506(07)60200-5**.

[3] Weinert, K., Inasaki, I., Sutherland, J.W., Wakabayashi, T. (2004). Dry machining and minimum quantity lubrication. *CIRP Annals*, vol. 53, no. 2, p. 511-537, **DOI:10.1016/S0007-8506(07)60027-4**.

[4] Jawahir, I.S., Attia, H., Biermann, D., Duflou, J., Klocke, F., Meyer, D., Newman, S.T., Pušavec, F., Putz, M., Rech, J., Schulze, V., Umbrello, D. (2016). Cryogenic manufacturing processes. *CIRP Annals*, vol. 65, no. 2, p. 713-736, **DOI:10.1016/j.cirp.2016.06.007**.

[5] Pušavec, F., Krajnik, P., Kopač, J. (2010). Transitioning to sustainable production – part I: application on machining technologies. *Journal of Cleaner Production*, vol. 18, no. 2, p. 174-184, **DOI:10.1016/j.jclepro.2009.08.010**.

[6] Courbon, C., Pušavec, F., Dumont, F., Rech, J., Kopač, J. (2013). Tribological behavior of Ti6Al4V and Inconel 718 under dry and cryogenic conditions–Application to the context of machining with carbide tools. *Tribology International*, vol. 66, p. 72-82, **DOI:10.1016/j.triboint.2013.04.010**.

[7] Pušavec, F., Grguraš, D., Koch, M., Krajnik, P. (2019). Cooling capability of liquid nitrogen and carbon dioxide in cryogenic milling. *CIRP Annals*, vol. 68, no. 1, p. 73-76, **DOI:10.1016/j.cirp.2019.03.016**.

[8] Kramer, A. (2015). *Gestaltungsmodell der kryogenen Prozesskühlung in der Zerspanung*. Apprimus Verlag, RWTH Aachen University, Aachen. (in German)

[9] Grguraš, D., Sterle, L., Krajnik, P., Pušavec, F. (2019). A novel cryogenic machining concept based on a lubricated liquid carbon dioxide. *International Journal of Machine Tools and Manufacture*, vol. 145, ID 103456, **DOI:10.1016/j.ijmachtools.2019.103456**.

[10] Cordes, S., Hübner, F., Schaarschmidt, T. (2014). Next generation high performance cutting by use of carbon dioxide as cryogenics. *Procedia CIRP*, vol. 14, p. 401-405, **DOI:10.1016/j.procir.2014.03.091**.

[11] Jerold, B.D., Kumar, M.P. (2012). Experimental comparison of carbon-dioxide and liquid nitrogen cryogenic coolants in turning of AISI 1045 steel. *Cryogenics*, vol. 52, no. 10, p. 569-574, **DOI:10.1016/j.cryogenics.2012.07.009**.

[12] Bergs, T., Pušavec, F., Koch, M., Grguraš, D., Döbbeler, B., Klocke, F. (2018). Investigation of the solubility of liquid CO_2 and liquid oil to realize an internal single channel supply in milling of Ti6Al4V. *Procedia Manufacturing*, vol. 33, p. 200-207, **DOI:10.1016/j.promfg.2019.04.024**.

[13] Hanenkamp, N., Amon, S., Gross, D. (2018). Hybrid supply system for conventional and CO_2/MQL-based cryogenic cooling. *Procedia CIRP*, vol. 77, p. 219-222, **DOI:10.1016/j.procir.2018.08.293**.

[14] Patil, N.G., Asem, A., Pawade, R.S., Thakur, D.G., Brahmankar, P.K. (2014). Comparative study of high speed machining of Inconel 718 in dry condition and by using compressed cold carbon dioxide gas as coolant. *Procedia CIRP*, vol. 24, p. 86-91, **DOI:10.1016/j.procir.2014.08.009**.

[15] Cayli, T., Klocke, F., Lung, D. (2014). The Influence of high-pressure lubricoolant supply variant on cutting performance in turning of 42CrMo4+QT. *Advances in manufacturing technology: 11th International Conference High Speed Machining*, Praque.

[16] Supekar, S.D., Clarens, A.F., Stephenson, D.A., Skerlos, S.J. (2012). Performance of supercritical carbon dioxide sprays as coolants and lubricants in representative metalworking operations. *Journal of Materials Processing Technology*, vol. 212, no. 12, p. 2652-2658, **DOI:10.1016/j.jmatprotec.2012.07.020**.

[17] Wika, K.K., Litwa, P., Hitchens, C. (2019). Impact of supercritical carbon dioxide cooling with minimum quantity lubrication on tool wear and surface integrity in the milling of AISI 304L stainless steel. *Wear*, vol. 426-427, p. 426-427, **DOI:10.1016/j.wear.2019.01.103**.

[18] Augspurger, T., Koch, M., Klocke, F., Döbbeler, B. (2019). Investigation of transient temperature fields in the milling cutter under CO_2 cooling by means of an embedded thermocouple. *Procedia CIRP*, vol. 79, p. 33-38, **DOI:10.1016/j.procir.2019.02.007**.

[19] United States Department of Labor. Occupational Safety and Health Administration (OSHA), from *https://www.osha.gov/dsg/annotated-pels/tablez-1.html*, accessed on 2019-09-19.

[20] Klocke, F., Lung, D., Kramer, A., Cayli, T., Sangermann, H. (2013). Potential of modern lubricoolant strategies on cutting performance. *Key Engineering Materials*, vol. 554-557, p. 2062-2071, **DOI:10.4028/www.scientific.net/KEM.554-557.2062**.

[21] Pušavec, F., Kramar, D., Kenda, J., Krajnik, P., Kopač, J. (2009). Experimental analysis of sustainability in machining of Inconel 718. *Proceedings of the 42nd CIRP Conference on Manufacturing Systems.*

[22] Courbon, C., Kramar, D., Krajnik, P., Pušavec, F., Rech, J., Kopač, J. (2009). Investigation of machining performance in high-pressure jet assisted turning of Inconel 718: An experimental study. I*nternational Journal of Machine Tools and Manufacture*, vol. 49, no. 14, p. 1114-1125, **DOI:10.1016/j.ijmachtools. 2009.07.010**.

[23] Klocke, F. (2011). *Manufacturing Processes 1: Cutting*. Springer Verlag, RWTH Aachen University, Aachen.

[24] Sangermann, H. (2013). *Hochdruck-Kühlschmierstoffzufuhr in der Zerspanung*. Apprimus Verlag, RWTH Aachen University, Aachen. (in German)

[25] Cayli, T., Klocke, F., Veselovac, D. (2015). Effect of Jet Guidance Geometries in turning of aerospace materials with High-Pressure Lubricoolant Supply. RWTH Aachen University, Aachen, from *https://core.ac.uk/download/pdf/36662783.pdf*, accessed on 2019-09-19.

[26] Cayli, T. (2017). *Surface Anomalies in Turning of Difficult-To-Cut Materials with High-Pressure Coolant Supply*. Apprimus Verlag, RWTH Aachen University, Aachen.

[27] Cayli, T., Klocke, F., Döbbeler, B., Pušavec, F., Bernstorff, O. (2016). *Patent applied DE 102016119852.8 Verfahren und Anordnung zur Zufuhr eines Kühlfluids hin zu einer Bearbeitungsstelle eines metallischen Werkstücks*. RWTH Aachen University, Aachen. (in German)

[28] Varadarajan, A.S., Philip, P.K., Ramamoorthy, B. (2002). Investigations on hard turning with minimal cutting fluid application (HTMF) and its comparison with dry and wet turning. *International Journal of Machine Tools and Manufacture*, vol. 42, no. 2, p. 193-200, **DOI:10.1016/S0890-6955(01)00119-5**.

[29] Thepsonthi, T., Hamdi, M., Mitsui, K. (2009). Investigation into minimal-cutting-fluid application in high-speed milling of hardened steel using carbide mills. *International Journal of Machine Tools and Manufacture*, vol. 49, no. 2, p. 156-162, **DOI:10.1016/j.ijmachtools.2008.09.007**.

[30] Zhang, S., Liao, Z., Chen, D. (2011). Pulsed cutting fluid improved machining process. *Journal of the Chinese Institute of Engineers*, vol. 34, no. 2, p. 233-237, **DOI:10.1080/02533 839.2011.565584**.

[31] Bashir, M.A., Mia, M., Dhar, N.R. (2015). Effect of pulse jet MQL in surface milling of hardened steel. *Journal of Mechanical Engineering*, vol. 45, no. 2, p. 67-72, **DOI:10.3329/jme.v45i2.28118**.

[32] Gnanadurai, R.R., Varadarajan, A.S. (2016). Investigation on the effect of cooling of the tool using heat pipe during hard turning with minimal fluid application. *Engineering Science and Technology, an International Journal*, vol. 19, no. 3, p. 1190-1198, **DOI:10.1016/j.jestch.2016.01.012**.

[33] Gnanadurai, R.R., Varadarajan, A.S. (2014). Investigation on the effect of an auxiliary pulsing jet of water at the top side of chip during hard turning of AISI 4340 steel with minimal fluid application. *International Journal of Precision Engineering and Manufacturing*, vol. 15, no. 7, p. 1435-1441, **DOI:10.1007/s12541-014-0488-5**.

[34] Sam Paul, P., Varadarajan, A.S., Gnanadurai, R.R. (2016). Study on the influence of fluid application parameters on tool vibration and cutting performance during turning of hardened steel. *Engineering Science and Technology, an International Journal*, vol. 19, no. 1, p. 241-253, **DOI:10.1016/j.jestch.2015.07.017**.

[35] Wlaschitz, P., Höflinger, W. (2007). A new measuring method to detect the emissions of metal working fluid mist. Journal of Hazardous Materials, vol. 144, no. 3, p. 736-741, **DOI:10.1016/j.jhazmat.2007.01.104**.

Pulses on Demand in Fibre and Hybrid Lasers

Rok Petkovšek[1,*] – Vid Agrež[1] – Jaka Petelin[1] – Luka Černe[1] – Udo Bünting[2] – Boštjan Podobnik[3]

[1]University of Ljubljana, Faculty of Mechanical Engineering, Slovenia
[2]LPKF Laser & Electronics AG, Germany
[3]LPKF Laser & Electronics d.o.o., Slovenia

This paper presents an investigation of pulse-on-demand operation in fibre and hybrid lasers. Two methods for efficient gain control that enable the generation of laser pulses at arbitrary times with controlled pulse parameters are presented. The method of direct modulation of the pump power in the high-power laser oscillator is shown to generate pulses with a duration in the nanosecond range, with repetition rates varying during operation from a single shot to over 1 MHz. An advanced method using a combination of marker and idler seeding a fibre amplifier chain is investigated. Such a system can easily achieve repetition rates of several tens of MHz. The lasers' performances were successfully tested in a real environment on an industrial platform for laser transfer printing. Similar concepts were used for a laser source with ultrashort laser pulses (femtosecond range) on demand by using a mode-locked seed as a source and a solid-state amplifier to achieve high pulse energy and peak power.
Keywords: pulse on demand, fibre lasers, gain control, arbitrary repetition rate

Highlights
- *Pulse-on-demand operation of fibre lasers was demonstrated.*
- *Different approaches to gain control and pulse stabilization are presented.*
- *The advanced concept of pulse on demand spanning from nanosecond to fs is realized.*
- *The application of the pulse-on-demand laser for laser transfer printing is demonstrated.*

0 INTRODUCTION

Where there is a need for high-precision manufacturing processes, laser-based tools are used. With the demands for increasing production throughput and also for the capability of handling different processes with the same tool, the need for highly flexible laser systems, capable of processing advanced patterns and structures at high speeds, has emerged. This imposes stringent requirements on two key components of a laser processing unit, i.e., the laser-beam scanning system and the laser source. The purpose of the scanning system is to deliver high-speed scanning of the laser beam over the workpiece, while the laser source must meet the requirements for high beam quality, efficiency, ease of maintenance, and rapid laser-power modulation, matching that of the laser-beam scanning system. The latter enables custom pattern generation and precise synchronization with the scanning system.

Fast laser beam steering over the workpiece can be achieved, for example, by using polygon scanners, [1] resonant scanners, [2] or an acousto-optics deflector (AOD) [3] and [4]. An AOD allows precise laser scanning with high resolution but is usually limited to a small working area. For larger working areas and very high scanning speeds, the first two scanning elements are therefore normally used.

State-of-the-art polygon scanners can achieve laser-beam scanning speeds over the workpiece in the range of km/s; however, they are limited to constant scanning speeds. This means that with conventional laser sources which can only operate at a constant repetition rate, it is only possible to produce equidistant structures on the workpiece. To take advantage of the high scanning speed that the polygon scanners offer and still produce arbitrarily spaced structures, the laser source must be capable of operating at continuously variable repetition rates; thus, generating arbitrary output patterns. Such laser sources are said to deliver pulses-on-demand.

Resonant scanners have a similar disadvantage. The scanning angle and, consequently, the position of the laser beam on the workpiece follows the nonlinear response (sinusoidal oscillation) of the scanner's mirror. This nonlinear response makes it difficult to synchronize the scanning system with the laser source. As previously mentioned, only an advanced laser source capable of delivering pulses-on-demand can overcome this problem.

In the literature, we can find different methods for pulse-on-demand laser operation. Laser sources producing variable pulses on a nanosecond scale are usually based on a continuous wave (CW) or fixed-repetition-rate laser [5] and use an external electro-optical modulator (EOM) or acousto-optical modulator (AOM) [6] to modulate the laser output in

such a way that the desired pulse shape or pattern is achieved [7]. In some laser-processing applications the output laser head is also moved over a larger workpiece (e.g., batch processing) which can put a limit on the size and weight of the laser head. Also, external modulators are usually polarization-sensitive, have limited damage thresholds and in the case of AOM also limited modulation speed, especially when used in a high-power laser system.

With the development of high-power diode lasers, another approach has been made possible. The direct modulation of high-power laser-diode lasers enables lightweight laser-head designs; however, a major downside is the much lower beam quality, when compared to single-mode or nearly-single-mode (few-mode) lasers.

The high modulation bandwidth of high-power diode lasers that are used for pumping the laser system allows for the gain switching technique [8] to [10] to be used, where we can achieve good control over the pulse-generation dynamics and consequently enable pulse-on-demand operation for nearly single-mode beam quality. The gain-switching technique uses modulation of the pump power (provided by the high-power diode lasers) to select only the first spike of the relaxation oscillations that form a single laser pulse [11]. With precise gain control pulses as short as 28 ns [12] were generated from a ytterbium-doped fibre laser and the achievable (but not limited to) peak power was over 4 kW [13]. Even shorter laser pulses [14] were generated by a more complicated core-pumping scheme in a thulium-doped fibre. Using clad pumping at 790 nm, an efficient system [15] can be realized, which also has the benefit of not being susceptible to the photodarkening effect [16], which usually causes problems in highly pumped fibre lasers.

Gain-switched lasers can be designed without any modulators and can work in a wide range of spectral regions depending on the active dopant and the substrate used. Using thulium- and holmium-doped fibres, a gain-switched laser operating at wavelengths up to 2.1 μm was realized [17]. On the other hand, using an erbium-doped fluoride fiber [18], pulses at 2.8 μm were generated.

The laser pulses generated at arbitrary repetition rates with a duration of several 10 s of nanoseconds and peak power in the kilowatt range are suitable for applications such as direct colour marking, micromachining, laser-transfer printing, selective photocoagulation, etc. In contrast, such pulses are too long to achieve cold ablation [19], where bursts of picosecond pulses [20] and [21] are used to efficiently ablate the material, supercontinuum generation [22]

or applications for which high-speed, high-resolution micromachining is required.

To address this requirement for shorter pulses, an advanced laser setup using the gain control of its amplifier stages can be employed to mitigate the transients in the output pulse train when changing the repetition rate of the laser. The pump power modulation [23] can be used, but it can lead to relatively slow response times and, in some cases, must include an advanced thermal management control for pump-wavelength stabilization [24]. The solution that offers laser-pulse generation with a true pulse-on-demand mode uses a combination of idler and marker sources that seed the laser's amplifier chain. The idler signal keeps the gain of the amplifiers constant between marker pulses [25] to [27]. The benefit of this approach is also that the controlled idler signal prevents the build-up of the amplified spontaneous emission (ASE) and enables the formation of marker pulses at very low repetition rates. At the output of the amplification stages, the idler and marker light must be separated so that only the marker signal is sent to the workpiece.

There are two main techniques for marker and idler separation. One is to use either polarization or wavelength filtering, where the idler and marker have either orthogonal polarization or slightly different wavelengths [28] and the filtering can be achieved by a polarizer or a Bragg grating respectively [26] and [27]. The other technique is to use nonlinear filtering, which is more suitable for applications in which the system generates very short marker pulses while the idler seeds the amplifiers with low-power long-duration pulses (or CW power) in between the marker pulses. The nonlinear filtering is then realized at the laser output by second harmonic generation (SHG) [29] and [30].

In this paper, we present a compact (using the already-mentioned gain-switching technique) and an advanced (using marker and idler seeding) laser sources, both capable of producing pulses on demand with the ability to efficiently synchronize with the high-speed polygon and resonant scanners for covering different laser applications. Their capabilities are analysed, and the application of laser transfer printing (LTP) in the form of a laser-induced forward transfer (LIFT) is demonstrated.

1 METHODS

The output power of lasers is stable when operated under constant conditions, i.e., either continuous wave operation or operation at a fixed repetition rate. In both cases, a steady state is reached in the laser-

gain media. Changing the repetition of the laser pulses causes the laser to transit to a new steady state, which can be seen as the output-power fluctuation. Driving the laser in the pulse-on-demand operation mode with long pauses between the output pulses results in the active ion inversion population reaching high levels and consequently the production of giant pulses that can exceed the damage thresholds of the laser's optical elements. In contrast, when switching to high repetition rates, the inversion population in the gain media gradually decreases, and laser pulses with a lower peak power are generated. This effect can also be observed in lasers producing bursts of pulses [31] and can be addressed by reshaping the input seed burst so that the output burst consists of pulses with equal peak powers [32].

In this paper, two methods are presented (Fig. 1) that can efficiently control the level of inversion between the laser pulses and, as such, enable pulse-on-demand operation with stable pulse parameters decoupled from the effect of changing the repetition rate. One is the gain control in which the pump power is modulated to generate the desired marker pulses from a high power laser oscillator. The other is using a combination of marker and idler seeding in a MOPA (Master Oscillator Power Amplifier) amplifying a chain pumped with constant power.

1.1 Gain Control via Pump-Power Modulation

Gain control with pump modulation can be used in laser-amplifier chains or in a laser oscillator. The latter is more suitable for high-power oscillator laser systems and is based on the precise pump energy input before the marker pulse formation. The compact system can be realized with the gain-switching technique that can operate over a broad range of repetition rates [33].

The generated pulses are dependent on the pump rate and typically have a ratio of laser peak power to pump peak power equal to ten to one. The duration of the generated laser pulses is dependent on the oscillator's parameters, mainly its length and pump absorption. Combining the oscillator with the pump recovery amplifier [34] enables pulse-duration tuning by at least a factor of two [35].

Upgrading this architecture with an improved pumping source using high-power pump diode lasers providing the high peak pump power needed for the marker pulse formation and low average pump power between these pulses for loss compensation enables building a pulse-on-demand laser. The losses that have to be compensated in this way are mainly the result of the spontaneous emission, which depletes the inversion population during long pauses between the marker pulses. Because all the control and gain compensation are done by the laser's pump system,
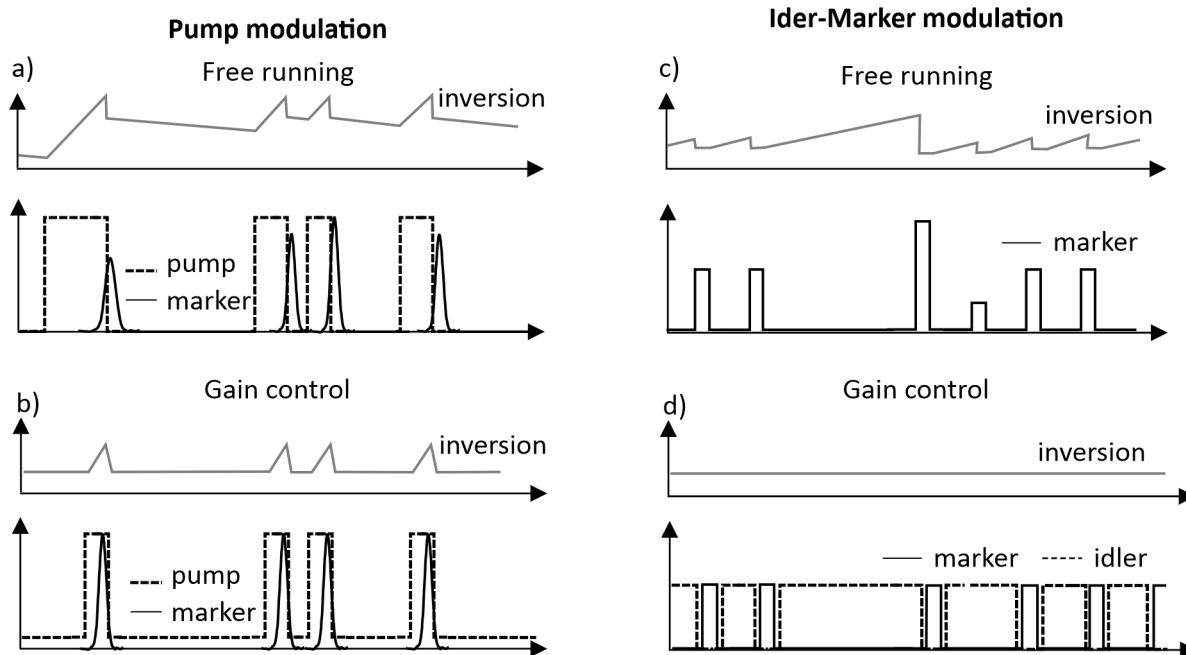
Fig. 1. *Comparison of two methods: a) and b) pump-modulation method for high-power oscillator setup, and c) and d) idler-marker seeds for MOPA-based laser systems; in a) and c) the free-running laser output and inversion at arbitrary repetition rate are shown while in b) and d) the corresponding gain control is used*

this enables a compact and cost-effective way of producing pulses on demand when the target marker pulse duration is varied in the nanosecond region.

1.2 Gain Control via idler and marker Seeds

For generating picosecond or even femtosecond pulses on demand, gain control using the idler and marker seeds is usually required. Such a laser replaces the pump recovery amplifier with at least one separately pumped amplifying stage. The goal of the idler seed is to prevent the population inversion reaching high values and, as a consequence, gain build-up, which would cause transients when switching on the laser marker signal. The idler is then filtered out after the last amplifying stage.

The combination of two seed-laser diodes with wavelengths separated by 1 nm was used in a laser setup to generate pulses on demand in the so-called quasi-CW mode of operation. At the output of the laser, a volume Bragg grating was used to filter out the idler signal. The laser is capable of modulating the full 200 W of output power with a bandwidth of several 10 s of MHz, producing stable marker pulses with a duration from 50 ns to CW [26].

The marker seed-laser diode can be exchanged with a mode-locked laser seeder to expand the marker pulse duration tuning into the ultrashort pulse domain. Here one must take care as the energy of the ultrashort pulses in the last amplifying stage causes unwanted nonlinear effects that can damage the laser system. For this, a cost-effective solution is to upgrade the pulse-on-demand laser setup with a solid-state gain crystal that replaces the last power-amplifying stage and shortens the nonlinear interaction length. With this, the threshold for the onset of nonlinear phenomena is greatly increased due to the larger mode field diameter when compared to the fibre power amplifier. This makes possible the production of high-energy picosecond pulses in the pulse-on-demand operation mode.

2 EXPERIMENTAL

Three proof-of-concept experimental setups were built to test the operation of the previously mentioned pulse-on-demand lasers. A compact gain-switched fibre laser setup covering the kW peak-power range and nanosecond pulses was built while the advanced setup using a double seeded MOPA fibre laser architecture was used for tests performed over a wider duration tuning range of marker pulses. The latter was also tested on a commercial laser transfer printing system.

Furthermore, the advanced setup was upgraded with a solid-state amplifier and a mode-locked marker seed to generate picosecond pulses on demand.

2.1 Compact Setup

A compact pulse-on-demand laser based on a highly adaptable gain-switched fibre laser was realized by using an advanced pump system in a ytterbium-doped fibre oscillator and a pump-recovery amplifier. The oscillator and the pump-recovery amplifier are both pumped by the same pump system and thus retain a low complexity. The advanced pump system consisted of a primary and a secondary pump module. The primary module generated high-power pump pulses with a duration from 500 ns to 1 μs serving as the main energy source for forming the marker pulses in the fibre oscillator. The secondary pump module, operating at a constant pump power of around 1 W, counteracted the losses to the population inversion caused by the spontaneous emission. Switching the pump power from a high to a low value, thus selecting only the first spike of the relaxation oscillation, an arbitrary marker pulse pattern was achieved. The repetition rate could be varied on the fly from a single pulse to above 1 MHz. The average power achieved was over 20 W, and the peak power was around 1 kW. The experimental setup shown in Fig. 2 proved the feasibility of a compact pulse-on-demand laser concept and the possibility for further power scaling.

2.2 Advanced Setup

The advanced setup used two seed laser diodes (marker and idler), which were wavelength-separated by 1 nm. The marker generated a selected pattern of pulses with a continuously variable repetition rate and pulse duration, while the idler was used to maintain a constant seeding power to the fibre amplifiers at all times, preventing gain build-up between the marker pulses. This made it possible to use a continuous pumping of the amplifiers, preventing the slow response of the pump to affect the overall dynamic performance of the system.

Two fibre amplifiers (Fig. 3) were used to reach 200 W of output power, and a volume Bragg grating (VBG) was used to filter out the idler signal, which was sent into a beam dump. The laser was capable of modulating the full 200 W of output power with a bandwidth of several 10 s of MHz, and both the output power and modulation bandwidth are further scalable; however, in our case, the laser generated stable pulses with 200 W of power and a duration from a few 10
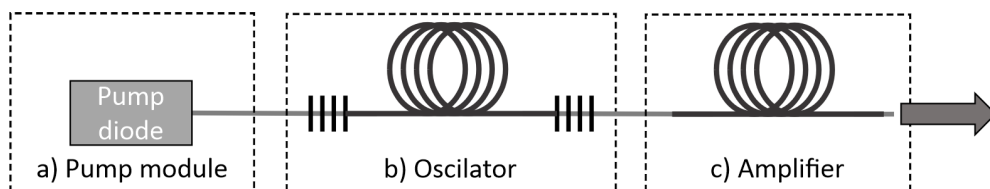
Fig. 2. *A compact setup for pulse-on-demand generation based on the gain-switching technique; the pump module a) is used to pump the b) oscillator and c) amplifier; modulation of the pump power in time allows for pulse-on-demand operation*
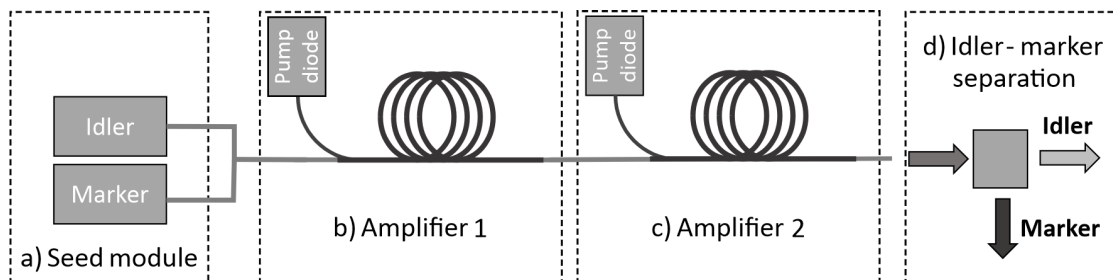
Fig. 3. *The advanced system for pulse-on-demand generation; seed module a) consisting of the seed and marker laser diodes keeps the gain balance through the amplifiers b) and c) constant regardless of the marker pulse shape and repetition on the output; the marker and idler signals are separated at the output d) by the volume Bragg grating (VBG)*

s of nanoseconds up to continuous (CW) operation at arbitrary repetition rates.

Such laser parameters are useful for many applications, such as thin-film scribing; however, it was designed specifically for LTP in a commercial LTP system, in which the advantage of high modulation bandwidth could be directly evaluated. The printing results are presented in Section 3.1.

2.3 Advanced Setup – Hybrid Version

When combining long (nanosecond) idler pulses and short (picosecond or femtosecond) marker pulses, nonlinear filtering can be used to separate idler and marker pulses at the laser output. In our case, second harmonic generation (SHG) was used as a nonlinear filter.

The efficiency of SHG strongly depends on the pulse peak power. Therefore, the efficiency of SHG for long idler pulses with lower peak power is much smaller than the efficiency of SHG for ultrashort marker pulses. In our case, the achieved contrast ratio was 1:3000. The experimental setup for a hybrid pulse-on-demand laser system is shown in Fig. 4.

As already mentioned in the Introduction, nonlinear optical effects can cause problems in ultrashort-fiber laser systems. Due to the small core diameters of the optical fibres, the light intensities in fibre lasers are extremely high. This leads to nonlinear effects such as self-phase modulation

(SPM), which can lead to a shattered pulse temporal profile. To overcome this problem, the chirped-pulse amplification (CPA) technique is used. In CPA systems, the laser pulse is stretched in time prior to amplification. This reduces the pulse peak power in the amplifier and therefore lowers the effect of nonlinear phenomena. The laser pulse is then temporally recompressed outside of the fibre amplifier using a chirped volume Bragg grating (CVBG) or grating compressor.

However, when reaching even higher pulse energies, even CPA systems can no longer achieve pedestal-free pulses at the laser output. To achieve higher energies and a clean temporal profile, an additional solid-state amplifier is added to the fibre amplifying stages. Due to a larger beam diameter in the solid-state amplifier, the nonlinear effects in such an amplifier are almost negligible.

When combining fibre and solid-state amplifiers in pulse-on-demand systems care must be taken to ensure that the idler and marker pulses have the same gain in both fibre and solid-state amplifiers. This is not trivial as the solid-state amplifier has different gain media to the fibre amplifier.

In the fibre amplifier, the gain media has a broad emission spectrum. This means that a broad range of wavelengths around the centre laser wavelength exhibits the same amplification. This is not true in the solid-state gain medium, which has a relatively narrow emission spectrum. Because the spectra of the
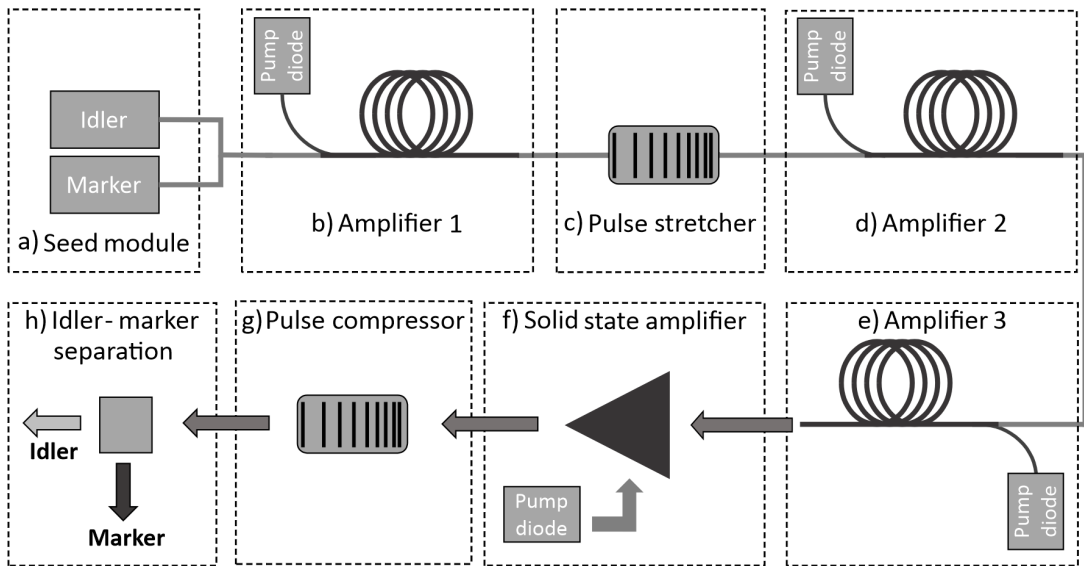
Fig. 4. *The advanced hybrid laser system for pulse-on-demand generation; seed module a) where marker seed is exchanged for the mode locked oscillator and b) pre-amplified before it undergoes chirped pulse amplification in the fibre amplifier chain c), d), e); the last amplifying stage f) is a ytterbium-doped amplifier; the marker - signal separation is made in h) by the second harmonic generation*

idler pulses and marker pulses are not the same, this leads to a different gain for the marker and idler in the solid-state amplifier, whereas the gain is the same for both the idler and marker in the fibre amplifier.

The different gain in the solid-state amplifier leads to transient pulse dynamics when switching from marker to idler pulses and vice versa. To compensate for a different gain in the solid-state amplifier, amplitude modulation of marker and idler pulses is required before amplification. This is similar to the modulation required in burst lasers.

3 RESULTS

With the compact gain-switched laser setup a pulse on demand was tested to over 1 MHz repetition rate. In the tested configuration the system could provide pulses tuneable from 40 ns to 100 ns with a peak power of around 1 kW. An arbitrary pulse pattern could be generated. Fig. 5a shows a pulse pattern with the pulse delay changing in a nonlinear way. Such a pattern is required to generate evenly spaced pulses on the workpiece when using a scanner with a nonlinear
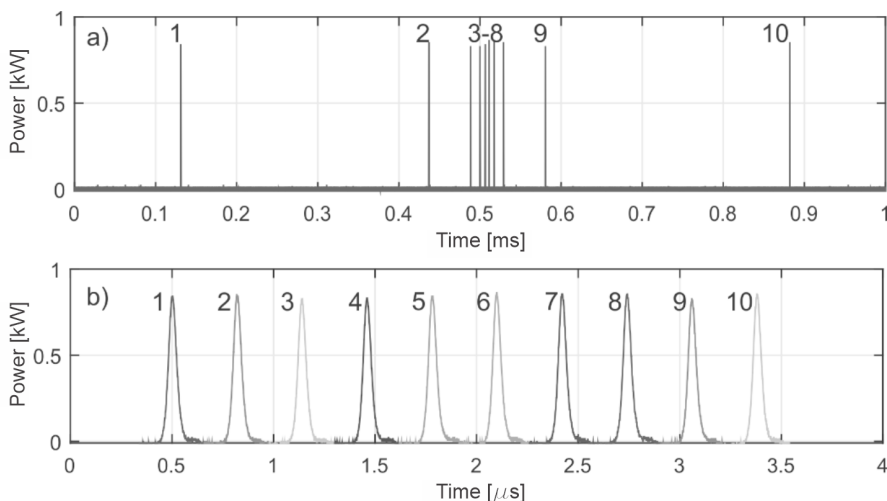
Fig. 5. *a) An arbitrary pulse train generated by the compact gain-switched laser setup; b) zoom in on the successive pulses from the trace shown in a); the error in the stability of the pulse width is less than 0.7 %*
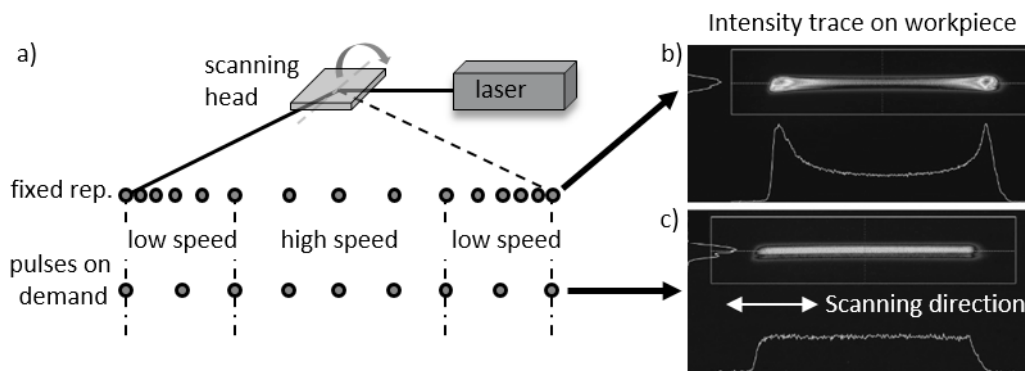
Fig. 6. *a) Using a resonant scanner to generate a pattern with laser source operating at a fixed repetition rate captured on the beam profiler camera b); and with the laser source compensating the pulse delay to evenly distribute the laser power over the line trace c)*

response function, such as a resonant scanner. A zoom in on the successive pulses in a trace is shown in Fig. 5b. The delays are omitted on the plot for a better representation of the pulse. The pulse duration was stable with a standard deviation of less than 0.7 %, while the peak power fluctuated by less than 1.5 %.

The comparison between the laser pulse trace with the nonlinear pulse delay and the pulse trace with the fixed repetition rate made using a resonant scanner is shown in Fig. 6. The intensity distribution for a single trace is shown in Fig. 6b for a fixed repetition rate and Fig. 6c for a pulse-on-demand laser operation synchronized to the resonant scanner. The intensity distribution was captured with the beam-profiler camera. It can be seen that the nonlinear response of the resonant scanner causes more power to be deposited on the trace edges where the scanning speed is low. To make more complex structures, an arbitrary pulse pattern must be used that can compensate for

the scanner position in time and still write an arbitrary pulse pattern on the workpiece.

The advanced pulse-on-demand laser system was designed to generate an arbitrary pulse patter with peak power up to 200 W and modulation of several 10 s of MHz to accommodate scanners with higher scanning speeds. A typical laser output (measured with a photodiode) is shown in Fig. 7.

After the marker seed laser diode was exchanged with the mode-locked oscillator and acousto-optics modulator as a low-power pulse picker, the tests were made on the advanced hybrid setup. With appropriate modulation of input idler and marker signal, a stable pulse train with no transient pulse dynamics was achieved when switching between the marker and idler pulses. An oscilloscope trace of a pulse-on-demand sequence after SHG is shown in Fig. 8.

With the presented laser system picosecond pulse-on-demand operation with pulse energies up to 300 µJ and 450 fs pulse durations were achieved.
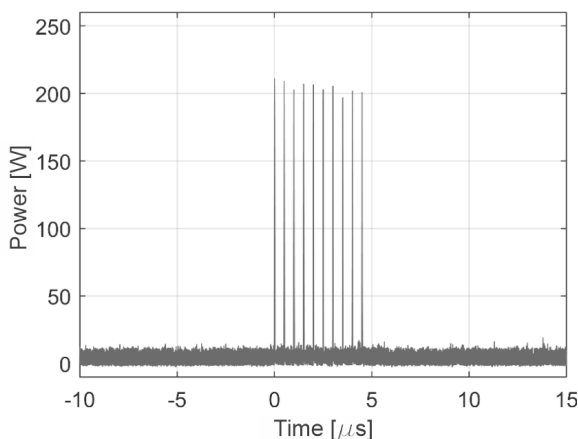
Fig. 7. *A typical output (after filtering with a VBG) of the advanced laser; a burst consisting of 10 pulses is shown with a nearly constant power of 200 W*
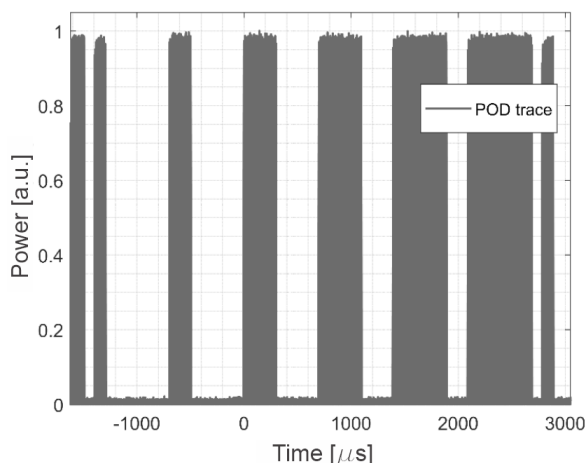
Fig. 8. *Pulse-on-demand trace from an advanced hybrid setup (after filtering using the SHG)*

3.1 Laser Transfer-Printing Application

The advanced laser setup presented in Section 2.2 was tested in a commercial LTP system. In this particular LTP system, the laser beam was focused onto a thin ink film which was spread over a transparent ink-carrier belt, positioned 150 μm above the glass acceptor substrate. The energy deposited by the laser heats the ink, which forms a bubble and is finally ejected onto the substrate. The conventional laser used in this LTP system was a 200 W CW fibre laser with an external acousto-optical modulator, with a damage-threshold-limited (due to the required tight focusing in the AOM) modulation bandwidth of 5 MHz. The beam was scanned using a polygon scanner with a 500 m/s scanning speed. The combination of high scanning speed and the limited modulation bandwidth of the conventional laser limits the achievable printing resolution (i.e., the smallest dot that can be transferred onto the substrate).

The advanced pulse-on-demand laser enabled printing with higher resolution or alternatively should, in theory, enable higher printing speeds at the same resolution. The latter would, however, require a faster polygon scanner and was therefore not tested. As for the achieved printing resolution, the laser successfully transferred a single pixel (1px) sized dot (1px = 50 ns pulse), as seen in Fig. 7, whereas the conventional externally modulated CW laser only reliably transferred > 4px dots (> 200-ns-long pulses).
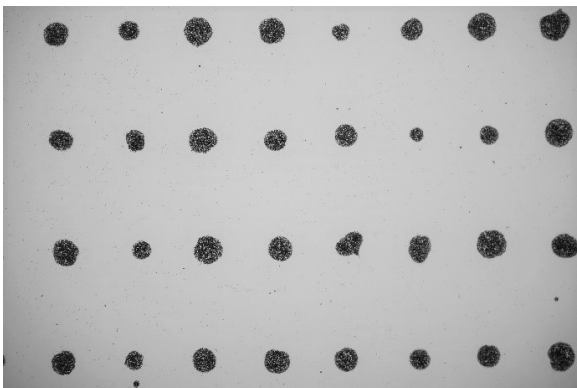
Fig. 9. *A series of 1px dots successfully transferred with the advanced laser; the pulse pattern used in this case is shown in Fig. 7; the variations of the printed dot sizes are mostly due to the technical limitations of the LTP process (e.g., ink-thickness variations on the ink-carrier belt)*

4 CONCLUSIONS

Pulse-on-demand laser operation and its application are presented in this paper. Two methods of efficient gain control that allow for laser pulse parameters to be decoupled from the change in the repetition rate are presented and analysed. The method of direct pump modulation in the high-power laser oscillator was shown to generate pulses on demand from a single shot to repetition rates over 1 MHz. The demonstrated result of several tens-of-nanoseconds pulses with a kW peak power is ideal for applications such as direct colour marking, micromachining and selective photocoagulation.

The advanced method of using a combination of marker and idler seeding in a MOPA (Master Oscillator Power Amplifier) amplifying chain was demonstrated to realize the modulation of a pulse repetition rate of several tens of MHz. The advanced method was tested on an industrial laser transfer-printing system where the synchronization and high modulation bandwidth were evaluated. Furthermore, the advanced method was augmented by a solid-state amplifier providing nonlinear-effect-free operation when the marker seed is producing pulses in the picosecond range.

The benefit of the presented laser systems is that they can be merged into a highly adaptable laser for producing pulses on demand, allowing for precise synchronization with the new generation of high-speed resonant and polygon scanners and thus cover many laser applications.

5 ACKNOWLEDGEMENTS

6 REFERENCES

[1] De Loor, R. (2013). Polygon scanner system for ultra short pulsed laser micro-machining applications. *Physics Procedia*, vol. 41, p. 544-551, **DOI:10.1016/j.phpro.2013.03.114**.

[2] Harth, F., Piontek, M.C., Herrmann, T., Ľhuillier, J.A. (2016). Ultra high-speed micromachining of transparent materials using high PRF ultrafast lasers and new resonant scanning systems. *Proceedings SPIE (vol. 9736) Laser-Based Micro- and Nanoprocessing X*, 97360N, **DOI:10.1117/12.2212816**.

[3] Mur, J., Kavčič, B., Poberaj, I. (2013). Fast and precise Laguerre–Gaussian beam steering with acousto-optic deflectors. *Applied Optics*, vol. 52, no. 26, p. 6506-6511, **DOI:10.1364/AO.52.006506**.

[4] Mur, J., Podobnik, B., Poberaj, I. (2017). Laser beam steering approaches for microstructuring of copper layers. *Optics*

& Laser Technology, vol. 88, p. 140-146, **DOI:10.1016/j.optlastec.2016.08.009**.

[5] Šajn, M., Petelin, J., Agrež, V., Vidmar, M., Petkovšek, R. (2017). DFB diode seeded low repetition rate fiber laser system operating in burst mode. *Optics & Laser Technology*, vol. 88, p. 99-103, **DOI:10.1016/j.optlastec.2016.09.006**.

[6] Bollig, C., Hofmeister, P.-G., Kunze, M., Schmidt, J., Fayed, S., Reuter, R. (2013). Efficient single-frequency pulsed all-fibre amplifier for coherent lidar. *Conference on Lasers and Electro-Optics - International Quantum Electronics Conference*, **DOI:10.1109/CLEO-IQEC.2013.6801383**.

[7] Klehr, A., Liero, A., Wenzel, H., Bugge, F., Brox, O., Fricke, J., Ressel, P., Knigge, A., Heinrich, W., Tränkle, G. (2017). 1030-nm diode-laser-based light source delivering pulses with nanojoule energies and picosecond duration adjustable by mode locking or pulse gating operation. *Novel In-Plane Semiconductor Lasers XVI (vol. 10123)*, 101230D, **DOI:10.1117/12.2250093**.

[8] Petkovšek, R., Agrež, V., Bammer, F., Jakopič, P., Lenardič, B. (2013). Experimental and theoretical study of gain switched Yb-doped fiber laser. *Proceedings Fiber Lasers X: Technology, Systems, and Applications (vol. 8601)*, 860128, p. 860128-860128, **DOI:10.1117/12.2002324**.

[9] Agrež, V., Petkovšek, R. (2013). Gain-switched Yb-doped fiber laser for microprocessing. *Applied Optics*, vol. 52, no. 13, p. 3066-3072, **DOI:10.1364/AO.52.003066**.

[10] Yang, J., Tang, Y., Xu, J. (2013). Development and applications of gain-switched fiber lasers [Invited]. *Photonics Research*, vol. 1, no. 1, p. 52-57, **DOI:10.1364/PRJ.1.000052**.

[11] Agrež, V., Petkovšek, R. (2014). Gain switch laser based on micro-structured Yb-doped active fiber. *Optics Express*, vol. 22, no. 5, p. 5558-5563, **DOI:10.1364/OE.22.005558**.

[12] Petkovšek, R., Agrež, V. (2014). Single stage Yb-doped fiber laser based on gain switching with short pulse duration. *Optics Express*, vol. 22, no. 2, p. 1366-1371, **DOI:10.1364/OE.22.001366**.

[13] Petkovšek, R., Agrež, V., Sangla, D., Saby, J., Picard, R.B., Salin, F. (2014). Gain-switched ytterbium-doped rod-type fiber laser. *Laser Physics Letters*, vol. 11, no. 10, p. 105808, **DOI:10.1088/1612-2011/11/10/105808**.

[14] Grzes, P., Swiderski, J. (2018). Gain-switched 2-µm fiber laser system providing kilowatt peak-power mode-locked resembling pulses and its application to supercontinuum generation in fluoride fibers. *IEEE Photonics Journal*, vol. 10, no. 1, p. 1-8, **DOI:10.1109/JPHOT.2018.2791634**.

[15] Moulton, P.F., Rines, G.A., Slobodtchikov, E.V., Wall, K.F., Frith, G., Samson, B., Carter, A.L.G. (2009). Tm-doped fiber lasers: fundamentals and power scaling. *IEEE Journal of Selected Topics in Quantum Electronics*, vol. 15, no. 1, p. 85-92, **DOI:10.1109/jstqe.2008.2010719**.

[16] Šušnjar, P., Agrež, V., Petkovšek, R. (2018). Photodarkening as a heat source in ytterbium doped fiber amplifiers. *Optics Express*, vol. 26, no. 5, p. 6420-6426, **DOI:10.1364/OE.26.006420**.

[17] Luo, H., Liu, F., Li, J., Liu, Y. (2018). High repetition rate gain-switched Ho-doped fiber laser at 2.103 µm pumped by h-shaped mode-locked Tm-doped fiber laser at 1.985

µm. *Optics Express*, vol. 26, no. 20, p. 26485-26494, **DOI:10.1364/OE.26.026485**.

[18] Paradis, P., Fortin, V., Aydin, Y.O., Vallée, R., Bernier, M. (2018). 10 W-level gain-switched all-fiber laser at 2.8 µm. *Optics Letters*, vol. 43, no. 13, p. 3196-3199, **DOI:10.1364/OL.43.003196**.

[19] Mur, J., Petelin, J., Osterman, N., Petkovšek, R. (2017). High precision laser direct microstructuring system based on bursts of picosecond pulses. *Journal of Physics D: Applied Physics*, vol. 50, no. 32, ID 325104, **DOI:10.1088/1361-6463/aa7b5a**.

[20] Mur, J., Pirker, L., Osterman, N., Petkovšek, R. (2017). Silicon crystallinity control during laser direct microstructuring with bursts of picosecond pulses. *Optics Express*, vol. 25, no. 21, p. 26356-26364, **DOI:10.1364/OE.25.026356**.

[21] Mur, J., Petkovšek, R. (2019). Near-THz bursts of pulses – Governing surface ablation mechanisms for laser material processing. *Applied Surface Science*, vol. 478, p. 355-360, **DOI:10.1016/j.apsusc.2019.01.182**.

[22] Černe, L., Novak, J., Agrež, V., Petkovšek, R. (2019). Optimization of a supercontinuum source based on tapered ordinary fibers. *Laser Physics*, vol. 29, no. 2, ID 025103. **DOI:10.1088/1555-6611/aaf640**.

[23] Motoshima, K., Leba, L. M., Chen, D.N., Downs, M.M., Li, T., Desurvire, E. (1993). Dynamic compensation of transient gain saturation in erbium-doped fiber amplifiers by pump feedback control. *IEEE Photonics Technology Letters*, vol. 5, no. 12, p. 1423-1426, **DOI:10.1109/68.262563**.

[24] Novak, V., Podobnik, B., Možina, J., Petkovšek, R. (2013). Analysis of the thermal management system for a pump laser. *Applied Thermal Engineering*, vol. 57, no. 1-2, p. 99-106, **DOI:10.1016/j.applthermaleng.2013.03.060**.

[25] Harth, F., Herrmann, T., L'huillier, J.A. (2019). High power ultrafast laser with highly dynamic repetition rate and constant pulse energy from single pulse to 10 MHz. *Solid State Lasers XXVIII: Technology and Devices (vol. 10896)*, 108960H, **DOI:10.1117/12.2507821**.

[26] Petkovšek, R., Novak, V., Agrež, V. (2015). High power fiber MOPA based QCW laser delivering pulses with arbitrary duration on demand at high modulation bandwidth. *Optics Express*, vol. 23, no. 26, p. 33150-33156, **DOI:10.1364/OE.23.033150**.

[27] Petkovšek, R., Novak, V., Agrež, V. (2017). Fiber laser for high speed laser transfer printing. *Proceedings of XXI International Symposium on High Power Laser Systems and Applications*, vol. 10254, ID 1025403, **DOI:10.1117/12.2257862**.

[28] Tuennermann, A., Zellmer, H., Ruske, J.P. (2001). *Directly Modulatable Laser*. US 20010014107, US Patent and Trademark Office, Washington.

[29] Quentin, U., Kanal, F., Budnicki, A., Tan, C., Diekamp, H., Jansen, F., Scelle, R., Sutter, D. (2019). TruMicro 2000: Next-generation flexible ultrashort pulse fiber lasers for scientific and industrial applications (Conference Presentation). *Proceedings of Fiber Lasers XVI: Technology and Systems (vol. 10897)*, 108971M, **DOI:10.1117/12.2511120**.

[30] Munroe, M.J. (2011). *Method and Apparatus for Producing Arbitrary Pulsetrains from a Harmonic Fiber Laser*, US 7885298, US Patent and Trademark Office, Washington.

Petkovšek, R. – Agrež, V. – Petelin, J. – Černe, L. – Bünting, U. – Podobnik, B.

[31] Elahi, P., Yılmaz, S., Eldeniz, Y.B., Ilday, F.Ö. (2014). Generation of picosecond pulses directly from a 100 W, burst-mode, doping-managed Yb-doped fiber amplifier. *Optics Letters*, vol. 39, no. 2, p. 236-239, **DOI:10.1364/OL.39.000236**.

[32] Petelin, J., Podobnik, B., Petkovšek, R. (2015). Burst shaping in a fiber-amplifier chain seeded by a gain-switched laser diode. *Applied Optics*, vol. 54, no. 15, p. 4629-4634, **DOI:10.1364/AO.54.004629**.

[33] Agrež, V., Petkovšek, R., Sangla, D., Saby, J., Picard, R.B.; Salin, F. (2014). Effect of repetition rate on gain-switched fiber laser output pulses. *Laser Physics*, vol. 24, no. 10, ID 105108, **DOI:10.1088/1054-660x/24/10/105108**.

[34] Petelin, J., Agrež, V., Podobnik, B., Petkovšek, R. (2014). Short pulsed gain-switched fiber laser with improved efficiency utilizing unabsorbed pump recovery. *Optics Express*, vol. 22, no. 17, p. 20588-20594, **DOI:10.1364/OE.22.020588**.

[35] Agrež, V., Petkovšek, R. (2019). Highly adaptable gain-switched fiber laser with improved efficiency. *Optics Express*, vol. 27, no. 9, p. 12100-12109, **DOI:10.1364/OE.27.012100**.

Revealing the Thermodynamic Background of the Memory Effect in Phase Separating Cathode Materials

Klemen Zelič[1] – Igor Mele[1] – Ivo Pačnik[1] – Jože Moškon[2] – Miran Gaberšček[2] – Tomaž Katrašnik[1,*]

[1]University of Ljubljana, Faculty of Mechanical Engineering, Slovenia
[2]National Institute of Chemistry, Slovenia

Phase separating Li-ion battery cell cathode materials feature a well-known phenomenon called the memory effect. It manifests itself as an abnormal change in working voltage being dependent on cell cycling history. It was only recently that plausible mechanistic reasoning of the memory effect in Li-ion batteries was proposed. However, the existing literature does still not consistently reveal a phenomenological background for the onset or absence of the memory effect. This paper provides strong experimental and theoretical evidence of the memory effect in phase separating Li-ion battery cathode materials. Specifically, the background leading to the onset or absence of the memory effect and the underlying causal chain of phenomena from the collective particle-by-particle intra-electrode phenomena to macroscopic voltage output of the battery are presented and discussed. The results, clearly reveal that no memory effect is observed and predicted for low cut off voltages, whereas the absence of the first rest in memory writing cycle does not result in the absence of the memory effect, as previously believed. In addition, excellent agreement between the simulated and measured results is shown which, on one hand confirms the credibility of the combined analyses and, on the other, provides clear causal relations from macroscopic experimental parameters to simulated phenomena on the particle level.
Keywords: Li-ion battery, phase separating material, multi-particle porous electrode, memory effect

Highlights
- *Innovative evidence on the onset and absence of the memory effect in phase separating cathode materials is provided.*
- *Analysis is based on combining experimental results and advanced continuum modelling on porous battery electrodes.*
- *Memory effect is not present if the cut off voltage in memory writing cycle is sufficiently low.*
- *The absence of first rest in memory writing cycle still leads to the intra-particle distribution of lithium yielding a memory effect .*

0 INTRODUCTION

Batteries are one of the most widespread energy storage devices, covering a very broad range of mobile, and increasingly also stationary applications. They are thus enablers for more sustainable mobility and more user-friendly leisure applications. With the introduction of renewable energy sources, they are gaining on significance in energy applications.

In battery applications, one of the most important control parameters is the so called state-of-charge (SOC) representing the level of charge of an electric battery relative to its capacity. In most applications SOC estimation is performed via voltage reading. For batteries composed of layered materials, e.g. NMC, $LiCoO_2$, $LiMnO_2$, $LiNiO_2$, that are not subjected to phase transitions and are thus characterized by a relatively steep voltage gradient during the changing of the lithiation level of electrode [1], such a procedure is less demanding. By contrast, SOC estimation is much more demanding for batteries composed of olivine materials featuring a very flat voltage profile between spinodal points of the chemical potential which, more generally, is a characteristic feature of electrodes consisting of phase separating materials exposed to low currents [1] and [2].

Therefore, in order to ensure a credible SOC estimation in such types of batteries, it is very important to analyze potential influential factors that can bias the voltage level. Whereas the operating temperature of the battery and the applied current rate do bias the voltage level, their influences can for a certain battery type be relatively accurately determined in advanced SOC estimators. In contrast, one of the important phenomena that renders accurate SOC estimation difficult is the memory effect, which is well known in Ni-Cd and Ni-MH batteries. As reported in [3], the memory effect is manifested in a reduced voltage in the discharge curves when the batteries undergo a repeated shallow-depth discharge for a large number of cycles [4] to [7]; under such conditions the discharge voltage seems to memorize the depth of discharge of the previous cycling. This memory effect leads to a reduction in practical cell capacity at a fixed cutoff voltage and/or to a wrong estimate of the state of charge (SOC) of the cell.

In contrast to the memory effect observed in Ni-MH batteries, the memory effect in Li-ion batteries based on phase separating materials occurs after only one partial charge/discharge cycle [3]. In agreement with [3] the term memory effect denotes abnormal changes in working voltage, which does not include

hysteresis behavior during charge and discharge. As LiFePO$_4$ (LFP) is a phase separating material characterized by a very flat voltage profile between the spinodal points of the chemical potential, the small memory bump that already appears after only one cycle of partial charge and discharge can lead to substantial miscalculations in estimating the state of SOC by software algorithms.

Sasaki et al. [3] have developed a well-defined procedure to observe and study the memory effect in detail. As demonstrated in Fig. 2, this procedure consists of: a) partially charging the empty battery with moderate currents, b) a first rest period, c) a discharge with moderate currents, d) a second very short rest and e) a memory releasing cycle, during which the memory effect is observed in the vicinity of the terminal SOC of the partial charge in step a). Sasaki et al. have also clearly related this intra-electrode phenomenon to the macroscopic battery output, which has importance for most battery uses. They have shown a strong correlation between the initial SOCs of the memory writing and the releasing cycle and the magnitude of the memory effect. For example, the memory effect is much more pronounced if the partial discharge in the memory writing cycle stops at higher SOC values [3]. In addition, Jia et al. [8] investigated the influence of the rest time after the memory writing cycle on the magnitude of the memory effect and reported that a prolonged relaxation amplified the memory effect.

Farkhondeh et al. [9] were the first to successfully simulate experimental findings published in papers [3] and [8]. They used multi-particle model with the additionally introduced parameter of active particle surface resistance that was Gaussian distributed among particles. Even though their model was able to replicate the memory effect in multi-particle phase separating electrode, it lacks the insight that additionally introduced resistant parameter also corresponds to different particle sizes.

Although Sasaki et al. [3] had been the first to report this effect, it was not until the publication by Kondo et al. [10] that a consistent mechanistic explanation of the memory effect was proposed. They based their analyses on a simplified electrochemical model neglecting mass transport phenomena such as electronic conductivity and lithium diffusion in the solid and liquid phases while assuming a uniform concentration of Li within the active particles and in the electrode pores. Their model is similar to the one from [9] with the introduction of particle size distribution. They associate the memory effect, i.e. a bump in the voltage profile, with a reduced active particle population that appears as a consequence of

a shim shaped Li-composition distribution which, in turn, is a result of particle size distribution. Kondo et al. [10] further state that there is no memory effect if there is no rest after a first partial charge (step b) above). This statement is not fully consistent with their own results shown in the paper where it is clearly seen that this case is also characterized by a reduced active particle population and a bump in the voltage profile. However, the voltage bump occurs at a lower voltage and its magnitude is also slightly lower. This less intense but non-vanishing voltage bump can be explained by a larger active particle population due to the absence of a rest period.

Obviously, the memory effect only arises if the cathode is not fully lithiated during a discharge process (step c) above). Therefore, the memory effect is indeed important in real battery applications, as control algorithms in appliances prevent the battery of being fully discharged. Hence, this phenomenon needs to be further scientifically elucidated to form a solid basis for future research.

As shown above, the existing literature does not consistently reveal the phenomenological background for the onset or absence of the memory effect. The paper at hand, therefore, enriches the literature on the memory effect by providing, for the first time i) a clear experimental and theoretical description of the conditions that lead to the onset or absence of the memory effect and ii) the underlying causal chain of phenomena from the collective particle-by-particle intra-electrode phenomena to macroscopic voltage output of the battery.

1 METHODS

To provide a full reasoning of the addressed phenomena this analysis originates from very accurate experimental measurements, which clearly represent the macroscopic battery outputs. This experimental analysis is complemented by a detailed simulation study based on an advanced continuum level model, which reveals the intra-electrode phenomena thus reasoning the causal chain of phenomena and completing the overall analysis.

1.1 Experimental

1.1.1 Active Cathode Materials

In this study two types of LiFePO$_4$/C powder materials were used as active materials for LFP cathodes: a) A commercial powder provided by Targray Group (SLFP02002) further designated as "Targray LFP".

According to the specifications, this LFP material has a specific surface area of 11 ± 2 m^{2}g^{-1}, an agglomerate size of 3.0 ± 1.0 μm by the D50 criterion, and a native carbon content of 2.0 ± 0.5 wt.%. b) The second type of LFP material (LFP-pcrm) was prepared by a novel pulse combustion reactor method in a slightly reductive environment, as described in detail in our previous paper [11]. Briefly, the material was synthesized in a reactor setup consisting of a Helmholtz-type pulse combustor with a natural frequency of 280 Hz (at a temperature of around 1250 K) and a 4 m long stainless steel reactor pipe. Air is supplied to the combustor by way of a blower through an aerodynamic valve. The method allows very precise control of atmosphere in the reactor, as well as the frequency and amplitude of pulses, all of which have a pronounced effect on the reaction outcome [12].

In the present synthesis the spraying gas was 99.9 % nitrogen with a pressure of 1.5 bar and a flow of 45 mL min^{-1}, measured using a thermal mass flow meter. The precursor was composed of 13.5 g of $LiNO_3$, 76.1 g of $Fe(NO_3)_3 \cdot 9H_2O$, 36.4 g of triethyl phosphate, 78.5 g of glycine, 30.9 g of NH_4NO_3, everything dissolved in 400 g of deionized water. We used a 4 mole % excess of lithium due to losses in the reactor and annealing oven. The temperature at 0.5 m after the spray nozzle was maintained at (700 ± 5) °C with the amount of precursor sprayed (20 ± 1) mLmin^{-1}. The frequency of combustion was maintained at 240 Hz. The prepared material was collected in an electrostatic precipitator and annealed in an electrical oven under a constant argon flow and in presence of carbon at 700 °C for 6 hours. The annealed material had a tap density of approximately 1 gcm^{-3} and was used as prepared for the preparation of cathodes.

1.1.2 Electrode Composite and Electrode Preparation

Using the selected $LiFePO_4$/C material porous electrodes were prepared by a standard procedure for preparation of laboratory-scale LFP electrodes. We prepared a homogeneous slurry (dispersion) of the solid components in beforehand prepared 15 mg mL^{-1} solution of PVdF binder (182702 Aldrich) in NMP solvent (99.5 % pure, 8.06072.2500 Merck) to obtain the final (dry) electrode composite composition LFP/C : CB : PVdF = 90 : 5 : 5 (wt./wt.). The slurry was homogenized in a planetary mill for 30 min at 300 rpm. The slurry was applied to the surface of carbon coated Al foil by using automated doctor-blade applicator (the distance between the blade and the surface of Al foil was set to 200 μm). The

Al foil with coating was in the first step dried for 3 h at 90 °C at reduced pressure (10 mbar absolute). After that we cut out circular electrodes with 16 mm diameter (geometric area A = 2.01 cm^2). We pressed the electrodes by applying 5 t (2.5 tons per 1 cm^2) for 1 min in a hydraulic press. Before transferring in an argon-filled glove box the electrodes were dried under vacuum overnight at 90 °C in vacuum chamber. This means the prepared electrodes had LFP mass loadings of about 3 mg per cm^2 of the electrode geometric area (composite loading 3.3 mg per cm^2) and the obtained composite thickness was in the range 18 to 19 μm. We calculated the electrode porosity by taking the values of electrode composite mass, thickness and the bulk densities of the composite components to be 42 vol. %; which is comparable with the typical range found for LFP cathodes with good performance [13] and [14].

1.1.3 Cell Preparation and Electrochemical Measurements

All the electrochemical experiments were conducted by using vacuum sealed pouch-type cells. The conventional 2-electrode $LiFePO_4$-Li cells were assembled in an Ar-filled glove box by using metallic lithium foil (geometric area of 2.5 cm^2) as a counter electrode. As a separator, a glass fiber filter paper (Whatman, glass microfiber) was used. The electrolyte used was commercialized "LP-40", 1 M solution of $LiPF_6$ in ethylene carbonate/diethyl carbonate (EC:DEC = 1:1 wt/wt, Merck).

Standard chronopotentiometric (galvanostatic) measurements and all the memory effect experiments were performed using a "VPM3" (Bio-Logic) potentiostat/galvanostat running with EC-Lab® software. All the cells were electrochemically precycled (5 cycles C/10) in the voltage window 2.5 V to 4.1 V before testing for the memory effect. It is important to note that in order to diminish the effects of surrounding temperature variation, all the measurements were performed by keeping battery cell temperature constant in a thermostatic bath (dipped in silicone oil with temperature 25 ± 0.1 °C).

1.2 Simulation Model

Simulation analysis relies on an advanced continuum Li-ion battery modeling framework [15] featuring sequential multi-scale model linking [16]. This is achieved by thermodynamically consistent upscaling [17] of an advanced and detailed model of LFP particle potential as a function of lithiation determined by a thermodynamically consistent derivation [18]. Another merit of the advanced continuum

modelling framework arises from a more consistent reproduction of real multi-particle size distributions and particle connectivity and, therefore, electrode topology on the level of the entire electrode. This consistent transfer of a fundamental understanding of materials to the cell level and modeling of all relevant phenomena influencing battery performance on the continuum scale enhances the prediction capability of the proposed modeling framework in analyzing the memory effect compared to previous works [3], [9] and [10].

1.2.1 Constitutive Equations

The functioning of battery cells used in this study is described using Newman's approach [19], where electrochemical and transport phenomena are described by four partial differential equations for charge and mass conservation in the solid and the electrolyte (Eqs. (1) to (4)):

$$\frac{\partial \varepsilon c_e}{\partial t} = \nabla \cdot \left(D_e^{eff} \nabla c_e \right) + \left(1 - t_+ \right) a_p j_{BV}, \quad (1)$$

$$\nabla \cdot \left(\kappa^{eff} \nabla \phi_e - \frac{2RT\kappa^{eff}}{F} \left(1 - t_+ \right) \nabla \ln c_e \right) = F a_p j_{BV}, \quad (2)$$

$$\nabla \cdot \left(\sigma^{eff} \nabla \phi_s \right) = -F a_p j_{BV}, \quad (3)$$

$$\frac{\partial c_s}{\partial t} = \nabla \cdot \left(\frac{D_s c_s}{RT} \nabla \mu_s \right). \quad (4)$$

The same boundary conditions are used as in reference [20].

The intercalation current across the cathode active particle surface was modeled with the Butler-Volmer equation:

$$j_{BV} = \frac{i_0}{F} \left[\exp\left(-\frac{\alpha F}{RT} \eta \right) - \exp\left(\frac{(1-\alpha)F}{RT} \eta \right) \right]. \quad (5)$$

Nomenclature from Eqs. (1) to (5) is summarized in the Section 6 at the end of the paper.

For the chemical potential of active particles, the zero dimensional regular solution model was used as described in reference [17]. It has a shape of a spinodal curve at high overpotentials and a plateau-like shape at low overpotentials (Fig. 1).

Such a shape of the potential ensures a consistent description of intra-particle phase separation [18] and [21] to [28] as well as inter particle lithium exchange first modeled by Dreyer et al. [29].

In addition to the model by Dreyer et al [29], particle agglomeration and crystallographic orientations were taken into account by introduction

of connectivity [30] and [31] and permeability [15] parameters that govern inter particle lithium exchange.
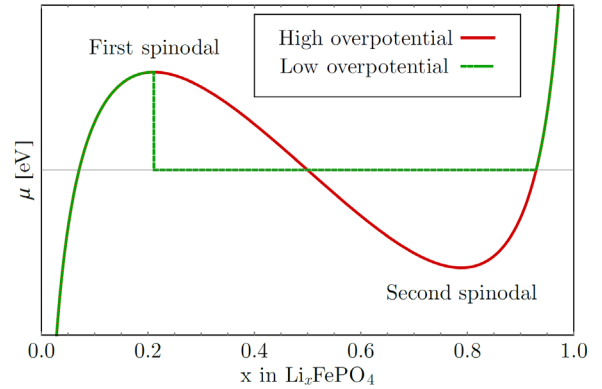
Fig. 1. *Spinodal shaped chemical potential μ dependency on particle state of charge (x in Li$_x$FePO$_4$) at charge for the case of high and low overpotential curve*

Intercalation rate dependency on the particle size was introduced to the model by a variable regular solution parameter as described in [17], which was crucial for plausibly simulating the memory effect. This is in agreement with Kondo et al. [10] who showed that the memory effect is a consequence of the shorter characteristic intercalation times for smaller particles. Log-normal particle size distribution was used based on scanning and transmission electron microscopy measurements.
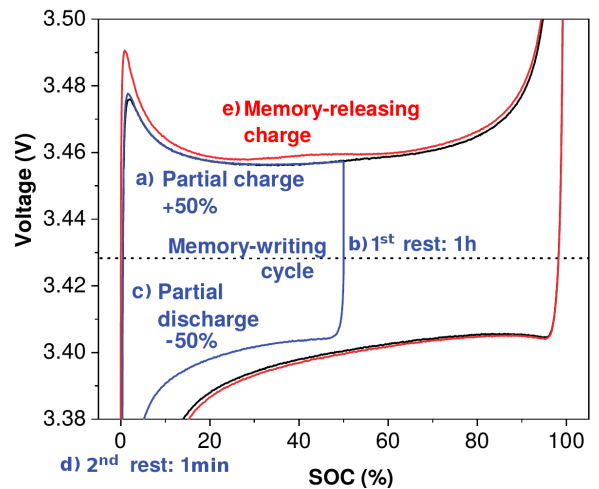
Fig. 2. Memory effect measured by the same protocol as used by Sasaki et al. [3]; blue line represents the memory writing cycle, red line is the memory releasing cycle and black line represents baseline discharge curve. Individual parts of the protocol chronologically follow: a) partial charge, b) 1st rest, c) partial discharge, d) 2nd rest and e) memory releasing cycle

All the simulations presented in the Results section were performed on a half cell with a phase separating multi-particle cathode material (LPF), separator and lithium metal anode.

2 RESULTS

Three distinctive experiments were made, that were later simulated with the model presented in section 1.2. The combined results of experiment and simulation offer new insights into the mechanism of memory effect.

2.1 Experimental Results

The experimental results presented in Fig. 2 were obtained by following exactly the same experiment procedure as proposed in the pioneering work of Sasaki et al. [3]. In agreement with the procedure presented in the Introduction, a battery cell was charged to half of its maximal capacity, left to rest for an hour (first rest) and then discharged back. This first half cycle is called the memory writing cycle [3]. After the battery had been fully charged, a memory releasing cycle was initiated. This cycle is characterized by a small bump in the voltage curve, called the memory effect [3]. Note that the memory effect appears in the vicinity of the SOC value of the first rest in the preceding memory writing cycle and should not been mistaken for the first, bigger bump seen in all curves at low SOCs.
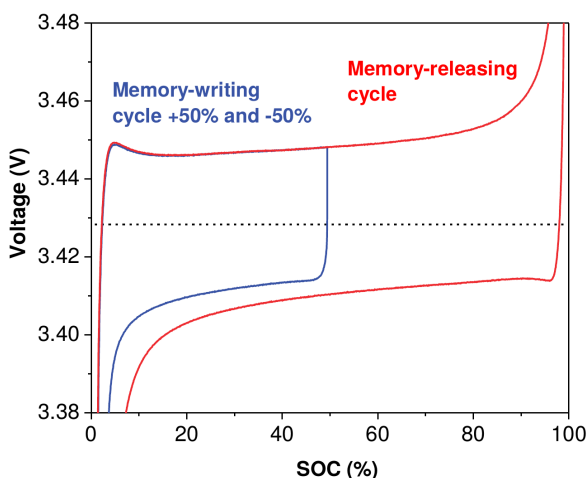
Fig. 3. *A memory effect experiment executed using the same protocol as in Fig 2, but to the cut off voltage of 2.8 V at the end of the memory writing cycle*

Fig. 3 shows experimental result where the cut off voltage of memory writing cycle was lowered to 2.8 V. The results clearly indicate that the memory

effect is absent if the cut off voltage in the memory writing cycle is sufficiently low thus erasing the memory effect, which was, based on simulation results, to a certain degree already discussed in paper of Farkhondeh et al. [9].
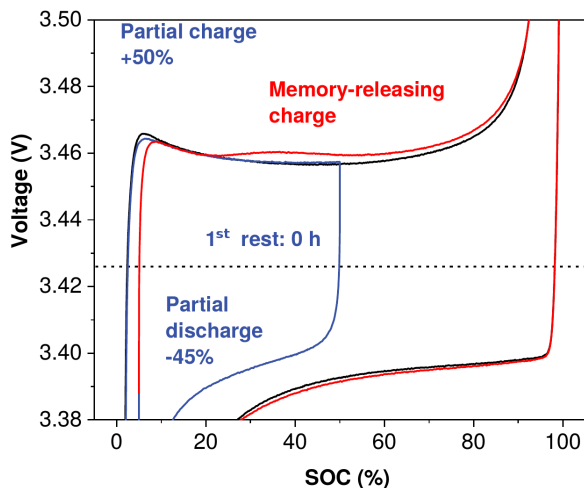
Fig. 4. *A memory effect experiment executed using the same protocol as in Fig. 2, but without first rest in the memory writing cycle*

Fig. 4 shows experimental evidence that the memory effect also exists in the limiting case where the time of the first rest in the memory writing cycle is reduced to zero. This has not been shown until now. In fact, an opposite claim was reported in [10], which however was not consistently supported by experimental and simulation evidence.

Figs. 2, 3 and 4 provide, for the first time, a consistent experimental detection of the onset or absence of the memory effect in phase separating Li-ion battery cell cathode materials at various conditions of interest. More detailed discussion of these results is given in the Discussion section in combination with the simulation results.

2.2 Simulation Results

To ensure clear causal relations from macroscopic experimental parameters to the simulated phenomena on the particle level, simulations performed by the model described in Section 1.2 were replicated for exactly the same scenarios as used in the experimental tests. Fig. 5, which presents results according to the scenario proposed by Sasaki et al. [3] (i.e. experimental results in Fig. 2) confirms the capability of the model to credibly replicate and predict the memory effect. It is for the first time that a fully coupled Newman-based continuum model was used for successful simulation
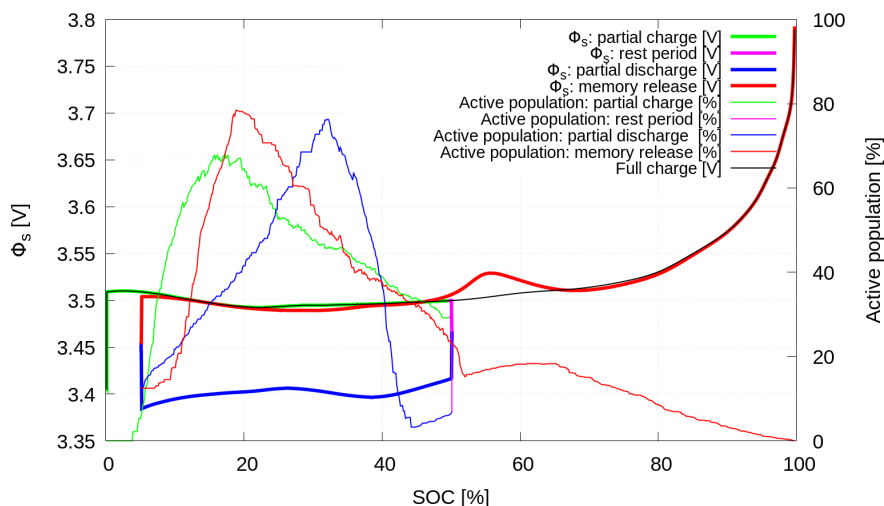
Fig. 5. *Simulation of memory effect calculated for the protocol presented in Fig. 2, with the model described in Section 1.2*
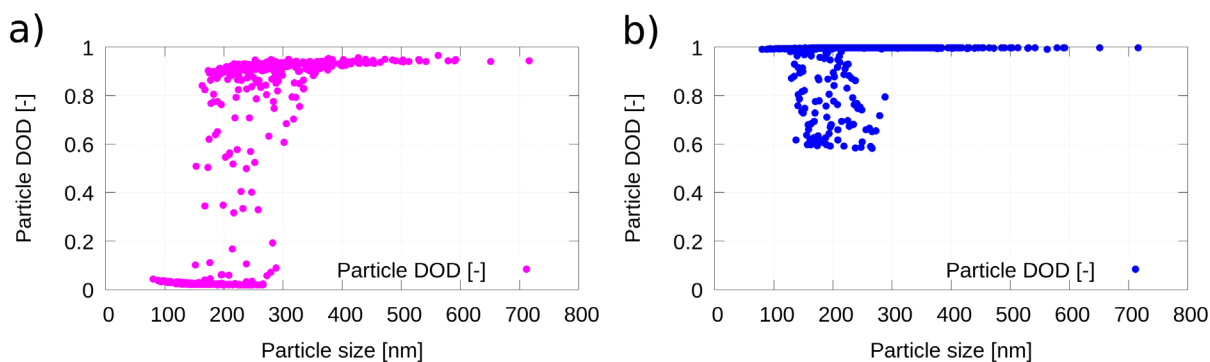
Fig. 6. *Simulation of inter-particle lithium distribution in the cathode, during a) first rest and b) second rest corresponding to the protocol presented in Fig. 5*

of the memory effect, which was made possible by innovative extensions presented in Section 1.2. The plausibility of the applied model is demonstrated in Fig. 6, where the average lithium concentration inside a particle (Particle DOD) is plotted versus particle size for particles in the cathode at two distinctive time instants of the memory writing protocol: at the end of first rest and at the end of the memory writing cycle (as presented in Figs. 2 to 4). Fig. 6b clearly presents the so called shim shaped particle distribution at the end of second rest, which is a prerequisite for the observation of the memory efect [10].

Likewise, Fig. 7 shows simulation results for the case with low cut-off voltages at the end of the memory writing cycle. Again, it can be concluded that the simulation results are in full agreement with the experimental observations presented in Fig. 3, as both cases predict memory erasure due to full particle lithiation at the end of memory writing cycle. This is

clearly confirmed in Fig. 8 showing particle DOD vs. particle size, where all particles are lithiated due to a low cut-off voltage thus erasing the memory effect due to absence of the shim shaped particle distribution at the end of the second rest.

Fig. 9 serves as simulation support to findings from Fig. 4, where the memory effect was observed even at the zero first rest and Fig. 10 shows the corresponding particle DOD vs. particle size.

All the simulation results coincide very well with the experimental results, thus presenting a strong joint platform for several new insights into the mechanism of memory effect, as explained in the Discussion section.

3 DISCUSSION

The result in Fig. 2 proves the reproducibility of the memory effect and serves as a calibration for the
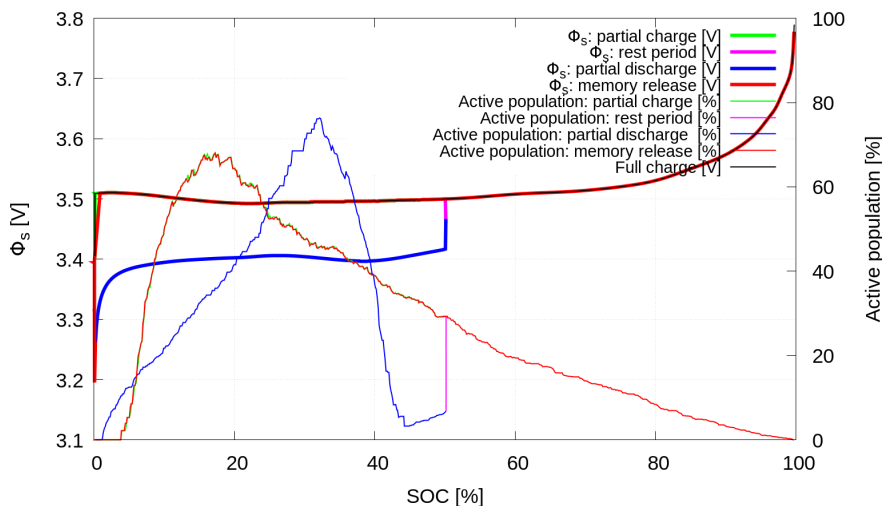
Fig. 7. *Simulation of memory effect calculated for the same protocol as in Fig. 5 but with the cut of voltage at the end of the memory writing cycle lowered to 2.8 V. No memory effect is observed in this case*
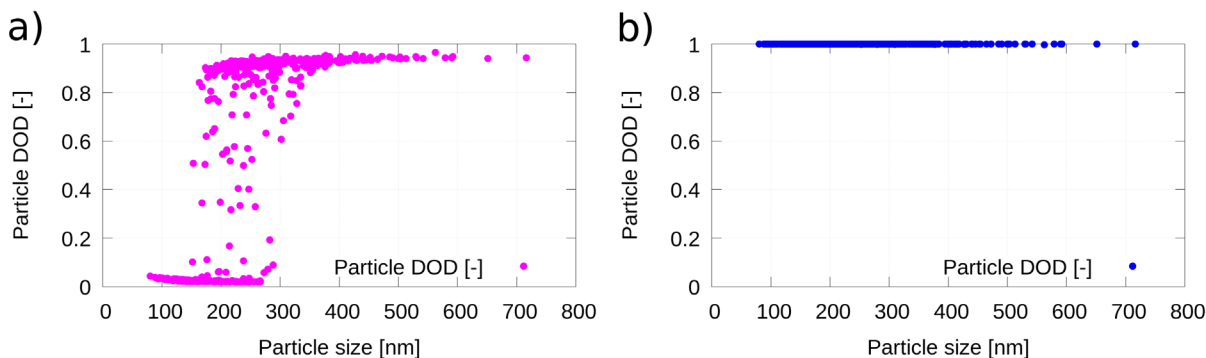
Fig. 8. *Simulation of inter-particle lithium distribution in the cathode, during a) first rest and b) second rest corresponding to the protocol presented in Fig. 7*

model, whereas the simulation result in Fig. 5 proves that a consistent continuum-level model of the full half-cell is capable of simulating the memory effect. From Fig. 6 it can be seen that the kinetics in smaller particles is faster in comparison to larger particles and the smaller particles are therefore depleted of lithium during the memory writing cycle, whereas larger particles remain full of lithium (Fig. 6a). It is worth noting that in Fig. 6 the division between lithiated and delithiated particles is not as sharp as schematically presented in **[10]**. This is reasoned by the fact that, unlike in **[10]**, a full half-cell model capable of considering variation of all electrode relevant parameters was used in the present study. Therefore, nonuniform concentration and potential fields partially compete with size dependent particle kinetics leading to a less sharp division between lithiated and delithiated particles.

As a result of this particle size dependent kinetics, the electrode becomes inter-particle phase separated at the end of the first rest, with a small portion of particles with a size of around 200 nm still being active (Fig. 6a). After the discharge part of the memory writing cycle, the faster kinetics of smaller particles favors their faster lithiation, as presented in Fig. 6b. As a result, only medium-sized particles remain partially delithiated (remain active). The same effect is also seen in Fig. 5, where the active particle population does not drop to zero at the second rest, i.e. between partial discharge and memory release. Resultantly, the so called shim shaped particle distribution is formed as presented in Fig 6b, which is quantitatively identical to the one calculated by Kondo et al. **[10]**. This aligns the present results with the ones shown in **[10]**, confirming the necessity of the shim shaped particle distribution to generate the
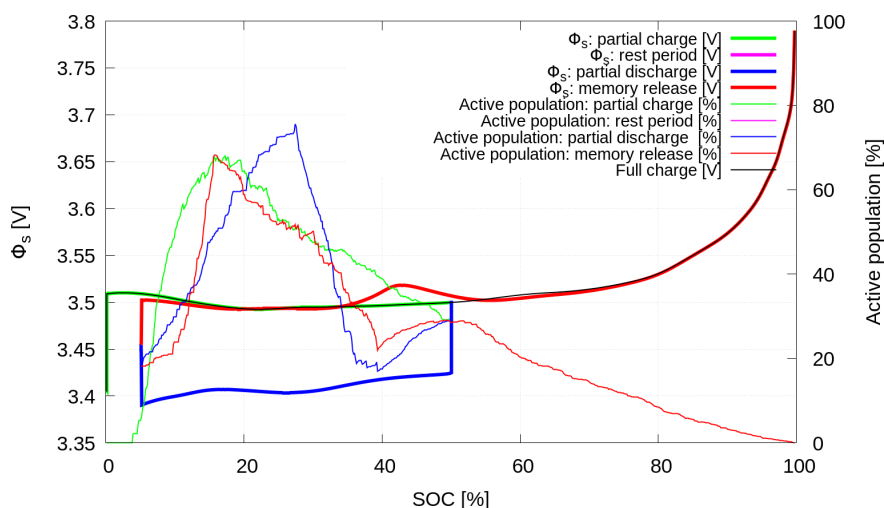
Fig. 9. *Simulation of memory effect calculated for the same protocol as in Fig. 5 but without fist rest*
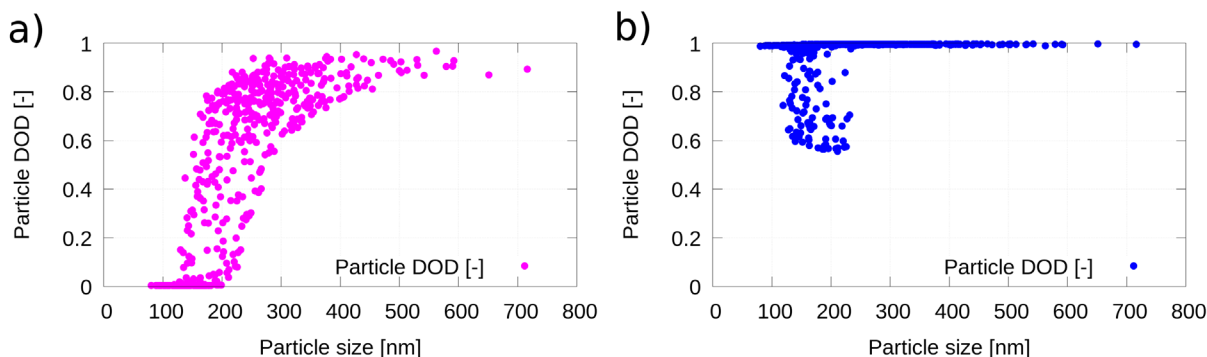
Fig. 10. *Simulation of inter-particle lithium distribution in the cathode, during a) first rest and b) second rest corresponding to the protocol presented in Fig. 9*

memory effect. Kondo et al. [10] further supported this statement with the need of a short second rest period that prevents relaxation of this shim shaped particle distribution.

In the subsequent memory releasing cycle a sharp drop in active particle population can be observed in the vicinity of the SOC value of the first rest in the preceding memory writing cycle, i.e. a SOC value of around 50 %. This observation, which is in-line with the one provided by [10], is reasoned by the fact that the active particle population drops when the lithiation level of the electrode approaches values at which partially delithiated particles in the shim shaped particle distribution become active. This effect is certainly observable only at sufficiently moderate currents that favor inter-particle phase separation.

Comparison of the results shown in Fig. 3 and Fig. 7 clarifies the speculations about the cases where memory effect was not observed [8] and [9]. Namely,

the memory effect can be erased by simply sufficiently lowering the cut-off voltage (2.8 V) at the end of the writing cycle. The same experimental result was also achieved by a longer voltage hold at cut-off voltage values up to 3.3 V at the end of the memory writing cycle.

The main precondition for the onset of the memory effect is, as analyzed earlier, the presence of the shim shaped particle distribution at the end of the second rest. This inherently implies that the electrode is not fully lithiated. A logical measure for erasing the memory effect is thus a full lithiation of the electrode, which can be achieved by any of the previously proposed methods: a very low cut-off voltage or a longer voltage hold at a cut-off voltage below the voltage of the lower spinodal (Fig. 1). Thus, all the particles are driven to the regime of high concentrations (above the second spinodal point − (Fig. 1), where the chemical potential dependency on

concentration is a monotonous function). Inter particle phase separation of the system in such a regime is, therefore, not possible and all the particles occupy equal state of charge at the same value of the chemical potential leading to the absence of the shim shaped particle distribution. This can clearly be seen in Fig. 8b and from the active particle population curve in Fig. 7, which indicates zero active particle population at the end of second rest. These observations are in line with the model of Dreyer et al. [29], Farkhondeh et al. [9] and also with the model of Kondo et al. [10], however until now the entire causal chain of phenomena from the macroscopic voltage output of the battery to collective particle-by-particle intra-electrode phenomena was not elucidated to that extent.

In short, the presented results provide a clear confirmation that the memory effect can only be observed if a battery cell is not fully discharged (discharged to low cut off voltages) in the memory writing cycle. Despite this important fact, addressing the influence of the memory effect in appliances equipped with Li-ion batteries composed of phase separating materials is still important, as control algorithms prevent the battery from being fully discharged.

The combined findings displayed in Figs. 4, 9 and 10 provide the basis for explaining another intriguing fact about the memory effect. Fig. 4 shows experimental evidence that the memory effect also exists in the limiting case where the first rest period in the memory writing cycle is reduced to zero. This result opposes the measurements by Jia et al. [8], where the absence of the memory effect at the zero first rest experiment can be attributed to the above average connectivity of active particles in the cathode, that prevents establishment of shim shaped inter-particle lithium distribution after memory writing cycle. Likewise, this opposes the statement published in [10] that the memory effect is not present in the absence of the first rest, although the simulation results in [10] do not fully support this statement, as they also predict a drop of active particle population also in this case.

The presence of the memory effect in the case of zero first rest period can be explained by the fact that, even though the particles are not relaxed after the partial charge part of the memory writing cycle, a wide distribution of particles across the full range of concentrations can be observed (Fig. 10a). Qualitatively this distribution, where smaller particles are delithiated and larger particles remain lithiated (Fig. 10a), looks similar to the one presented in Fig. 6a. The two distributions differ quantitatively as

expected. In the case with an absent first rest, the active particle population is larger. However, upon subsequent lithiation, the faster kinetics of smaller particles in combination with all particles not being fully lithiated again forms a shim shape particle distribution at the end of the second rest (Fig. 10b). This provides a reasoning for the experimental observation of the memory effect when the first rest period is zero, which is well aligned with the simulation results. The latter again predict a decrease of active particle population, which is associated with an increase in charging voltage as presented in Fig. 9.

4 CONCLUSIONS

The memory effect previously observed in several Li-ion phase separating multi-particle cathodes was investigated by a rigorous experimental and an advanced simulation approach. The good agreement between the simulated and measured results offered several new insights in the mechanistic origin of the memory effect. Experiment and simulation of low cut off voltage and the absence of a first rest in the memory writing cycle are shown as two previously insufficiently explained cases. It was shown that the memory effect is erased upon lithiation of the electrode after the memory writing cycle, which can be achieved by either a very low cut-off voltage or a longer voltage hold at a cut-off voltage below the voltage of the lower spinodal. In addition, it was shown that the absence of the first rest in the memory writing cycle itself is not a sufficient condition for erasing the memory effect.

5 ACKNOWLEDGEMENTS

6 NOMENCLATURES

a_p volumetric specific active, [m^{-1}]
α particle surface area charge transfer coefficient, [-]
c_e electrolyte Li concentration, [mol/m^3]
c_s solid phase Li concentration, [mol/m^3]
D_e^{eff} effective diffusion coefficient in electrolyte, [m^2/s]
D_s diffusion coefficient in solid phase, [m^2/s]

ε porosity of electrode, [-]

η overpotential, [V]

F Faraday constant, [As/mol]

ϕ_e electrolyte potential, [V]

i_0 Butler-Volmer exchange current density, [A/m^2]

j_{BV} Butler-Volmer intercalation current density, [A/m^2]

k^{eff} electrolyte effective ionic conductivity, [S/m]

μ_s solid phase chemical potential, [eV/mol]

σ^{eff} solid phase effective electric conductivity, [S/m]

R gas constant, [J/(molK)]

T temperature, [K]

t time, [s]

t_+ transference number, [-]

8 REFERENCES

[1] Ellis, B.L., Lee, K.T., Nazar, L.F. (2009). Positive electrode materials for Li-Ion and Li-batteries. *Chemistry of Materials Review*, vol. 22, p. 691-714, **DOI:10.1021/cm902696j**.

[2] Padhi, A.K., Nanjundaswamy, K.S., Goodenough, J.B. (1997). Phospho-olivines as positive-electrode materials for rechargeable lithium batteries. *Journal of the Electrochemical Society*, vol. 144, no. 4, p. 1188-1194, **DOI:10.1149/1.1837571**.

[3] Sasaki, T., Ukyo, Y., Novák, P. (2013). Memory effect in a lithium-ion battery. *Nature Materials*, vol. 12, p. 569-575, **DOI:10.1038/nmat3623**.

[4] Davolio, G., Soragni, E. (1998). The memory effect on nickel oxide electrodes: Electrochemical and mechanical aspects. *Journal of Applied Electrochemistry*, vol. 28, no. 12, p. 1313-1319, **DOI:10.1023/A:1003452327919**.

[5] Huggins, R.A. (2006). Mechanism of the memory effect in "Nickel" electrodes. *Solid State Ionics*, vol. 177, no. 26-32, p. 2643-2646, **DOI:10.1016/j.ssi.2006.03.005**.

[6] Sato, Y., Takeuchi, S., Kobayakawa, K. (2001). Cause of the memory effect observed in alkaline secondary batteries using nickel electrode. *Journal of Power Sources*, vol. 93, no. 1-2, p. 20-24, **DOI:10.1016/S0378-7753(00)00506-1**.

[7] Barnard, R., Crickmore, G.T., Lee, J.A., Tye, F. (1980). The cause of residual capacity in nickel oxyhydroxide electrodes. *Journal of Applied Electrochemistry*, vol. 10, no. 1, p. 61-70, **DOI:10.1007/BF00937339**.

[8] Jia, J., Tan, C., Liu, M., Li, D., Chen, Y. (2017). Relaxation-Induced Memory Effect of LiFePO$_4$ Electrodes in Li-Ion Batteries. *ACS Applied Materials & Interfaces*, vol. 9, p. 24561-24567, **DOI:10.1021/acsami.7b05852**.

[9] Farkhondeh M., Pritzker M., Fowler M., Safari M. and Delacourt C. (2014). Mesoscopic modeling of Li insertion in phase-separating electrode materials: application to lithium iron phosphate. *Physical Chemistry Chemical Physics*, vol. 16, no. 41, p. 22555-22565, **DOI:10.1039/C4CP03530E**.

[10] Kondo, H., Sasaki, T., Barai, P., Srinivasan, V. (2018). Comprehensive study of the polarization behavior of LiFePO$_4$ electrodes based on a many-particle model. *Journal of The Electrochemical Society*, vol. 165, p. A2047-A2057, **DOI:10.1149/2.0181810jes**.

[11] Križan, G., Križan, J., Dominko, R., Gaberšek, M. (2017). Pulse combustion reactor as a fast and scalable synthetic method for preparation of Li-ion cathode materials. *Journal of Power Sources*, vol. 363, pp. 218-226, **DOI:10.1016/j.jpowsour.2017.07.083**.

[12] Križan, G., Križan, J., Bajsić, I., Gaberšček, M. (2018). Control of a pulse combustion reactor with thermoacoustic phenomena. *Instrumentation Science and Technology*, vol. 46, no. 1, p. 43-57, **DOI:10.1080/10739149.2017.1320288**.

[13] Fongy, C., Gaillot, A.-C., Jouanneau, S., Guyomard, D., Lestriez, B. (2010). Ionic vs electronic power limitations and analysis of the fraction of wired grains in LiFePO$_4$ composite electrodes. *Journal of The Electrochemical Society*, vol. 157, no. 7, p. A885-A891, **DOI:10.1149/1.3432559**.

[14] Fongy, C., Jouanneau, S., Guyomard, D., Badot, J., Lestriez, B. (2010). Electronic and ionic wirings versus the insertion reaction contributions to the polarization in LiFePO$_4$ composite electrodes. *Journal of the Electrochemical Society*, vol. 157, no. 12, p. A1347-A1353, **DOI:10.1149/1.3497353**.

[15] Katrašnik, T., Mele, I., Zelič, K. (2019). advanced continuum Li-ion battery modelling framework. *11th International Conference on Applied Energy*, Västerås.

[16] Franco, A.A., Rucci, A., Brandell, D., Frayret, C., Gaberscek, M., Jankowski, P., Johansson, P. (2019). Boosting rechargeable batteries R&D by multiscale modeling: Myth or reality?. *Chemical Reviews*, vol. 119, p. 4569-4627, **DOI:10.1021/acs.chemrev.8b00239**.

[17] Zelič, K., Katrašnik, T. (2019). Thermodynamically consistent and computationally efficient 0D lithium intercalation model of a phase separating cathode particle. *Journal of the Electrochemical Society*, vol. 166, p. A3242-A3249, **DOI:10.1149/2.0381914jes**.

[18] Zelič, K., Katrašnik, T. (2019). Thermodynamically consistent derivation of chemical potential of a battery solid particle from the regular solution theory applied to LiFePO$_4$, *Nature Scientific Reports*, vol. 9, **DOI:10.1038/s41598-019-38635-2**.

[19] Newman, J., Tiedemann, W. (1975). Porous-electrode theory with battery applications. *AIChE Journal*, vol. 21, p. 25-41, **DOI:10.1002/aic.690210103**.

[20] Colclasure, A.M., Kee, R.J. (2010). Thermodynamically consistent modeling of elementary electrochemistry in lithium-ion batteries. *Electrochimica Acta*, vol. 55, p. 8960-8973, **DOI:10.1016/j.electacta.2010.08.018**.

[21] Bai, P., Cogswell, D.A., Bazant, M.Z. (2011). Suppression of phase separation in LiFePO$_4$ nanoparticles during battery discharge. *Nano Letters*, vol. 11, p. 4890-4896, **DOI:10.1021/nl202764f**.

[22] Bazant, M.Z. (2013). Theory of chemical kinetics and charge transfer based on nonequilibrium thermodynamics. *Accounts of Chemical Research*, vol. 46, p. 1144-1160, **DOI:10.1021/ar300145c**.

[23] Singh, G.K., Ceder, G., Bazant, M.Z. (2008). Intercalation dynamics in rechargeable battery materials: General theory and phase-transformation waves in LiFePO$_4$. *Electrochimica Acta*, vol. 53, p. 7599-7613, **DOI:10.1016/j.electacta.2008.03.083**.

[24] Kao, Y.H., Tang, M., Meethong, N., Bai, J., Carter, W.C., Chiang, Y.M. (2010). Overpotential-dependent phase transformation

pathways in lithium iron phosphate battery electrodes. *Chemistry of Materials*, vol. 22, p. 5845-5855, **DOI:10.1021/cm101698b**.

[25] Cogswell, D.A., Bazant, M.Z. (2012). Coherency strain and the kinetics of phase separation in LiFePO$_4$ nanoparticles. *ACS Nano*, vol. 6, p. 2215-2225, **DOI:10.1021/nn204177u**.

[26] Zeng, Y., Bazant, M.Z. (2013). Cahn-Hilliard reaction model for isotropic Li-ion battery particles. *MRS Proceedings*, vol. 1542, p. 13-15, **DOI:10.1557/opl.2013.740**.

[27] Tang, M., Huang, H.Y., Meethong, N., Kao, Y.H., Carter, W.C., Chiang, Y.M. (2009). Model for the particle size, overpotential, and strain dependence of phase transition pathways in storage electrodes: application to nanoscale olivines. *Chemistry of Materials*, vol. 21, p. 1557-1571, **DOI:10.1021/cm803172s**.

[28] Dargaville, S., Farrell, T.W. (2013). The persistence of phase-separation in LiFePO$_4$ with two-dimensional Li+ transport: The Cahn-Hilliard-reaction equation and the role of defects. *Electrochimica Acta*, vol. 94, p. 143-158, **DOI:10.1016/j.electacta.2013.01.082**.

[29] Dreyer, W., Jamnik, J., Guhlke, C., Huth, R., Moškon, J., Gaberšček, M. (2010). The thermodynamic origin of hysteresis in insertion batteries. *Nature Materials*, vol. 9, p. 448-453, **DOI:10.1038/nmat2730**.

[30] Orvananos, B., Ferguson, T.R., Yu, H.C., Bazant, M.Z., Thornton, K. (2014). Particle-level modeling of the charge-discharge behavior of nanoparticulate phase-separating Li-ion battery electrodes. *Journal of The Electrochemical Society*, vol. 161, p. A535-A546, **DOI:10.1149/2.024404jes**.

[31] Orvananos, B., Malik, R., Yu, H.C., Abdellahi, A., Grey, C.P., Ceder, G., Thornton, K. (2014). Architecture dependence on the dynamics of nano-LiFePO$_4$ electrodes. *Electrochimica Acta*, vol. 137, p. 245-257, **DOI:10.1016/j.electacta.2014.06.029**.

The Effect of Population Aging on Heating Energy Demand on National Level: A Case Study of Slovenia

Žiga Lampret[1] – Gorazd Krese[2] – Matjaž Prek[1,*]
[1]University of Ljubljana, Faculty of Mechanical Engineering, Slovenia
[2]Korona d.d., Slovenia

Residential energy demands are expected to change significantly in the future with increasing electrification, energy efficiency, and improved comfort as well as climate change. While many studies have been performed into how the aforementioned influential factors could affect the energy needs of the forthcoming generations, far less are present for how population aging affects the future heating demand. The latter is particularly relevant for Europe and Slovenia as declining fertility rates and lengthening life spans give rise to the increasing ratio of the elderly.

In this paper, the future residential space and water heating energy demands of the aging society in Slovenia, using a sample of geographically dispersed nursing homes as a proxy, are estimated. The results are compared against the latest EU reference scenario until 2050, whereby the adjusted estimates differ by up to 9.6 %. Thus, the study highlights the need for energy policy to be further refined and redefined to link the energy performance requirements of buildings to specific consumption characteristics of the elderly.

Keywords: energy forecasting, residential energy demand, space heating, domestic hot water (DHW), aging society, base temperature

Highlights
- *Projections for Slovenia's residential heating demand from the EU reference scenario 2016 were adjusted for population aging, using a representative sample of nursing homes as proxy.*
- *The gap between the reference and age-adjusted scenarios is grooving over time as the share of elderly is increasing.*
- *The useful energy demand for space heating differs up to 357 GWh or 6.5 % on the yearly level.*
- *The useful energy demand for water heating differs up to 117 GWh or 9.6 % on the yearly level.*
- *The total residential heating energy demand differs up to 474 GWh or 7.1 % on the yearly level.*

0 INTRODUCTION

In its 2030 Energy strategy the European Union (EU) is targeting 30 % reduction of greenhouse gas emissions (GHG) compared to year 1990 (and 80 % until 2050), renewable energy sources share increase to at least 27 % and an energy efficiency increase of at least 27 %. Improvements in the energy performance of the building stock represents one of the key opportunities in achieving these goals, as buildings represent 40 % of the end energy use in the EU [1] to [3]. However, in increasing the energy performance of the building stock, comfortable and quality indoor environment must not be compromised [4].

In addition to building characteristics, many studies have shown an important impact of indoor environment occupants on the residential energy demand [5] to [7]. This is especially emphasized in the case of the elderly, who usually tend to have indoor environment requirements linked to more intensive energy use. These different requirements are crucial to consider when modelling building energy use as well as when projecting future energy use [8].

The EU and other developed countries are encountering population aging, which presents a challenge in designing suitable living environment. Healthy aging is one of the main focus points of the World Health Organization and is included in their "Aging and Health" program [9]. Since elderly spend up to 90 % of the time in the indoor environment, a lot of concern is directed towards providing suitable living environments with a positive impact on their health and well-being.

Human body thermoregulation capabilities decrease with aging. Changes in the elderly thermoregulation contribute to changes in preferred indoor conditions and the ability of the human body to adapt to thermal stimuli [10]. Current thermal comfort standards and guidelines, based on the Fanger's model of thermal comfort [11], do not take into account effect of aging as they assume that different age groups do not perceive thermal environment differently. Other studies have, however, disputed that and shown that elderly prefer different optimal thermal environment conditions in comparison to younger adults. For example, Schellen et al. [12] showed that elderly group of subjects preferred warmer conditions as their younger counterparts, i.e. neutral thermal environment conditions of the younger subgroup were felt as cool by the elderly group. Similar results were obtained in [13], where the air temperature range of 20 °C to 24 °C, recognized as thermally comfortable by a younger group, was perceived as cool by the elderly, who expressed preference for warmer conditions.

Role of the occupant behaviour is often neglected when it comes to building energy modelling, by excessively focusing on the technical and physical attributes of buildings [14]. When it comes to future energy demand, projections primarily focus on climate change, economic drivers and demographic pattern in terms of population size. Even though studies have found relations between residential energy demand and household occupants age [15], there is a distinct lack of qualitative and quantitative research when it comes to precise deduction of age-related effects from the stand point of occupant behaviour and differentiation of thermal environment conditions, which subsequently results in higher space heating energy demand.

The focus of this study was to assess the effect of aging on the total residential heating demand on a national level. In order to quantify the difference between the energy use patterns of the elderly and the rest of the population, a representative sample of geographically dispersed nursing homes in Slovenia was used as proxy and compared against a control group of buildings with mainly residents from younger subgroups. In order to reveal the discrepancy in preferred thermal set-points, the sample buildings were analysed with regard to their base temperature values. In addition to space heating energy demand, possible variations in domestic hot water (*DHW*) demand were also investigated, which to our knowledge has yet to be researched from the standpoint of energy-related behavioural patterns. Finally, the results of the analysis were applied to adjust the energy demand projections for Slovenia, from the EU Reference Scenario 2016, for population aging.

1 DATA AND METHODS

1.1 Baseline

The baseline for our study represents the EU Reference Scenario 2016 (EUref2016) [16], which supports the European Commission's policy decision-making process via model-based energy system analysis until 2050 using the PRIMES energy system model [17]. In terms of modelling energy demand, the EUref2016 is analysed on sector level based on non-linear optimization routines and econometric functions [18]. Regarding useful residential energy demand, the PRIMES model uses two main drivers. Namely, number of persons per household and income per capita. Hence, the population trends are considered only in terms of projected number of residents and not in their age structure.

For our analysis, we limit ourselves only to trends for useful residential energy demand for space and water heating (see Table 1).

Table 1. *EUref2016 projections for Slovenia*

Year		2015	2020	2030	2040	2050
Useful energy [GWh]	Heating	5963	6127	5455	5706	5500
	DHW	1357	1395	1234	1277	1220

1.2 Demographic Trends

One of the key drivers affecting energy demand, particularly residential, are demographic trends. In our analysis, we use population projections from Eurostat with the base year 2018, i.e. EUROPOP2018 [19]. The EUROPOP projections provide the information on future population counts for all EU countries by sex and single year of age until 2100. We restrict our analysis to the period from 2020 to 2050 to be in line with EUref2016 (Table 2).

In our study, we use the same threshold age for the elderly as the European Commission [20], i.e. 65, which is also the minimum required age for admittance in nursing homes in Slovenia.

1.3 Heating Degree Days

Degree-days are commonly used to assess the impact of climate change on the annual and seasonal trends in the energy demand for space heating and cooling as well as the resulting GHG emissions [21] to [24]. Heating degree-days (*HDD*) are defined as sum of

Table 2. *EUROPOP2018 projections for Slovenia [19]*

Year		2020	2030	2040	2050
Population, January 1st		2,083,676	2,079,967	2,056,567	2,024,248
Population [%]	0 years to 14 years	15.2	13.6	13.0	14.1
	15 years to 65 years	64.5	61.4	58.5	54.5
	65 years and above	20.4	25.0	28.5	31.3
	80 years and above	5.5	6.8	9.8	11.6

positive differences between a reference or base temperature and the outdoor air (dry-bulb) temperature over a certain time period:

$$HDD = \sum_i \left(T_b - T_{o,i}\right)_{(\forall T_{o,i} < T_b)}, \qquad (1)$$

where HDD are heating degree-days, T_b is the base temperature, and $T_{o,i}$ is the mean daily outdoor temperature for the ith day.

The base temperature represents the maximum outside temperature at which no auxiliary heating is required to maintain the thermal comfort inside the building. The base temperature depends on the building's thermal characteristics (thermal insulation and inertia), internal (people, lights, appliances and equipment) and external (i.e. solar) heat gains as well as on the set indoor temperature and, is as such, specific for each building. Thus, if possible, the base temperature should be determined individually for each building as suggested in [25] and demonstrated by [26] to [31], instead of using common values prescribed by corresponding national bodies (e.g. 15 °C in Germany [32] and 12 °C in Slovenia [33]). One method for determining the base temperature from monthly energy data is the so-called performance line method proposed by Day et al. [34].

Performance lines are essentially best-fit straight lines through data on scatter plots of monthly heating energy use Q_{heat} against monthly HDD_m. The base temperature of a building is determined by putting a best-fit second order polynomial through data on a HDD_m versus Q_{heat} scatter plot and by varying the base until the polynomial best is almost equal to linear, i.e. the quadratic term's regression becomes zero as shown in Fig. 1.
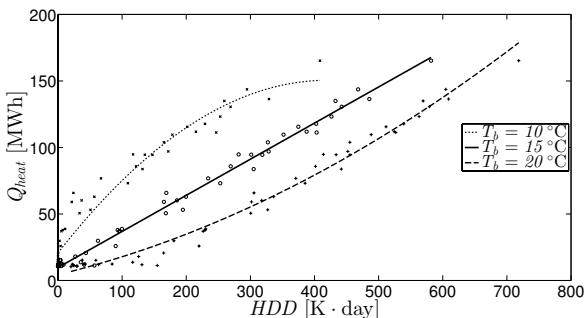
Fig. 1. *Base temperature determination according to the performance line method*

1.4 Population Aging Impact

In order to assess the effect of aging on the heating demand, a representative sample of geographically dispersed nursing homes in Slovenia (Fig. 2), i.e. representing 11.8 % nursing homes nationwide, was selected as proxy.

Based on the findings of the studies reviewed in the introduction, which indicate that the elderly prefer different indoor environment parameters than other age groups, we hypothesize that the heating base temperature of buildings occupied predominantly by seniors differs significantly from comparable residences of younger subpopulations due to different set-point temperature. To evaluate this hypothesis, we selected a control group of 16 buildings with similar thermal characteristics and heating systems as well as user profiles occupied primarily by younger (i.e. student dorms) and mixed-aged groups (Table 3).

Fig. 2. *Distribution of selected nursing homes according to Slovene statistical regions*

For both building groups, monthly calorimeter readings (separate space heating and *DHW*) from 2015 to 2018 were made available, while the corresponding mean daily air temperatures were obtained from local weather stations from the Slovenian Environment Agency's database [35].

Table 3. *Main building groups' characteristics – average values*

	Proxy nursing homes	Control group buildings
Number of occupants [-]	239 ± 57	265 ± 72
Gross net area [m²]	6,418 ± 2.556	5,358 ± 3.130
Wall U-value [Wm⁻²K⁻¹]	0.53 ± 0.13	0.57 ± 0.22
Window U-value [Wm⁻²K⁻¹]	1.71 ± 0.65	1.78 ± 0.55
Roof U-value [Wm⁻²K⁻¹]	0.35 ± 0.19	0.41 ± 0.22
Window – wall ratio [-]	0.127 ± 0.59	0.116 ± 0.66
Occupant density [m²/person]	26.5 ± 6.5	20.0 ± 7.8

The aging-adjusted space heating useful energy demand projections are then calculated as follows:

$$\hat{Q}_{heat,i} = Q_{heat,i} \cdot \left(1 - f_{old}\right) +$$

$$Q_{heat,i} \cdot f_{old,i} \cdot \frac{HDD_i\left(T_b \pm \Delta T_b\right)}{HDD_i\left(T_b\right)}, \qquad (2)$$

where $\hat{Q}_{heat,i}$ is the aging-adjusted space heating energy demand for the ith year, $Q_{heat,i}$ is the reference space heating energy demand for the ith year, $f_{old,i}$ is the elderly share of total population for the ith year, and ΔT_b is the base temperature difference between the nursing homes and the control group.

In Eq. (3), HDD on a national level was calculated as a population weighted sum of HDD of the 11 most populated cites in Slovenia (Appendix, Table 10), which represent 34.7 % of its total population:

$$HDD = \sum_j f_j HDD_j, \qquad (3)$$

where HDD_j is the HDD value for the jth city, and f_j is the population share of the jth city with regard to the total population of all the considered cites.

As DHW energy demand is not climate related, the following equation was used to estimate the future useful energy demand:

$$\hat{Q}_{DHW,i} = q_{DHW}^{yp} \cdot \left(N_{tot} - N_{old}\right) + q_{DHW}^{old} \cdot N_{old}, \qquad (4)$$

where $\hat{Q}_{DHW,i}$ is aging-adjusted DHW preparation energy demand, q_{DHW}^{yp} is the per capita DHW energy demand for the non-elderly subpopulation, q_{DHW}^{old} is the per capita DHW energy demand for the elderly subpopulation, N_{tot} is total number of citizens, and N_{old} is the number of elderly citizens.

2 RESULTS AND ANALYSIS

2.1 Space Heating

Tables 4 and 5 present base temperature values, for the selected nursing homes and the control group buildings, determined according to performance line method presented in subsection 1.3. Although the values seem quite similar at first glance, the nursing homes have on average a 1.34 °C higher base temperature, i.e. 16.76 °C versus 15.41 °C for the control group. This is in line with the studies summarized in the introduction, as seniors feel more comfortable at higher indoor temperatures.

The next step in assessing the impact of aging on space heating energy demand was to calculate the corresponding annual HDD. Here the question arose, which reference base temperature to select to appropriately represent Slovenia's dwelling stock, as

the control building group was too small to generalize its results across the entire country.

Table 4. *Base temperatures of the proxy nursing homes*

Nursing home	T_b [°C]	Nursing home	T_b [°C]
1	16.89	7	15.78
2	17.35	8	17.64
3	16.95	9	17.24
4	16.05	10	16.74
5	15.94	11	16.45
6	17.25	12	16.82

Table 5. *Base temperatures of the control group buildings*

Building	T_b [°C]	Building	T_b [°C]
1	15.22	9	15.49
2	14.45	10	16.32
3	18.36	11	14.86
4	16.88	12	17.50
5	11.68	13	14.56
6	15.88	14	15.72
7	13.25	15	16.20
8	14.89	16	15.37

As explained in subsection 1.3, the base temperature represents the balance temperature at which a building is in thermal equilibrium with its environment and, is as such, specific for each building. Therefore, it is not straightforward to determine a base temperature, which is representative for the entire dwelling stock on national level. For instance, the current Slovene legislation prescribes a base temperature of 12 °C [33] while Eurostat [36] as well as Germany [32] use 15 °C, which, essentially, means that the building stock in Slovenia has significantly better thermal characteristics than the average dwelling in the EU or Germany. Since this does not reflect the reality, i.e. average U-value of Slovene building stock 1.47 Wm^{-2}K^{-1} compared to 1.14 Wm^{-2}K^{-1} in Germany [37], and we did not have any data to support either of the proposed base temperature values, we decided to calculate HDD with multiple base temperatures between 12 °C and 15 °C with an 1 °C increment. The resulting HDD, calculated for 2015 as baseline (Eq. (3)), are shown in Table 6 while the corresponding corrected space heating projections (Eq. (2)) are depicted in Fig. 3.

As seen from Fig. 3, all the corrected projections are significantly higher than EUref2016. Particularly, the gap between the reference and age-adjusted projections is growing over time as the share of elderly is increasing (Table 2). The difference is most pronounced at the scenario with the lowest (12 °C)

base temperature, namely, between 4.2 % for 2020 and 6.5 % for 2050, and is decreasing with higher values of the reference base temperature, i.e. deviation between 3.4 % and 5.3 % at 15 °C. The changes between the corrected scenarios depend on the yearly air temperature distribution. Specifically, climates with distinctive temperature variations between seasons are more sensitive to chosen base temperature value and vice versa for moderate climates. This has serious implications for Slovenia and Europe as, due to climate change, transition seasons are getting shorter, while temperature extremes are becoming more frequent. Moreover, as thermal characteristics of buildings are constantly improving, we can expect that the base temperature of the future residential building stock will be more towards the lower end of our scale. Hence, aging will most probably have a more severe effect on space heating energy use than our adjustments suggest.

Table 6. *HDD values for projections correction*

T_b [°C]	$HDD(T_b)$ [K·day]	$HDD(T_b + \Delta T_b)$ [K·day]
12	1271	1534
13	1465	1745
14	1672	1972
15	1893	2211
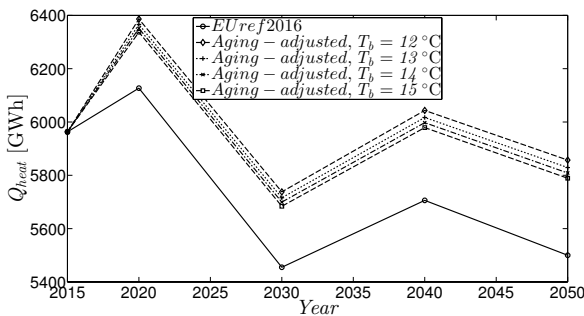
Fig. 3. *Comparison of space heating energy demand projections*

2.2 Domestic Hot Water

Contrary to space heating demand, *DHW* demand in far less researched even though it plays an important role in the total heat demand. With increasingly more energy efficient buildings in the future its role is expected to be even more important [38].

Since *DHW* heat demand is predominantly driven by occupant behavior [39], first, the energy use intensity variation between the selected nursing homes and the control group buildings had to be assessed (Table 7).

Table 7. *DHW annual energy use parameters*

	Energy use intensity		DHW share
	[kWh/m²]	[kWh/person]	[%]
Nursing homes	55.8	1497.6	27.7
Control group	44.5	822.5	33.4

Whereas the area energy use intensity of nursing homes was on average 25.2 % higher compared to the control group, a much higher differentiation, i.e. 82.1 %, was observed in terms of energy intensity per capita. This is a consequence of the lower occupant density in nursing homes, which is also characteristic for dwellings occupied by elderly households. On the other side, the *DHW* heat demand share was higher for the control group buildings, which is linked to the lower space heating energy demand as a consequence of lower base temperature values (Tables 4 and 5).

As the sample buildings do not represent actual dwellings, we could not directly apply the derived per capita energy intensities for the calculation of the corrected projections. Thus, Eq. (4) was modified as follows:

$$\widehat{Q}_{DHW,i} = \frac{Q_{DHW,i}}{N_{tot,i}} \cdot \left(N_{tot,i} - N_{old,i} \right) +$$

$$\frac{Q_{DHW,i}}{N_{tot,i}} \cdot \left(\frac{q_{DHW}^{nh}}{q_{DHW}^{cg}} \right) \cdot N_{old,i}, \tag{5}$$

where $Q_{DHW,i}$ is the reference *DHW* energy demand for the ith year, q_{DHW}^{nh} is the average per capita *DHW* energy demand of the proxy nursing homes, and q_{DHW}^{cg} is the average per capita *DHW* energy demand of the control group buildings.
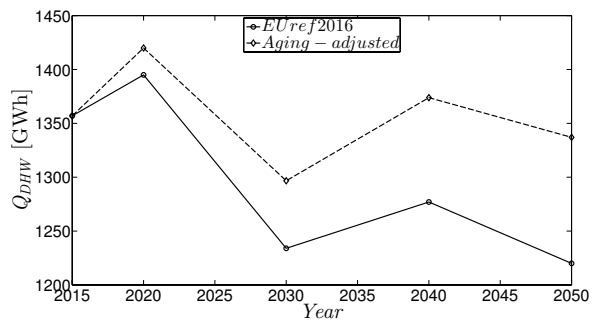
Fig. 4. *Comparison of DHW energy demand projections*

As was the case with space heating, the corrected projections for *DHW* are higher in comparison to the EUref2016 projections (Fig. 4). The discrepancy increases with years at a significantly higher rate as the gap at space heating projections, i.e. from 1.8 % in year 2020, to 9.6 % in year 2050. The reasons for this lies in the decreasing *DHW* energy intensity per capita

of the reference scenario (Table 8), which contradicts the recent trends [38].

Table 8. *DHW per capita energy intensity of the EUref2016 scenario*

	2015	2020	2030	2040	2050
$\dfrac{Q_{DHW,i}}{N_{tot,i}}$ [kWh/person]	658	669	593	621	603

2.3 Total Heating Demand

As indicated in subsection 2.1, we expect that the base temperature of buildings will decrease in the future. Therefore, for the total heating energy demand estimates only space heating projections, calculated with the lowest base temperature, were considered and summed together with the corresponding *DHW* projections from section 2.2.

As expected from the space and water heating results, the difference between the reference and aging-adjusted scenario increases together with the elderly share (Fig. 5), i.e. from 3.8 % or 284 GWh in 2020 to 7.1 % or 474 GWh in 2050.
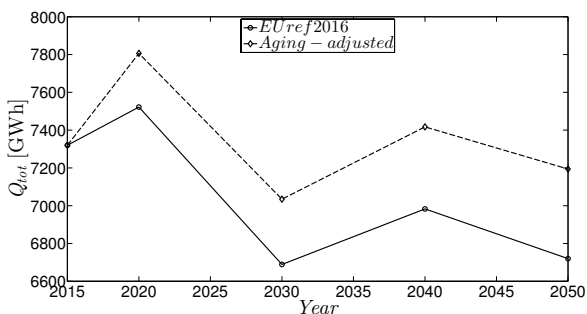
Fig. 5. *Comparison of total heating energy demand projections*

Particularly, the scenario gap is very similar as at space heating projections, since the latter represents a large majority of the total heating demand, namely from 81.8 % in 2020 and 81.4 % in 2050. This is not in line with the current trends, as the share of *DHW* in total heat requirement of new energy-efficient buildings is documented around 40″% to 50 % [40], although the impact of *DHW* is growing over the years (Table 9). This implies that the EUref2016 scenario, on which our corrections are based on, does not fully account for the thermal performance improvement of the building stock, envisioned by corresponding regulatory bodies, e.g. [41]. Furthermore, the reference scenario also does not consider the recent findings of increasing *DHW* consumption per capita [39], since it foresees a declining specific water heating demand, as already indicated in the previous subchapter (Table 8).

Table 9. *The effect of DHW on the scenario gap*

	2020	2030	2040	2050
$\Delta Q_{DHW}/\Delta Q_{tot}$ [%]	8.8	18.1	22.3	24.7

3 CONCLUSIONS

This paper presents a methodology for adjusting heating energy demand projections on a national level for population aging. The method is based on using heating energy measurements from a representative sample of real-life nursing homes as proxy. In this study, the data representing 11.8 % of nursing homes in Slovenia was used to adjust its foreseen residential heating energy demand according to the EUref2016 scenario.

In order to assess the effect of aging on the space heating demand, we determined the base temperature values of the observed nursing homes and compared them against a control group of buildings. The base temperature differed on average for 1.34 °C, which resulted in a projection deviation from 210 GWh to 357 GWh or 3.8 % to 6.5 %, respectively. This difference, basically, represents the discrepancy between the set-point temperatures of the elderly and the rest of the population, due to changes in the elderly thermoregulation. Hence, it implies that aging may nullify the positive effects of global warming on heating demands, as countries committed to the 2015 Paris Agreement (including Slovenia) strive to limit the temperature increase to 1.5 °C above pre-industrial levels. Furthermore, as the base temperature of the future dwelling stock is expected to decrease due to improved thermal performance of buildings, the discovered set-indoor temperature gap and with it population aging will most probably have a more severe effect on space heating energy use than our results imply.

On the other hand, the climate-unrelated *DHW* energy demand projections varied between 1.8 % and 9.6 % from the baseline scenario, whereby the gap is increasing over time as the foreseen share of seniors is growing. Contrarily, *DHW*'s share in the total heat requirement remains fairly stagnant over the future, at around 18 %, i.e. significantly lower than the sample buildings (Table 7). This contradicts the recent trends of the rising importance of water heating in the residential energy balance, which implies that the EUref2016 unsatisfactory accounts for the currently increasing *DHW* consumption per capita as well as the envisioned thermal performance improvement of the building stock.

Regarding the total heating energy demand, our aging-adjusted projections differ between 3.8 %, in 2020, and 7.1 %, in 2050, from the reference values for Slovenia. This results in an annual difference up to 474 GWh, which is more than the yearly energy production of small hydro power plants and almost twice of the annual generation of photovoltaic power plants in Slovenia in 2018 (i.e. 425.9 GWh and 259.1 GWh [42]). Hence, this discrepancy may have far-reaching implications for Slovenia's (sustainable) energy planning as well as for achieving its climate targets.

These results, however, should be interpreted with caution due to the assumptions and simplification made in this study. The most obvious simplification is that seniors admitted to nursing homes share the same energy usage patterns as independently living elderly, which currently represent more than 95 % of Slovenes aged 65 and above. This is especially critical when observing single-detached dwellings, as elderly households are typically smaller and, hence, a larger living area per capita must be heated to maintain thermal comfort, which implies that population aging may have a more profound effect on the residential energy balance than our research suggests. Thus, our study should be expanded to annual monitoring of energy use and energy-related behavioral patterns of dwellings occupied primarily by seniors as well as a reference group consisting of younger subpopulations. Here, the monitoring should be performed at least on an hourly basis, in order to discover potential deviations between daily energy profiles of different age groups, as this may become particularly important in light of the increasing electrification of the residential energy demand. Further research directions also include the effect of aging on the future space cooling energy demand as well as investigating possible interdependencies with energy poverty, since income of the elderly is generally decreasing with increasingly less sustainable pension systems all across Europe, which is again a consequence of population aging.

4 ACKNOWLEDGEMENTS

5 REFERENCES

[1] European Commission (2002). Directive 2002/91/EC of the European Parliament and of the Council of 16 December 2002 on the energy performance of buildings. *Official Journal of the European Union*, p. 65-71.

[2] EU (2010). Directive 2010/31/EU of the European Parliament and of the Council of 19 May 2010 on the energy performance of buildings (recast). *Official Journal of the European Union*, p. 13-35.

[3] Ivanovski, I., Goričanec, D., Salamunić, J.J., Žagar, T. (2018). The comparison between two high-temperature heat-pumps for the production of sanitary water. *Strojniški vestnik - Journal of Mechanical Engineering*, vol. 64, no. 7-8, p. 437-442, **DOI:10.5545/sv-jme.2017.5082**.

[4] Dovjak, M., Slobodnik, J., Krainer, A. (2019). Deteriorated indoor environmental quality as a collateral damage of present day extensive renovations. *Strojniški vestnik - Journal of Mechanical Engineering*, vol. 65, no. 1, p. 31-40, **DOI:10.5545/sv-jme.2018.5384**.

[5] van Dronkelaar, C., Dowson, M., Spataru, C., Mumovic, D. (2016). A review of the regulatory energy performance gap and its underlying causes in non-domestic buildings. *Frontiers in Mechanical Engineering*, vol. 1, p. 1-14, **DOI:10.3389/fmech.2015.00017**.

[6] International Energy Agency (2013). *Total Energy Use in Buildings - Analysis and Evaluation Methods*. International Energy Agency (IEA), Sendai, Japan.

[7] Wei, S., Jones, R., de Wilde, P. (2014). Driving factors for occupant-controlled space heating in residential buildings. *Energy and Buildings*, vol. 70, p. 36-44, **DOI:10.1016/j.enbuild.2013.11.001**.

[8] Yu, B., Wei, Y.M., Kei, G., Matsuoka, Y. (2018). Future scenarios for energy consumption and carbon emissions due to demographic transitions in Chinese households. *Nature Energy*, vol. 3, p. 109-118, **DOI:10.1038/s41560-017-0053-4**.

[9] Ormandy, D., Ezratty, V. (2012). Health and thermal comfort: from WHO guidance to housing strategies. *Energy Policy*, vol. 49, p. 116-121, **DOI:10.1016/j.enpol.2011.09.003**.

[10] Blatteis, C.M. (2012). Age-dependent changes in temperature regulation - a mini review. *Gerontology*, vol. 58, p. 289-295, **DOI:10.1159/000333148**.

[11] Fanger, P.O. (1970). *Thermal Comfort: Analysis and Applications in Environmental Engineering*. Danish Technical Press, Copenhagen.

[12] Schellen, L., van Marken Lichtenbelt, W.D., Loomans, M.G.L.C., Toftum, J., de Wit, M.H. (2010). Differences between young adults and elderly in thermal comfort, productivity, and thermal physiology in response to a moderate temperature drift and a steady-state condition. *Indoor Air*, vol. 20, p. 273-283, **DOI:10.1111/j.1600-0668.2010.00657.x**.

[13] Hwang, R.L., Chen, C.P. (2010). Field study on behaviors and adaptation of elderly people and their thermal comfort requirements in residential environments. *Indoor Air*, vol. 20, p. 235-245, **DOI:10.1111/j.1600-0668.2010.00649.x**.

[14] Estiri, H., Zagheni, E. (2019). Age matters: Ageing and household energy demand in the United States. *Energy Research and Social Science*, vol. 55, p. 62-70, **DOI:10.1016/j.erss.2019.05.006**.

[15] Deutsch, M., Timpe, P. (2013). The effect of age on residential energy demand. *ECEEE 2013 Summer Study Proceedings*, p. 2177-2188.

[16] Capros, P. (2016). *EU Reference Scenario 2016, Energy, Transport and GHG Emissions Trends to 2050*. EU Commission, Brussels.

[17] E3MLab (2018). *Primes model version 2018: Detailed model description*. National Technical University of Athens, Athens.

[18] Herbst, A., Reiter, U., Rehfeldt, M. (2017). Benchmarking the EU reference scenario 2016: An alternative bottom-up analysis of long-term energy consumption in europe. *ECEEE 2017 Summer Study Proceedings*, p. 159-169.

[19] Eurostat (2018). Europop2018: European population projections 2018-based, from *https://ec.europa.eu/eurostat/web/population-demography-migration-projections/population-projections-data*, accessed on 2019-10-22.

[20] European Commission (2014). *Population Ageing in Europe: Facts, Implications and Policies*. European Commision, Brussels.

[21] D'Amico, A., Ciulla, G., Panno, D., Ferrari, S. (2019). Building energy demand assessment through heating degree days: The importance of a climatic dataset. *Applied Energy*, vol. 242, p. 1285-1306, **DOI:10.1016/j.apenergy.2019.03.167**.

[22] Berger, M., Worlitschek, J. (2019). The link between climate and thermal energy demand on national level: A case study on Switzerland. *Energy and Buildings*, vol. 202, ID 109372, **DOI:10.1016/j.enbuild.2019.109372**.

[23] Jakubcionis, M., Carlsson, J. (2017). Estimation of European Union residential sector space cooling potential. *Energy Policy*, vol. 101, p. 225-235, **DOI:10.1016/j.enpol.2016.11.047**.

[24] Streicher, K.N., Padey, P., Parra, D., Bürer, M.C., Schneider, S., Patel, M.K. (2019). Analysis of space heating demand in the Swiss residential building stock: Element-based bottom-up model of archetype buildings. *Energy and Buildings*, vol. 184, p. 300-322, **DOI:10.1016/j.enbuild.2018.12.011**.

[25] Day, T. (2006). *Degree-Days - Theory and Application - TM41: 2006*. The Chartered Institution of Building Services Engineers, London.

[26] Day, A.R. (2005). An improved use of cooling degree-days for analysing chiller energy consumption in buildings. *Building Services Engineering Research and Technology*, vol. 26, p. 115-127, **DOI:10.1191/0143624405bt125oa**.

[27] Layberry, R. (2008). Degree days for building energy management — presentation of a new data set. *Building Services Engineering Research and Technology*, vol. 29, p. 273-282, **DOI:10.1177/0143624408093886**.

[28] Karlsson, J., Roos, A., Karlsson, B. (2003). Building and climate influence on the balance temperature of buildings. *Building and Environment*, vol. 38, p. 75-81, **DOI:10.1016/S0360-1323(02)00025-2**.

[29] Krese, G., Prek, M., Butala, V. (2011). Incorporation of latent loads into the cooling degree days concept. *Energy and Buildings*, vol. 43, p. 1757-1764, **DOI:10.1016/j.enbuild.2011.03.042**.

[30] Hitchin, R., Knight, I. (2016). Daily energy consumption signatures and control charts for air-conditioned buildings. *Energy and Buildings*, vol. 112, p. 101-109, **DOI:10.1016/j.enbuild.2015.11.059**.

[31] Krese, G., Lampret, Ž., Butala, V., Prek, M. (2018). Determination of a building's balance point temperature as an energy characteristic. *Energy*, vol. 165, p. 1034-1049, **DOI:10.1016/j.energy.2018.10.025**.

[32] VDI 2067-1 (2012). *Economic Efficiency of Building Installations (Fundamentals and Economic Calculation)*. Verein Deutscher Ingenieure (VDI), Düsseldorf.

[33] Ministry for Infrastructure RS (2015). *Rules on Dividing and Billing Heating Costs in Multiple-Dwelling and Other Buildings with Several Units*. Ministry for Infrastructure, Republic of Slovenia, Ljubljana.

[34] Day, A.R., Knight, I., Dunn, G., Gaddas, R. (2003). Improved methods for evaluating base temperature for use in building energy performance lines. *Building Services Engineering Research and Technology*, vol. 24, no. 4, p. 221-228, **DOI:10.1191/0143624403bt073oa**.

[35] Slovenian Environment Agency (2019). Meteo.Si - national meteorological service of slovenia, from *http://meteo.arso.gov.si/met/en/*, accessed on 2019-10-12.

[36] Eurostat (2019). Energy statistics - cooling and heating degree days, from *https://ec.europa.eu/eurostat/cache/metadata/en/nrg-chdd/esms.htm*, accessed on 2019-10-12.

[37] European Commission (2019). EU buildings database, from *https://ec.europa.eu/energy/en/eu-buildings-database*, accessed on 2019-10-22.

[38] Yang, X., Li, H., Svendsen, S. (2016). Energy, economy and exergy evaluations of the solutions for supplying domestic hot water from low-temperature district heating in denmark. *Energy Conversion and Management*, vol. 122, p. 142-152, **DOI:10.1016/j.enconman.2016.05.057**.

[39] Marszal-Pomianowska, A., Zhang, C., Pomianowski, M., Heiselberg, P., Gram-Hanssen, K., Rhiger Hansen, A. (2019). Simple methodology to estimate the mean hourly and the daily profiles of domestic hot water demand from hourly total heating readings. *Energy and Buildings*, vol. 184, p. 53-64, **DOI:10.1016/j.enbuild.2018.11.035**.

[40] Erhorn, H., Erhorn-Kluttig, H. (2014). Selected examples of nearly zero- energy buildings. EASME, Brussels.

[41] European Commission (2018). Energy performance of buildings directive (EU) 2018/844. *EU Official Journal (L156)*, vol. 276 LNCS, p. 17.

[42] Energy Agency of the Republic of Slovenia (2018). *Report on the energy sector in Slovenia 2018*. Energy Agency of the Republic of Slovenia, Maribor. (in Slovene)

[43] Statistical Office of the Republic of Slovenia (2019). Sistat database, from *https://pxweb.stat.si/SiStat/en*, accessed on 2019-10-15.

6 APPENDIX

Table 10. *Population size of the 11 largest municipalities in Slovenia in 2015* [43]

City	Population size	City	Population size
Ljubljana	287,347	Velenje	32,736
Maribor	111,735	Novo Gorica	31,771
Kranj	56,108	Ptuj	23151
Koper	51,053	Murska Sobota	18,935
Celje	48,901	Slovenj Gradec	16,758
Novo mesto	36,344	Σ	714,839

Green Tribology for the Sustainable Engineering of the Future

Mitjan Kalin* – Marko Polajnar – Maja Kus – Franc Majdič
University of Ljubljana, Faculty of Mechanical Engineering, Slovenia

Environmental awareness and especially the legislation that requires the reduction of polluting emissions are strong driving forces toward more sustainable engineering and greener solutions in the design, use and overall life span of machinery. However, providing novel concepts that will exclude non-environmentally adapted, but over many years developed and optimized solutions, is not an easy task. It clearly requires time if the same level of technical performance is to be maintained. Green tribology is one of the fields that has been closely involved in these actives in the past two decades. The research and use of tribology science and technology toward green and sustainable engineering include natural material usage, lower energy consumption, reducing natural oil resources, reducing pollution and emissions, fewer maintenance requirements and thus reduced machinery-investment cycles. This report is not an attempt to cover all the existing concepts, attempts or literature available in the field, but mainly those efforts that our group has been working on over the past 20 years, which mainly includes novel green-lubrication concepts that come from exploring and exploiting surface engineering through the use of diamond-like-carbon (DLC) coatings.

Highlights
- *Green tribology is closely involved and required field in a sustainable engineering of the future.*
- *New and innovative contacts with lower wear and friction and with lubrication concepts at a more sustainable and environmental level need to be developed.*
- *Green tribology is a newly developing and challenging field of modifying and innovating new tribology concepts, but having as a benchmark high-performance contacts that did not required to fully consider the sustainable engineering needs and were developed over many decades. This is thus a challenging task.*
- *We present some conceptual issues with green tribology in this work.*
- *Eight combinatorial green tribology concepts, involving DLC coatings and various lubrication technologies are presented with some results and potential for implementation.*

0 INTRODUCTION

0.1 The Need for Green Tribology in Sustainable Engineering

It is becoming very clear, with overwhelming evidence from researchers worldwide, that the use of fossil-based fuels is the key source of climate change. The consequences of this are rising temperatures, which are more than obvious, as well as rising sea levels and many catastrophic situations due to extreme weather. Therefore, we need to act immediately to reduce these energy-consumption levels as well as pollution in many forms, such as limitations on CO_2 and particle emissions in internal combustion engines, by, for example, EURO regulations, [1] (Fig. 1). What is more, through the UN Framework Convention on Climate Change (UNFCCC) [2], the Kyoto protocol [3] and the 2015 United Nations Climate Change Conference [4] held in Paris in 2015, 170 countries are now legally bound to reduce the amounts of energy they use from conventional fuel resources. In order to meet these obligations, lowering friction and reducing wear will play a critical role, Fig. 2.

If we consider all of the energy consumed on the planet, from industry to the home, and from the oceans to the skies, a massive 25 % is taken up by friction [5] and [6]. The 2015 figures from the International Energy Agency [7] suggest these frictional losses amount to a massive 5000 kWh for every person on earth. Moreover, every device or machine has a limited life-time due to the material damage caused by the wear of moving contacting surfaces. This wear leads to problems such as poor production quality, vibrations, noise and malfunctions.

This is expensive in terms of both the energy costs and the financial costs associated with the wear-related replacement of parts [8] and [9], machinery and vehicles that leads to increased demands for more production, and thus more energy consumption and so more pollution. Indeed, 2 % to 3 % of gross domestic product (GDP) in industrialized regions such as Europe is spent on wear-related replacements [10] and [11], which gives us an idea of how much energy is involved in this. Advances in tribology – the science

*Corr. Author's Address: University of Ljubljana, Faculty of Mechanical Engineering, Laboratory for Tribology
and Interface Nanotechnology, Aškerčeva 6, 1000 Ljubljana, Slovenia, mitjan.kalin@tint.fs.uni-lj.si

709
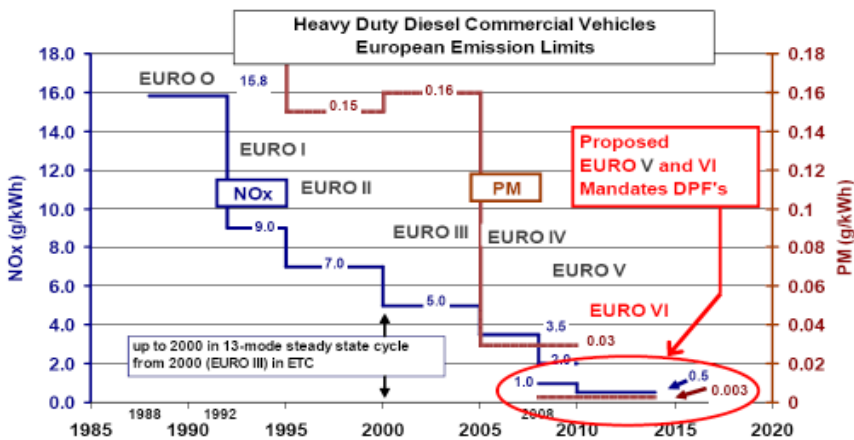
Fig. 1. *Demands of the novel EURO standards for the emission limits of internal combustion engines*

and technology of friction, wear and the lubrication of contacting surfaces in relative motion – are crucial for reducing friction and thereby saving energy and reducing climate change.

Lubricants consisting of a base oil and additives are the obvious and the most common means to reduce friction and wear, by interacting with materials and surface coatings to develop wear-protective and low-friction interface layers. However, the constituents of most effective lubricants are made from sulfur, phosphorus, zinc and other environmentally polluting elements. Here, national and international legislations have already placed severe constraints on the use of and demands for abandoning several of the most effective lubricant additives [12]. It has been estimated that if new green-lubrication technologies are not developed by 2021, the performance of a massive range of machinery will deteriorate, with serious technical and economic consequences [13].

Fig. 2. *Potential annual energy, cost and
CO_2 emission savings globally after 8 years
of intensive advanced tribology implementation
(1 EJ = 1018 J, G€ = Euro GDP, MtCO$_2$ = million tons of CO_2) [6]*

Thus, the challenge for green tribology is to reduce both friction and wear and improve lubrication in a sustainable way. However, in today's extremely advanced state of technology it is not sufficient to merely design a new, green lubricant or additive, adapt novel bulk materials or produce advanced low-friction surface coatings. The compatibility between these various components is complex and current solutions have taken years of development and optimization. If any new engineering contact is to result in substantially lower friction and wear, it needs to be sensitively tailored into an innovative combination of substrate, coatings, lubricant and additive, adapted to an optimized joint performance with low friction and wear, typically through the formation of particular nm-scale interface layers in these contacts.

0.2 The Challenges in Green Tribology

Green tribology was only defined as a scientific term in 2009 [14]. When we look at the content in publications dealing with green tribology, it turns out that they mainly describe what green-tribology research means [15], present some individual green-tribology goals or individual green-tribology principles, which are not entirely generalized [15], and describe the areas in which green tribology can be achieved [16] and [17], and in which applications it can be employed [16]. From an engineer's perspective, as someone who tends to employ or design a green tribological system, the term green tribology has tended to be used in the context of three principal thematics: biodegradable lubricants, biomimetic surfaces and green technologies such as wind turbines or tidal electric generators, etc. [18] and [19]. However, in this

way green tribology is frequently thought of in terms of isolated, or even hypothetical, solutions without a clear and feasible industrial scope, thus lacking a wide-ranging applicability. The general concepts of how to tackle the needs of green and sustainable tribological solutions are not widely explored and such contact systems are not well defined. However, several studies have already demonstrated that original, innovative, breakthrough green concepts are possible in tribology. The following section describes some of the current commonly discussed green-tribology solutions and their challenges.

For example, original, innovative approaches include chemical-based interactions with organic, environmentally adapted chemistry [20] and [21], and especially biodegradable lubricants (Fig. 3). To date, green tribology has been broadly considered as the use of biodegradable oils, lessening our impact on the environment [22] and [23]. However, biodegradable oils have already been used to reduce pollution for decades. Many studies [17] and [24], products [25] and [26] and legislation requirements [27] and [28] have already been developed. Accordingly, biodegradable lubrication is not a "new" concept of green tribology itself. However, it certainly represents one of the pillars that can be further developed in combination with different contacting materials that will reduce pollution overall. So, thinking in terms of the entire contacting system – a full-contact engineering approach – may further alter the green impact of biodegradable lubricants. However, there are many more potential options that need to be explored and evaluated.

Fig. 3. *Biodegradable lubricants from sunflowers have excellent lubricating properties at moderate temperatures, and are noticeably less harmful for the environment than fossil-based lubricants*

Furthermore, biomimetics and the behaviors of natural surfaces, such as a shark's skin or a water strider's hydrophobic microhairs [15], [29] and [30] that exhibit low friction and serve as examples

for mimicking them in the technical world, also show the potential for reducing friction and energy consumption; however, it still has an extremely limited or no role in green tribology or sustainable engineering. They are applied in only a few specific products, thus their impacts on energy consumption, polluting emissions, and resource depletion are very limited or non-existent. One such example is Speedo's famous Fastskin swimsuit (Fig. 4), inspired by the varying texture of a shark's skin that increased the efficiency of swimming, but it has no obvious impact on sustainable living. Therefore, green tribology needs to re-focus from these limited areas to the engineering areas where society can benefit the most.

The first idea of the sharkskin concept, with the specific design of the skin features, implies a reduction of the turbulence at the solid-liquid boundary layer and smoother and easier flow of the fluid over the surface. This idea can be roughly related to attempts to modify the lubricated friction via surface texturing [31]. There are many examples of friction and energy-consumption reduction through surface texturing due to optimized fluid flow, which is now becoming an affordable and used technology in many applications. This concept is certainly green; however, in such a generally defined result, all tribological solutions can be considered as green, because all tribology studies aim to reduce friction and/or wear. Therefore, future original and innovative green solutions that will employ new surface topographies and functionalities will have to synergistically integrate other concepts to become novel, system-generic, green technologies.
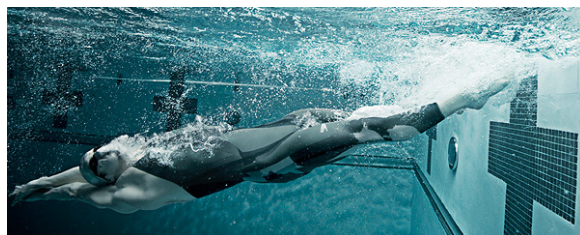
Fig. 4. *Speedo's Fastskin swimsuit inspired by the texture of a shark's skin*

Finally, green tribology should be closely related to many fast-developing green applications, such as producing green energy [15] and [23]. Namely, wind turbines (Fig. 5), wave- and tide-energy devices, are clearly bringing more green and sustainable engineering, similar to electrical and hybrid cars. However, it turns out that very often these systems do not employ any inherently green tribology concepts during their construction, operation, maintenance, or

decommissioning. This means they are only giving the impression of true, green innovation, whereas in fact the device itself may be devoid of green lubrication, and might have been built without any thought to resource depletion. From this it is very clear that generic green-tribology contacts and systems must be developed with proper green-engineering concepts in order to have a measurable green impact, which should span the product's whole life cycle. We must remember, it is only green if it is green from start to finish, "from cradle to grave".

Fig. 5. *Wind turbines in an offshore field; is this system designed in a truly green way?*

1 SOME GREEN-TRIBOLOGY CONCEPTS ASSOCIATED WITH DLC COATING ENGINEERING

Our studies include a number of green-tribology concepts that have been investigated over the past 20 years. These include, in all cases, diamond-like carbon (DLC) coatings, Fig. 6. DLC coatings are an amorphous material consisting mainly of carbon atoms in the sp^2 or sp^3 hybridization, typically with some hydrogen content, with many doping strategies being employed to tailor their properties.
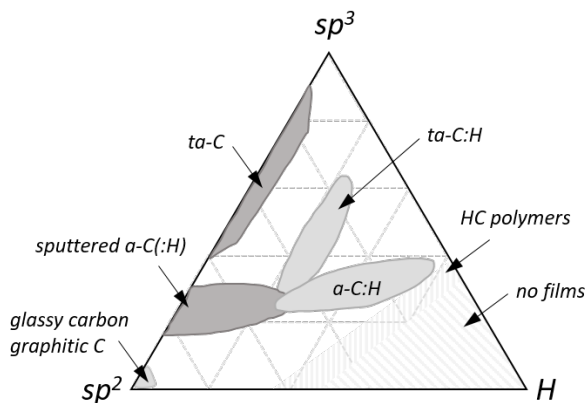
Fig. 6. *Ternary phase diagram of the amorphous carbon–hydrogen system*

In the search for the best surface solutions under lubricated conditions, DLC coatings are becoming very attractive due to their inherent low-wear and low-friction properties [32] to [35]. However, the key benefit, but also a challenge with DLC coatings and so with their lubrication, is their low reactivity [33] and [36] to [38]. They exhibit very low adhesion, which gives them a low-friction property, but on the other hand this means that their interactions with lubricants are weak, and difficult to control or predict. So, DLC coatings give problems and opportunities at the same time, and thus a great potential for innovative lubrication solutions – including green tribology. So far these coatings have already been implemented in many components in the automotive industry, such as gears, cam shafts, and piston rings (Fig. 7).

Fig. 7. *Some of typical components in automotive applications that are often coated with DLC coatings*

1.1 Biodegradable Oils

The most obvious way to reduce the environmental danger and harm associated with conventional lubricating oils was to employ biodegradable oils. In the early days, the DLC reactivity toward oils was still very much under question and many controversial results were reported because of a lack of a detailed methodology and the novelty of the field of DLC lubrication. However, the idea of employing bio-degradable oils with DLC was tempting. We showed that biodegradable lubricants actually perform very well with DLC coatings. Moreover, due to the large number of polar functional groups, biodegradable oils are highly polar and so more reactive than regular mineral or synthetic oils. This has shown to be a very effective lubrication mechanism for bio-degradable oils with DLC coatings [39], Fig. 8. This beneficial effect of green lubrication was also proved in several applications, such as gears [40], grinding machines [41] and hydraulics [42].
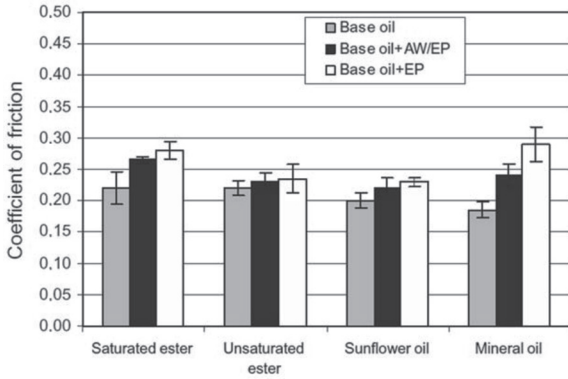
Fig. 8. *Coefficient of friction in DLC/DLC contacts for mineral and different bio-degradable oils* [39]

Fig. 9. *Friction-force modulation (FFM) and AFM topography image; for FFM the darker area represents a lower stiffness and the brighter area a higher stiffness; LS stands for low SAPS, HS for high SAPS and ZDDP for this additive in base oil* [53]
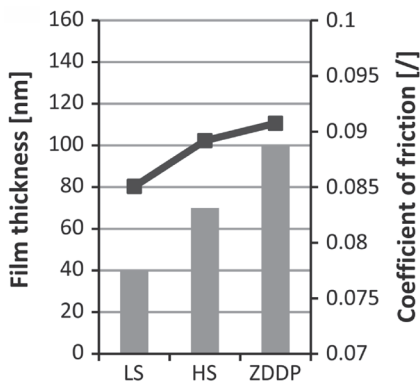
Fig. 10. *Correlation between film thickness and macroscopic coefficient of friction on Si-DLC surfaces* [53] *(Note: Columns represent the film nano-thickness, line represent the friction.)*

1.2 Low-SAPS Oils

In the past 20 years many chemically based interactions between different additives and DLC coatings were studied. Initially, strong extreme-pressure (EP) additives or the most effective types of anti-wear (AW) additives were investigated to first find the clear interactions between the additives and the DLC [36], [37] and [43] to [45], which were at that time still questioned. Nevertheless, direct chemical evidence of the interactions between additives and DLC surfaces were obtained using different surface-sensitive techniques [45] to [49]. Indeed, these interactions were weaker than those with steel and

occurred to a lesser extent. Moreover, the positive effect of DLC doping with different elements was proposed and shown empirically with several coatings [37] as well as by chemical analyses [46] and [50]. Accordingly, evidence of the chemical reactivity of DLC coatings with relatively strong additives (mainly sulfur-containing, as well as phosphorus-containing) was presented in the literature. In view of these and many other studies it became obvious that very strong interactions between the DLC and the additives would hardly be possible with contemporary additives. The requirement for greener lubrication was then a clear push to developing even stronger DLC-tailored additives, which may not be the best route for DLC lubrication solutions, and especially green sustainable
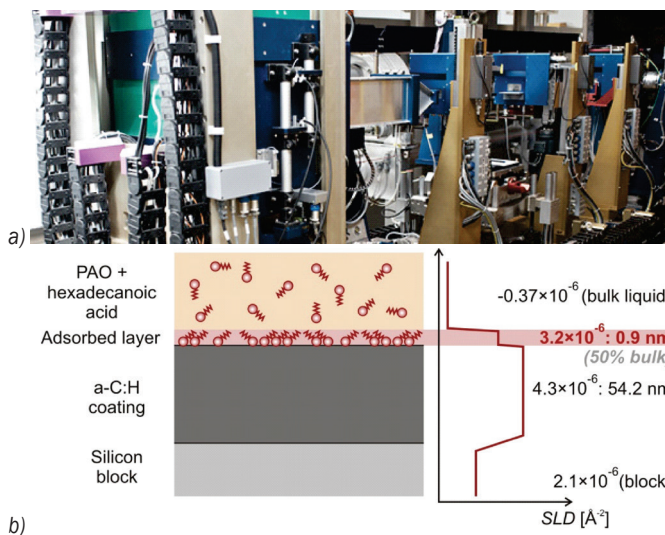
Fig. 11. *a) Photograph of a neutron-reflectivity final stage set-up; and b) a model of adsorbed boundary film (SLD is scattering length density) based on the results of neutron reflectometry from* **[58]**

engineering. Accordingly, many studies have focused on low-sulphated ash, phosphorus and sulfur (SAPS) oils and their interactions with DLC **[51]** to **[54]**. These studies showed that even low-SAPS oils can effectively protect the surfaces and reduce the friction. Moreover, in many cases the friction was lower with low-SAPS than with high-SAPS oils or with the well-known Zinc dialkyldithiophosphate (ZDDP)-based oils **[53]** and **[54]**. These observations were associated with the mechanical properties of the films that were revealed by using an atomic force microscope in the force-modulation mode and shown in terms of the mechanical properties of two different film areas, Fig. 9. Detailed analyses of the tribofilms from low-SAPS oils revealed the low film thickness of the films, which was nevertheless sufficient to reduce the wear and friction. In fact, in contrast to steel, the DLC-coated surfaces resulted in lower friction if the tribofilms were thinner **[53]** and **[54]**, Fig. 10.

1.3 Simple Mild Organic Additives

The above-mentioned findings led to further thoughts on the effect of mild additives, with low coverage or low thickness, which may be sufficient to reduce wear and friction. Several detailed studies of the adsorption ability of these additives were performed using atomic-force microscope (AFM) and neutron reflectometry **[55]** to **[59]**. The latter technique is very sensitive to a determination of the sub-nanoscale boundary layers of the additives, Fig. 11. These studies included detailed, nano-scale analyses of the

adsorbed layers from alcohols and fatty acids, as well as their density and thickness, Fig. 11b. Indeed, it was found that alcohols and fatty acids do form adsorbed layers on DLC coatings, Fig. 12. These are not complete mono-layers, but may only partially
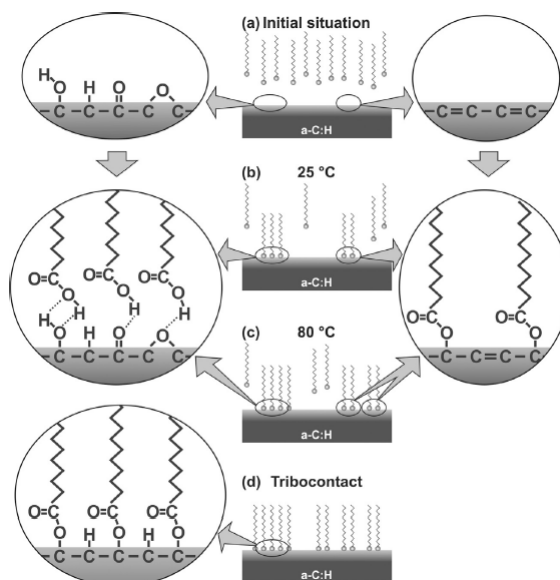
Fig. 12. *Schematic representation of the physical and chemical adsorption of a fatty acid onto a DLC surface for: a) the initial situation where the surface is partially covered with oxides and hydroxides (due to ambient air and moisture); b) at 25 °C where hydrogen bonds are formed; c) at 80 °C that promotes the adsorption significantly; and d) in the tribocontact where rubbing induces chemisorption* **[55]**

cover the surfaces, since densities of only 50 % were measured and the layer thicknesses were less than 1 nm. This is in agreement with molecular-dynamics and quantum-chemistry investigations that showed very similar behavior [60]. A model for the interaction of simple alcohols and fatty acids was proposed, with a clear conclusion that fatty acids are more effective than alcohols [56], but friction can be clearly reduced with such mild, organic additives on DLC coatings [55] and [57].

1.4 Base Oil Molecular Structure and Rheology Effects

One more phenomenon was revealed during a study of various oils in DLC lubrication. Namely, that the lubricated friction of a very smooth DLC is typically larger than non-lubricated. The reason lies in the fact that low-adhesion DLC coatings, when very smooth, which further surpresses the friction from asperity deformation or scratching, results in very low friction values. However, when adding a lubricant, viscous friction is actually added to the contacts. Accordingly, lubricant layers with a longer molecule or a higher viscosity have higher cohesion energies and thus stronger molecular forces. Such lubricant layers should be more difficult to shear and/or penetrate through for the asperities; therefore, they should separate the surfaces at the asperity contacts better. However, completely different behavior related to the increased friction with increased chain lengths and viscosity was noted for the DLC surfaces. Namely, compared to the non-lubricated conditions, additional energy was needed to move and penetrate through the lubricant molecules in the contact under high pressure,
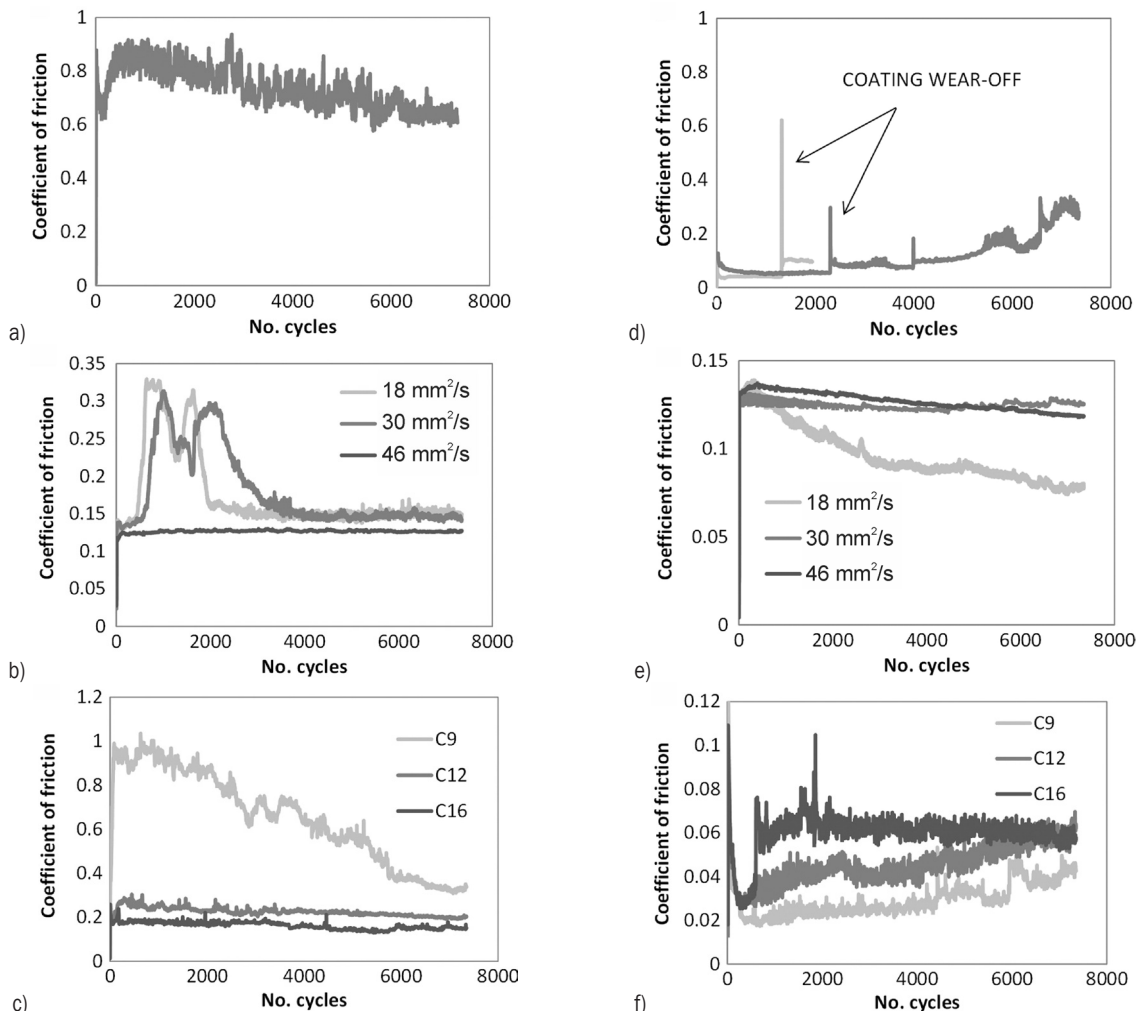
Fig. 13. *Coefficient of friction in steel/steel (a, b, c) and DLC/DLC contacts (d, e, f) for: (a, d) unlubricated conditions, (b, e) lubricated with polyalphaolefin oils with different viscosities and (c, f) for oils with different chain length* [64]

which were adsorbed on the contacting surfaces, and so the friction increased (compare Figs. 13d, e and f). This is because when the material has inherently low-friction properties under non-lubricated conditions, as is the case with the DLC coatings, [61] to [63], the additional force needed to shear the lubricant layers in the contact is higher than the reduction of adhesion or deformation, which are the two main sources of friction in the boundary lubrication of conventional metal surfaces, Fig. 14. The higher the molecular chain length or viscosity, the higher the cohesive energy of the layer, and thus more energy is required to break or shear it, and thus the friction is higher. Our results clearly confirm these relations, both for the poly-alpha olefin (PAO) oils and the pure alkanes [64]. In contrast, in the case of steel, the oil significantly reduces the adhesive interactions and thus the tangential forces required to break the metallic covalent bonds, which otherwise occur easily under non-lubricated conditions, [65], (compare Figs. 13a, b and c).
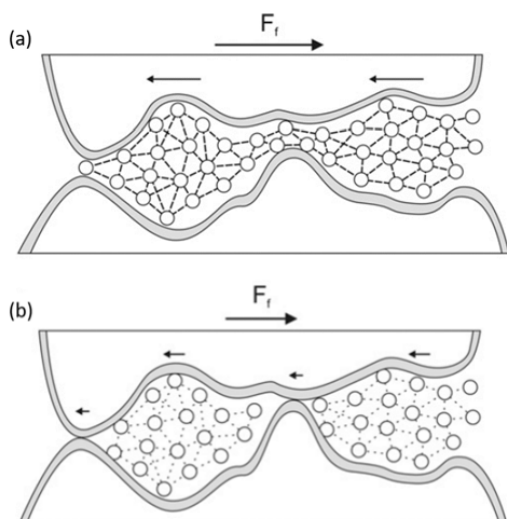
Fig. 14. *Schematic of a DLC/DLC contact lubricated with a) high-shear and (b) low-shear lubricant, representing its high- and low-cohesion strengths, respectively* [64]

It is thus very important to note that DLC provides both low wear and friction also with the base oils only. Accordingly, although strong reactive additives were found to improve the wear behavior of the DLC, they may not be required for DLC-coated systems, especially since sometimes they also increase the friction, and the wear of the coatings is already low compared to steel surfaces. From this point of view, milder additives, such as low- or no-SAPS additives, may be sufficient to protect even the most heavily loaded contacts, when coated with DLC, while being able to maintain other non-coated surfaces in the system under satisfactory tribological conditions.

1.5 Nanoparticles

Since it has become clear that DLC coatings are not adequately active toward chemical-based additives, other concepts that are predominantly physical based seem very welcome as potential lubrication solutions for DLC green technology. Self-lubricating nanoparticles are thus an interesting lubricating concept to be explored from various points of view. The idea of nanoparticle-assisted lubrication was proposed as a promising concept some time ago. However, despite the numerous types of nanoparticles that have already been tested and some that have already been used in practical applications, several tribological mechanisms and the relevant influential parameters under different contact conditions have yet to be determined.

Following the advances in conventional solid lubrication and the established theory of the transfer films [66] and [67], research has focused on the tribology of graphite-like nanostructures, i.e., C60 fullerenes [68] and [69], carbon nanotubes [70] and [71] and carbon nano-onions [72] and [73]. In lubricated conditions, however, the nanoparticles used were mainly fullerene-like structures of IF-MoS$_2$ (Fig. 15) and IF-WS$_2$, where it was revealed that these inorganic nanoparticles perform very effectively as additives in lubrication fluids [74] to [77].
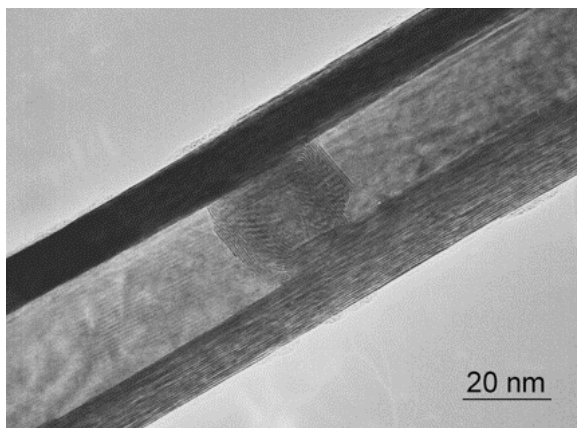
Fig. 15. *TEM image of the MoS$_2$ nanotube, i.e., "mama-tube" (Courtesy dr. Maja Remškar, Jožef Stefan Institute, Ljubljana, Slovenia)*

The proposed low-friction mechanisms of the nanoparticles are similar to their macro-scale structures, i.e., based on low-shear basal planes
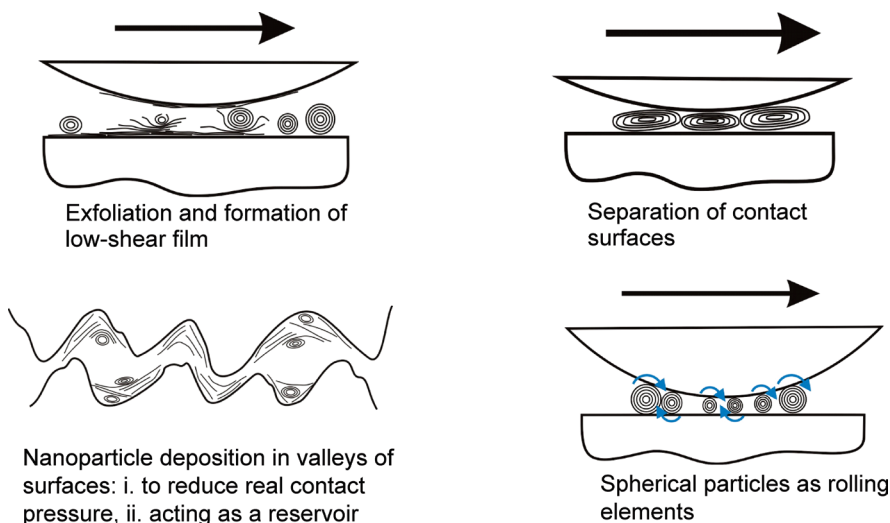
Fig. 16. *Lubrication using nanoparticles, based on physical mechanisms, without any SAPS*

of layered materials, such as MoS_2, WS_2, and/or graphite. There have also been other mechanisms proposed (Fig. 16), most frequently the rolling of the nanoparticles, and this mechanism again does not include any chemical reactions with elements and compounds associated with environmental emissions. It should be stressed that MoS_2, which is one of the best-known solid lubricants, is also a very chemically stable compound, which means it is not likely to contribute to emissions. Accordingly, it seems that nanoparticles, once placed in a lubricated mechanical system, can form protective nano-sheets at the surface and provide low friction and wear with a limited environmental impact, representing the potential for novel green-lubrication technologies.
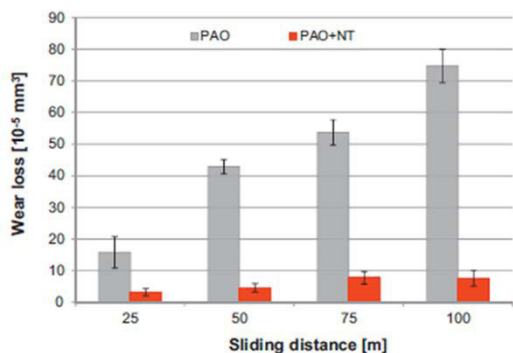
Fig. 17. *Wear loss of steel balls in a contact lubricated with pure base oil (PAO) and base oil with 5 wt.% MoS_2 nanotubes (PAO+NT) depending on the sliding distance* [77]

However, the nanoparticle-lubrication mechanisms are not yet fully agreed, and the research still tackles some fundamental problems related to the dispersion, agglomeration/aggregation and sedimentation of nanoparticles in oils. For this reason, available studies and results with nanoparticles in oils are still mainly in combination with steel or other metal surfaces, and these results suggest huge improvements in friction and wear performance, such as, for example, those in our own work [78] using MoS_2 nanotubes in PAO oils, Fig. 17.

Accordingly, solid-lubricating layered structures, such as MoS_2 and WS_2 nanoparticles, which are effective through a physically based lubrication mechanism (Fig. 16), can simultaneously provide a solution for the two above-discussed problems. Firstly, they can act as physical-based additives in lubricants for poorly reactive surfaces such as DLC coatings and similar non-conventional materials that cannot react effectively with today's chemically based additives. Secondly, since inorganic nanoparticles of MoS_2 and WS_2 are synthesized in closed forms with highly inert basal planes [79], they are chemically non-reactive and do not result in harmful emissions. So, their second advantage is in reducing the emissions and consequently – at least partially – solving the problem of the necessary elimination of high-SAPS additives and thus providing the possibility for a novel, green-lubrication technology.

In addition to the common nanoparticles of MoS_2, WS_2 and carbon nano tube (CNT), graphene is another very promising material with many positive examples and potential. There has been a huge global interest in and study of graphene properties; however, it is surprising that there are very few studies on macro-

scale tribology dealing with graphene as an additive to lubricants [80] to [83]. Our resent work has shown the great potential of graphene as a green oil additive, having much better tribological performance than conventional graphite or CNT [84]. This is another novel result from a series of nanoparticle studies that we made in the past decade, to look at the potential of graphene as an oil additive.

1.6 Oil-Surface Boundary Slip

Another concept for green lubrication can be realized through tailored physical-chemical interactions at the solid-liquid interfaces that induce slip at the lubricated contacting surfaces, Fig. 18. This solid-liquid slip is a well-known phenomenon and can be observed in nature, as the lotus-leaf effect, or in everyday life, as the slip of an oil droplet on a polytetrafluoroethylene (PTFE)-coated pan, Fig. 19.
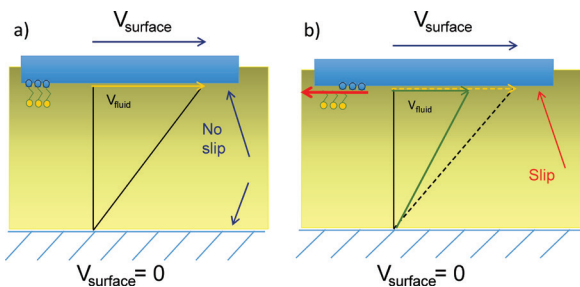
Fig. 18. *Solid-liquid interface: a) without boundary slip; and b) with boundary-slip conditions*

Recently, we have shown that, based on modified surface energies for tailored lubricants to reduce wetting behavior, friction can be significantly reduced, by up to 50 %, and lubrication design can be modified based on these parameters. Several papers describe

this new concept in lubrication design [85], the effect of various materials and wetting properties [86], and the contact configuration [87], Fig. 20.

The DLC coating was used as a model material, since DLC coatings are known to have a lower surface energy than steel and poorer wetting. Fig. 21 shows the friction reduction in the elasto-hydrodynamic lubrication (EHL) regime only due to the use of surfaces where at least one surface possesses poorer wetting and/or surface energy compared to steel. Similar results supporting this concept were also reported in some other studies [88] and [89].
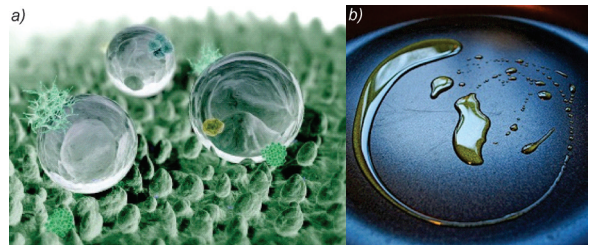
Fig. 19. *Two examples of solid-liquid slip: a) the lotus-leaf effect; and b) an oil droplet in a PTFE-coated pan*

We have further verified these suggestions and the concept by purposely using several different DLC coatings, having a variety of different surface characteristics, and the same conclusion was always confirmed [86] and [87]: DLC surfaces result in less friction than steel in the EHL regime, and also during the transition from mixed to EHL. Moreover, when only one such surface is in contact, the friction is higher than in the case of two such surfaces, but it is lower than with both steel surfaces (steel/steel) in contact (see Fig. 21). The results in the boundary regime appear the same, but further tests need to be conducted to confirm the behavior in this regime.
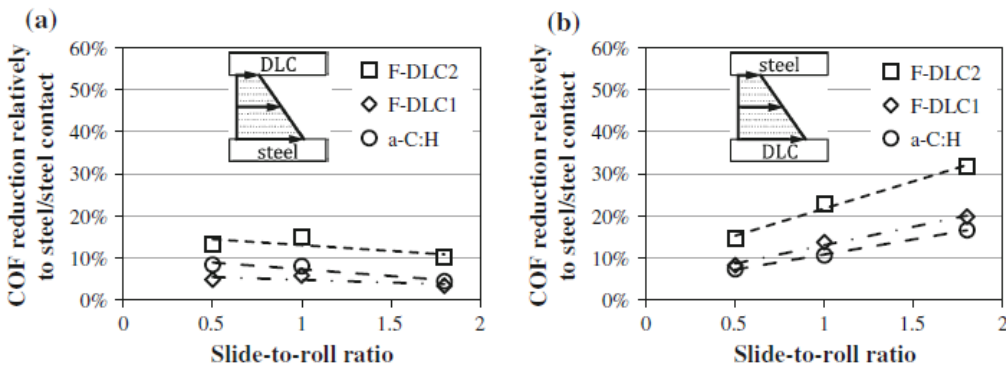
Fig. 20. *Relative decrease in the coefficient of friction in the case of mixed steel/DLC contacts compared to a steel/steel contact for DLC on: a) slow; and b) fast surface [87]*
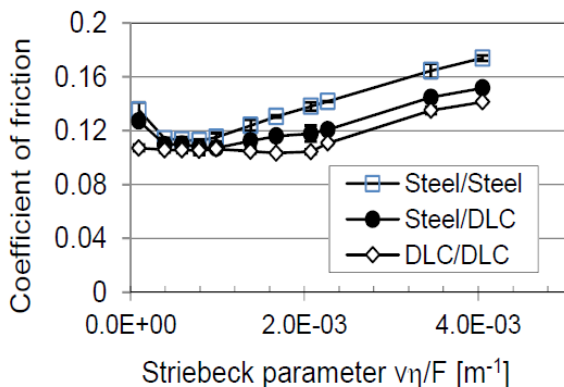
Fig. 21. *Friction reduction using one or two DLC surfaces with a lower surface energy and wetting [85]*

Although the concept of solid-liquid slip is well-known and was previously already observed to reduce friction drag under different circumstances, primarily theoretically, using various model materials or experiments on the nano scale [90] to [94], this was not comprehensively investigated on the macro scale with engineering materials and lubricants, with the exception of a few studies [85] to [89] and [93]. Accordingly, it turns out that although the relevance of solid-liquid interface properties is well-accepted,

a model that correlates these parameters and friction does not yet exist, and only indirect, empirical correlations to establish these parameters are available today [85].

Considering the above findings on wetting effects, one can reasonably assume that if the wetting conditions change the elasto-hydrodynamic (EHD) friction due to the use of low-surface-energy DLC coatings, similar effects can be obtained by modifying the wetting with adsorbed additive layers. However, there is almost no information about whether, and how, the additives change the wetting and the role that the temperature plays. Moreover, if the additives can affect the wetting properties, instead of hard surface coatings such as DLC, this would have a huge beneficial economic effect due to the lower cost and easier application method than the surface coatings on the most commonly used steel surfaces. Our latest investigations showed that additives indeed modify the wetting, both at room [95] and elevated temperatures. As seen in Fig. 22, advancing contact angles that were varied systematically for several molecular structures of simple organic additives, change a lot, indicating the strong potential for the additives to be tailored for a specific wetting and slip property. Moreover, it
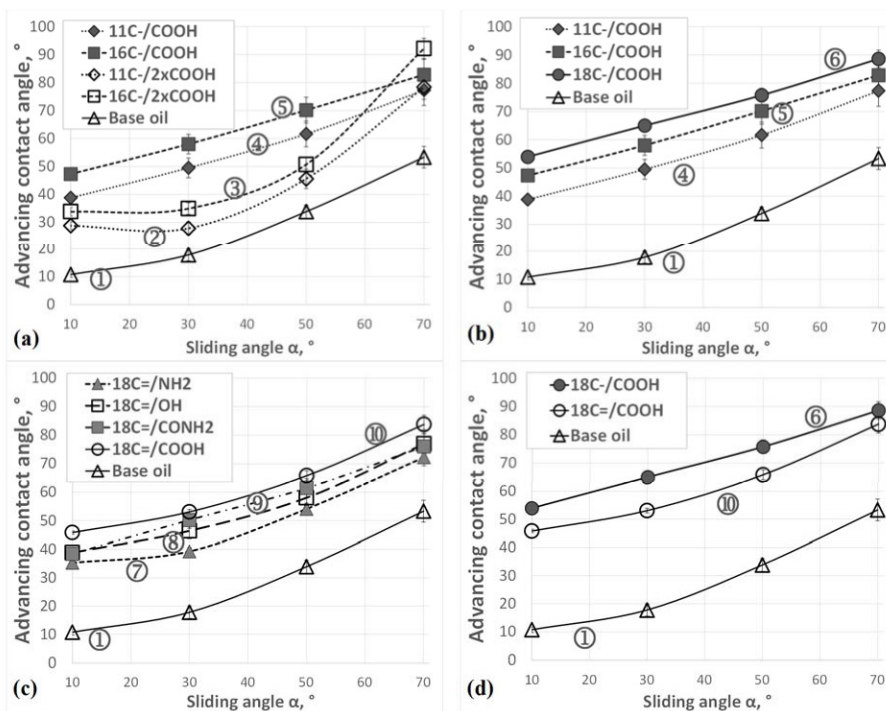
Fig. 22. *Influence of a) different number of COOH groups; b) different chain length of the additive; c) different polarity of functional groups; and d) saturation of additive on advancing contact angle for steel with and without additives [95] (Note: nine polar molecules were used as additives, having different chain length, polar head-group, saturation and number of polar head-groups.)*

Fig. 23. *Some potential applications where wetting effects and solid-liquid slip concept could be implemented to reduce the friction in a green and sustainable way*

was found that these adsorbed layers also noticeably reduce the EHD friction.

The concept of slip tailored by wetting properties is thus a promising concept for enormous savings in terms of energy consumption for all applications with solid-liquid interfaces where the fluid resistance represents a major part of the drag force and friction, Fig. 23.

3.7 Ionic Liquids

One of the latest attempts to develop green and efficient lubricated contacts is to use DLC coatings with ionic liquids, which are salts that are liquid at temperatures below 100 ºC. The reason lies in the fact that ionic liquids are very reactive molecules, which may strongly interact with the DLC, especially when doped, as well as being green in nature. Namely, ionic liquids are salts composed of positively charged cations and negatively charged anions [96], Fig. 24. They exhibit some unique properties, which make them good candidates for lubrication additives, for example, low vapor pressure, high thermal stability, electrochemical range, non-flammability and being benign to the environment [97] to [99]. So far, there are no literature reports on whether such lubricated contacts can perform satisfactorily and whether ionic liquids can indeed be a potential additive for DLC. This study is on going, but some of the results suggest an extremely low coefficient of friction under selected conditions, thus giving hopes for niche applications, where such a green-lubrication technology could be introduced.
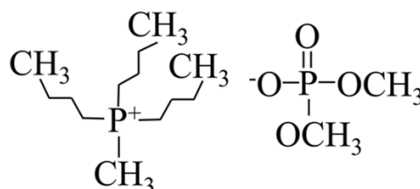
Fig. 24. *Molecular structure of a phosphate-based ionic liquid (Tributylmethylphosphonium dimethylphosphate ($C_{15}H_{36}O_4P_2$)) with positive and negative ionic parts*

1.8 Water Lubrication

Finally, water has been generating huge interest over the years as the ultimate environmentally acceptable fluid, especially if used without additives. Environmental awareness and its protection are becoming increasingly important when it comes to lubrication in engineering applications, in particular in open-air environments, where oil spilling directly pollutes nature, such as in forests, marine, mining, agriculture, etc. In this view, water lubrication represents a green-lubrication technology that could replace conventional oil lubrication [100]. However, due to its low viscosity and very poor lubrication with respect to conventional steels, water is not suitable for the lubrication of machines in its present form. Thus, tribological engineering needs to be introduced in the contacting surfaces and to modify the conventional contacts.

In the past, extremely successful cases were shown where water was used as a lubricant in ceramic contacts, with applications including a water pump with ceramic seals (Fig. 25), or tap-water valves.

Namely, silicon nitride or silicon carbide provide super-low friction of 0.002 and 0.0035 when sliding in water [100] to [103].
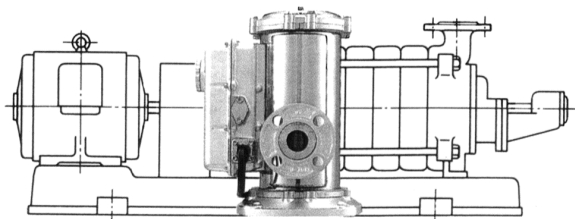
Fig. 25. Water pump with 5-imes-reduced volume due to the implementation of SiC seals (Courtesy prof. K. Kato, K. Adachi, Tohoku University, Sendai, Japan)

However, the strong effect of water pH, zeta-potential, ionic composition and so geographical dependence was recognized [104] to [107], Fig. 26.
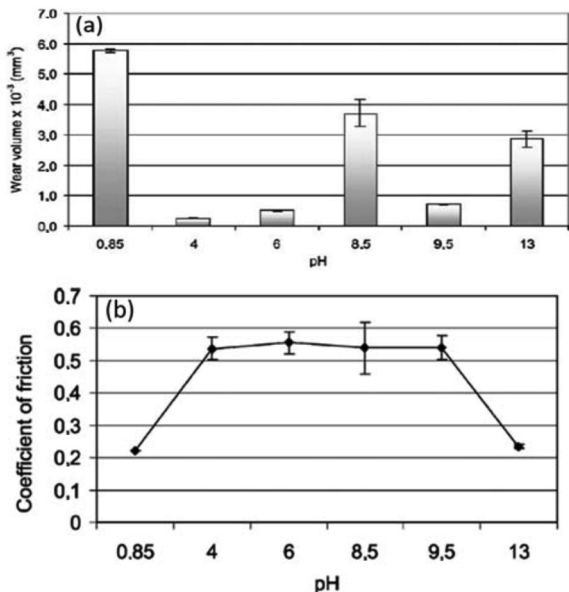
Fig. 26. Effect of water pH on: a) wear volume of alumina pins; and (b) steady-state coefficient of friction [104]

For the broader use of water in engineering applications, however, steel surfaces are of interest. Accordingly, surface-engineering techniques for steel substrates need to be introduced to overcome the limitations of water lubrication on a broader scale. DLC [108] is one possible coating for improving the tribological behavior under water-lubricated conditions [109] and [110]. Namely, water-lubricated DLC has proved to be a tribologically successful combination [111] to [113]. Detailed mechanistic analyses regarding DLC in water were conducted by Ohana [114] to [117]. DLC under water-lubricated

conditions results in very low wear [114] and moreover, friction below 0.1 when DLC is sliding in water against steel is typically observed [109].

We have also shown earlier that surface engineering with DLC coatings in water can notably improve the performance of a proportional 4/3 water–hydraulic valve [118], Fig. 27. In this work, both a model tribological study and a full-scale test with a hydraulic valve's life-testing, corresponding to 6 months of operation at 8 hours per day, was performed. In life-testing, the DLC-coated components remained within an acceptable 1 % leakage, compared to 20 % leakage in steel contacts, while model tribological tests showed up to 6-times lower friction.
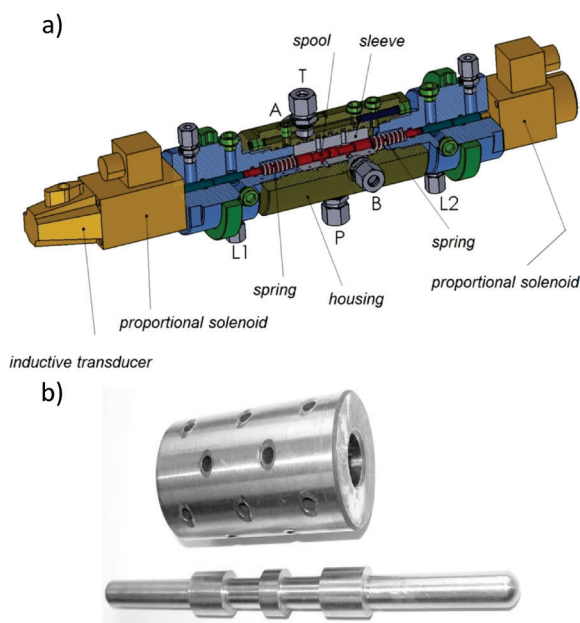
Fig. 27. a) Schematic of a 4/3 water–hydraulic valve operating with a DLC coating in water; and b) spool and sleeve samples that were tested in 4/3 water–hydraulic valve [118]

The above-mentioned application and experiments were performed at low contact pressures, but our very recent work focused on a high-contact-pressure application. Namely, to a low-speed, but high-torque, orbital hydraulic motor, which normally operates under oil-lubricated conditions [119]. Such a hydraulic motor is a highly loaded mechanical component that converts hydraulic energy into the rotational motion of the shaft. A combination of an appropriate geometry of the mechanical parts, the holes in the valve plate and the pressure differences in the lobes ensures that the rotational speed of the shaft is up to 25 min^{-1} and that the torque is up to 1000 Nm. A problem with the hydraulic motor is its

low overall efficiency, which is closely related to the friction and wear [119]. However, this work showed that with an appropriate modification of the contacts, with the appropriate roughness, DLC coatings can greatly improve the contact performance, and so reduce the friction and wear. In fact, friction in steel/DLC contacts with water, even in such highly loaded contacts, is lower than steel/steel in oil. Moreover, the application of DLC to several contacts in an orbital hydraulic motor (Fig. 28) allowed the motor to run, which was not the case with only the steel parts. Although an efficiency of only 23 % was achieved [120], the highly loaded orbital hydraulic motor was able to operate in water-lubricated conditions. In spite of much more work being required, this points the way toward green water-lubrication even in the most heavily loaded contacts in machinery used in natural environments.
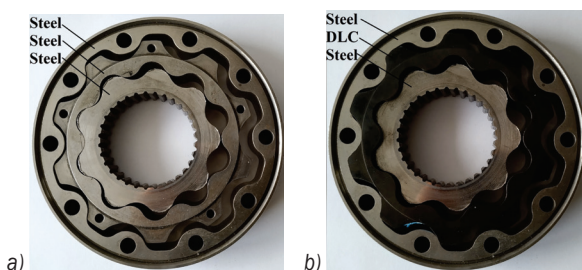
Fig. 28. *Mechanical parts of hydraulic motor: a) original steel design and; b) modified design employing a DLC coating* [120]

2 DISCUSSION AND CONCLUSIONS

Creating a sustainable engineering future will require a more comprehensive understanding of green tribology as a concept that encompasses the complete engineering life-cycle and the skills, knowledge and expertise to provide environmentally sustainable solutions and more general green tribological contacts and solutions, applicable in many engineering mechanical systems. To ensure that green tribology becomes central to engineering design, researchers will need information and knowledge covering these topics in the public domain. In fact, this is also the focus of a recent European-wide research activity to develop general and green tribology concepts within the framework of the GreenTRIBOS initiative [121]. The GreenTRIBOS project aims to develop several green-tribology contacts and systems, complete designs including materials, coatings, lubricants and surfaces that will be green in their essence. This is just one systematic attempt and many more systematic and comprehensive approaches from many groups world-

wide is needed to achieve the challenging goals of green and sustainable engineering.

In this work we have shown some of current issues related to the question, what green tribology actually means and how to tackle it. Although there are many more individual studies, approaches and definitely success stories, a lot more can be achieved in the future. It is not the intention of this work to cover all these, to make a fully and complete review study, so the authors apologize for not being able to cover every aspect. Namely, this report is made on the occasion of the 100-year anniversary of the University of Ljubljana (1919-2019) and mechanical engineering studies, which have been part of the university since then. The major emphasis was thus on the work of the group of current authors in this field. Nevertheless, we believe this is a relevant collection and summary of many possible approaches that we already attempted or even pioneered in the field. These include DLC coatings due to their specific and truly fantastic properties, enabling so many various functionalities.

We believe DLC coatings can also serve as a model approach, where not only green lubricants, but also the surfaces, with all their many different properties, can contribute to a novel functionality. In this work we show as many as eight different green-lubrication concepts due to such a property-combinatorial approach. We can call it an inter- and multi-disciplinary approach as well. Namely, it is clear that novel design concepts, including novel green-lubrication concepts, will need to combine ideas and knowledge out of the box. By doing so, unexpected successes can be anticipated. We should not forget that current successful lubrication technologies are based on century-long studies and research. Accordingly, we look forward to many more successful green-lubrication solutions in the coming years.

3 ACKNOWLEDGEMENT

4 REFERENCES

[1] Blaž, J., Zupan, S., Ambrož, M. (2019). Study on the eligibility of introducing hybrid-drive buses into the public passenger transport. *Strojniški vestnik – Journal of Mechanical Engineering*, vol. 65, no. 1, p. 553-558, **DOI:10.5545/sv-jme.2018.5637**.

[2] United Nations Framework Convention on Climate Change (2015). From: *http://unfccc.int/2860.php*, accessed on 2015-12-14.

[3] Kyoto Protocol (2015). From: *https://en.wikipedia.org/wiki/Kyoto_Protocol*, accessed on 2019-09-16.

[4] United Nations Climate Change Conference (2015). From: *https://en.wikipedia.org/wiki/2015_United_Nations_Climate_Change_Conference*, accessed on 2019-09-16.

[5] Dake, L.S., Russell, J.A., Debrodt, D.C. (1986). A review of DOE ECUT tribology surveys. *Journal of Tribology,* vol. 108, no. 4, p. 497-501, **DOI:10.1115/1.3261252**.

[6] Holmberg, K., Erdemir, A. (2017). Influence of tribology on global energy consumption costs and emissions. *Friction*, vol. 5, no. 3, p. 263-284, **DOI:10.1007/s40544-017-0183-5**.

[7] KeyWord Statistic (2015). From: *https://www.iea.org/publications/freepublications/publication/KeyWorld_Statistics_2015.pdf*, accessed on 2019-09-16.

[8] Luo, K., Wang, Y., Liu, H., Dular, M., Chen, J., Zhang, Z. (2019). Effect of coating thickness on a solid-liquid two-phase flow centrifugal pump under water medium. *Strojniški vestnik – Journal of Mechanical Engineering*, vol. 65, no. 4, p. 251-262, **DOI:10.5545/sv-jme.2018.5865**.

[9] Zhang, J., Ma, P., Gan, S., Hu, X., Wang, S. (2019). A novel approach for identifying gas cavitation in oil jet pumps for lubrication systems. *Strojniški vestnik – Journal of Mechanical Engineering*, vol. 65, no. 2, p. 113-122, **DOI:10.5545/sv-jme.2018.5656**.

[10] Oak Ridge National Laboratory (USA) (2015). From: *http://web.ornl/sci/physical_sciences directorate/mst/SurfacePM/tribology.html*, accessed on 2019-09-16.

[11] Jost, H.P. (1966). *Lubrication (Tribology) – A Report on the Present Position and Industry's Needs*. Department of Education and Science, H. M. Stationary Office, London.

[12] Euro VI Emission standards (2015). From: *https://en.wikipedia.org/wiki/European_emission_standards*, accessed on 2019-09-16.

[13] Euro Emission Standards Explained (2015). From: *https://www.carkeys.co.uk/guides/euro-emission-standards-explained*, accessed on 2019-09-16.

[14] Jost, H.P. (2009). Green Tribology – A Footprint Where Economies and Environment Meet. *4th World Tribology Congress*, Kyoto.

[15] Nosonovsky, M., Bhushan, B. (2010). Towards the "Green Tribology": Biomimetic surfaces, biodegradable lubrication, and renewable energy. *Proceedings of STLE/ASME International Joint Tribology Conference*, San Francisco, p. 435-437, **DOI:10.1115/ijtc2010-41157**.

[16] Bartz, W.J. (2006). Ecotribology: Environmentally acceptable tribological practices. *Tribology International*, vol. 39, no. 8, p. 728-733, **DOI:10.1016/j.triboint.2005.07.002**.

[17] Pettersson, A. (2013). Tribological characterization of environmentally adapted ester based fluids. *Tribology International*, vol. 36, no. 11, p. 815-820, **DOI:10.1016/S0301-679X(03)00098-7**.

[18] Šauperl, I., Wimmer, A., Dimitrov, D., Zelenka, J., Pirker, G., Schnessl, E., Winter, H. (2018). LDM COMPACT – a highly efficient method for developing gas engines for use with low environmental impact non-natural gas. *Strojniški vestnik – Journal of Mechanical Engineering*, vol. 64, no. 12, p. 743-752, **DOI:10.5545/sv-jme.2018.5344**.

[19] Chen, Y., He, J., Wu, K., Zhao, Y., Wang, Z. (2018). Investigation of the energy regeneration and control strategy of a crane hoisting system. *Strojniški vestnik – Journal of Mechanical Engineering*, vol. 64, no. 3, p. 157-168, **DOI:10.5545/sv-jme.2017.4717**.

[20] Simič, R., Kalin, M., Kovač, J., Jakša, G. (2016). Adsorption of alcohols and fatty acids onto hydrogenated (a-C:H) DLC coatings. *Applied Surface Science*, vol. 363, p. 466-476, **DOI:10.1016/j.apsusc.2015.12.066**.

[21] Sin, J.R., Suñer, S., Neville, A., Emami, N. (2014). Fretting corrosion of hafnium in simulated body fluids. *Tribology International*, vol. 75, p. 10-15, **DOI:10.1016/j.triboint.2014.03.003**.

[22] Jost, H.P. (2009). The Presidential address. *World Tribology Congress*, Kyoto, Japan.

[23] Kandeva, M., Assenova, E., Daneva, M. (2009). Triboecology as a methodological center of modern science, *2nd ECOTRIB Proceedings*, Pisa.

[24] Bartz, W.J. (1998). Lubricants and the environment. *Tribology International*, vol. 31, no. 1-3, p. 35-47, **DOI:10.1016/S0301-679X(98)00006-1**.

[25] TOTAL, Biodegradable lubricants for industry. (2015). From: *http://www.lubricants.total.com/industry/business-sectors/biodegradable-lubricants.html*, accessed on 2019-09-16.

[26] Fuchs, Biodegradable (2015). From: *http://www.fuchslubricants.com/hydraulic-oils-biodegradable*, accessed on 2019-09-16.

[27] EC Council Directive 75/439/EEC on the disposal of waste oils (1975). *Official Journal of the European Communities*, Brussels.

[28] Waste Oils (2015). From: *http://ec.europa.eu/environment/waste/oil_index.htm*, accessed on 2019-09-16.

[29] Bhushan, B. (2009). Biomimetics: lessons from nature – an overview. *Philosophical Transactions of the Royal Society A*, vol. 367, p. 1445-1486, **DOI:10.1098/rsta.2009.0011**.

[30] Fratzl, P. (2007). Biomimetic materials research: what can we really learn from nature's structural materials?. *Journal of the Royal Society Interface*, vol. 4, p. 637-642, **DOI:10.1098/rsif.2007.0218**.

[31] Nosonovsky, M. (2007). Multiscale roughness and stability of superhydrophobic biomimetic interfaces. *Langmuir*, vol. 23, no. 6, p. 3157-3161, **DOI:10.1021/la062301d**.

[32] Robertson, J. (2003). Requirements of ultrathin carbon coatings for magnetic storage technology. *Tribology*

International, vol. 36, no. 4-6, p. 405-415, **DOI:10.1016/S0301-679X(02)00216-5**.

[33] Sánchez-López, J. C., Erdemir, A., Donnet, C., Rojas, T.C. (2003). Friction-induced structural transformations of diamondlike carbon coatings under various atmospheres. *Surface and Coatings Technology*, vol. 163-164, p. 444-450, **DOI:10.1016/S0257-8972(02)00641-2**.

[34] Schulz, H., Leonhardt, M., Scheibe, H.-J., Schultrich, B. (2005). Ultra hydrophobic wetting behaviour of amorphous carbon films. *Surface and Coatings Technology*, vol. 200, no. 1-4, p. 1123-1126, **DOI:10.1016/j.surfcoat.2005.02.019**.

[35] Roy, R.K., Choi, H.-W., Park, S.-J., Lee, K.-R. (2007). Surface energy of the plasma treated Si incorporated diamond-like carbon films. *Diamond and Related Materials*, vol. 16, no. 9, p. 1732-1738, **DOI:10.1016/j.diamond.2007.06.002**.

[36] Grischke, M., Hieke, A., Morgenweck, F., Dimigen, H. (1998). Variation of the wettability of DLC-coatings by network modification using silicon and oxygen. *Diamond and Related Materials*, vol. 7, no. 2-5 p. 454-458, **DOI:10.1016/S0925-9635(97)00237-9**.

[37] Kalin, M., Vižintin, J., Barriga, J., Vercammen, K., Van Acker, K., Arnšek, A. (2004). The effect of doping elements and oil additives on the tribological performance of boundary-lubricated DLC/DLC contacts. *Tribology Letters*, vol. 17, no. 4, p. 679-688, **DOI:10.1007/s11249-004-8073-1**.

[38] Neville, A., Morina, A., Haque, T., Voong, M. (2007). Compatibility between tribological surfaces and lubricant additives—How friction and wear reduction can be controlled by surface/lube synergies. *Tribology International*, vol. 40, no. 10-12, p. 1680-1695, **DOI:10.1016/j.triboint.2007.01.019**.

[39] Kalin, M., Vižintin, J., Vercammen, K., Barriga, J., Arnšek, A. (2006). The lubrication of DLC coatings with mineral and biodegradable oils having different polar and saturation characteristics. *Surface and Coatings Technology*, vol. 200, no. 14-15, p. 4515-4522, **DOI:10.1016/j.surfcoat.2005.03.016**.

[40] Kalin, M., Vižintin, J. (2005). The tribological performance of DLC-coated gears lubricated with biodegradable oil in various pinion/gear material combinations. *Wear*, vol. 259, no. 7-12, p. 1270-1280, **DOI:10.1016/j.wear.2005.02.028**.

[41] Barriga, J., Kalin, M., Van Acker, K., Vercammen, K., Ortega, A., Leiaristi, L. (2006). Tribological performance of titanium doped and pure DLC coatings combined with a synthetic bio-lubricant. *Wear*, vol. 261, no. 1, p. 9-14, **DOI:10.1016/j.wear.2005.09.004**.

[42] Kalin, M., Majdič, F., Vižintin, J., Pezdirnik, J., Velkavrh, I. (2008). Analyses of the long-term performance and tribological behavior of an axial piston pump using diamondlike-carbon-coated piston shoes and biodegradable oil. *Journal of Tribology*, vol. 130, no. 1, **DOI:10.1115/1.2805442**.

[43] Kalin, M., Vižintin, J. (2006). Differences in the tribological mechanisms when using non-doped, metal-doped (Ti, WC), and non-metal-doped (Si) diamond-like carbon against steel under boundary lubrication, with and without oil additives. *Thin Solid Films*, vol. 515, no. 4, p. 2734-2747, **DOI:10.1016/j.tsf.2006.03.034**.

[44] Haque, T., Morina, A., Neville, A., Kapadia, R., Arrowsmith, S. (2007). Non-ferrous coating/lubricant interactions in tribological contacts: assessment of tribofilms.

Tribology International, vol. 40, no. 10-12, p. 1603-1612, **DOI:10.1016/j.triboint.2007.01.023**.

[45] Kalin, M., Roman, E., Vižintin, J. (2007). The effect of temperature on the tribological mechanisms and reactivity of hydrogenated, amorphous diamond-like carbon coatings under oil-lubricated conditions. *Thin Solid Films*, vol. 515, no. 7-8, p. 3644–3652, **DOI:10.1016/j.tsf.2006.09.049**.

[46] De Barros'Bouchet, M.I., Martin, J.M., Le-Mogne, T., Vacher, B. (2005). Boundary lubrication mechanisms of carbon coatings by MoDTC and ZDDP additives. *Tribology International*, vol. 38, no. 3, p. 257-264, **DOI:10.1016/j.triboint.2004.08.009**.

[47] Haque, T., Morina, A., Neville, A., Kapadia, R., Arrowsmith, S. (2007). Study of the ZDDP antiwear tribofilm formed on the DLC coating using AFM and XPS techniques. *Journal of ASTM International*, vol. 4, no. 7, p. 1-11, **DOI:10.1520/JAI100937**.

[48] Topolovec-Miklozic, K., Lockwood, F., Spikes, H. (2008). Behaviour of boundary lubricating additives on DLC coatings. *Wear*, vol. 265, no. 11-12, p. 1893-1901, **DOI:10.1016/j.wear.2008.04.051**.

[49] Equey, S., Roos, S., Mueller, U., Hauert, R., Spencer, N.D., Crockett, R. (2008). Tribofilm formation from ZnDTP on diamond-like carbon. *Wear*, vol. 264, no. 3-4, p. 316-321, **DOI:10.1016/j.wear.2007.03.012**.

[50] Kalin, M., Roman, E., Ožbolt, L., Vižintin, J. (2010). Metal-doped (Ti, WC) diamond-like carbon coatings: reactions with extreme-pressure oil additives under tribological and static conditions. *Thin Solid Films*, vol. 518, no. 15, p. 4336-4344, **DOI:10.1016/j.tsf.2010.02.066**.

[51] Yang, L., Neville, A., Brown, A., Ransom, P., Morina, A. (2015). Effect of lubricant additives on the WDLC coating structure when tested in boundary lubrication regime. *Tribology Letters*, vol. 57, no. 14, **DOI:10.1007/s11249-015-0464-y**.

[52] Durham, J., Kidson, A. (2014). The effects of low sulfated ash, phosphorus and sulfur oils on camshaft/tappet tribocouples with various diamond-like-carbon coated tappets in motored and fired engines. *Lubrication Science*, vol. 26, no. 6, p. 411-427, **DOI:10.1002/ls.1251**.

[53] Oblak, E., Kalin, M. (2015). Relationship between the nanoscale topographical and mechanical properties of tribochemical films on DLC coatings and their macroscopic friction behavior. *Tribology Letters*, vol. 59, no. 49, p. 1-16, **DOI:10.1007/s11249-015-0575-5**.

[54] Kalin, M., Oblak, E., Akbari, S. (2016). Evolution of the nano-scale mechanical properties of tribofilms formed from low- and high-SAPS oils and ZDDP on DLC coatings and steel. *Tribology International*, vol. 96, p. 43-56, **DOI:10.1016/j.triboint.2015.12.013**.

[55] Simič, R., Kalin, M. (2013). Adsorption mechanisms for fatty acids on DLC and steel studied by AFM and tribological experiments. *Applied Surface Science*, vol. 283, p. 460-470, **DOI:10.1016/j.apsusc.2013.06.131**.

[56] Simič, R., Kalin, M. (2013). Comparison of alcohol and fatty acid adsorption on hydrogenated DLC coatings studied by AFM and tribological tests. *Strojniški vestnik - Journal of Mechanical Engineering*, vol. 59, no. 12, p. 707-718, **DOI:10.5545/sv-jme.2013.1228**.

[57] Kalin, M., Simič, R. (2013). Atomic force microscopy and tribology study of the adsorption of alcohols on diamond-like

carbon coatings and steel. *Applied Surface Science*, vol. 271, p. 317-328, **DOI:10.1016/j.apsusc.2013.01.192**.

[58] Simič, R., Kalin, M., Hirayama, T., Korelis, P., Geue, T. (2014). Fatty acid adsorption on several DLC coatings studied by neutron reflectometry. *Tribology Letters*, vol. 53, no. 1, p. 199-206, **DOI:10.1007/s11249-013-0257-0**.

[59] Kalin, M., Simič, R., Hirayama, T., Geue, T., Korelis, P. (2014). Neutron-reflectometry study of alcohol adsorption on various DLC coatings. *Applied Surface Science*, vol. 288, p. 405-410, **DOI:10.1016/j.apsusc.2013.10.047**.

[60] Loehlé, S., Matta, C., Minfray, C., Le Mogne, T., Iovine, R., Obara, Y., Miyamoto, A., Martin, J.M. (2016). Mixed lubrication of steel by C18 fatty acids revisited. Part II: Influence of some key parameters. *Tribology International*, vol. 94, p. 207-216, **DOI:10.1016/j.triboint.2015.08.036**.

[61] Fontaine, J., Donnet, C., Grill, A., Le Mogne, T. (2001). Tribochemistry between hydrogen and diamond-like carbon films. *Surface and Coatings Technology*, vol. 146-147, p. 286-291, **DOI:10.1016/S0257-8972(01)01398-6**.

[62] Donnet, C., Fontaine, J., Grill, A., Le Mogne, T. (2000). The role of hydrogen on the friction mechanism of diamond-like carbon films. *Tribology Letters*, vol. 9, no. 3-4, p. 137-142, **DOI:10.1023/A:1018800719806**.

[63] Erdemir, A. (2001). The role of hydrogen in tribological properties of diamond-like carbon films. *Surface and Coatings Technology*, vol. 146-147, p. 292-298, **DOI:10.1016/S0257-8972(01)01417-7**.

[64] Velkavrh, I., Kalin, M. (2012). Comparison of the effects of the lubricant-molecule chain length and the viscosity on the friction and wear of diamond-like-carbon coatings and steel. *Tribology International*, vol. 50, p. 57-65, **DOI:10.1016/j.triboint.2012.01.008**.

[65] Maugis, D. (2001). *Adhesion of Solids: Mechanical Espects. Modern Tribology Handbook, Volume One*, (Bhushan, B. ed.), 163-203, CRC Press, Boca Raton.

[66] Roberts, E.W. (1990). Thin solid lubricant films in space. *Tribology International*, vol. 23, no. 2, p. 95-104, **DOI:10.1016/0301-679X(90)90042-N**.

[67] Singer, I.L. (1992). Solid lubrication processes. Fundamentals of Friction: Macroscopic and Microscopic Processes, (Singer, I.L., Pollock, H.M., eds.), Kluwer Academic Publishers, Dordrecht, p. 237-261, **DOI:10.1007/978-94-011-2811-7_13**.

[68] Martin, J.M., Donnet, C., Le Mogne, Th., Epicier, Th. (1993). Superlubricity of molybdenum disulphide. *Physical Review B*, vol. 48, no. 14, p. 10583-10586, **DOI:10.1103/PhysRevB.48.10583**.

[69] Singer, I.L. (1996). Mechanics and chemistry of solids in sliding contact. *Langmuir*, vol. 12, no. 19, p. 4486-4491, **DOI:10.1021/la951056n**.

[70] Rapoport, L., Bilik, Y., Feldman, Y., Homyonfer, M., Cohen, S. R., Tenne, R. (1997). Hollow nanoparticles of WS2 as potential solid-state lubricants. *Nature*, vol. 387, p. 791–793, **DOI:10.1038/42910**.

[71] Rapoport, L., Feldman, Y., Homyonfer, M., Cohen, H., Sloan, J., Hutchison, J.L., Tenne, R. (1999). Inorganic fullerene-like material as additives to lubricants: structure-function relationship. *Wear*, vol. 225-229, p. 975-982, **DOI:10.1016/S0043-1648(99)00040-X**.

[72] Greenberg, R., Halperin, G., Etsion, I., Tenne, R. (2004). The effect of WS2 nanoparticles on friction reduction in various lubrication regimes. *Tribology Letters*, vol. 17, no. 2, p. 179-186, **DOI:10.1023/B:TRIL.0000032443.95697.1d**.

[73] Joly-Pottuz, L., Dassenoy, F., Belin, M., Vacher, B., Martin, J.M., Fleischer, N. (2005). Ultralow-friction and wear properties of IF-WS2 under boundary lubrication. *Tribology Letters*, vol. 18, no. 4, p. 477-485, **DOI:10.1007/s11249-005-3607-8**.

[74] Moshkovith, A., Perfiliev, V., Verdyan, A., Lapsker, I., Popovitz-Biro, R., Tenne, R., Rapoport, L. (2007). Sedimentation of IF-WS2 aggregates and a reproducibility of the tribological data. *Tribology International*, vol. 40, no. 1, p. 117-124, **DOI:10.1016/j.triboint.2006.02.067**.

[75] Rosentsveig, R., Gorodnev, A., Feuerstein, N., Friedman, H., Zak, A., Fleischer, N., Tannous, J., Dassenoy, F., Tenne, R. (2009). Fullerene-like MoS2 nanoparticles and their tribological behavior. *Tribology Letters*, vol. 36, no. 2, p. 175-182, **DOI:10.1007/s11249-009-9472-0**.

[76] Tannous, J., Dassenoy, F., Lahouij, I., Le Mogne, T., Vacher, B., Bruhács, A., Tremel, W. (2011). Understanding the tribochemical mechanisms of IF-MoS2 nanoparticles under boundary lubrication. *Tribology Letters*, vol. 41, no. 1, p. 55-64, **DOI:10.1007/s11249-010-9678-1**.

[77] Kalin, M., Kogovšek, J., Remškar, M. (2012). Mechanisms and improvements in the friction and wear behavior using MoS2 nanotubes as potential oil additives. *Wear*, vol. 280-281, p. 36-45, **DOI:10.1016/j.wear.2012.01.011**.

[78] Kogovšek, J., Remškar, M., Mrzel, A., Kalin, M. (2012). Influence of surface roughness and running-in on the lubrication of steel surfaces with oil containing MoS2 nanotubes in all lubrication regimes. *Tribology International*, vol. 61, p. 40-47, **DOI:10.1016/j.triboint.2012.12.003**.

[79] Salmeron, M., Somorjai, G.A., Wold, A., Chianelli, R.R., Liang, K.S. (1982). The adsorption and binding of thiophene, butene and H2S on the basal plane of MoS2 single crystals. *Chemical Physics Letters*, vol. 90, no. 2, p. 105-107, **DOI:10.1016/0009-2614(82)83620-8**.

[80] Berman, D., Erdemir, A., Sumant, A.V. (2013). Few layer graphene to reduce wear and friction on sliding steel surfaces. *Carbon*, vol. 54, p. 454-459, **DOI:10.1016/j.carbon.2012.11.061**.

[81] Song, H.-J., Li, N. (2011). Frictional behavior of oxide graphene nanosheets as water-base lubricant additive. *Applied Physics A*, vol. 105, no. 4, p. 827-832, **DOI:10.1007/s00339-011-6636-1**.

[82] Lin, J., Wang, L., Chen, G. (2011). Modification of graphene platelets and their tribological properties as a lubricant additive. *Tribology Letters*, vol. 41, no. 1, p. 209-215, **DOI:10.1007/s11249-010-9702-5**.

[83] Choudhary, S., Mungsea, H.P., Khatri, O.P. (2012). Dispersion of alkylated graphene in organic solvents and its potential for lubrication applications. *Journal of Materials Chemistry*, no. 39, **DOI:10.1039/C2JM34741E**.

[84] Kogovšek, J., Kalin, M. (2019). Lubrication performance of graphene-containing oil on steel and DLC-coated surfaces. *Tribology International*, vol. 138, p. 59-67, **DOI:10.1016/j.triboint.2019.05.026**.

[85] Kalin, M., Velkavrh, I., Vižintin, J. (2009). The Stribeck curve and lubrication design for non-fully wetted surfaces. *Wear*, vol. 267, no. 5-8, p. 1232-1240, **DOI:10.1016/j.wear.2008.12.072**.

[86] Kalin, M., Polajnar, M. (2013). The effect of wetting and surface energy on the friction and slip in oil-lubricated contacts. *Tribology Letters*, vol. 52, no. 2, p. 185-194, **DOI:10.1007/s11249-013-0194-y**.

[87] Polajnar, M., Kalin, M. (2015). Effect of the slide-to-roll ratio and the contact kinematics on the elastohydrodynamic friction in diamond-like-carbon contacts with different wetting behaviours. *Tribology Letters*, vol. 60, no. 8, p. 1-10, **DOI:10.1007/s11249-015-0593-3**.

[88] Jahanmir, S., Hunsberger, A.Z., Heshmnat, H. (2011). Load capacity and durability of H-DLC coated hydrodynamic thrust bearings. *Journal of Tribology*, vol. 133, no. 3, **DOI:10.1115/1.4003997**.

[89] Evans, R.D., Cogdell, J.D., Richter, G.A., Doll, G.L. (2009). Traction of lubricated rolling contacts between thin-film coatings and steel. *Tribology Transactions*, vol. 52, no. 1, p. 106-113, **DOI:10.1080/10402000802180144**.

[90] Vinogradova, O.I. (1999). Slippage of water over hydrophobic surfaces. *International Journal of Mineral Processing*, vol. 56, no. 1-4, p. 31-60, **DOI:10.1016/S0301-7516(98)00041-6**.

[91] Spikes, H., Granick, S. (2003). Equation for slip of simple liquids at smooth solid surfaces. *Langmuir*, vol. 19, no. 12, p. 5065-5071, **DOI:10.1021/la034123j**.

[92] Hild, W., Optiz, A., Schaefer, J.A., Scherge, M. (2003). The effect of wetting on the microhydrodinamics of surfaces lubricated with water and oil. *Wear*, vol. 254, no. 9, p. 871-875, **DOI:10.1016/S0043-1648(03)00238-2**.

[93] Choo, H., Spikes, H.A., Ratoi, M., Glovnea, R., Forrest, A. (2007). Friction reduction in low-load hydrodynamic lubrication with a hydrophobic surface. *Tribology International*, vol. 40, no. 2, p. 154-159, **DOI:10.1016/j.triboint.2005.09.006**.

[94] Maali, A., Bhushan, B. (2008). Nanorheology and boundary slip in confined liquids using atomic force microscopy. *Journal of Physics: Condensed Matter*, vol. 20, no. 31, p. 1-11, **DOI:10.1088/0953-8984/20/31/315201**.

[95] Kus, M., Kalin, M. (2019). Influence of additives and their molecular structure on the static and dynamic wetting of oil on steel at room temperature. *Applied Surface Science*, vol. 490, p. 420-429, **DOI:10.1016/j.apsusc.2019.06.111**.

[96] Welton, T. (1999). Room-temperature ionic liquids. Solvents for synthesis and catalysis. *Chemical Reviews*, vol. 99, no. 8, p. 2071-2084, **DOI:10.1021/cr980032t**.

[97] Keskin, S., Kayrak-Talay, D., Akman, U., Hortaçsu, Ö. (2007). A review of ionic liquids towards supercritical fluid applications. *The Journal of Supercritical Fluids*, vol. 43, no. 1, p. 150-180, **DOI:10.1016/j.supflu.2007.05.013**.

[98] Abrusci, C., Palomar, J., Pablos, J.L., Rodriguez, F., Catalinac, F. (2011). Efficient biodegradation of common ionic liquids by Sphingomonas paucimobilis bacterium. *Green Chemistry*, vol. 13, no. 3, p. 709-717, **DOI:10.1039/C0GC00766H**.

[99] Blanco, D., Oulego, P., Ramos, D., Fernández, B., Cuetos, M. (2017). Model-free kinetics applied to evaluate the long-term thermal stability of three [NTf$_2$] anion-based ionic liquids. *Thermochimica Acta*, vol. 656, p. 70-84, **DOI:10.1016/j.tca.2017.08.002**.

[100] Tomizawa, H., Fischer, T.E. (1987). Friction and wear of silicon nitride and silicon carbide in water: Hydrodynamic lubrication at low sliding speed obtained by tribochemical wear. *ASLE Transactions*, vol. 30, no. 1, p. 41-46, **DOI:10.1080/05698198708981728**.

[101] Jordi, L., Iliev, C., Fischer, T.E. (2004). Lubrication of silicon nitride and silicon carbide by water: Running in, wear and operation of sliding bearings. *Tribology Letters*, vol. 17. no. 3, p. 367-376, **DOI:10.1023/B:TRIL.0000044485.77019.fb**.

[102] Chen, M., Kato, K., Adachi, K. (2002). The comparisons of sliding speed and normal load effect on friction coefficients of self-mated Si3N4 and SiC under water lubrication. *Tribology International*, vol. 35, no. 3, p. 129-135, **DOI:10.1016/S0301-679X(01)00105-0**.

[103] Jahanmir, S., Fisher, T.E. (1989). Friction and wear of slilicon nitride lubricated by humid air, water, hexadecane and hexadecane + 0.5 percent stearic acid. *Tribology Transactions*, vol. 31, no. 1, p. 32-43, **DOI:10.1080/10402008808981795**.

[104] Kalin, M., Novak, S., Vižintin, J. (2003). Wear and friction behaviour of alumina ceramics in aqueous solutions with different pH. *Wear*, vol. 254, no. 11, p. 1141-1146, **DOI:10.1016/S0043-1648(03)00326-0**.

[105] Novak, S., Drazic, G., Kalin, M. (2005). Structural changes in ZrO$_2$ ceramics during sliding under various environments. *Wear*, vol. 259, no. 1-6, p. 562-568, **DOI:10.1016/j.wear.2004.12.001**.

[106] Kalin, M., Dražič, G., Novak, S., Vižintin, J. (2006). Wear mechanisms associated with the lubrication of zirconia ceramics in various aqueous solutions. *Journal of the European Ceramic Society*, vol. 26, no. 3, p. 223-232, **DOI:10.1016/j.jeurceramsoc.2004.10.026**.

[107] Kalin, M., Novak, S., Vižintin, J. (2006). Surface charge as a new concept for boundary lubrication of ceramics with water. *Journal of Physics D: Applied Physics*, vol. 39, no. 15, p. 3138-3149, **DOI:10.1088/0022-3727/39/15/S03**.

[108] Erdemir, A. (2004). Diamond-like carbon films. Vižintin, J., Kalin, M., Dohda, K., Jahanmir, S. (eds.), *Tribology of Mechanical Systems: A Guide to Present and Future Technologie*s. ASME Press, New York. p. 139-156, **DOI:10.1115/1.802094.ch8**.

[109] Sato, T., Besshi, T., Sato, D., Tsutsui, I. (2001). Effect of water based lubricants on wear of coated material. *Wear*, vol. 249, no. 1-2, p. 50-55, **DOI:10.1016/S0043-1648(01)00522-1**.

[110] Kano, M., Martin, J.M., Bouchet, M.I.D.B. (2017). Green superlubrication by hydrogen-free amorphous carbon with human friendly lubricants. *Sensors and Materials*, vol. 29, no. 6, p. 771-784, **DOI:10.18494/SAM.2017.1630**.

[111] Uchidate, M., Liu, H., Iwabuchi, A., Yamamoto, K. (2007). Effects of water environment on tribological properties of DLC rubbed against stainless steel. *Wear*, vol. 263, no. 7-12, p. 1335-1340, **DOI:10.1016/j.wear.2006.10.024**.

[112] Yamamoto, K., Matsukado, K. (2006). Effect of hydrogenated DLC coating hardness on the tribological properties under water lubrication. *Tribology International*, vol. 39, no. 12, p. 1609-1614, **DOI:10.1016/j.triboint.2006.01.004**.

[113] Tokoro, M., Aiyama, Y., Masuko, M., Suzuki, A., Ito, H., Yamamoto, K. (2009). Improvement of tribological characteristics under water lubrication of DLC-coatings by

surface polishing. *Wear*, vol. 267, no. 12, p. 2167-2172, **DOI:10.1016/j.wear.2009.04.009**.

[114] Ohana, T., Wu, X., Nakamura, T., Tanaka, A. (2007). Formation of lubrication film of diamond-like carbon films in water and air environments against stainless steel and Cr-plated balls. *Diamond and Related Materials*, vol. 16, no. 4-7, p. 1336-1339, **DOI:10.1016/j.diamond.2007.01.036**.

[115] Ohana, T., Suzuki, M., Nakamura, T., Tanaka, A., Koga, Y. (2004). Tribological properties of DLC films deposited on steel substrate with various surface roughness. *Diamond and Related Materials*, vol. 13, no. 11-12, p. 2211-2215, **DOI:10.1016/j.diamond.2004.06.037**.

[116] Tanaka, A., Suzuki, M., Ohana, T. (2004). Friction and wear of various DLC films in water and air environments. *Tribology Letters*, vol. 17, no. 4, p. 917-924, **DOI:10.1007/s11249-004-8100-2**.

[117] Suzuki, M., Tanaka, A., Ohana, T., Zhang, W. (2004). Frictional behavior of DLC films in a water environment. *Diamond and Related Materials*, vol. 13, no. 4-8, p. 1464-1468, **DOI:10.1016/j.diamond.2003.10.068**.

[118] Majdič, F., Velkavrh, I., Kalin, M. (2013). Improving the performance of a proportional 4/3 water–hydraulic valve by using a diamond-like-carbon coating. *Wear*, vol. 297, no. 1-2, p. 1016-1024, **DOI:10.1016/j.wear.2012.11.060**.

[119] Strmčnik, E., Majdič, F., Kalin, M. (2019). Water-lubricated behaviour of AISI 440C stainless steel and a DLC coating for an orbital hydraulic motor application. *Tribology International*, vol. 131, p. 128-136, **DOI:10.1016/j.triboint.2018.10.032**.

[120] Strmčnik, E., Majdič, F., Kalin, M. (2019). Influence of a diamond-like carbon-coated mechanical part on the operation of an orbital hydraulic motor in water. *Metals*, vol. 9, no. 4, p. 466, **DOI:10.3390/met9040466**.

[121] GreenTRIBOS – European Network for Joint Doctoral-Level Training in Green Tribology Marie-Sklodowska-Curie actions: H2020-MSCA-ITN-2019 (2019). from *http://www.greentribos. org*, accessed on 2019-10-22.

Semi-Analytical Multidimensional Algorithm for Aircraft Design Optimisation: Student Design Build Fly (DBF) Competition

Viktor Šajn [*]

University of Ljubljana, Faculty of Mechanical Engineering, Slovenia

The winner of American Institute of Aeronautics and Astronautics (AIAA)/Textron Aviation/Raytheon Missile Systems Design/Build/Fly (DBF) Competition 2019 was Edvard Rusjan team from Faculty of Mechanical Engineering, University of Ljubljana, Slovenia. Edvard Rusjan team use a strict scientific approach to beat opposing teams from most prestigious US Universities. Team developed a semi-analytic multidimensional algorithm for aircraft design optimization with an aim to maximize competition score in accordance with the competition rules. Two intermediate prototype models were produced and tested for single ground and three flying missions to fine tune algorithm empirical coefficients. Aircraft model aerodynamics was predicted with RANS numerical simulations and dynamic stability with Inviscid Panel method. By measurement in Low Turbulence Wind Tunnel the low drag of selected aircraft external load configuration was verified. Wing and fuselage of competition aircraft model named by Ljubljana students "Pretty Boy" were made of carbon-glass sandwich composite and Aramide honeycomb as sandwich filler. At final fly-off at TIMPA field in Tucson, in final flight mission team pilot Timotej Hofbauer with "Pretty Boy" scored 18 laps in 10 minutes time slot which was absolute record of competition. Runner-up Georgia Institute of Technology team was 22% slower and finished with 14 scored laps.

Keywords: carbon-glass sandwich composite construction, number of laps in time slot, take-off, design parameters, aerodynamic drag, DBF competition 2019, Edvard Rusjan team

Highlights
- *Semi-analytic multidimensional algorithm for aircraft design optimization was developed.*
- *A detail mathematical model of each flight mission was built.*
- *Algorithm predicts that in third Mission aircraft is capable of scoring 19 turns in 10 minutes. At competition team completed 18 laps.*
- *NiMh battery cells capacity shows great level of uncertainty which degrade mathematical model accuracy.*
- *Wining aircraft "Pretty Boy" was made of carbon-glass sandwich composite and Aramide honeycomb as sandwich filler.*

0 INTRODUCTION

The final fly-off 2018-19 American Institute of Aeronautics and Astronautics (AIAA)/Textron Aviation/Raytheon Missile Systems Design/Build/Fly Competition Fly-off was organized at TIMPA Field in Tucson, AZ from April 11 to 14, 2019. From 138 competition team proposals, 113 were invited to submit a formal report, which 104 did. Final fly-off attended 77 teams, 65 successfully completed tech inspection. Just 26 teams accomplished all four missions.

Every year there is a new contest theme, this year Aircraft Carrier Operations. Wingspan has to be larger than 4 foot, aircraft has to roll trough 3 foot x 2 foot box with folded wings, which unfold remotely.

Aircraft has to complete one ground and three flight mission, taking off from 4 foot by 10 foot platform. For the first mission aircraft without payload has to fly three laps in five minutes. In the second mission aircraft has to use radome in flight. The final mission included payload of foam toys with popular name attack stores. During the mission duration of 10

minutes aircraft has to make as many as possible laps while dropping one store per lap. Competition winning team was Edvard Rusjan of University of Ljubljana, Slovenia, second Georgia Institute of Technology and third FH Joanneum University of Applied Sciences.

Edvard Rusjan team introduced a series of optimization algorithms, procedures for aircraft design and production. Team also used special procedures and technique to build high-performance composite aircraft. In the paper we presented the whole path of winning aircraft creation: design, build, optimization and proof of concept by flying and winning the competition. Official competition system of units was Imperial.

1 CONCEPTUAL DESIGN

The main objective of the 2019 AAIA Design Build Fly competition was to design a multi-purpose aircraft to support carrier operations. The rules specify a ramp take-off and ground landing. The aircraft was designed for the optimal total score with the highest achievable

score in each mission. The total *SCORE* is calculated using Eq. (1).

$$SCORE = WRS \cdot TMS , \qquad (1)$$

where *WRS* is Written Report Score. The Total Mission Score *TMS* is a sum of scores, obtained in Ground Mission *GM* and Missions One *M*1, Two *M*2 and Three *M*3, as shown in Eq. 2 :

$$TMS = GM + M1 + M2 + M3 . \qquad (2)$$

Each flight mission requires completion of a specified number of laps where each lap consists of four individual sections: a 180° turn, 1000 ft straight flight with a 360° turn, another 180° turn and landing at the end of specified mission time. The lap requires both left and right turns and a successful landing within the bounds of the runway. Fig. 1 shows the scheme of the official competition flight course [1].

360 Degree Turn

Starting Line

500 ft   500 ft

Course Layout
Shown To Scale
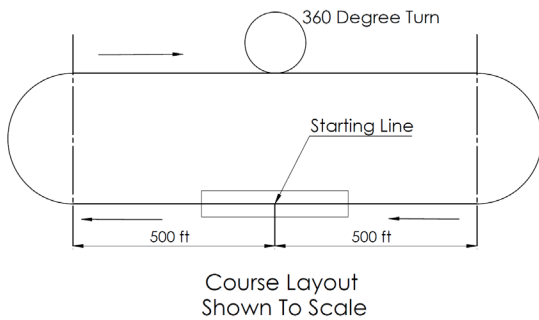
Fig. 1. *Official flight course*

In Mission One the aircraft must take-off without any payload on a 10 ft ramp at a roughly 5° angle, complete three laps, and perform a successful landing in order to receive the full score shown in Eq. (3). This mission should be completed in a five minute time window. If the mission is successfully completed:

$$M1 = 1.0 . \qquad (3)$$

In Second Mission the time frame, number of laps and take-off ramp are identical to Mission One, however, a rotating radome must be installed. The radome must start rotating at the command of a line judge while the aircraft is in flight. To receive a score as described in Eq. (4) a successful landing must be performed:

$$M2 = 1 + \frac{Min_{time}}{N_{time}}, \qquad (4)$$

where Min_{time} is the competition best achieved time and N_{time} team time. In third Mission, take-off

is the same as in previous missions with the added payload of attack stores, without the rotating radome. A scoring lap is one where the aircraft drops a single store on the down-wind leg of the lap. The time window for this mission is 10 minutes. The aircraft must complete a successful landing in order to get a score described by Eq. (5).

$$M3 = 2 + N_{sclps} , \qquad (5)$$

where N_{sclps} is number od scoring laps. Ground Mission is a timed mission for ground demonstrations of Missions 2 and 3. The Mission is broken down into 4 parts, two of which are timed. The first timed part is the remote command of the unfolding mechanism and the installing of the radome. Following is a non-timed demonstration of the radome rotation. The next part is a timed removal of the radome and an installation of 4 attack stores under the wing. The final part of the Ground Mission (*GM*) is not timed and consists of arming the aircraft and demonstrating the capability to remote drop the stores one by one, as well as the working of all propulsion and flight controls.

$$GM = \frac{Min_{time}}{N_{time}} . \qquad (6)$$

The aircraft should be designed with regard to certain basic constraints. Any design is allowed except rotary wing or aircraft lighter than air. The electrical power must be provided from NiCd or NiMh batteries, no form of external take-off system is allowed. The propeller must be a commercially available model. The aircraft must be capable of carrying at least four stores under the wings, minimum 0.5 in clearance between stores and any part of the aircraft except the mounting hardware and be capable of remote detachment. The radome must be at least 12 in in diameter and a minimum of 1*in* thick at the point of attachment must be mounted on the aircraft centerline with a minimum of 3 in clearance between any part of the radome to any other part of the aircraft. It must be capable of spinning and stopping by remote command. The aircraft must be capable of taking off from a 10 ft ramp at a roughly 5° angle. Requirements for individual missions, scoring equations and guidelines were inspected and translated into design parameters crucial for each individual mission. The total score maximization was approached with the analysis of different aircraft configurations and mission scoring. Translation of mission requirements into design requirements is shown in Table 1.

Table 1. *Design parameters*

Mission	Problem statement	Key design parameters
Ground Mission	Fast mounting of attack stores and radome	Time
Mission 2	High aircraft speed, secured rotating radome	Power, remote rotation of radome
Mission 3	High number of scoring laps, fast individual lap, take-off from the ramp	Number of attack store, total weight, drag and power

1.1 Sensitivity Study of Design Parameters

The design parameters were analyzed in a quantitative way as much as possible. To achieve that, certain relationships had to be modelled mathematically. The first crucial relationship to determine was the effect of extra load on speed, endurance and take-off distance of the airplane. A mathematical model of each individual flight mission was created, which also included some empirical data based on previous competitions [**2**]. Crucial identified design parameters were roughly evaluated.

Empty weight influences flight parameters (angle of attack, flight speed) and take-off requirements. Empty weight was estimated by calculating structural weight, wing weight, empennage weight and propulsion weight. Propulsion weight was approximated by estimating the weight of a battery pack and weight of Electric Motor (EM). A second-order equation was created to aid the comparison of weight to power for several different EM. Structural weight was roughly calculated by assessing the increase in weight for each additional attack store. Wing weight was calculated by finding the wing area required for the aircraft to fly. Empennage weight was estimated by calculating the desired volume coefficient. In Eq. (7) motor weight W_{mt} second order prediction model is presented:

$$W_{mt} = k_{m0} + k_{m1} \cdot P_{mt} + k_{m2} \cdot P_{mt}^2 , \qquad (7)$$

where P_{mt} is motor power and k_{m0}, k_{m1} and k_{m2} are weighting coefficients. Battery pack weight W_{bp} is a function of required energy E_{req}, cell energy E_{cell} and number of cells m_{cell}, (Eq. (8):

$$W_{bp} = \frac{E_{req}}{E_{cell}} \cdot m_{cell} . \qquad (8)$$

Structure weight W_{str} is calculated in Eq. (9):

$$W_{str} = W_{base} + N_{attstr} \cdot k_{s1} , \qquad (9)$$

where W_{base} is base weight, N_{attstr} is a number of attack stores and k_{s1} weighting coefficient. Wing weight W_{wing} is calculated from wing area A_{wing} and wing surface density ρ_{wing}, Eq. (10):

$$W_{wing} = A_{wing} \cdot \rho_{wing} . \qquad (10)$$

Analogue equations are used to predict stabilizer and rudder weight. The number of attack stores is directly proportional to flight Mission 3 score, but it also increases aircraft weight due to higher required endurance and speed and the required thrust to ensure aircraft take-off from the ramp. In order to reduce stall speed and consequently the required take-off thrust, the aircraft needed to have a large wing area. Larger wing area meant larger induced drag, due to wingspan being limited and larger weight that affected take-off distance. Stall velocity v_{stall} is calculated from aircraft take-off mass m, gravity constant g, air density ρ, maximum lift coefficient $C_{l,max}$ and wing area A, Eq. (11):

$$v_{stall} = \sqrt{\frac{2 \cdot m \cdot g}{\rho \cdot C_{l,max} A}} . \qquad (11)$$

With every attack store, the aircraft take-off weight increased and consequently larger static thrust was required. For every additional attack store, an additional lap must be flown in M3, affecting the number of required battery packs to successfully complete the mission. Since mission time is limited to 10 minutes, the average speed must increase as well. A considerable aircraft limitation is the ability to take-off from the ramp. It is primarily influenced by stall speed, static thrust and aircraft weight and drag.

1.2 Aircraft Design

From three basic design configurations conventional design was chosen. With FOM analysis it was found superior to bi-fuselage and flying wing design. At first sight, the bi-fuselage configuration might offer better take-off capabilities and payload accommodation, but the team was confident to come up with other ways to increase payload capacity without negatively affecting take-off weight.

As the main configuration was chosen, the goal was to define some of the main aircraft parts in greater detail. In order to reduce the drag
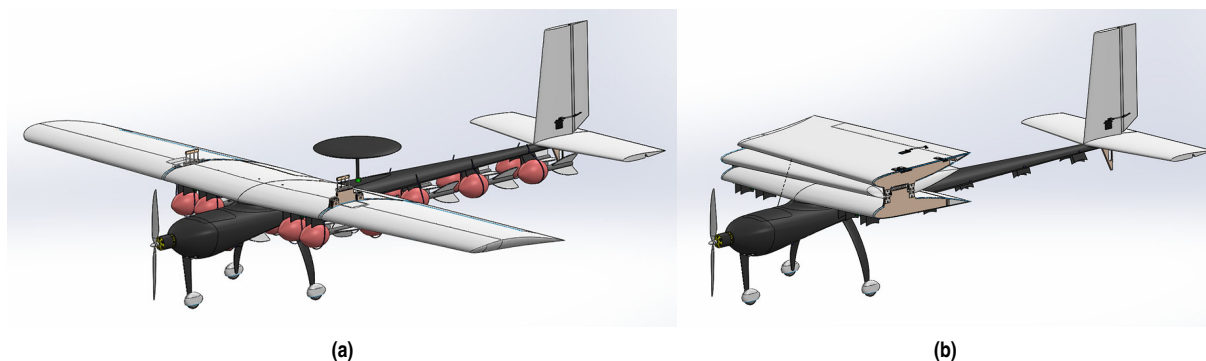
Fig. 2. *Final conceptual design; a) flightready, and b) stowed configuration*

of each individual attack store while maintaining structural integrity and payload capacity, the following options were considered: round fuselage with attack stores attached without any drag reduction geometry, modified convectional fuselage design with attack stores as hidden inside as possible, and a combination of both. We chose the most aerodynamic version despite additional weight penalty. At the competition, we found that we are the only team which optimized attack stories drag by blending them into fuselage which gave us significant advance because our model was significantly faster.

Three different folding designs were compared: rotary, folding along the fuselage and collapsing wing folding; and two folding mechanisms: layered carbon spring and torsion spring. Rotary configuration consists of rotating an entire wing. Because the plane would not fit in bounding box dimensions, a fold was necessary. This demands a design of two different mechanisms; one to rotate the wing and another one to unfold it. Wing Folding Along Fuselage: With this positioning, we gain room in the bounding box, however, the centre of gravity moves too far back and the plane would tilt back. It is also too complicated to manufacture as it demands movement in multiple degrees of freedom. The team decided on Collapsing Wing Foldin option because the wings fold onto itself. This way the centre of gravity does not move and the same sort of mechanism is used on both wings in contrast to a rotary configuration. Two folding mechanisms were compared and tested: layered carbon spring and torsion spring. The torsion spring was chosen over the layered carbon spring due to easier implementation of the design.

The final configuration consists of a high wing conventional aircraft with wings that can fold and roll through a 3 ft by 2 ft box, with a conventionally

designed tail that can carry up to 19 attack stores and a rotating radome. The aircraft has a conventional landing gear and can take-off from a $10\,ft$ ramp at an angle of $5°$. The final conceptual design is shown in Fig. 2.

2 PRELIMINARY DESIGN

The aircraft design was further optimized by varying the parameters of the conceptual design in order to maximize the final score. By taking into account the sizing/design trades, aerodynamics, and mission model, the score analysis simulation (SAS), programmed by Python computer language [3], managed to calculate the optimal aircraft parameters and estimated mission performance.

2.1 Design and Analysis Methodology

Due to its robustness and easy implementation, the iteration procedure which would yield the highest final score was used in determining the parameters of the aircraft. Over the course of the iteration, wing area, airfoils, number of attack stores and propulsion configurations (propellers, ESC, cell number, motor) were determined. The Score analysis simulation (SAS) scheme is shown in Fig. 3.
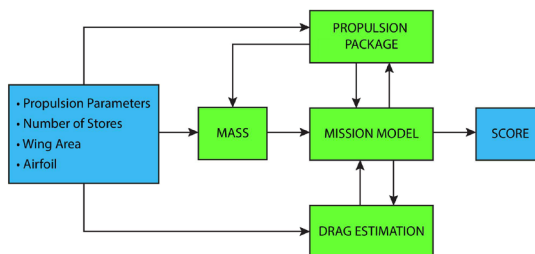
Fig. 3. *Score analysis simulation diagram*

Since the quantity of all parameter combinations would be too demanding for our processing capabilities, the iteration procedure was carried out in stages. In the first stage only the main parameters, such as wing area and number of attack stores, were iterated. Other parameters, such as airfoils, wingspan and empennage, were kept constant at this stage. Propulsion parameters were crudely estimated by estimating efficiency. In the second stage, the priority was to determine the optimal propulsion configuration and airfoil.

The optimal aircraft configuration was found to be the one that would perform best in mission 3, since the maximum score was not limited by the success of other competitors. Therefore the success in mission 3 was prioritized.

2.2 Design Trade Studies

The number of attack stores is directly proportional to the score achieved in mission 3. With each attack store an additional lap must be flown, which in turn meant that a faster aircraft with a heavier battery pack was needed. In Fig. 4 the relationship between the attack stores and weight can be seen.
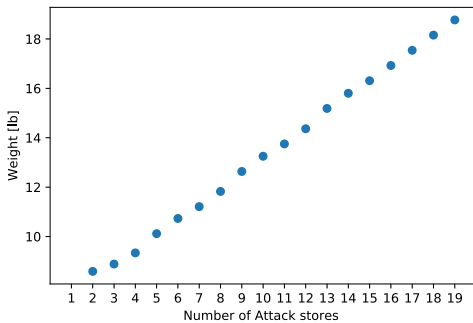
Fig. 4. *Relationship between the number of attack stores and estimated aircraft take-off weight for Mission 3*

The aircraft must be able to take-off from a 10 ft ramp, which in turn meant that it must be able to achieve stall speed determined by considering aircraft take-off mass, $C_{l,max}$, lift increase by flaps, wing area, drag coefficient and static thrust. Stall speed was determined by Eq. (11).

In Fig. 5 the relationship between the required take-off force and wing area can be seen. The required thrust was determined with Eq. (13) and by considering the Second Newton's law.

The propulsion configuration was chosen through the iteration of 102 BLDC motors, 132 propellers, 10
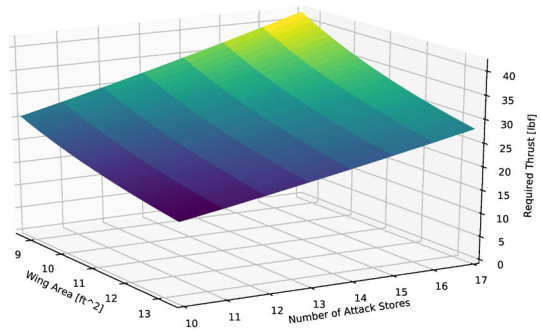
Fig. 5. *Relationship between static thrust, wing area and number of attack stores*

electronic speed controls (ESC) and 3 different types of batteries. In each iteration, the of components were passed down to propulsion module, which produced the proper thrust curve for desired throttle settings. The obtained thrust curve was used as one of 4 nonlinear equations of motion of straight flight module, which is a submodule in the mission module of SAS. Propulsion module scheme along with its integration to straight flight module is presented in Fig. 6.
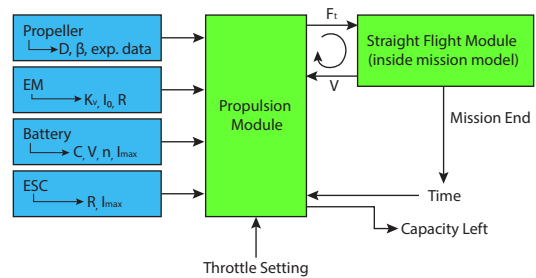
Fig. 6. *SAS propulsion module diagram*

As mission 3 requires a 10 minute flight time at a relatively high velocity, propulsion endurance was greatly considered. SAS's flight module offered a time calculation of each lap. That, combined with velocities of each lap, enabled the propulsion module to accurately determine burned battery pack capacity. Based on the required battery capacity for a 10 minute flight and high power to weight ratio, Scorpion SII-4035-450KV with APC 16x8 propeller and batteries wired two cells in parallel and 24 pairs in series 5000 mAh Turnigy cells were chosen to be the best fit for the propulsion configuration.

2.3 Mission Model

The missions were simulated by calculating the time needed to complete each lap. A single lap was

simplified to four turns, two straight flights and one take-off. Take-off v_{tf} was modelled by solving Eq. (13) given that the speed acquired by the end of the ramp was larger than stall speed:

$$m \frac{dv_{tf}}{dt} = F_t - \frac{\rho v_{tf}^2}{2} A C_d ,\qquad (12)$$

$$v_{tf}(t) = \sqrt{\frac{2F_t}{\rho A C_d}} \tanh\left(\frac{1}{m}\sqrt{\frac{A C_d F_t \rho}{2}}\, t \right) ,\qquad (13)$$

where C_d is drag coefficient, t time and F_t trust force. Take off time is very short and we assumed that trust force F_t is constant.

Straight flight was modeled by solving nonlinear Eqs. (14) and (15):

$$m \cdot g - \frac{\rho v^2}{2} C_l A = 0 ,\qquad (14)$$

$$F_t(v) - \frac{\rho v^2}{2} A C_d(C_l, Re) = 0 ,\qquad (15)$$

where $F_t(v)$ is propeller thrust. Turning flight was simplified to take place at maximum lift the aircraft can produce. By solving Eqs. (16) and (17), turning speed v_{turn} and radius R were calculated for roll angle ϕ:

$$F_t(v_{turn}) - \frac{\rho v_{turn}^2}{2} A C_{d,C_{l,max}} = 0 ,\qquad (16)$$

$$R = \frac{2 \cdot m}{\rho \cdot A \cdot C_{l,max} \cdot \sin \phi} .\qquad (17)$$

In Eq. (16) there was also included induced drag coefficient C_{ind} because of high g turn. Eqs. (18) and (19) were later used to calculate lap times. Lap time was additionally increased by 2 seconds in order to compensate for the time needed to position the aircraft for turning manoeuvre.

$$t_{lap}(P,AR,m,A,C_l) = \frac{2 \cdot l}{v_0(P,m,A,AR)} + $$
$$+ \frac{4 \cdot \pi \cdot R(P,m,n,C_{l,max},AR)}{v} + 2,\qquad (18)$$

$$t_{lap,first}(P,AR,m,A,C_l) = \frac{2 \cdot l - l_{tkff}}{v_0(P,m,A,AR)} + $$
$$+ \frac{4 \cdot \pi \cdot R(P,m,n,C_{l,max},AR)}{v_{turn}} + \qquad (19)$$
$$+ 2 + t_{tkff},$$

where AR is wing aspect ratio, l length of single lap and t_{tkff} time required for take-off.

2.4 Aircraft Lift, Drag and Stability Characteristics

Choosing the correct airfoil was crucial for a fast and stable aircraft. The airfoil was chosen primarily on $C_{l,max}$ due to extreme take-off requirements. The aircraft must take-off from 10 ft ramp, with velocity close to stall speed where Reynolds number is $Re \approx 3 \cdot 10^5$. To be on safe side airfoils were analyzed at Reynolds number of $Re = 2 \cdot 10^5$. The three most promising airfoils were chosen using SAS, they are shown in Fig. 7.
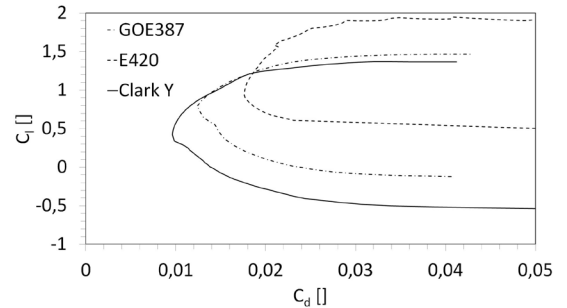
Fig. 7. *Airfoil polars*

C_l and C_d are airfoil lift and drag coefficients. Finally, ClarkY (Fig. 8) was chosen for the final aircraft, since GOE387 was considered to be too thick and Eppler420 was having questionable characteristics at a lower Reynolds number. Airfoil polars were obtained from Airfoil tools [4].

Fig. 8. *ClarkY airfoil*

The lift and drag analysis was carried out in 2 separate stages. During the iteration procedure the AVL analysis was too demanding, so cruise lift and drag coefficients, and max lift coefficients were calculated based on airfoil polars [4].

Drag coefficients from other components, such as the fuselage, were acquired by assuming turbulent flow and using Schlighting's empirical equation [5] for skin friction drag. Drag from attack stores was determined experimentally. The described empirical function was properly adjusted in order to coincide with the drag coefficient values obtained from experiments. Drag contributions can be seen in Fig. 9.

Table 2 contains the lift and drag coefficients of initial optimal aircraft design. Since our main concern was the ability of the aircraft to take-off from the ramp, it was necessary to account for flaps in
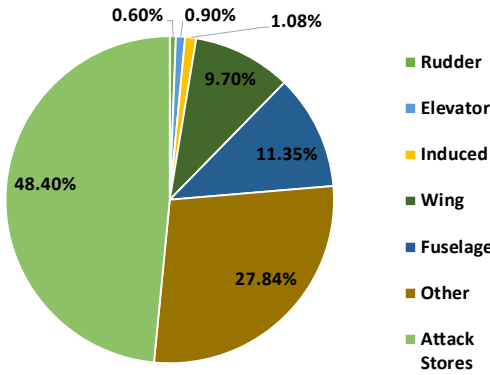
Fig. 9. *Drag contributions*

Table 2. *Initial lift and drag estimations during iteration process using SAS*

Parameter	$C_{l,max}$	$C_{l,avg}$	$C_{d,avg}$
Value	1.75	0.16	0.07

calculation of $C_{l,max}$ lift coefficient. Due to attack stores being dropped in each lap the total drag of the aircraft was decreasing. By experimentation, we confirm the thesis that drag from wing-mounted attack stores was significantly larger than the drag from fuselage-mounted attack stores.
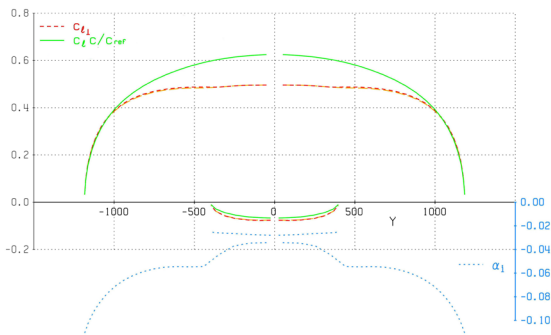
Fig. 10. *Lift distribution*

AVL [6] was further used to perform Treffz plane analysis that enabled the determination of trimmed flight conditions as well as lift distribution across the wing and horizontal tail. The green curves in Fig. 10 denote normalized lift distributions across the wing and tail for M3. The result applies to cruise flight at 91.7 ft/s.

2.5 CFD Analysis

Several aerodynamic characteristics of the final model were determined with the use of computational fluid dynamics (CFD). The team was interested in determining the influence of the wingtip geometry on

lift and drag coefficients, as well as in calculating the aforementioned aerodynamic coefficients pertaining to the airplane fuselage. In both cases, CFD simulations were done using OpenFOAM for Windows 18.02 (version 1) [7].

The primary objective of fuselage analysis was to determine drag coefficient of the fuselage as a function of the free stream velocity. The computational mesh utilized in this simulation was based on the geometry of the bare airplane fuselage with no other aerodynamic surfaces and attack stores attached. A graphical representation of the calculated airflow velocity field and static pressure field acting on the airplane fuselage is shown in Fig. 11:
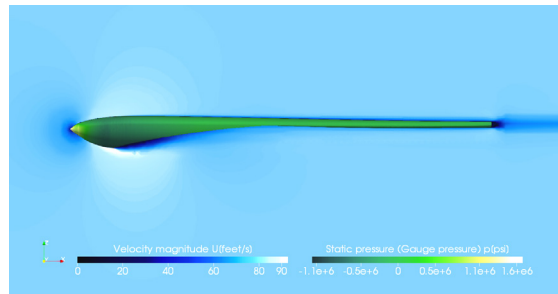
Fig. 11. *Airflow velocity field and pressure field for v = 82.0 ft/s*

We solved the momentum equations using the in-built SIMPLE algorithm (simpleFoam), and we used the $k - \omega$ SST (Shear stress transport) turbulence model as a means of equation closure. We resolved the boundary layer close to the wall with a very fine computational mesh ($y^+ < 10$). Computations were done for free stream velocities of $v_1 = 49.2$ ft/s and $v_2 = 82.0$ ft/s.

Table 3. *Additional relevant parameters for CFD analysis*

Parameter	$\rho[lb/ft^3]$	$v[ft^2/s]$	$A_{ref}[ft^2]$
Value	0.0765	$16.2 \cdot 10^{-5}$	$27.0 \cdot 10^{-2}$

The reference surface area S_{ref}, defined for this calculation, is understood to be the fuselage cross section at the position of its maximum value. Additional parameters relevant to the simulation are displayed in Table 3.

Table 4. *CFD analysis calculated aerodynamic coefficients*

Parameter	Value	
$v[ft/s]$	49.2	82.0
$C_d[/]$	0.361	0.357
$C_l[/]$	-0.0427	-0.0525

Lift and drag coefficients, calculated via the simulation, are displayed in Table 4.

2.6 Wing Tip Analysis

The primary objective of the wing tip analysis was to determine the wing tip lift and drag coefficients as functions of the airflow velocity and wingtip geometry, that are characterized by the characteristic wingspan distance between the upper and lower edge of the wing tip facet, which we denote as $l_{w,ch}$. Computations were made for the free stream velocity of $v = 49.2$ ft/s and characteristic lengths $l_{w,ch}$ of 0 in, 2.76 in, 3.94 in and 5.12 in. Computational meshes utilized in this simulation were based on the geometry of the outer portion of the wing measuring $l = 31.7$ in in length. The simulation settings were identical to those described in the previous section. The reference surface area S_{ref}, in this case, is the wing cross section normal to the lift direction. Additional parameters which are relevant to the simulation are displayed in Table 5.

Table 5. *Additional parameters*

Parameter	$\rho\ [lb/ft^3]$	$\nu\ [ft^2/s]$	$A_{ref}\ [ft^2]$
Value	0.0765	$16.1 \cdot 10^{-5}$	3.77

Lift and drag coefficients calculated via the simulation are displayed in Table 6.

Table 6. *Calculated lift and drag coefficients*

Parameter	Value			
$l_{w,ch}$ [in]	0	2.76	3.94	5.12
v [ft/s]	49.2	49.2	49.2	49.2
C_l [/]	0.434	0.434	0.444	0.446
C_d [/]	0.0304	0.0302	0.0310	0.0312

Airflow velocity field and static pressure field acting on the wing tip are graphically represented in Fig. 12.
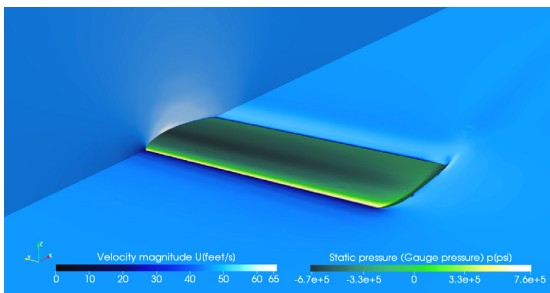
Fig. 12. *Airflow velocity field and pressure field for $l_{w,ch}$ = 2.76 in*

The wing tip geometry was consequently chosen on the basis of simulation results, which suggest that there is an optimal characteristic length where the drag coefficient is minimal. It was concluded that out of the four wing tip geometries simulated, the second case ($l_{w,ch} = 2.76$ *in.*) has the most favourable aerodynamic characteristics considering its coefficient of drag is lower than for the other three.

2.7 Stability and Control

One of the main issues was the aircraft stability. Due to a large centre of gravity (CG) uncertainty, a large CG envelope was required as well as a small aspect ratio. Stability derivatives were calculated via AVL and are located in Table 7 for M2 and Table 8 for M3.

Table 7. *Static stability at take-off for M2*

	α	β	p'	q'	r'
C_l	-0.0	-0.022	-0.41	-0.0	0.064
C_m	-3.327	0.00	0.00	-28.93	-0.00
C_n	-0.00	0.15	0.010	-0.0	-0.227

Table 8. *Static stability at take-off for M3*

	α	β	p'	q'	r'
C_l	-0.0	-0.087	-0.40	-0.0	0.19
C_m	-3.14	0.00	0.00	-27.67	-0.00
C_n	-0.00	0.16	-0.084	-0.0	-0.24

For both missions, the derivatives were calculated at take-off speed. The neutral point for M3 was calculated at approximately 10.6in behind the leading edge of the wing, making the aircraft longitudinally stable according to Table 11. In M2 the effect of radome must be considered. We simulated this effect by replacing it with a lifting surface with similar surface area, as seen in Fig. 13.
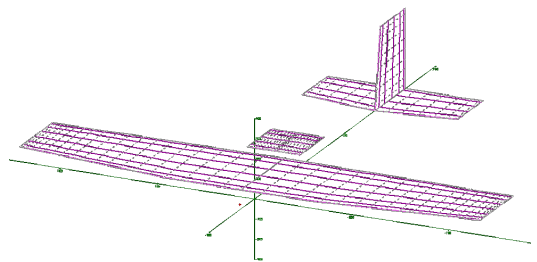
Fig. 13. *AVL geometry with radome attached*

The AVL linearized model of nonlinear equations of motion was used for predicting the modes of dynamic stability. The calculated poles of the system

matrix for an empty and a loaded aircraft are shown in Table 9.

All poles of the system matrix except one, indicating spiral instability, lie in the left half of the plane (shown in Fig. 14), which indicates stable modes. Even though the aircraft is considered spirally unstable, the spiral mode time constant is $T_{S,M2} = 24.4$ s and $T_{s,M3} = 27$ s, which gives pilot enough time to compensate.
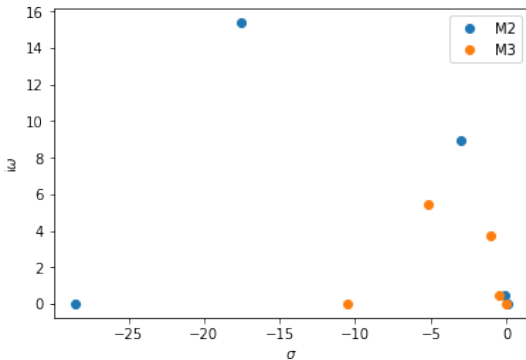
Fig. 14. *Real and imaginary components of eigenvalues for M2 and M3*

3 DETAIL DESIGN

In accordance with all demands for aircraft design, the first draft was proposed. In Table 10 gross aircraft dimensions are presented.

The fuselage design was chosen based on testing, done in the wind tunnel. The final design enables attack stores mounted under the fuselage to produce minimal drag force as shown in Fig. 15. The front section was shaped aerodynamically to accommodate all propulsion components as well as the necessary equipment to enable RC capabilities. From the initial part the fuselage tappers towards a shape that enables the stores to have as much ground clearance as possible. Design shown in Fig. 15 enables the attack stores to be as hidden from the airflow as possible, while still maintaining a high moment of inertia.

To ensure that the wing weighs as little as possible and the shape is kept as close to the original profile and end design as possible, each section was made from a separate mould. Critical points were additionally reinforced with a carbon fibre mesh to ensure structural integrity.

The team wanted to go with a full carbon fibre design due to improved mechanical characteristics but decided against it as it would be too cost-prohibitive.
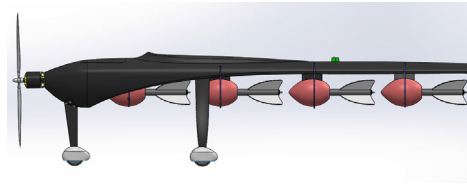
Fig. 15. *Fuselage side view*

The main structural support along the wings is provided by a vertically mounted balsa wood profile and carbon fiber mesh at the top and bottom part of the balsa wood with additional herex foam and fiberglass composite ribs for added structural rigidity. The flaps are located on the center plane of the wing, while ailerons are mounted as close to the edge of the wings as possible. The flaps follow a classic design as it was determined that more complex designs, such as Fowler flaps, are not necessary.
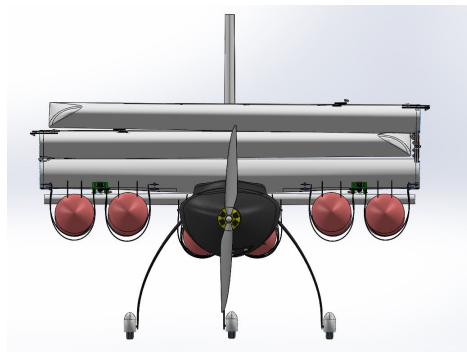
Fig. 16. *Stowed configuration of the aircraf*

The design shown in Fig. 16 enables a maximal wingspan while still maintaining centre of gravity at the same spot as when in the flight-ready configuration. This design permits the undercarriage to be as far forward as possible. The wings fold on top of the other as shown in Figure 16 to ensure the smallest possible stowed dimensions. The point of rotation of one wing is raised compared to the other, to enable the aforementioned stacking.

The momentum required is provided by two torsion springs on each wing, attached to the reinforced surface on the wings as shown in Fig. 17. Once the folding part crosses over the vertical point, the spring stops providing momentum and the force of gravity forces the wing to the final position where it is mechanically locked by three hooks on each side that hook to the underside of the wing.

The radome is attached behind the wing at the top of the aircraft, as shown in Fig. 18, to enable the

Table 9. *Dynamic stability of empty and loaded aircraft*

		Eigenvalue		Damping ratio		Undamped frequency [Hz]	
Longitudinal modes		M2	M3	M2	M3	M2	M3
I	Short Period	$-17.59 \pm i15.39$	$-5.15 \pm i5.47$	0.659	0.73	23.37	7.51
II	Phugoid	$-0.061 \pm i0.45$	$-0.047 \pm i0.47$	0.991	1.00	0.45411	0.47
Lateral modes		M2	M3	M2	M3	M2	M3
III	Dutch Roll	$-2.98 \pm i8.94$	$-1.05 \pm i3.70$	0.95	0.96	9.4236	3.85
IV	Roll	-28.501	-10.48	/	/	/	/
V	Spiral	0.041	0.037	/	/	/	/

Table 10. *Final aircraft dimensional characteristics*

Fuselage		Vertical Tail	
Total Length [in]	77.55	Airfoil	NACA 0010
Nose Length [in]	19.68	Span [in]	12.6
Tail Length [in]	57.87	Chord-base [in]	10.24
Width [in]	9.05	Chord-tip [in]	7.87
Height [in]	7.08	Wing area [in^2]	114.1
Wing		Aspect ratio	3.74
Airfoil	CLARK Y	Angle of attack [°]	0
Span [in]	95.27	Horizontal tail	
Chord-base [in]	19.68	Airfoil	NACA 0010
Chord-tip [in]	15.75	Span [in]	31.50
Wing area [in^2]	1627	Chord-base [in]	10.24
Aspect ratio	5.38	Chord-tip [in]	7.87
Angle of attack [°]	3.5	Wing Area [in^2]	285.2
		Aspect ratio	3.48
		Angle of attack [°]	0

Fig. 18. *Rotating radome position*

quick-release mechanism consists of plastic zip ties, attached to the wing at one end and a wire at the other.
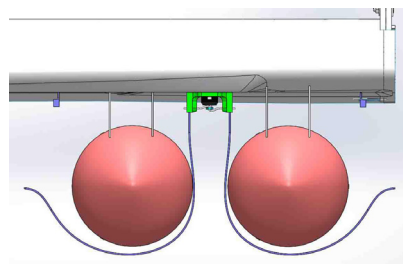
Fig. 19. *Attack store mounting*

To release the store, the wire is pulled by a servomotor to disengage the wire and the attack store as shown in Figs. 19 and 20. To mount each store the plastic zip ties are tightened and the attack stores are squished to the mounting sheets.

Fig. 17. *Actuator torsion springs*

least interference in flight. It enables easy assembly during the Ground Mission and while mounting the wing to the fuselage. An electric motor is attached within the fuselage and provides continuous rotation when necessary. The attachment point of the radome is a threaded nut attached to a threaded rod, with minimal thread engagement to ensure a fast mounting time crucial during the Ground mission. A 3D printed bushing, shaped as an aerodynamic drop, enables smooth rotation.

Each attack store is mounted on two carbon fibre sheets that act as a part of mounting hardware. The

Fig. 20. *Attack store quick release*

3.1 Weight and Balance

The correct centre of gravity (CG) location is crucial to achieve aircraft stability during flight. CG was determined by considering the weight of all aircraft components and their location on X axes. The weight of components was estimated based on CAD model or manufacturer specifications. The CG of aircraft in flight-ready configuration was calculated to be 17.91 in relative to X axis, as seen in Fig. 21.
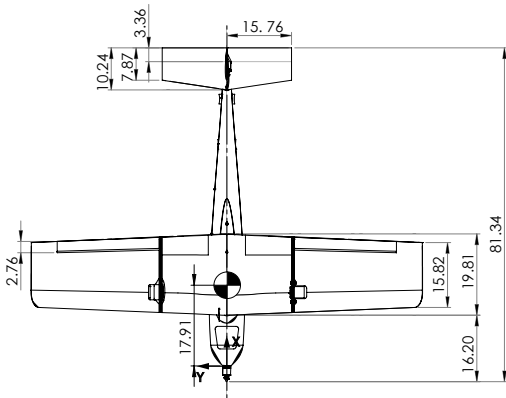
Fig. 21. *Airplane centre of gravity, units [in]*

Table 11 contains complete weight and balance data for all flight missions. Flight parameters for each individual mission are gathered in Table 12 where $C_{l,avg}$ is average lift coefficient and $C_{d,0}$ zero lift drag coefficient.

4 TESTING AND COMPETITION

A number of tests of key components are necessary to compare theoretical knowledge and predictions to real life situations and to achieve the top scores. Testing enables a quick check for errors in decision making, regarding aerodynamic performance, stability, control and propulsion performance. Detailed and extensive testing objectives were proposed for that purpose.

The purpose of the initial tests was to improve the accuracy of SAS as seen in Fig. 3, later tests served as a validation of proposed changes based on the initial tests. Laboratory and field tests were performed.

To determine the effects of aerodynamic drag of the attack stores attached to the wings and the fuselage we conducted a wind tunnel test. The aim was to understand the relationship that the stores have on the flight dynamics, drag and take-off distance. Drag force was measured with an external scale, velocity was measured with Pitot tube as in Fig. 22 . It was

Table 11. *Airplane weight and balance*

Aircraft component	Weight [lb]	X [in]
M1		
Fuselage	1.95	31.4
Wing	4.08	19.2
Tail	0.82	72.6
Motor	0.96	-1.3
Propeller	0.13	-3.1
Flight batteries	7.61	10.4
Front landing gear	0.29	3.2
Rear landing gear	0.71	20.3
Miscellaneous	1.05	20
Total	17.6	17.9
M2		
Rotating radome	0.08	34.6
Flight batteries	7.61	10.2
Total	17.68	17.9
M3		
Attack store #1	0.1375	11.2
Attack Store #19	0.1375	66.4
Flight batteries	7.61	8
Total-start	20.21	18.9
Total-finish	17.6	17.9

Table 12. *Performance parameters for final design*

Performance Parameter	M1	M2	M3
$C_{l,max}$	1.15	1.15	1.15
$C_{l,avg}$	0.133	0.135	0.16
$C_{d,0}$	0.054	0.065	0.07
Lift-to-drag ratio L/D_{cruise}	2.46	2.1	2.28
Wing loading [lbs/ft^2]	1.23	1.24	1.55
v_{avg} [ft/s]	98.1	98.0	91.6
v_{stall} [ft/s]	16.5	16.5	18.5
Aircraft weight [lbs]	17.6	17.68	18.9
Carried payload	0	Radome	19 Att. St.
Number of laps	3	3	19
Mission score	1	1.8	21

found that attack store in a free-stream has high drag coefficient $C_{d,as} = 0.32$ [8]. The aircraft will have much lower drag if stores are hidden from air-stream by putting them in the line attached on the fuselage than locating them on the wing and accumulating enormous drag.

In addition, the team tested different fuselage configurations mainly due to a high degree of drag from each individual attack store. Testing was done in a wind tunnel on a 1:4 scale to remove any negative effects the wind tunnel walls would have on the final measurements. Each variation was 3D printed and primed to have a similar surface finish to the final fuselage design. Attack stores were also printed in a similar fashion in 1:4 scale. Testing was conducted with three different fuselage designs with different number of attack stores. Each fuselage was tested at different speeds in the same fashion as individual

Fig. 22. *Attack store during drag testing*

attack stores as is presented in Fig. 23. It was found that with 10 stores (five in file, two in the line) drag coefficient of fuselage was still in the range $C_{d,fs} = 0.2$

Fig. 23. *Fuselage drag measurement in wind channel*

4.1 Test Flights and Fly-off

In order to understand the aircraft flight capabilities and increase pilot familiarity with the chosen design, numerous flight tests were conducted with a purpose-build Arduino-based data collection system with an SD-cared based storage unit on board. In this way, the team gained better insights into the flight characteristics, instead of pilot feedback only. During the majority of the tests the system was mounted on the aircraft and recorded GPS data, height, velocity, accelerations, voltage and current.

At the testing, it was found that aircraft with a maximum of 19 attack stores shows instability in flight but was still manageable. In presented configuration was found that during flight Mission 3, aircraft is capable of safely scoring just 17 laps in 10 minutes time slot. The problem was located in the unpredictability of NiMh cells (mandatory usage) internal resistance. The team decided to fly a third Mission at competition with the same number of attack stores.

At TIMPA Field in Tucson, Edvard Rusjan team successfully finish all missions at first flying day of

competition without notable problems. Despite 10 % lower air density in Tucson than in Ljubljana, aircraft was capable of performing take-off with full weight from the ramp. In Fig. 24 moment of aircraft take-off from the 10 ft ramp is presented.

Fig. 24. *"Pretty Boy" take-off at TIMPA field in Tucson*

The aircraft successfully finished the third flying mission with 17 attack stores and 12th of April officially finished all task with huge advance regarding to other teams. In Fig. 25 "Pretty Boy" aircraft was shown flying 17 attack stores onboard.

Fig. 25. *"Pretty Boy" at TIMPA Field in Tucson with 17 attack stores*

Still, team members were not satisfied with results and wanted to return to the competition to repeat Mission 3 and improve the result. Residual cell energy capacity after the third mission was measured and was found that there is no enough energy left in battery cells for an additional lap. Decision was made to extend battery pack with 4 additional cells and try to fly 18 laps. Battery and software upgrade was done on April 13th. Pilot was warned that in new configuration all-electric motor and driver performance limitations are fully exceeded and devices can be easily burned. Full power usage was prohibited even at the time of

take-off. On April 14th, last day of competition, team pilot Timotej Hofbauer scored 18 laps in 10 minutes time slot which was an absolute record of the competition.

5 CONCLUSIONS

Edvard Rusjan team from Faculty of Mechanical Engineering, University of Ljubljana, Slovenia is the winner of DBF 2019 competition. The success is result of strict scientific approach in optimizing of aircraft design to maximize its score in the competition. Team developed semi-analytic multidimensional algorithm for aircraft geometry and functionality optimization. With measurements of prototypes performance in flight and in wind tunnel algorithm coefficients value were fine tuned. By measurement of attack stores drag it was found that the best position is in line on the fuselage instead on widely accepted wings. New arrangement was found to have much lower drag and enables higher aircraft velocities with the same trust force. With the fundamental advantage in lower aerodynamic drag, aircraft of Edvard Rusjan team at final fly-off at TIMPA Field in Tucson scored 18 laps in 10 minutes time slot. Second best team from Georgia Institute of technology was 22 % slower and finish with 14 scored laps.

6 ACKNOWLEDGEMENTS

Members of Edvard Rusjan team are specialist for wide fields of activities, from process modelling, CAD/CAM, composite structure building, etc. Every member has the unique task and just as a group they are successful. Author of the paper would like to thank every member of the team for their contribution to team success.

List of Edvard Rusjan team members (Faculty of Mechanical Engineering, University of Ljubljana, Slovenia), which attended the final fly-off Design/Build/Fly Competition at TIMPA Field in Tucson, AZ from April 11 to 14, 2019 and won competition: Timotej Hofbauer (pilot and student leader), Vid Pugelj, Viktor Govže, Matej Gorjan, Jaka Romih, Nejla Kambič, Emil Zubalic, Martin Kocijančič, Filip Plešnik, Klemen Ambrož, Andraž Vene, Tilen Košir, Enej Istenič, Patrik Tarfila, Klemen Mlakar, Andraž Kladnik, and Viktor Šajn as Faculty advisor. In Fig. 26 is Edvard Rusjan team at DBF 2019 winner announcement.

Fig. 26. *DBF 2019 winning Edvard Rusjan team*

7 REFERENCES

[1] DBF Rules 2018-2019. AIAA [online], Previous Competitions, from *http://www.aiaadbf.org/*, accessed on 2019-11-13.

[2] Edvard Rusjan Team (2019). *Pretty Boy, AIAA Design/Build/Fly, 2018-2019 Design Report.* AIAA [online], Previous Competitions, from *http://www.aiaadbf.org/* , accessed on 2019-11-13.

[3] PythonCoreTeam (2019). *Python: A dynamic open source programming.* Python Software Foundation [online], from *https://www.python.org*, accessed on 2019-11-13.

[4] Airfoil tools (2017). *Airfoil database* [online], from *http://airfoiltools.com/*, accessed on 2019-11-13.

[5] Schlichting, H. (1979). *Turbulent Boundary Layers at Zero Pressure Gradient; Flat Plate; Rotating Disk; Roughness, Boundary Layer Theory.* 7th ed. McGraw-Hill, New York, p. 635-667.

[6] Drela, M., Youngren, H. (2017). *Athena Vortex Lattice [Computer software].* from *http://web.mit.edu/drela/Public/web/avl/*, accessed on 2019-11-13.

[7] Greenshields, C.J. (2019). *OpenFOAM, User Guide, ver. 7.* OpenFOAM Foundation Ltd.[online], from *https://openfoam.org*, accessed on 2019-11-13.

[8] Anderson, J.D.Jr. (2011). Fundamentals of inviscid incompressible flow. *Fundamentals of Aerodynamics.* 5th ed., McGraw-Hill, New York, p. 177-276.

Vsebina

Strojniški vestnik - Journal of Mechanical Engineering

Uvodnik

Začetek velike dobe za mali slovenski narod, ustvarjeno je ognjišče znanosti, vede in (tehniške) kulture

Ob jubileju 100 letnice Univerze v Ljubljani in 100 letnici študija strojništva

23. julija 1919 je v Ljubljani regent Aleksander Karađorđević s podpisom zakona, ki je imel samo tri člene, ustanovil Vseučilišče Kraljestva Srbov, Hrvatov in Slovencev – današnjo Univerzo v Ljubljani (UL). Tako preprosto je bilo takrat v novoustanovljeni državi Kraljevine Srbov, Hrvatov in Slovencev. Ustanovitvene članice so bile filozofska, medicinska, pravna, tehniška in teološka fakulteta. Če spregledamo pomisleke, da čas ustanovitve slovenske univerze seže več kot sto let, po nekaterih mnenjih celo tristo let v preteklost, letos praznujemo enega od prvih mejnikov ob rojstvu visokega šolstva pri nas.

Med zaslužnimi za ustanovitev slovenske Univerze v Ljubljani ima posebno mesto župan mesta Ljubljane Ivan Hribar (od leta 1896 do leta 1910 župan). Na njegovo pobudo je je bil pri ljubljanskem občinskem svetu že leta 1912 ustanovljen Vseučiliški odsek, ki je iskal mlade, nadarjene slovenske strokovnjake in jih gmotno podpiral pri pripravah na akademsko kariero. Pomembni mesti pa imata tudi dr. Mihajlo Rostohar, sicer docent na praški univerzi, ki je novembra 1918 ustanovil Vseučiliško komisijo pri Narodni vladi in dr. Danilo Majaron, ki je bil na seji Vseučiliške komisije 5. decembra 1919 izvoljen za njenega predsednika. Dr. Danilo Majaron je bil 22. junija 1929 proglašen za prvega častnega doktorja ljubljanske univerze.

Prva predavanja so bila 3. decembra 1919, kar se šteje za uradni rojstni datum UL. Če pa bi rojstvo UL premaknili na čas nastanka prvih kateder filozofskega študija v Ljubljani (za logiko in cerkveno pravo ter za fiziko in matematiko) bi bila stara več kor tristo let. UL praznuje stoletnico univerze izvajanja predavanj v slovenskem jeziku. Namreč, v sredo, 3. decembra 1919, od devete do desete ure, je imel dr. Fran Ramovš v deželni zbornici poslopja Deželnega dvorca, današnji zbornični dvorani univerze, prvo predavanje v slovenskem jeziku: »Z današnjim dnem, ko pričakujemo novo dobo, novo življenje, ko ustanavljamo slovensko univerzo, naj vas iskreno pozdravim kot prve slušatelje naše Alme matris. S tem svetim trenutkom stopa naš narod v zgodovino, ki je ne izbriše nihče nikoli več« je takrat nagovoril študente na predavanju o historični gramatiki slovenskega jezika.

Začetek velike dobe za mali slovenski narod, ustvarjeno je ognjišče znanosti, vede in kulture.

Prvi rektor je postal eden najpomembnejših matematikov z začetka dvajsetega stoletja dr. Josip Plemelj, prvi dekan Tehniške fakultete je postal dr. Karol Hinterlechner, geolog in zunanji član čehoslovaške akademije znanosti v Pragi, prva doktorandka je bila Ana Mayer, ki je 15. julija 1920 uspešno zagovarjala disertacijo z naslovom: »O učinkovanju formalina na škrob«.

Prvo leto je bilo v ustanovnih pet fakultet vpisanih 942 študentov, od tega le 3 odstotke žensk. S kraljevim ukazom je bilo 31. avgusta 1919 imenovanih prvih 18

profesorjev ljubljanske univerze pri čemer eden ni sprejel delovnega mesta profesorja. V prvem desetletju obstoja se jim je pridružilo več kot deset vrhunskih ruskih učenjakov, ki so iz svoje domovine pobegnili zaradi revolucije. Ruski predavatelji so vpeljali več novih znanstvenih področij, kar je omogočilo, da se je UL, kljub mladosti, povzpela na raven drugih primerljivih univerz v Evropi. Na kakovost predavanj na univerzi so poleg slovenskih znanstvenikov, kot so bili matematik dr. Josip Plemelj, kemik dr. Maks Samec in dr. Milan Vidmar, ki so že prej delovali v mednarodnem akademskem prostoru, pomembno vplivali tudi tuji znanstveniki.

Tudi v tistem času je imel denar pomembno vlogo, saj so smo bili priča poskusom ukinitve Tehniške fakultete oziroma so se pojavile ideje o razporeditvi raznih oddelkov tehniških fakultet v Beogradu, Zagrebu in Ljubljani. S tem pa bi bila Tehniška fakulteta v Ljubljani, ki jo je skoraj v celoti opremil zasebni kapital slovenske industrije, okrnjena. Koncem tridesetih let prejšnjega stoletja so pričeli z deli za strojni in kemijski inštitut Tehniške fakultete.

Za primerjavo, v letu 2019 je na 26 članicah UL vpisanih 37874 študentov, od tega 60 odstotkov žensk, univerza se uvršča med tri odstotke najboljših univerz na svetu. Na eni najpomembnejših akademskih lestvic - ARWU lestvici (Academic Ranking of World Universities) se že vrsto let uvršča med 500 najboljših univerz, na lestvici CWUR (The Center for World University Rankings) zaseda 370. mesto, na THE lestvici (Times Higher Education) se uvršča v skupino 601-800.

Organizacijski razvoj Tehniške fakultete in Fakultete za strojništvo:
- 1919-1945: UL, Tehniška fakulteta, Elektrostrojni oddelek (dveletni študij strojništva),
- 1945-1950: UL, Tehniška fakulteta, Oddelek za strojništvo (popoln študij strojništva),
- 1950-1954: Tehniška visoka šola, Fakulteta za strojništvo,
- 1954-1957: UL, Tehniška fakulteta, Oddelek za strojništvo,
- 1957-1960: UL, Fakulteta za elektrotehniko in strojništvo,
- Od 1960 naprej UL, Fakulteta za strojništvo.

Še pred formalno ustanovitvijo UL, so se 19. maja 1919 začela visokošolska predavanja strojništva, elektrotehnike in gradbeništva, pri čemer so do jeseni slušatelji absolvirali snov celotnega prvega letnika. Leta 1919 so bili vpisani v »Začasni tehniški visokošolski tečaj« med drugimi tudi Dobromil Uran, Albert Struna in Franc Smolik, ki so bili po drugi svetovni vojni imenovani za visokošolske učitelje na

Tehniški fakulteti, pri čemer so pred imenovanjem imeli vsi trije uspešno kariero v industriji. V okviru Tehniške fakultete je bil predmetnik razdeljen na skupine: matematični predmeti, naravoslovni predmeti, gradnje in arhitektura, strojništvo in elektrotehnika, rudarstvo in plavžarstvo, državo- in pravoslovni predmeti ter dva predmeta označena pod razno.

Med prvimi 18 profesorji je bil tudi strokovnjak elektro-strojniške stroke dr. Milan Vidmar, ki je leta 1922 doktoriral iz klasičnega strojništva, delo ima naslov: Teorija centrifugalne črpalke (Theorie der Kreiselpumpe). Dr. Vidmar, sicer šahovski velemojster, se je poleg svoje ljubezni do elektrotehnike zavedal pomembnosti strojništva in predaval predmet Teoretično strojeslovje. Vpis na Tehniško fakulteto UL je bil relativno velik, v prvem letu študija sta bili vpisani tudi dve dami. Padec vpisa se je zgodil v tridesetih letih prejšnjega stoletja, verjetno kot posledica gospodarske krize.

Na osebno povabilo dr. Milana Vidmarja je prišel na Tehniško fakulteto Feliks Lobe, ki je bil zaradi velikih izkušenj v industriji, takoj imenovan za izrednega profesorja. S prihodom Feliksa Lobeta na Tehniško fakulteto se je področje strojništva bistveno okrepilo, pri čemer pa se je področje strojništva na UL ni polno razvilo iz različnih vzrokov. Dr. Milana Vidmarja štejemo za idejnega pobudnika študija strojništva na UL, ki je dojel pomen stroke in je vseskozi podpiral Feliksa Lobeta. Slednji je z večletnim osebnim trudom in s predavanji predmetov Termodinamika in Pogonski stroji uresničil popoln študij strojništva, po letu 1937 pa predaval še predmet Mehanska tehnologija. Njegov asistent je bil Leopold Andrée, sodelavec pa Boris Černigoj, ki sta po svetovni vojni postala visokošolska učitelja. Široki duh poznejšega akademika in častnega doktorja UL Feliksa Lobeta je predvidel dve glavni veji strojništva: - mehanike trdnih teles in mehanike fluidov oziroma enakomeren razvoj tehnološkega in energetskega strojništva.

V študijske letu 1940/41 so predavali: izr. prof. Romeo Strojnik (Strojno risanje, Strojni elementi II, Dvigala), redni prof. Feliks Lobe (Pogonski stroji I, Pogonski stroji II, Obča mehanska tehnologija II), doc.dr. Dušan Avsec (Termodinamika), honorarno Albert Struna, poznejši redni profesor in rektor UL (Gradnja in teorija motornih vozil) in honorarno Ciril Rekar (Obča mehanska tehnologija II). Po drugi svetovni vojni se je Tehniška fakulteta razdelila na šest oddelkov, med njimi omenimo oddelek Strojništva. S popolnim študijem strojništva je bil razširjen učni načrt, prišlo je več novih predavateljev, ki jih je večino

izbral Feliks Lobe. Tako so bili leta 1946 imenovani v visokošolski naziv in postali redno zaposleni doc. Leopold Andrée, redni prof. Leon Kavčnik, izr. prof. Franček Kovačec, izr. prof. Bojan Kraut, redni prof. Zoran Rant in redni prof. Anton Vakselj. Na oddelku za strojništvo Tehniške fakultete je bilo ustanovljenih devet inštitutov, približno polovica inštitutov je bila obarvana energetsko, druga polovica pa tehnološko.

31. julija 1948 sta diplomirala prva inženirja strojništva Jožef Herman in Josip Kuralt, eden prvih doktorjev strojne stroke pa je leta 1950 postal Zoran Rant.

Poleg že navedenih so do leta 1960 na področju razvoja študija strojništva pomembno pustili svoj pečat predavatelji (navedeni so po abecedi): Josip Boncelj, Jože Hlebanja, Leon Kavčnik, Branko Kozina, Anton Kuhelj, Boleslav Likar, Ervin Prelog, Stane Premelč, Ciril Rekar, Viktor Savnik, Franc Smolik, Albert Struna, Vladimir Staněk, Dobromil Uran, Anton Vakselj in Ivo Vušković.

Leta 1957 je bila ukinjena Tehniška fakulteta, oddelka za elektrotehniko in strojništvo sta se združila z imenom Fakulteta za elektrotehniko in strojništvo, vendar je ta zveza trajala le tri leta. 1. oktobra 1960 je nastala Fakulteta za strojništvo, samostojna enota UL. FS se je pričela kadrovsko in prostorsko širiti. Prvi dekan samostojne Fakultete za strojništvo (FS) je bil Zoran Rant.

Ob ustanovitvi je FS imela štiri katedre: Katedra za matematiko in druge osnovne predmete, Katedra za delovne stroje in transport, Katedra za tehnologijo in Katedra za pogonske stroje in termične naprave. V študijskem letu 1960/61 je bilo vpisanih v prvi letnik 264 slušateljev, v drugi letnik 167, v tretji letnik 143 in v četrti letnik pa 113 slušateljev in 214 absolventov. V študijskem letu 1971/72 se je število kateder povečalo na šest, naslednje leto na sedem kar je ostalo nespremenjeno 25 let. Tretjina kateder je bila usmerjena v energetiko, dve tretjini pa v tehnologijo in proizvodnjo.

Takratni fakultetni svet je leta 1962 ustanovil Inštitut za strojništvo, kot finančno samostojni zavod neločljivo povezan s FS. Namen inštituta je je bilo raziskovalno delo in povezava z industrijo. V letu 1960 je bil vpeljan tristopenjski študij (diploma, magisterij, doktorat). Diplomski študij se je skrajšal za en semester (iz deset na devet), vključno z diplomo, opravljen magistrski študij pa je postal pogoj za doktorski študij. To je bila sprememba od več desetletne tradicije s čimer se je podaljšala pot do doktorske disertacije. Po približno 40 letih se je program študija vrnil na stari model – deset semestrski

študij vključno z diplomo in neposredni prehod na izdelavo doktorske disertacije.

V študijskem letu 1996/97 je fakulteta začela izobraževati slušatelje na univerzitetni stopnji, ki je bila obarvana bolj teoretično (10 semestrov), in na visokošolski strokovni študij (8 semestrov vključno s šest mesečnim praktičnim usposabljanjem in diplomskim delom) namenjen inženirjem v praksi. Fakultetni senat so sestavljali samo redni profesorji; odločitev, da je vsak redni profesor lahko dobil svojo katedro, je v študijskem letu 1997/98 število kateder povečalo iz sedem na trinajst. V študijskem letu 2008/09 je FS začela izvajati prenovljen študijski program na univerzitetni stopnji in tudi na visokošolski strokovni stopnji skladno z bolonjskimi načeli.

FS je danes vodilna multidisciplinarna raziskovalno orientirana fakulteta na področju strojništva v Sloveniji. Prepoznava mlade talente in jih vzgaja v odlične znanstvenike in napredne strokovnjake. Na FS so študirali in diplomirali številni znani Slovenci, ki so danes na vodilnih položajih ali delajo v številnih znanstvenih institucijah po svetu, gospodarstvu, politiki, itd. Študenti in fakultetna mobilnost sta sestavna dela internacionalizacije, ki omogoča mednarodno izmenjavo študentov in mladih raziskovalcev.

V študijskem letu 2018/19 je bilo na FS vpisanih 1652 študentov na I. (univerzitetni program) in II. (magistrski program) bolonjski stopnji ter visokošolskem strokovnem študiju (visokošolski program), na III. stopnji (doktorski program) je bilo vpisanih 95 doktorandov. V letu 2018 je diplomiralo (graduate) 415 študentk in študentov, 11 jih je doktoriralo. V letu 2018 je bilo na FS 44 učiteljev, 79 asistentov in 158 raziskovalcev med 373 zaposlenimi; ki so sodelovali na 45 mednarodnih raziskovalnih projektih ter 179 tržnih projektih z industrijo, objavili so 161 originalnih znanstvenih člankov ter prijavili 6 patentov. FS je imela 18 kateder z 39 raziskovalnimi laboratoriji in centri.

Rektorji Univerze v Ljubljani iz Tehniške fakultete in Fakultete za strojništvo so bili: Milan Vidmar (1928-1929), Anton Kuhelj (1954-1956), Albert Struna (1964-1967), Ervin Prelog (1976-1978), Polde Leskovar (1987) in Janez Peklenik (1987-1989).

Ustanovitev UL pred 100 leti je omogočilo, da so se znanstveniki začeli izobraževati v Sloveniji. Že prej so slovenski znanstveniki dosegali velike uspehe, a so delovali navadno na germanskem področju ter pisali in predavali v nemščini. Z ustanovitvijo UL pa je slovenščina postala tudi jezik znanosti. Promocija znanosti je nepogrešljiva za izobraženo družbo, za

uporabo slovenskega jezika v visokem šolstvu - za ohranjanje slovenskega jezika malega naroda.

Jubilejna številka SV-JME ob 100 letnici UL in 100 letnici studija strojništva je posvečena predstavitvi raziskovalnih dosežkov slovenskih znanstvenikov na področju strojništva UL. Postali smo del slovenske inteligence, ki objektivno omogoča rast razvoja in napredka slovenskega naroda. Celovitost kulture posameznega naroda je razumnost živega življenja.

VIVAT, CRESCAT, FLOREAT!

Vincenc Butala
Glavni in odgovorni urednik

Uporabljena literatura:

Univerza v Ljubljani, Fakulteta za strojništvo: Zgodovina strojništva in tehniške kulture na Slovenskem, Ljubljana, 2010.
75 let Univerze v Ljubljani, Ljubljana, 1994.
Zbornik Slavnostna akademija ob 90 letnici študija strojništva, Univerza v Ljubljani, Fakulteta za strojništvo, 2010.
Univerza v Ljubljani, https://www.uni-lj.si/o_univerzi_v_ljubljani/100_let_ul/, odčitano 2019-10-29.
Univerza v Ljubljani, Fakulteta za strojništvo: Annual Report 2018.

Elastokalorično hlajenje: Pregled razvoja in nadaljnji izzivi pri razvoju regenerativnih elastokaloričnih naprav

Parham Kabirifar – Andrej Žerovnik – Žiga Ahčin – Luka Porenta – Miha Brojan – Jaka Tušek*

Univerza v Ljubljani, Fakulteta za strojništvo, Slovenija

Elastokalorični hlajenje, ki temelji na izkoriščanju latentne toplote sproščene/absorbirane pri napetostno povzročeni martenzitni transformaciji v zlitinah z oblikovnim spominom, se v zadnjih letih kaže kot ena najperspektivnejših alternativ relativno neučinkovite ter še vedno okoljsko sporne parno-kompresijski tehnologiji hlajenja. Elastokalorično hlajenje je potencialno lahko bolj učinkovito od parno-kompresijskega ter zaradi uporabe neškodljivih hladilnih sredstev (materialov z oblikovnim spominom) okolju prijazno.

V prvem delu prispevka je opisan elastokalorični učinek v zlitinah z oblikovnim spominom ter pregled stanja na področju elastokaloričnih materialov in naprav. V splošnem lahko vse zlitine z oblikovnim spominom, ki so pri želeni delovni temperaturi v avstenitni fazi, obravnavamo kot potencialne elastokalorične materiale. Elastokalorični krožni proces temelji na štirih osnovnih korakih. Ko elastokalorični material obremenimo z zunanjo silo, to povzroči avstenitno-martenzitno transformacijo, in material se segreje. Nato material toploto odda v okolico in se s tem ohladi nazaj na začetno temperaturo. Sledi razbremenjevanje materiala, pri čemer pride do povratne martenzitno-avstenitne transformacije in material se ohladi pod temperaturo okolice. Hladen elastokaloričen material je nato sposoben črpati toploto iz okolice in s tem hladiti želen prostor/telo. Pri najboljših danes poznanih elastokaloričnih materialih so lahko adiabatne spremembe temperature med obremenjevanjem in razbremenjevanjem tudi več kot 30 K. Do danes je bilo na svetu razvitih in testiranih okoli 10 demonstracijskih elastokaloričnih naprav. Najboljše med njimi, ki temeljijo na principu aktivne elastokalorične regeneracije, že dosegajo komercialno zanimive hladilne karakteristike s temperaturnimi razponi okoli 20 K, specifičnimi hladilnimi/toplotnimi močmi okoli 800 W na kilogram elastokaloričnega materiala in eksergijskimi učinkovitostmi okoli 20 %. Aktivni elastokalorični regenerator je porozna struktura iz elastokaloričnega materiala preko katerega se črpa tekočina za prenos toplote (npr. voda). Glavna prednost takšnega principa izkoriščanja elastokaloričnega učinka je, da se ob ustreznih obratovalnih pogojih vzdolž regeneratorja ustvari temperaturni profil med virom in ponorom toplote. S tem je lahko temperaturni razpon regenerativne elastokalorične naprave večji od temperaturnih sprememb generiranih v materialu zaradi elastokaloričnega učinka.

V drugem delu prispevek obravnava dva ključna izziva pri razvoju regenerativne elastokalorične hladilne naprave oziroma toplotne črpalke. To sta razvoj poroznih struktur iz elastokaloričnih materialov, ki bi lahko služili kot aktivni elastokalorični regeneratorji ter razvoj učinkovitega pogonskega sistema za obremenjevanje/razbremenjevanje takšnih regeneratorjev. Predstavljene so različne geometrije aktivnih elastokaloričnih regeneratorjev izdelane iz različnih oblik elastokaloričnih materialov. Predstavljene so tudi dosedanje raziskave aditivne proizvodnje poroznih struktur iz materiala z oblikovnim spominom. V splošnem lahko aktivne elastokalorične regeneratorje obremenimo z natezno ali tlačno silo, pri čemer imata oba načina obremenjevanja nekatere prednosti oziroma slabosti za elastokalorično hlajenje. Glavna prednost nateznega obremenjevanja je možnost uporabe tankih elementov (žic, ploščic) z veliko specifično površino, kar omogoča hiter in učinkovit prenos toplote med elastokaloričnim materialom ter tekočino za prenos toplote, medtem ko je glavna slabost nateznega obremenjevanja omejena doba utrujanja. Prikazano je, da je lahko doba utrujanja pri tlačnem obremenjevanju bistveno boljša kot pri nateznem (preko 10^6 obremenitev brez poškodb), a se pri tem pojavlja problem uklonske stabilnosti elastokaloričnih materialov ter s tem povezane nezmožnosti uporabe poljubno tankih elastokalorični elementov, ki bi omogočali hiter prenos toplote. Druga ključna komponenta elastokalorične naprave pa je pogonski sistem, ki mora na učinkovit način zagotavljati relativno velike sile potrebne za obremenjevanje elastokaloričnih materialov in hkrati koristno izrabljati sproščeno mehansko delo med njihovim razbremenjevanjem. Prikazana je analiza pogonskega sistema z integriranim vstajnikom, ki omogoča tudi do 70 % regeneracijo celotnega vloženega dela (preostanek predstavljajo histerezne izgube elastokaloričnega učinka).

Ključne besede: elastokalorični učinek, hlajenje, aktivni elastokalorični regenerator, doba utrujanja, pogonski mehanizem

*Naslov avtorja za dopisovanje: Univerza v Ljubljani, Fakulteta za strojništvo, Laboratorij za hlajenje in daljinsko energetiko, Aškerčeva 6, 1000 Ljubljana, Slovenija, jaka.tusek@fs.uni-lj.si

Ekvivalenca harmonskih in impulznih obremenitev v vibracijskem utrujanju

Primož Ogrinec – Janko Slavič* - Miha Boltežar

Univerza v Ljubljani, Fakulteta za strojništvo, Slovenija

V vibracijskem utrujanju se tipično srečujemo s tremi tipi obremenitev: naključnimi, harmonskimi in impulznimi. V praksi pa so možne vse njihove kombinacije. Obvladovanje dobe trajanja sodobnim inženirjem predstavlja vse večji izziv, saj strukture zaradi optimizacije mase s svojo lastno dinamiko intenzivneje prehajajo v frekvenčno območje obremenitev.

Dobo trajanja je mogoče analizirati v frekvenčni ali časovni domeni. Oba pristopa temeljita na števnih metodah, ki popisujejo obremenitve strukture. V časovni domeni števne metode obratujejo na znanih zgodovinah, med njimi pa se je najbolj uveljavila padavinska števna metoda. Identifikaciji obremenitvenih ciklov, v analizi utrujanja, sledi seštevek doprinosa posameznih ciklov v cenilko poškodovanosti materiala. Na področju strukturne dinamike, kjer so obremenitve pogosto stohastične in zato predstavljene v časovni domeni, se časovni pristop k analizi dobe trajanja izkaže za numerično zahtevnega in časovno potratnega. V ta namen so se razvile števne metode v frekvenčni domeni, ki imajo pogosto za osnovo spektralne momente močnostnega spektra odziva obravnavane strukture. Večina teh metod deluje na predpostavki, da je močnostni spekter odziva strukture Gaussovo porazdeljen in stacionaren. To ne velja za primer, ko so v obremenitvah prisotni impulzi. Ti impulzi so lahko posledica geometrijskih nelinearnosti, kontaktnih pogojev, povečanih nivojev obremenitve, obrabe v kontaktih ali pa nepredvidene rabe komponente.

Nedavne študije so pokazale, da napovedovanje dobe trajanja z metodami v frekvenčni domeni za nestacionarne, ne-Gaussove signale vrnejo bistveno napačne rezultate. Iz praktičnih razlogov se v praksi najpogosteje uporablja sinusne signale za utrujenostne teste. Vendar pa se ob prej omenjenih pogreških pri napovedi dobe trajanja s frekvenčnimi metodami pojavlja vprašanje o veljavnosti parametrov Wöhlerjeve krivulje, ki so bili identificirani s harmonskimi utrujenostnimi testi. Zato je eksperimentalna validacija, kot tudi analitična obravnava enakosti teh dveh tipov obremenitev z vidika identifikacije materialnih parametrov ključnega pomena.

Ta raziskava se osredotoča na teoretično analizo ekvivalentnosti harmonskih in impulznih obremenitev za primer sistema z eno prostostno stopnjo, ki potrjuje uporabnost impulznih testiranj za potrebe vibracijskega utrujanja. V tem delu je prikazano razmerje med impulznimi in harmonskimi obremenitvami, ki je povezano z dinamskimi lastnostmi strukture (npr. dušenje, lastna frekvneca). V časovni domeni je za primerjavo služila padavinska števna metoda, v frekvenčni pa t.i. ozko-spektralna števna metoda. Z uporabo modalne dekompozicije se lahko teoretična analiza na nivoju sistema z eno prostostno stopnjo prevede na sistem z več prostostnimi stopnjami.

Na podlagi teoretične analize, je bilo zasnovano preskuševališče tako za impulzna, kot za harmonska vibracijska testiranja. Pol-sinusni impulz je bil izbran za validacijo teoretičnega postopka, saj se le-ta izkaže za najbolj realno aproksimacijo impulzov, s katerimi se srečujemo v praksi. Testiranih je bilo 18 vzorcev, 9 je bilo vzbujanih impulzno, 9 pa harmonsko. S spreminjanjem uteži je bilo mogoče predlagano hipotezo preveriti tudi za različne lastne frekvence in razmernike dušenja vzorca.

Predlagani analitični časovno-frekvenčni model potrjuje ekvivalenco harmonskih in impulznih obremenitev v vibracijskem utrujanju.

Ključne besede: Vibracijsko utrujanje, naključne obremenitve, spektralne metode, utrujanje materiala, stacionarne in ne-stacionarne obremenitve

Kavitacija kot potencialna tehnologija za revitalizacijo odpadnih voda – primer povečanega sproščanja hranil iz odpadnega biološkega mulja papirne industrije

Mija Sežun[1] – Janez Kosel[2] – Mojca Zupanc[3] – Marko Hočevar[3] –
Janez Vrtovšek[3] – Martin Petkovšek[3] – Matevž Dular[3,*]

[1]Institut za celulozo in papir, Slovenija
[2]Zavod za varstvo kulturne dediščine Slovenije, Slovenija
[3]Univerza v Ljubljani, Fakulteta za Strojništvo, Slovenija

Na globalni ravni se obseg celulozne industrije povečuje iz leta v leto pri čemer se vsak dan ustvari ogromna količina različnih odpadnih materialov. Najpogostejši odpadni material vključuje pepel, drobljenec, odpadni biološki mulj in veliko količino odpadne vode. Sistemi za obdelavo odpadnih vod in muljev vključujejo anaerobno obdelavo, aerobno razgradnjo v lagunah z aktivnim biološkim muljem in sisteme za bistrenje ter filtracijo. Omenjeni čistilni sistemi za papirno industrijo predstavljajo kar 60 % vseh procesnih stroškov in posledično je velik delež razvojnih stroškov namenjen iskanju novih in alternativnih rešitev. Ena izmed možnih alternativ je mehanska pred-obdelava z uporabo hidrodinamske kavitacije (HK), kjer zaradi lokalno povečane hitrosti toka pride do padca tlaka in posledičnega uparjanja kapljevine. Pri tem se generirajo intenzivni udarni valovi, ekstremne temperature na mikro lokalni ravni, prihaja pa tudi do razpada vode na •OH radikale.

Cilj študije je določiti učinkovitost HK za obdelavo odpadnih bioloških muljev, ki so sekundarni produkt čistilne naprave v papirni industriji. S tem smo želeli predvsem povečati stopnjo sproščanja hranil iz vzorca in razpad njegovih bioloških komponent. Testirali smo sistem z simetrično Venturijevo zožitvijo ter sitem z rotacijsko napravo, ki omogoča intenzivni razvoj številnih kavitacijskih con. Slednjo napravo smo izdelali tudi v pilotni različici za obdelavo 500 L vzorcev. Za karakterizacijo vzorcev smo določevali skupno kemijsko potrebo po kisiku (KPK_s), topni KPK (KPK_t), skupni dušik (N_s) in fosfor (P_s). Izmerjene so bile tudi trdne snovi, pH vrednost, redoks potencial in kalorične vrednosti.

Rezultati iz laboratorijskih analiz so pokazali, da sta obe kavitacijski napravi znatno zmanjšali vrednosti KPK_s v odpadnem biološkem mulju. Do zmanjšanja je prišlo zaradi razgradnje organskih molekul do osnovnih hranil (dušik, fosfor). Nadalje smo s HK povečali vrednosti KPK_t in N_s. Predvidevamo, da so ekstremne razmere med HK povzročile poškodbe na celični membrani mikroorganizmov in posledični izpust celične vsebine v okolje. Sproščena celična vsebina lahko nadomesti del hranil, ki jih sicer moramo dovajati v biološki proces čiščenja. Razpad mikroorganizmov se je odražal v zmanjšani vsebnosti netopnih usedlin, kar ugodno vpliva na končno obdelavo muljev. Poskusi s pilotno napravo s 500 L vzorci mulja so dosegli največje povečanje v KPK_t vrednosti (iz 509 mg/L na 1023 mg/L) in znatno povečanje v P_s in N_s vrednostih. Ko smo s kavitacijo 15 minut tretirali 500 L vzorec s povišano pH vrednostjo 10 (NaOH) je prišlo do še dodatnega izboljšanja v KPK_t vrednosti (povečanje za 2400 mg/L) in v sproščanju N_s (povečanje za 120 mg/L). Alkalna pred-obdelava sproži postopek razgradnje beljakovin, HK pa tvori reaktivne kisikove radikale (•OH), ki so potrebni za pospešitev te razgradnje in za posledični razkroj v osnovna hranila. Po izračunih ekonomske učinkovitosti alkalnega tretmaja s HK bi 1,9 kg sproščenega KPK_t stalo komaj 1 euro kar kaže na visoko energijsko varčnost rotacijske naprave.

Ključne besede: hidrodinamska kavitacija, hranila, papirna industrija, odpadni biološki mulj, razgradnja muljev, obdelala odpadnih voda

Distribuirani proizvodni sistemi z digitalnimi dvojčki

Niko Herakovič* – Hugo Zupan – Miha Pipan – Jernej Protner – Marko Šimic

Univerza v Ljubljani, Fakulteta za strojništvo, Slovenija

Prispevek predstavlja nov pristop integracije izboljšane strukture proizvodnih vozlišč, ki so vključeni kot inteligentni distribuirani podsistemi v proizvodnih procesih sestavljeni iz kombinacije naprednih tehnologij digitalnih dvojčkov, holonov in digitalnih agentov. Enega od pomembnejših raziskovalnih rezultatov predstavlja nova arhitektura proizvodnih vozlišč za ponazoritev celotnega distribuiranega proizvodnega omrežja.

Današnja proizvodnja mora zagotavljati hitro in učinkovito prilagajanje trenutnim zahtevam naročnikom, to je veliki variantnosti izdelkov. Trenutne informacijske tehnologije, kot so internet stvari, podatkovne baze in umetna inteligenca zagotavljajo dobro povezljivost in komunikacijo med distribuiranimi kibernetsko-fizičnimi sistemi (KFS) za izvajanje kontrole in krmiljenja procesov in so sposobni reševati probleme in sprejemati odločitve. Na podlagi obstoječe literature in raziskav je razvidno, da glavni problem predstavlja prenos velike količine podatkov iz glavne podatkovne baze do podsistemov in nazaj, za učinkovito spremljanje in krmiljenje proizvodnje.

Metodologija raziskovanja je zato osredotočena na učinkovito povezljivost distribuiranih sistemov, digitalne dvojčke sposobne upravljanja logističnih procesov in materialnega toka ter na kontrolo in sprejemanje odločitev na globalnem in lokalnem nivoju. Podrobneje je predstavljena struktura sodobnih distribuiranih sistemov, katerim dodamo digitalne dvojčke in inteligentne digitalne agente. Takšni sistemi so sposobni povezovanja z drugimi sistemi/agenti, zaznavanja okolice, učenja, odločanja, nadziranja in vodenja. Predstavljena je nova arhitekturna mreža distribuiranih sistemov, ki določa prenos le pomembnih informacij med posameznimi podsistemi in njihovimi lokalnimi podatkovnimi bazami, kar močno izboljša zanesljivost in hitrost pretoka informacij.

Eksperimentalni sistem je sestavljen iz transportne linije, dveh robotskih celic, skladišča, šestih delovnih mest in enega pametnega ročnega delovnega mesta. Distribuirano kontrolno strukturo sestavlja devet vozlišč. Osem vozlišč vključuje digitalne agente, holone in lokalne digitalne dvojčke (sedem delovnih mest in skladišče), deveto vozlišče (imenovano vozlišče 0) pa sestoji iz digitalnih agentov, holona in globalnega digitalnega dvojčka. Vozlišča so medsebojno povezana, kadar je to potrebno, razen v primeru vozlišča 0, ki je povezano z vsemi ostalimi vozlišči. Testiranje realnega sistema in digitalnega dvojčka je potekalo v dveh fazah. Prva faza predstavlja simulacijo izvedbe proizvodnega plana za dva produkta (P1 in P2) v digitalnem dvojčku, kjer smo beležili simulacijske čase vhoda in izhoda transportne palete na posameznem proizvodnem vozlišču. Druga faza predstavlja zagon fizičnega sistema z distribuiranimi enotami in beleženje časov prihoda in odhoda palete z izdelkom na proizvodnem vozlišču. Čase pridobljene z digitalnim dvojčkom smo primerjali z izmerjenimi časi realnega distribuiranega sistema. Rezultati časovne analize so pokazali, da povprečen odstopek med rezultati simulacije in realnega sistema znaša 3,90 sekunde za izdelek P1 in 6,71 sekunde za izdelek P2. Skupni proizvodni čas znaša 8 minut in 54 sekund za izdelek P1 in 8 minut in 12 sekund za izdelek P2. Izračunan korelacijski koeficient za izdelek P1 znaša 0,9979 in 0,8748 za izdelek P2, iz česar lahko sklepamo na 98 % točen popis realnega distribuiranega sistema z digitalnim dvojčkom.

Ključne besede: pametne tovarne, distribuirani sistemi, vozlišča, holoni, izmenjava podatkov, digitalni dvojčki, digitalni agenti

*Naslov avtorja za dopisovanje: Univerza v Ljubljani, Fakulteta za strojništvo, Laboratorij za strego, montažo in pnevmatiko, Aškerčeva 6, 1000 Ljubljana, Slovenija, niko.herakovic@fs.uni-lj.si

Večfizikalni in večnivojski brezmrežni simulacijski sistem za polkontinuirno ulivanje aluminijevih zlitin

Božidar Šarler[1,2,*] – Tadej Dobravec[2] – Gašper Glavan[1] – Vanja Hatić[1,2] – Boštjan Mavrič[1,2] –
Robert Vertnik[2] – Peter Cvahte[3] – Filip Gregor[3] – Marina Jelen[3] – Marko Petrovič[3]

[1]Univerza v Ljubljani, Fakulteta za strojništvo, Slovenija
[2]Inštitut za kovinske materiale in tehnologije, Slovenija
[3]IMPOL 2000, d.d., Slovenija

V članku je opisan eksperimentalno validiran brezmrežni simulacijski sistem, ki opisuje fizikalne pojave pri polkontinuirnem ulivanju (PU) aluminijevih zlitin pod vplivom nizkofrekvenčnega elektromagnetnega polja. Nizkofrekvenčno elektromagnetno ulivanje (NFEU) je proces, ki omogoča znatno izboljšanje kvalitete izdelkov v primerjavi s klasičnim PU. Modeliranje in projektiranje NFEU je zelo pomembno zaradi velikih stroškov eksperimentov med proizvodnim procesom. Simulacijski sistem je razdeljen na štiri poglavitne module. V prvem, makroskopskem termofluidnem modulu se rešujejo enačbe za ohranitev mase, gibalne količine, energije in sestavin. Za modeliranje interakcije med trdno in kapljevito fazo se uporablja formulacija volumskega povprečenja, linearizirani evtektični fazni diagram ter vzvodno pravilo. V drugem modulu se indukcijska elektromagnetna enačba uporabi za izračun vektorskega magnetnega potenciala in Lorentzove sile. Lorentzova sila je vključena v enačbo za ohranitev gibalne količine kot volumska sila. Tretji, termomehanski modul, je formuliran v približku majhnih deformacij za elasto-viskoplastičen material. Viskoplastični del deformacije je določen z Garafalovim zakonom. Termične deformacije so določene iz temperaturnega polja. Napetostno in deformacijsko polje sta uporabljena za izračun kriterijev za pojav vročega trganja. Za določitev slednjega se uporablja Lahaie-Bouchardov in Suyitno-Kool-Katgermanov model. Namen četrtega, mikrostrukturnega modula, je napoved mikroizcejanja in velikosti dendritiskih zrn pri strjevanju večsestavinskih zlitin. Model opiše nukleacijo in rast dendritskih zrn v odvisnosti od temperaturnega polja in koncentracijskih polj izračunanih na makroskopskem nivoju. Za opis gostote nukleacije v odvisnosti od podhladitve se uporabi normalno porazdelitev. Hitrost rasti posameznega zrna se izračuna glede na temperaturne in koncentracijske razmere na njegovem medfaznem robu. Snovne lastnosti za poljubno aluminijevo zlitino so pridobljene s programom JmatPro.

Termofluidni in termomehanski model sta formulirana v Eulerjevem sistemu, mikrostrukturni model pa pridobiva podatke iz termofluidnega modela v Lagrangeovem sistemu in izračunava mikrostrukturo dela zlitine 3 mm x 3 mm na robu ter v notranjosti droga. Vse parcialne diferencialne enačbe se rešujejo z brezmrežnimi metodami. V izračunih sta uporabljena dva različna lokalna brezmrežna pristopa; metoda difuzijskih približkov in metoda lokalne kolokacije z radialnimi baznimi funkcijami. Temperatura, tlak, hitrost in delež kapljevite faze se izračunajo v termofluidnem modelu in se uporabijo kot vhodni podatki za izračun termomehanskega modela. Vhodni podatki za mikrostrukturni model so temperatura, gradient temperature in koncentracija sestavin vzdolž tokovnic, ki so izračunane s termofluidnim modelom. Fizikalni model za nukleacijo in rast trdne faze je rešen z metodo točkovnih avtomatov, ki je sestavljena iz dveh korakov; prvi korak je naključna postavitev točk in določitev soseščine vsaki točki. V drugem koraku so določena možna stanja in pravila za prehod med stanji. Pravila opisujejo nukleacijo in rast trdne faze v odvisnosti od temperature in koncentracije legirnih elementov na makroskopskem nivoju.

V članku so prikazni rezultati celotnega simulacijskega sistema za tipične parametre pri polkontinuirnem ulivanju drogov iz aluminijevih zlitin. Prikazani rezultati vključujejo: temperaturo, makroizcejanje, primerjavo tokovnih struktur v primeru PU in NEFU, plastično deformacijo, obodne napetosti, napoved poroznosti, napoved vročega trganja, mikrostrukturo zrn in mikroizcejanje. Sistem je bil validiran na podlagi številnih eksperimentov med proizvodnjo (meritve temperature, položaja medfaznega roba in EM polja) in v laboratoriju (mikroizcejanje, makroizcejanje). Predstavljeni simulacijski sistem omogoča izpeljavo virtualnih eksperimentov s parametri ulivanja, sestavo zlitine, geometrijo ulitka in projektom livne naprave. Sistem je unikaten, saj omogoča sklopitev termofluidnih, elektromagnetnih in termomehanskih pojavov na makroskopskem nivoju (~1 m) s pojavi na mikroskopskem nivoju (~ 0.1 mm). Na ta način je možno na ekonomičen način preučevati in optimirati vpliv vseh vplivnih parametrov na kvaliteto izdelkov in ekonomičnost procesa.

Ključne besede: polkontinuirno ulivanje, aluminijeve zlitine, računalniška dinamika tekočin in trdnin, večfizikalno modeliranje, večnivojsko modeliranje, brezmrežne metode, metoda točkovnih avtomatov

Ocena trajnosti naprednih tehnologij odrezavanja

Luka Sterle – Damir Grguraš – Matjaž Kern – Franci Pušavec*

Univerza v Ljubljani, Fakulteta za strojništvo, Slovenija

Kriogeno odrezavanje z asistenco kapljevitega CO_2 in odrezavanje z asistenco pulzirajočega visokotlačnega dovoda hladilno mazalne tekočine predstavljata trajnostno alternativo konvencionalnim odrezovalnim procesom, saj ponujata učinkovitejše hlajenje in mazanje rezalne cone pri odrezavanju težko obdelovalnih materialov, hkrati pa zagotavljata nižje stroške obdelave pri manjšem vplivu na okolje in delavca.

V tej raziskavi sta predstavljeni napredni tehnologiji odrezavanja: (i) kriogeno odrezavanje (ang. *Cryogenic Machining*) z asistenco kapljevitega CO_2 - LCO_2 (ang. *Liquid Carbod Dioxide*) v kombinaciji z minimalno količino olja in (ii) odrezavanje z asistenco pulzirajočega visokotlačnega dovajanja hladilno mazalne tekočine – Pulsating HPJAM (ang. *Pulsating High Pressure Jet Assisted* Machining). Obe tehnologiji sta bili vpeljani v proces odrezavanja težko obdelovalnega materiala s ciljem raziskati njun vpliv na stroške in varnost izbrane tehnologije v primerjavi s konvencionalnim načinom odrezavanja.

Eksperimenti kriogenega odrezavanja z asistenco LCO_2 so bili izvedeni na težko obdelovalni titanovi zlitini Ti-6Al-4V. Pri kriogenem frezanju se je tako v rezalno cono dovajalo mazalni kapljeviti CO_2, t.j. enokanalni dovod LCO_2 + olja, kjer je bil masni pretok CO_2 12 kg/h in volumski pretok olja 60 mL/h. Mešanica CO_2 in olja se je v rezalno cono dovajala s pomočjo lastniškega sistema enokanalnega kriogenega dovoda. Pri frezanju so se uporabljala standardna 4-rezilna stebelna frezala premera 8 mm z naslednjimi rezalnimi parametri: v_c = 60 m/min, f_z = 0,08 mm/zob, a_p = 8 mm, a_e = 2,4 mm. Med kriogenim frezanjem se je spremljalo obrabo frezala in obliko odrezkov. Merili smo tudi koncentracijo CO_2 v zraku v neposredni bližini CNC obdelovalnega centra in rabo električne energije, potrebne za delovanje kriogenega sistema. Referenca kriogenemu frezanju glede obstojnosti orodja je bilo konvencionalno frezanje z uporabo emulzije Blazer B-Cool 9665 s 7 % koncentracijo.

Eksperimenti struženja z asistenco pulzirajočega dovajanja hladilno mazalnega sredstva so bili izvedeni na težko obdelovalni nikljevi zlitini Inconel 718. Uporabljalo se je emulzijo Blazer B-Cool 9665 s 7 % koncentracijo, katero se je v rezalno cono pulzirajoče dovajalo s pomočjo lastniškega sistema, ki omogoča popoln nadzor nad dovodom emulzije v smislu trajanja pulza in tlaka emulzije. Frekvenca pulziranja curka emulzije je znašala 5 Hz, kjer je visokotlačni del pulza trajal 60 ms pri 200 bar (20 MPa), nizkotlačni del pa 140 ms pri tlaku 1 bar (0,1 MPa). Pri struženju se je uporabljalo standardne rezalne ploščice z naslednjimi rezalnimi parametri: v_c = 50 m/min, f_n = 0,28 mm/vrt, a_p = 0,5 mm. Med struženjem se je spremljalo obrabo rezalnih ploščic in obliko odrezkov ter rabo električne energije, potrebne za nadzor pulzirajočega dovoda emulzije. Rezultate se je primerjalo z referenčnim konvencionalnim načinom obdelave in visokotlačnim načinom obdelave s konstantnim tlakom dovoda emulzije 200 bar (20 MPa).

Rezultati kažejo, da predstavljeni napredni tehnologiji obdelave težko obdelovalnih zlitin ponujata daljšo obstojnost rezalnega orodja v primerjavi s konvencionalnim načinom odrezavanja, ugotovilo se je 169 % (LCO_2 + olje) in 33 % (Pulsating HPJAM) daljšo obstojnost orodja. Pri kriogenem odrezavanju značilne razlike v obliki odrezkov ni bilo moč zaznati, medtem ko je uporaba pulzirajočega dovajanja hladilno mazalnega sredstva zagotovila idealno dolžino odrezkov. Stroškovna analiza je pokazala, da obe predstavljeni tehnologiji predstavljata stroškovno ugodnejšo tehnologijo v primerjavi s konvencionalno tehnologijo odrezavanja, saj smo zasledili 44,7 % znižanje stroškov pri kriogenem odrezavanju in 5,2 % znižanje pri pulzirajočem načinu dovoda emulzije. Hkrati obe tehnologiji nimata negativnega odtisa na operaterja in delovno okolje. Iz meritev koncentracije CO_2 prisotnega v zraku okolice obdelovalnega centra zaključujemo, da koncentracija CO_2 v zraku ne presega zakonsko predpisanih mejnih vrednosti. Pulzirajoči način dovajanja emulzije pa omogoča 30 % hitrejši dostop do delovnega prostora znotraj CNC obdelovalnega centra na račun značilno manjšega meglenja v primerjavi z običajnim visokotlačnim dovodom emulzije. Nadaljnje delo bo usmerjeno v detajlno analizo ozračja v delovnem prostoru (velikost kapljic olja v zraku in njihova porazdelitev).

Ključne besede: kriogeno odrezavanje, visokotlačno odrezavanje, trajnost, stroškovna analiza, analiza varnosti

*Naslov avtorja za dopisovanje: Univerza v Ljubljani, Fakulteta za strojništvo, Laboratorij za odrezavanje, Aškerčeva 6, 1000 Ljubljana, Slovenija, franci.pusavec@fs.uni-lj.si

Pulzi na zahtevo v vlakenskih in hibridnih laserjih

Rok Petkovšek[1,*] – Vid Agrež[1] – Jaka Petelin[1] – Luka Černe[1] – Udo Bünting[2] – Boštjan Podobnik[3]

[1]Univerza v Ljubljani, Fakulteta za strojništvo, Slovenija
[2]LPKF Laser & Electronics AG, Nemčija
[3]LPKF Laser & Electronics d.o.o., Slovenija

Pri visoko natančnih obdelavah se vse pogosteje uporabljajo orodja na osnovi laserjev. Z željo povečanja učinkovitosti procesa, uporabnosti orodja za različne procese obdelave materiala in hitrosti proizvodne linije je nastala potreba po visoko prilagodljivih laserskih sistemih sposobnih generiranja naprednih vzorcev in struktur. Še posebej pomembna je prilagodljivost laserskega sistema skenirnemu sistemu visokih hitrosti, kot sta poligonski in resonančni skener. Pri obeh je pomanjkljivost zmanjšana prilagodljivost pozicije laserskega žarka na račun hitrosti. To lahko kompenzira laser, ki omogoča generacijo pulzov ob točno določenem času s poljubno amplitudo in trajanjem. V industriji se za to že uporabljajo kontinuirani laserji, kjer z zunanjim modulatorjem oblikujemo laserske pulze. Problem takšne realizacije so relativno dolgi pulzi, kompleksna laserska glava in omejene izhodne moči. Redkeje se uporabljajo pulzni laserji, saj v splošnem delujejo stabilno zgolj pri konstantnih ponavljalnih frekvencah. Da lahko takšni generirajo stabilne pulze v poljubnih časih morajo imeti kompleksen sistem nadzora ojačenja.

V članku sta predstavljeni metodi s katerima se lahko učinkovito nadzira ojačenje oziroma načrpanost zgornjega laserskega nivoja med posameznimi laserskimi pulzi. Metodi omogočata, da laser generira pulze na zahtevo, pri čemer imajo pulzi stabilne parametre, ki se ne spreminjajo s spreminjanjem ponavljalne frekvence. Prva metoda uporablja modulacijo črpalne moči za generacijo ustreznega zaporedja pulzov iz laserskega oscilatorja velikih moči. Druga metoda uporablja kombinacijo dveh vzbujevalnih virov, primarnega in jalovega, ki vzbujata verigo laserskih ojačevalnikov črpanih s konstantno močjo.

Meritve stabilnosti parametrov pulzov na zahtevo so bile izvedene na treh eksperimentalnih postavitvah. Kompaktni laser s preklopom ojačenja je pokril območje vršnih moči okoli enega kW in trajanjem nekaj deset ns pri poljubnih ponavljalnih frekvencah. Napredna laserska postavitev je uporabljala zaporedje vlakenskih ojačevalcev, ki sta ga vzbujala dva laserska vira in je omogočala širok razpon spreminjanja trajanja laserskih pulzov. Preizkus uporabe tako generiranih pulzov na zahtevo je bil uspešno demonstriran na postaji za lasersko transferno tiskanje. Nadalje se je napredno lasersko postavitev nadgradilo s trdninskim ojačevalnikom in v primarnem vzbujevalnem viru lasersko diodo zamenjalo s fazno vklenjenim oscilatorjem. Namen nadgradnje je bil preizkus stabilnosti ps/fs pulzov na zahtevo.

S kompaktno postavitvijo laserja je bilo uspešno doseženo delovanje s pulzi na zahtevo od posameznega pulza do frekvence 1 MHz. Vršna moč pulzov je odstopala od povprečja za manj kot 1,5 % pri čemer njihovo trajanje ni odstopalo za več kot 0,7 %. Pri testu nelinearnega spreminjanja časovnega razmaka med pulzi se je pokazala nujnost kompenzacije ojačenja s pomočjo modulacije črpalnih diod.

Na napredni laserski postavitvi je bila hitrost modulacije preizkušena do nekaj deset MHz pri moči 200 W. Tako izoblikovani pulzi so imeli stabilno vršno moč in so skupaj s poligonskim skenerjem zagotovili uspešen prenos črnila na substrat pri procesu laserskega transfernega tiskanja.

Preizkus stabilnosti ps pulzov na zahtevo je bil narejen na nadgrajeni napredni laserski postavitvi. Način nadzora ojačenja s pomočjo jalovega vzbujevalnega vira med laserskimi pulzi se je izkazal za učinkovitega tudi v primeru ultrakratkih primarnih pulzov in uporabe dodatnega trdninskega ojačevalca. Doseženi se bili pulzi na zahtevo z energijami do 300 μJ in trajanjem 450 fs.

Predstavljeni rezultati kažejo, da je z ustreznim nadzorom ojačenja v laserskem sistemu mogoče doseči učinkovito delovanje pri poljubnih ponavljalnih frekvencah brez uporabe zunanjega modulatorja. Takšno delovanje pulznih laserjev je redkost in predstavljeni rezultati podpirajo razvoj hitrih laserskih obdelovalnih sistemov. Prednost predstavljenih rešitev je, da so lahko združene v enovit visoko prilagodljivi hibridni laserski sistem, ki bi omogočal natančno sinhronizacijo z novo generacijo hitrih poligonskih skenerjev, ki omogočajo ultrahitre laserske procese.

Ključne besede: pulzi na zahtevo, vlakenski laserji, nadzor ojačenja, poljubna ponavljalna frekvenca

*Naslov avtorja za dopisovanje: Univerza v Ljubljani, Fakulteta za strojništvo, Laboratorij za fotoniko in laserske sisteme,
Aškerčeva 6, 1000 Ljubljana, Slovenija, rok.petkovsek@fs.uni-lj.si

Termodinamsko ozadje spominskega efekta v katodnih materialih s fazno separacijo

Klemen Zelič[1] – Igor Mele[1] – Ivo Pačnik[1] – Jože Moškon[2] – Miran Gaberšček[2] – Tomaž Katrašnik[1,*]

[1] Univerza v Ljubljani, Fakulteta za strojništvo, Slovenija
[2] Kemijski inštitut, Slovenija

Litij ionske baterijske celice, ki temeljijo na katodnih materialih s fazno separacijo so zaradi ustrezne energijske gostote in visoke stopnje varnosti med obratovanjem pogosto uporabljene. Za učinkovito vsakdanjo uporabo ter produkcijo takšnih baterijskih celic je ključno razumevanje osnovnih kemijsko fizikalnih procesov, ki vplivajo na njihovo delovanje. Znan pojav v katodnih materialih s fazno separacijo je spominski efekt, ki pa še ni docela razumljen in ustrezno opisan na mehanističen način. Nerazumevanje spominskega efekta predstavlja težavo pri določanju napolnjenosti baterije, saj se glede na predhodni potek polnjenja in praznjenja, baterija lahko znajde v stanjih z različnimi napetostmi pri enaki stopnji napolnjenosti.

Namen predstavljene raziskave je dopolnitev dosedanje teoretične razlage za spominski efekt, na podlagi eksperimentov, ter implementacija ugotovitev v elektrokemijski model celotne baterijske celice. Takšen model je ustrezen za napovedovanje pojava spominskega efekta v katodnih materialih s fazno separacijo in posledično pomembna izboljšava v razvoju tehnologije za spremljanje napolnjenosti baterije med polnjenjem in praznjenjem.

Na baterijskih celicah LFP/kovinski litij, ki smo jih sestavili sami, smo opravili meritve časovne odvisnosti napetosti pri predpisnem tokovnem protokolu. Protokol po katerem smo uravnavali tok skozi celice, je bil osnovan na podlagi predhodno objavljenih meritev o spominskem efektu. Prvi eksperimentalni rezultat dokaže, da je spominski efekt mogoče reproducirati in je uporabljen za parametrizacijo in validacijo modela, s katerim smo spominski efekt simulirali. Drugi eksperimentalni rezultati prvič pokažejo brisanje spominskega efekta z nizko spodnjo dovoljeno napetostjo (2,8 V) in prisotnost spominskega efekta ob odsotnosti prvega počitka v apliciranem tokovnem protokolu. Oba eksperimentalna rezultata, ki sta v članku prikazana prvič, sta v diskusiji uporabljena kot razširitev trenutnega znanja na področju spominskega efekta.

Nedvoumnost predlagane razlage za spominski efekt je potrjena s simulacijskimi rezultati. Simulacijski rezultati so bili pridobljeni s kontinuumskim elektrokemijskim modelom baterijske celice, ki smo ga razvili. Model vsebuje opis nemonotonega kemijskega potenciala aktivnih katodnih delcev, velikostno porazdelitev aktivnih delcev v katodi ter odvisnost oblike kemijskega potenciala od velikosti delcev, kar so ključni parametri, ki vplivajo na spominski efekt, in torej nujni pogoji za simuliranje spominskega efekta. Rezultati simulacije dobro sovpadajo z izmerjenimi rezultati, kar potrjuje teoretično razlago spominskega efekta predstavljeno v diskusiji.

Prispevek tega dela je razrešitev nejasnosti glede obstoja spominskega efekta pri nizkih spodnjih dovoljenih napetostih ter kratkih časih prve relaksacije v tokovnem protokolu. Obe nejasnosti sta v članku obravnavani tako eksperimentalno kot simulacijsko in ustrezno teoretično utemeljeni. Ponujena razlaga popolnoma sovpada s predhodno objavljenimi razlagami spominskega efekta, vendar je ustrezno razširjena. S takšno razširitvijo teoretski opis mehanizma spominskega efekta pojasni vse do sedaj znane eksperimente v zvezi s spominskim efektom.

Ključne besede: Litij ionske baterije, spominski efekt, katodni material s fazno separacijo, večdelčna porozna elektroda

Vpliv staranja prebivalstva na potrebe po toploti na nacionalni ravni: študija primera Slovenije

Žiga Lampret[1] – Gorazd Krese[2] – Matjaž Prek[1,*]
[1]Univerza v Ljubljani, Fakulteta za strojništvo, Slovenija
[2]Korona inženiring d.d., Slovenija

V tem prispevku so ocenjene prihodnje potrebe energije za ogrevanje prostorov in priprave tople sanitarne vode starajoče se družbe v Sloveniji z uporabo vzorca geografsko razpršenih domov za ostarele. Rezultati so primerjani z zadnjim referenčnim scenarijem EU do leta 2050, pri čemer se prilagojene ocene razlikujejo do 9,5 %.

Predstavljena je metodologija za prilagajanje napovedi rabe energije za ogrevanje na nacionalni ravni ob upoštevanju staranja prebivalstva. Metoda temelji na uporabi rezultatov meritev rabe energije reprezentativnega vzorca domov za starejše. V tej raziskavi smo podatke, ki predstavljajo 11,8 % domov za starejše v Sloveniji, uporabili za prilagoditev predvidenih potreb po toploti gospodinjstev po referenčnem scenariju EU 2016 (EUref2016).

Da bi ocenili vpliv staranja na potrebno energijo za ogrevanje prostorov smo določili bazno temperaturo analiziranih domov in jih primerjali s kontrolno skupino stavb. Bazna temperatura se je v povprečju razlikovala za 1,34 °C, kar posledično predstavlja povečanje letne rabe energije od 210 GWh do 357 GWh oziroma 3,8 % do 6,5 %. Ta razlika v bistvu predstavlja neskladje med nastavljeno temperaturo ogrevanja za starejše in ostale (mlajše) populacije zaradi termofizioloških lastnosti starejših. To pomeni, da starejša populacija lahko kompenzira pozitivne učinke globalnega segrevanja na potrebe po ogrevanju, saj si države, zavezane Pariškemu sporazumu iz leta 2015 (vključno s Slovenijo), prizadevajo omejiti zvišanje temperature na 1,5 °C nad predindustrijsko raven. Ker se pričakuje, da se bo bazna temperatura prihodnjega stanovanjskega sklada znižala zaradi izboljšanih toplotnih lastnosti stavb in energijske učinkovitosti sistemov, bo ta vpliv zelo verjetno večji kot to trenutno kažejo prikazani rezultati.

Po drugi strani pa so projekcije rabe energije za ogrevanje sanitarne vode med 1,8 % in 9,6 % višje glede na izhodiščni scenarij, zaradi česar se vrzel sčasoma povečuje, saj predvideni delež starejših narašča. Nasprotno pa delež tople sanitarne vode v celotni potrebi po toploti ostaja dokaj konstanten in znaša okoli 18 %. To je v nasprotju z nedavnimi trendi naraščajočega pomena ogrevanja vode v stanovanjski energijski bilanci, kar pomeni, da EUref2016 nezadovoljivo predstavlja trenutno povečano porabo sanitarne vode na prebivalca.

Glede na skupno potrebo po toploti se naše projekcije, prilagojene staranju prebivalstva, glede na referenčne vrednosti za Slovenijo razlikujejo med 3,8 % za leto 2020 in 7,1 % za leto 2050. Posledično je razlika na letnem nivoju do 474 GWh, kar je več od letne proizvodnje malih hidroelektrarn in skoraj dvakratne letne proizvodnje fotonapetostnih elektrarn v Sloveniji v letu 2018. Zato ima lahko to neskladje daljnosežne posledice za slovensko (trajnostno) energetsko načrtovanje kot tudi za doseganje zastavljenih podnebnih ciljev Slovenije.

Ključne besede: napovedovanje rabe energije, raba energije v gospodinjstvih, ogrevanje prostorov, sanitarna topla voda (STV), staranje družbe, bazna temperatura

*Naslov avtorja za dopisovanje: Univerza v Ljubljani, Fakulteta za strojništvo, Laboratorij za ogrevalno,
sanitarno in solarno tehniko ter klimatizacijo, Aškerčeva 6, 1000 Ljubljana, Slovenija, matjaz.prek@fs.uni-lj.si

Okolju prilagojena »zelena« tribologija za trajnostno inženirstvo prihodnosti

Mitjan Kalin* – Marko Polajnar – Maja Kus – Franc Majdič

Fakulteta za strojništvo, Univerza v Ljubljani, Slovenija

Okoljska ozaveščenost in še posebej zakonodaja, ki zahtevata zmanjšanje emisij v ozračje, sta močni gonilni sili trajnostnega inženirstva in okolju prilagojenih »zelenih« rešitev pri konstruiranju, uporabi in celotni uporabni dobi delovanja strojev. Kljub temu pa zagotavljanje novejših konceptov, ki izključujejo okolju ne-prilagojene rešitve, terja veliko časa in razvoja, saj so se sedanje učinkovite rešitve razvijale več desetletij, pri čemer pa jim niti ni bilo potrebno dosegati sedanjih okoljskih zahtev. Te nove, okolju prilagojene, rešitve torej terjajo svoj čas, sploh če hočemo hkrati zagotoviti in vzdrževati enak nivo tehničnega delovanja. Okolju prilagojena »zelena« tribologija je eno od področij, ki je bilo tesno vpeto v te aktivnosti v zadnjih dveh desetletjih. Raziskave in uporaba tribološke znanosti in tehnologije v smeri zelenega in trajnostnega inženirstva tako vključuje zmanjševanje porabe naravnih virov, še posebej fosilnih goriv in olja ter redkih materialov, nižje trenje in s tem nižjo rabo energije, zmanjšanje onesnaževanja in izpustov, manj obrabe in poškodb ter s tem manj vzdrževanja in posredno podaljšanje investicijskih ciklov v stroje. V tem prispevku ne povzemamo vseh obstoječih konceptov ali celotne literature s tega področja, temveč predstavljamo delo raziskovalne skupine avtorjev prispevka v zadnjih dvajsetih letih, ki v glavnem vključuje novejše koncepte zelenega mazanja, ki izhajajo iz raziskovanj in uporabe površinskega inženiringa z uporabo prevlek na osnovi diamantu podobnega ogljika (DLC). V članku je tako predstavljenih osem različnih konceptov zelenega mazanja DLC prevlek, ki so plod raziskav naše skupine.

Najprej prikazujemo uporabo biološko razgradljivih olj, ki se izkažejo za boljša bazna maziva od običajnih mineralnih olj in nadaljujemo z uporabo olj z aditivi z nizko vsebnostjo žveplovega pepela, fosforja in žvepla (SAPS), za katere smo pokazali, da lahko učinkovito ščitijo DLC površine in zagotavljajo nizko trenje. Sledijo primeri uporabe še bolj blagih aditivov, in sicer od preprostih organskih aditivov za katere smo pokazali, da lahko celo na DLC prevlekah tvorijo zelo tanek mazalnih film in ščitijo površine, do nano-delcev, ki lahko le na podlagi fizikalnega delovanja učinkujejo kot odlični aditivi v olju in uspešno zmanjšujejo tako trenje kot obrabo. Predstavljene pa so tudi najnovejše raziskave z uporabo ionskih tekočin, kot potencialnih aditivov za mazanje DLC prevlek za doseganje nizkega trenja.

Naslednji vsebinski sklop prikazuje rezultate, kjer smo za povsem bazna olja in preproste ogljikovodike - oboje povsem brez aditivov - pokazali, da lahko samo s spreminjanjem molekulske strukture, reologije in mejnih pogojev med površino in tekočino znatno vplivamo na zmanjšanje trenja v kontaktu. Za DLC prevleke smo tako ugotovili, da že z baznimi olji dosegamo nizko trenje in tudi nizko obrabo, ter da z razliko od običajnih jeklenih kontaktov za sočasno nizko trenje in obrabo, ne potrebujemo visoko viskoznega olja, saj DLC prevleke same po sebi preprečujejo adhezijo. V drugem delu pa je prikazano, kako lahko le z uporabo različnih vrst DLC prevlek, ki imajo z mazalnim oljem različno omočljivost, dosegamo znatno znižanje trenja in sicer celo do 50 %. In to brez uporabe aditivov.

V zadnjem delu so predstavljeni primeri vodnega mazanja, tako DLC prevlek, kot tudi keramičnih površin. Pri tem so prikazani tudi trije primeri uporabe vodnega mazanja v realno aplikacijo. Kot primer vodnega mazanja keramike je predstavljen primer vodne črpalke s keramičnimi tesnili. Kot primera vodnega mazanja DLC prevleke, pa sta predstavljena, ventil vodne hidravlike in hidravlični motor.

Ključne besede: zeleno mazanje, DLC prevleke, olja z nizkim deležem SAPS aditivov, biološko razgradljiva olja, nanodelci, mejni zdrs, ionske tekočine, vodno mazanje

*Naslov avtorja za dopisovanje: Univerza v Ljubljani, Fakulteta za strojništvo, Laboratorij za tribologijo
in površinsko nanotehnologijo, Aškerčeva 6, 1000 Ljubljana, Slovenija, mitjan.kalin@tint.fs.uni-lj.si

Semianalitični večdimenzionalni algoritem za optimizacijo zasnove letala: Študentsko tekmovanje Zasnuj – izdelaj - leti!

Viktor Šajn*

Univerza v Ljubljani, Fakulteta za strojništvo, Slovenija

Zmagovalec natečaja Ameriškega inštituta za letalstvo in astronavtiko (AIAA), Textron, Raytheon Zasnuj – izdelaj – leti leta 2019 je bilo moštvo Edvarda Rusjana s Fakultete za strojništvo, Univerze v Ljubljani. Moštvo Edvarda Rusjana je pristopilo k tekmovanju strogo znanstveno ter premagalo konkurenčne ekipe iz najbolj prestižnih univerz. Razvili smo semi-analitični večdimenzionalni algoritem za optimizacijo snovanja letal, ki glede na pravila tekmovanja išče zasnovo letala, ki omogoča čim večji tekmovalni rezultat. Izdelana in testirana sta bila dva vmesna prototipa za fino nastavitev empiričnih količnikov algoritma za letalske misije. Aerodinamika modela letala je bila napovedana z numeričnimi RANS simulacijami in dinamična stabilnost z metodo neviskoznih panelov. Z meritvami v vetrovniku z nizko turbulenco je bil verificiran nizek upor izbrane postavitve zunanjega tovora na letalu. Krila in trup modela tekmovalnega letala, ki so ga ljubljanski študentje poimenovali „Pretty Boy“, sta bila narejena iz kompozita ogljikovih in steklenih vlaken ter epoksidne smole. Aramidno satje je bilo uporabljeno kot polnilo sendvič konstrukcije.

Glede na izbrano zasnovo letala, motorja, propelerja, baterij (čez 20 različnih velikosti) je algoritem napovedal njegove zmogljivosti, predvsem hitrost, s katero lahko letalo leti, ter čas, potreben za izvedbo enega kroga, ki je bil sestavljen iz premočrtnega leta in dveh celotnih krogov. Algoritem je tudi napovedoval, ali bo letalo v podani zasnovi zmožno vzleteti s podlage dolge le 3 m ter koliko krogov bo sposobno odleteti z izbranim paketom baterij. Marsikateri parametri letala so namreč v medsebojnem nasprotju pri doseganju čim boljših zmogljivosti. Zato lahko z visoko verjetnostjo pričakujemo lokalne ekstreme optimizacijske funkcije. Pri zadnji misiji, kjer letalo vzleti s tovorom igrač iz pene ter pri vsakem krogu po pravilniku odvrže eno, je algoritem določal optimalno hitrost za posamezni krog glede na omejeno zalogo energije v baterijah. Študenta Timotej in Tilen sta določila način postavitve igrač na trupu. Le ta je bil zasnovan tako, da je ustvarjal zračno zaveso in ščitil igrače pred vetrom ter zmanjševal skupni zračni upor letala. Z meritvami v vetrovniku je bilo potrjeno, da imata predlagana zasnova trupa in postavitev tovora značilno nižji zračni upor, kot če bi bil tovor klasično postavljen pod krili, kar je naredila večina moštev. Z analizo občutljivosti parametrov v območju širše optimalne zasnove letala pri prvi iteraciji, smo ugotovili katere velikosti imajo največji vpliv na zmogljivost. Tako smo v nadaljevanju optimizacije zmanjšali število pristopnih stopenj in potrebo po računalniški moči s ciljem maksimiziranja cenilne funkcije nelinearnega sistema enačb. Slaba napoved akumulirane energije v celicah baterij ter njene notranje upornosti je imela za posledico, da je bila določitev optimalne zasnove nezanesljiva - zamegljena. Prvi izračuni so pokazali, da je letalo sposobno odleteti 19 krogov v času 10 minut, pri testih pa je zanesljivo dosegalo le 17 krogov. S to zasnovo je moštvo nastopilo na tekmovanju in kljub skromnejšemu pričakovanju zanesljivo prevzelo vodstvo. Z meritvami preostale energije v baterijskih celicah takoj po poletih, je bilo ugotovljeno, da so kapacitete celic manjše, kot so bile izmerjene v Sloveniji. Optimizacijski izračuni so bili ponovljeni z novo izmerjeno kapaciteto celic. Pri tem je bilo ugotovljeno, da je letalo sposobno odleteti 18 krogov ob povečanju števila celic paketa letala. Temu je posledično sledilo povečanje mase letala, sprememba optimalne lege težišča ter problemi z majhno hitrostjo pri vzletu. Moštvo se je odločilo, da izvede predelavo na samem tekmovanju in v ponavljalnem poletu (dovoljen le eden) poskusi popraviti lasten rekord. Pri ponavljalnem poletu tretje misije na TIMPA terenu v Tucsonu je pilot Timotej Hofbauer z letalom „Pretty Boy“ dosegel 18 krogov v 10 minutah, kar je bil absolutni rekord tekmovanja. Drugo uvrščena ekipa iz Georgia Institute of Technology, je bila za 22 % počasnejša in je končala tekmovanje s 14 doseženih krogi. Moštvo Edvarda Rusjana s Fakultete za strojništvo, Univerze v Ljubljani v letu 2019: Timotej Hofbauer (pilot in študentski vodja), Vid Pugelj, Viktor Govže, Matej Gorjan, Jaka Romih, Nejla Kambič, Emil Zubalic, Martin Kocijančič, Filip Plešnik, Klemen Ambrož, Andraž Vene, Tilen Košir, Enej Istenič, Patrik Tarfila, Klemen Mlakar, Andraž Kladnik in Viktor Šajn kot mentor.

Ključne besede: kompozitna konstrukcija letala iz ogljikovega stekla, število krogov v časovnem režimu, vzlet, konstrukcijski parametri, aerodinamični upor, DBF tekmovanje 2019, ekipa Edvarda Rusjana

*Naslov avtorja za dopisovanje: Univerza v Ljubljani, Fakulteta za strojništvo,
Laboratorij za nelinearno mehaniko, Aškerčeva 6, 1000 Ljubljana, Slovenija, viktor.sajn@fs.uni-lj.si

Information for Authors

All manuscripts must be in English. Pages should be numbered sequentially. The manuscript should be composed in accordance with the Article Template given above. The maximum length of contributions is 10 pages. Longer contributions will only be accepted if authors provide juastification in a cover letter. For full instructions see the Information for Authors section on the journal's website: http://en.sv-jme.eu .

SUBMISSION:

Submission to SV-JME is made with the implicit understanding that neither the manuscript nor the essence of its content has been published previously either in whole or in part and that it is not being considered for publication elsewhere. All the listed authors should have agreed on the content and the corresponding (submitting) author is responsible for having ensured that this agreement has been reached. The acceptance of an article is based entirely on its scientific merit, as judged by peer review. Scientific articles comprising simulations only will not be accepted for publication; simulations must be accompanied by experimental results carried out to confirm or deny the accuracy of the simulation. Every manuscript submitted to the SV-JME undergoes a peer-review process.

The authors are kindly invited to submit the paper through our web site: http://ojs.sv-jme.eu. The Author is able to track the submission through the editorial process - as well as participate in the copyediting and proofreading of submissions accepted for publication - by logging in, and using the username and password provided.

SUBMISSION CONTENT:

The typical submission material consists of:
- A **manuscript** (A PDF file, with title, all authors with affiliations, abstract, keywords, highlights, inserted figures and tables and references),
- Supplementary files:
  - a **manuscript** in a WORD file format
  - a **cover letter** (please see instructions for composing the cover letter)
  - a ZIP file containing **figures** in high resolution in one of the graphical formats (please see instructions for preparing the figure files)
  - possible **appendicies** (optional), cover materials, video materials, etc.

Incomplete or improperly prepared submissions will be rejected with explanatory comments provided. In this case we will kindly ask the authors to carefully read the Information for Authors and to resubmit their manuscripts taking into consideration our comments.

COVER LETTER INSTRUCTIONS:

Please add a **cover letter** stating the following information about the submitted paper:
1. Paper **title**, list of **authors** and their **affiliations**.
2. **Type of paper**: original scientific paper (1.01), review scientific paper (1.02) or short scientific paper (1.03).
3. A **declaration** that neither the manuscript nor the essence of its content has been published in whole or in part previously and that it is not being considered for publication elsewhere.
4. State the **value of the paper** or its practical, theoretical and scientific implications. What is new in the paper with respect to the state-of-the-art in the published papers? Do not repeat the content of your abstract for this purpose.
5. We kindly ask you to suggest at least two **reviewers** for your paper and give us their names, their full affiliation and contact information, and their scientific research interest. The suggested reviewers should have at least two relevant references (with an impact factor) to the scientific field concerned; they should not be from the same country as the authors and should have no close connection with the authors.

FORMAT OF THE MANUSCRIPT:

The manuscript should be composed in accordance with the Article Template. The manuscript should be written in the following format:
- A **Title** that adequately describes the content of the manuscript.
- A list of **Authors** and their **affiliations**.
- An **Abstract** that should not exceed 250 words. The Abstract should state the principal objectives and the scope of the investigation, as well as the methodology employed. It should summarize the results and state the principal conclusions.
- 4 to 6 significant **key words** should follow the abstract to aid indexing.
- 4 to 6 **highlights;** a short collection of bullet points that convey the core findings and provide readers with a quick textual overview of the article. These four to six bullet points should describe the essence of the research (e.g. results or conclusions) and highlight what is distinctive about it.
- An **Introduction** that should provide a review of recent literature and sufficient background information to allow the results of the article to be understood and evaluated.
- A **Methods** section detailing the theoretical or experimental methods used.
- An **Experimental section** that should provide details of the experimental set-up and the methods used to obtain the results.
- A **Results** section that should clearly and concisely present the data, using figures and tables where appropriate.
- A **Discussion** section that should describe the relationships and generalizations shown by the results and discuss the significance of the results, making comparisons with previously published work. (It may be appropriate to combine the Results and Discussion sections into a single section to improve clarity.)
- A **Conclusions** section that should present one or more conclusions drawn from the results and subsequent discussion and should not duplicate the Abstract.
- **Acknowledgement** (optional) of collaboration or preparation assistance may be included. Please note the source of funding for the research.
- **Nomenclature** (optional). Papers with many symbols should have a nomenclature that defines all symbols with units, inserted above the references. If one is used, it must contain all the symbols used in the manuscript and the definitions should not be repeated in the text. In all cases, identify the symbols used if they are not widely recognized in the profession. Define acronyms in the text, not in the nomenclature.
- **References** must be cited consecutively in the text using square brackets [1] and collected together in a reference list at the end of the manuscript.
- **Appendix(-icies)** if any.

SPECIAL NOTES

Units: The SI system of units for nomenclature, symbols and abbreviations should be followed closely. Symbols for physical quantities in the text should be written in italics (e.g. v, T, n, etc.). Symbols for units that consist of letters should be in plain text (e.g. ms^{-1}, K, min, mm, etc.). Please also see: http://physics.nist.gov/cuu/pdf/sp811.pdf .

Abbreviations should be spelt out in full on first appearance followed by the abbreviation in parentheses, e.g. variable time geometry (VTG). The meaning of symbols and units belonging to symbols should be explained in each case or cited in a **nomenclature** section at the end of the manuscript before the References.

Figures (figures, graphs, illustrations digital images, photographs) must be cited in consecutive numerical order in the text and referred to in both the text and the captions as Fig. 1, Fig. 2, etc. Figures should be prepared without borders and on white grounding and should be sent separately in their original formats. If a figure is composed of several parts, please mark each part with a), b), c), etc. and provide an explanation for each part in Figure caption. The caption should be self-explanatory. Letters and numbers should be readable (Arial or Times New Roman, min 6 pt with equal sizes and fonts in all figures). Graphics (submitted as supplementary files) may be exported in resolution good enough for printing (min. 300 dpi) in any common format, e.g. TIFF, BMP or JPG, PDF and should be named Fig1.jpg, Fig2.tif, etc. However, graphs and line drawings should be prepared as vector images, e.g. CDR, AI. Multi-curve graphs should have individual curves marked with a symbol or otherwise provide distinguishing differences using, for example, different thicknesses or dashing.

Tables should carry separate titles and must be numbered in consecutive numerical order in the text and referred to in both the text and the captions as Table 1, Table 2, etc. In addition to the physical quantities, such as t (in italics), the units [s] (normal text) should be added in square brackets. Tables should not duplicate data found elsewhere in the manuscript. Tables should be prepared using a table editor and not inserted as a graphic.

REFERENCES:

A reference list must be included using the following information as a guide. Only cited text references are to be included. Each reference is to be referred to in the text by a number enclosed in a square bracket (i.e. [3] or [2] to [4] for more references; do not combine more than 3 references, explain each). No reference to the author is necessary.

References must be numbered and ordered according to where they are first mentioned in the paper, not alphabetically. All references must be complete and accurate. Please add DOI code when available. Examples follow.

Journal Papers:
Surname 1, Initials, Surname 2, Initials (year). Title. Journal, volume, number, pages, DOI code.
[1] Hackenschmidt, R., Alber-Laukant, B., Rieg, F. (2010). Simulating nonlinear materials under centrifugal forces by using intelligent cross-linked simulations. *Strojniški vestnik - Journal of Mechanical Engineering*, vol. 57, no. 7-8, p. 531-538, DOI:10.5545/sv-jme.2011.013.
Journal titles should not be abbreviated. Note that journal title is set in italics.

Books:
Surname 1, Initials, Surname 2, Initials (year). Title. Publisher, place of publication.
[2] Groover, M.P. (2007). *Fundamentals of Modern Manufacturing*. John Wiley & Sons, Hoboken.
Note that the title of the book is italicized.

Chapters in Books:
Surname 1, Initials, Surname 2, Initials (year). Chapter title. Editor(s) of book, book title. Publisher, place of publication, pages.
[3] Carbone, G., Ceccarelli, M. (2005). Legged robotic systems. Kordić, V., Lazinica, A., Merdan, M. (Eds.), Cutting Edge Robotics. Pro literatur Verlag, Mammendorf, p. 553-576.

Proceedings Papers:
Surname 1, Initials, Surname 2, Initials (year). Paper title. Proceedings title, pages.
[4] Štefanić, N., Martinčević-Mikić, S., Tošanović, N. (2009). Applied lean system in process industry. *MOTSP Conference Proceedings*, p. 422-427.

Standards:
Standard-Code (year). Title. Organisation. Place.
[5] ISO/DIS 16000-6.2:2002. *Indoor Air – Part 6: Determination of Volatile Organic Compounds in Indoor and Chamber Air by Active Sampling on TENAX TA Sorbent, Thermal Desorption and Gas Chromatography using MSD/FID*. International Organization for Standardization. Geneva.

WWW pages:
Surname, Initials or Company name. Title, from http://address, date of access.
[6] Rockwell Automation. Arena, from *http://www.arenasimulation.com,* accessed on 2009-09-07.

EXTENDED ABSTRACT:

When the paper is accepted for publishing, the authors will be requested to send an **extended abstract** (approx. one A4 page or 3500 to 4000 characters). The instruction for composing the extended abstract are published on-line: http://www.sv-jme.eu/information-for-authors/ .

COPYRIGHT:

Authors submitting a manuscript do so on the understanding that the work has not been published before, is not being considered for publication elsewhere and has been read and approved by all authors. The submission of the manuscript by the authors means that the authors automatically agree to transfer copyright to SV-JME when the manuscript is accepted for publication. All accepted manuscripts must be accompanied by a Copyright Transfer Agreement, which should be sent to the editor. The work should be original work by the authors and not be published elsewhere in any language without the written consent of the publisher. The proof will be sent to the author showing the final layout of the article. Proof correction must be minimal and executed quickly. Thus it is essential that manuscripts are accurate when submitted. Authors can track the status of their accepted articles on http://en.sv-jme.eu/.

PUBLICATION FEE:

Authors will be asked to pay a publication fee for each article prior to the article appearing in the journal. However, this fee only needs to be paid after the article has been accepted for publishing. The fee is 380 EUR (for articles with maximum of 6 pages), 470 EUR (for articles with maximum of 10 pages), plus 50 EUR for each additional page. The additional cost for a color page is 90.00 EUR. These fees do not include tax.

Contents

Papers